Παντα ρει
Panta rhei
Everything flows
Alles fließt

(Simplikios)

The Creep Equilibrium Analysis Method (CrEAM)

A novel approach for the analysis of creeping slides
in soil and rock

presented by

Daniela Anna Engl

A dissertation submitted to the

GRAZ UNIVERSITY OF TECHNOLOGY

In conformity with the requirements for the degree of

DOCTOR OF SCIENCE

Statement of originality

I hereby confirm that the work described within this thesis is my original work, and that I have authored this thesis independently. Ideas and data from the work of others are fully acknowledged in accordance with the standard referencing practices.

Daniela Anna Engl
May 2013

Acknowledgements

I am very grateful to my two main supervisors, Scott Kieffer (Graz University of Technology) and Wolfgang Fellin (University of Innsbruck). Through the years, Scott and Wolfgang have been a constant and valuable source of support. Wolfgang has inspired and motivated me since the early days of this research and always has been open-minded for discussions on details and new ideas. Scott has always been positive and enthusiastic about my work and significantly enriched my research with his experience, visions and challenging questions. Their constructive comments during all stages of this dissertation were greatly appreciated. I feel very fortunate to have worked with both Scott and Wolfgang.

A very special thank is directed to Christian Zangerl. He gave me much freedom for my work and the opportunity to devise my own ideas within a fantastic team. It is an honour to be part of the alpS landslide group. Many thanks to him and my team collegues Christine Fey, Christoph Prager and Thomas Strauhal for pleasant conversations and discussions on geology and all other important issues of life.

Much thanks to the entire staff of the Division of Geotechnical and Tunnel Engineering at the University of Innsbruck for valuable feed back during the regular sci-

Table of Contents

Chapter 3
Constitutive models for describing time dependent deformation

Chapter 4
Limit Equilibrium Analysis Methods (LEAM's)

Chapter 5
The Creep Equilibrium Analysis Method (CrEAM) – Theoretical framework

Chapter 6
Case Studies

Chapter 7
Summary and Conclusions

Appendix

Acronyms

CrEAM   Creep Equilibrium Analysis Method

D-CrEAM^{inf} Deviatoric stress based CrEAM for infinite slopes
D-CrEAM^{rot} Deviatoric stress based CrEAM for rotational slides
D-CrEAM^{trans} Deviatoric stress based CrEAM for translational slides

DS   Strain-controlled direct shear strength test
DSc   Load-controlled direct shear creep test

E-CrEAM^{inf} Effective stress based CrEAM for infinite slopes
Simplified E-CrEAM^{rot} Simplified effective stress based CrEAM for rotational slides
Ordinary E-CrEAM^{rot} Ordinary effective stress based CrEAM for rotational slides
E-CrEAM^{trans} Effective stress based CrEAM for translational slides

HPBPSA   High Pressure Back Pressure Direct Shear Apparatus
HPTA   High Pressure Triaxial Apparatus

LEAM   Limit Equilibrium Analysis Method

TX   Strain-controlled triaxial strength test
TXc   Load-controlled triaxial creep test

Variables

α — Inclination of basal slip surface or creep interface [°]

$\boldsymbol{\varepsilon}$, $\boldsymbol{\varepsilon}^p$ — General and principal linearized strain tensor [-]

ε_{ii}, ε_{ij} — Normal and shear strain components [-]

ε_i — Principal strain [-]

$\dot{\boldsymbol{\varepsilon}}$, $\dot{\boldsymbol{\varepsilon}}^p$ — General and principal logarithmic strain rate tensor [s^{-1}]

$\dot{\varepsilon}_{ii}$, $\dot{\varepsilon}_{ij}$ — Normal and shear strain rate components [s^{-1}]

$\dot{\varepsilon}_i$ — Principal strain rate [s^{-1}]

$\dot{\varepsilon}_{vol}$ — Volume change rate [s^{-1}]

φ (φ_{peak}, φ_{res}) — Friction angle (peak, residual) [°]

γ — Wet (unsaturated) specific weight [N/m³]

γ_r — Saturated specific weight [N/m³]

γ_w — Specific weight of water [N/m³]

$\dot{\gamma}$ — Angular strain rate [s^{-1}]

η — Factor of Safety [-]

$\bar{\mu}^{Bingham}$ — Bingham shear viscosity [Pa s]

$\bar{\mu}^{Newton}$ — Newtonian shear viscosity [Pa s]

$\bar{\mu}^{Norton}$ — Norton shear viscosity [Pa^m s]

$\boldsymbol{\sigma}$, $\boldsymbol{\sigma}^p$ — General and principal Cauchy stress tensor [Pa]

$\boldsymbol{\sigma}_{dev}$, $\boldsymbol{\sigma}_{dev}^p$ — General and principal deviatoric stress tensor [Pa]

$\boldsymbol{\sigma}_{hyd}$ — Hydrostatic (spherical) stress tensor [Pa]

σ_{ii}, σ_{ij} — Normal and shear stress components [Pa]

σ_i — Principal stress [Pa]

σ_m — Mean normal stress [Pa]

σ_{devII} ($\sigma_{devII,f}$) — Second invariant of the deviatoric stress tensor (at failure) [Pa²]

$\sigma_{\dot{\gamma}}$ — Normal stress related to a viscous constitutive relationship [Pa]

σ_{η} — Normal stress related to a Factor of Safety calculation [Pa]

$\tau_{\dot{\gamma}}$	Shear stress related to a viscous constitutive relationship [Pa]
τ_{η}	Shear stress related to a Factor of Safety calculation [Pa]
$\tau_y^{Bingham}$	Bingham yield shear stress (creep threshold) [Pa]
τ_y^{Norton}	Modified Norton yield shear stress (creep threshold) [Pa]
τ_f	Shear stress at failure [Pa]
b	Slice width [m]
c (c_{peak}, c_{res})	Cohesion (peak, residual) [Pa]
d	Shear zone thickness [m]
h	Slice height [m]
h_w	Saturated slice height [m]
m^{Norton}	Norton exponent [-]
$m^{VH_{DP}}$	Original Vulliet-Hutter exponent [-]
$m^{VH_{MC}}$	Modified Vulliet-Hutter exponent [-]
n	Number of slices [-]
p_h, p_v	Horizonal and vertical surcharge stress [Pa]
r	Radius of slip circle or creep interface [m]
u	Hydrostatic water pressure [Pa]
v	Creep velocity [m/s]
$A^{VH_{DP}}$	Original Vulliet-Hutter rate factor [s^{-1}]
$A^{VH_{MC}}$	Modified Vulliet-Hutter rate factor [s^{-1}]
C	Cohesion force [N]
$E'_{\dot{\gamma}}$	Effective interslice (earth pressure) force related to CrEAM [N]
E'_{η}	Effective interslice (earth pressure) force related to LEAM [N]
M	Moment [Nm]
$N_{\dot{\gamma}}$	Total normal force related to CrEAM [N]
N_{η}	Total normal force related to LEAM [N]
P_h, P_v	Horizontal and vertical surcharge load forces [N]
$T_{\dot{\gamma}}$	Shear force related to CrEAM [N]
T_{η}	Shear force related to LEAM [N]
U	Water pressure force [N]
W	Weight force [N]

CHAPTER 1

Introduction

1.1 Preamble

Slow landslides are widespread in hilly terrains and alpine regions all over the world. The displacement rates are in the range of millimetres to metres per year, and therefore, these mass movements are commonly referred to as creeping landslides. They occur both in deep soil profiles and solid rock and can involve large areas or even entire valley flanks. Many of them are located in remote and isolated regions and usually remain unrecognized. However, whenever creeping landslides interfere with human settlements and infrastructure, progressive slope movements lead to disturbance and damage, sometimes with enormous social and economic impacts (Glastonbury & Fell 2008b; Mansour et al. 2011).

This thesis is dedicated to the better understanding of creeping landslides and related phenomena and, thereby, aims to contribute to the mitigation of socio-economic effects.

This first chapter introduces in the central theme of this thesis, by considering the following issues:

▪ **What are creeping landslides and where do they occur?**
Section 1.2 introduces to the phenomenon of creeping landslides and defines the object of research.

- **Who is affected, why is it important?**

Section 1.3 gives insight in the abundance and variety of the phenomenon and emphasizes the manifold impacts of creeping landslides on society.

- **What is the purpose of this work?**

The motivation and intentions for this specific research are described and discussed in Section 1.4.

- **What is the fundamental hypothesis?**

Section 1.5 formulates the central research question of this thesis.

- **How is the problem investigated?**

The research methods applied for the examination of the hypothesis are presented in Section 1.6.

- **What has been achieved?**

Section 1.7 briefly summarizes the most important results achieved in this work.

The concluding Section 1.8 provides an overview of the structure of the thesis and, thereby, establishes the thread through the following chapters.

1.2 Characteristics of creeping landslides

The term "creep" is widely used in hillslope studies (e.g. Bonzanigo et al. 2007; Chigira 1992; Noverraz 1996; Mahr & Nemcok 1977; Puzrin & Schmid 2011; Peteley & Allison 1997; Radbruch-Hall 1978; Schneider-Muntau 2012; Tavenas & Leroueil 1981; Ter-Stepanian 1966 & 1975). Commonly, it refers to the slow motion of a slope, whereas the underlying processes may be manifold and the distinctions between them often remain unrecognised and unaccounted (Selby 1993). In this thesis, the term "creep" is exclusively used in the engineering sense, hence denoting viscous deformation of material.

There are two basic requirements of a system in order to creep:
- one or more component(s) of the system have viscous properties; and
- movement is kinematically possible, thus strain is not externally constrained

Both requirements are fulfilled for many slopes both in soil and rock.

Natural and engineered slopes consist of geomaterials which exhibit viscous behaviour. Clays are reported to show the most significant viscous behaviour (e.g. Feda 1992; Mitchell 1993; Leroueil & Marques 1996; Ter-Stepanian 1975; Krieg 2000). To a comparatively smaller degree, time dependent deformation is also observed in sands and similar materials (e.g. Di Benedetto & Tatsuoka 1997; Lade & Liu 1998; Bowman & Soga 2003). Even intact specimens of high-strength igneous and metamorphic rock exhibit creep behaviour at low stresses and surface temperatures (e.g. Lomnitz 1955; Singh 1975).

The second requirement of kinematical freedom is intrinsically satisfied by slopes, since slopes are bounded by the free space and are, hence, able to move into it. The potential mechanisms of slope movement are variable (e.g. Varnes 1978) and depend on multiple factors e.g. rheology of the involved materials, slope geometry, structural predisposition, etc. Numerous creeping slopes move with a sliding mechanism (e.g. Noverraz 1996). The main deformation localizes within one or more shear horizons while the bulk mass experiences minor deformation.

Such strain concentrations in the slope are in practice detected by subsurface monitoring at selected points, e.g. inclinometer and extensometer records (e.g. Thüringer Fernwasserversorgung 2007; Zangerl et al. 2010a), or less commonly, measurements on plumb line sequences (e.g. Barla et al. 2010c). Similar observations at different locations in the slope suggest the existence of one (or more) coherent shear zone(s). Figure 1.1 exemplifies a cross-section as well as surface and subsurface monitoring data of a creeping landslide.

Movement horizons commonly follow preexisting structures, e.g. primarily weak layers or tectonic faults (e.g. Agliardi et al. 2001; Ambrosi & Crosta 2006; Massironi et al. 2003; compare also with the Utiku landslide in Section 6.3) or originate from previous landslide movement (e.g. Chigira 1992; Chigira & Kiho 1994; compare also with the Beauregard rockslide in Section 6.2). They usually contain sheared soil or highly disintegrated and crushed bedrock material with soil-like characteristics (kakirites, gouges). Laboratory testing of such shear zone materials show time dependent deformation behaviour (Martinotti 2010; Renk 2006; Schneider-Muntau 2012) that reflect a viscous rheology.
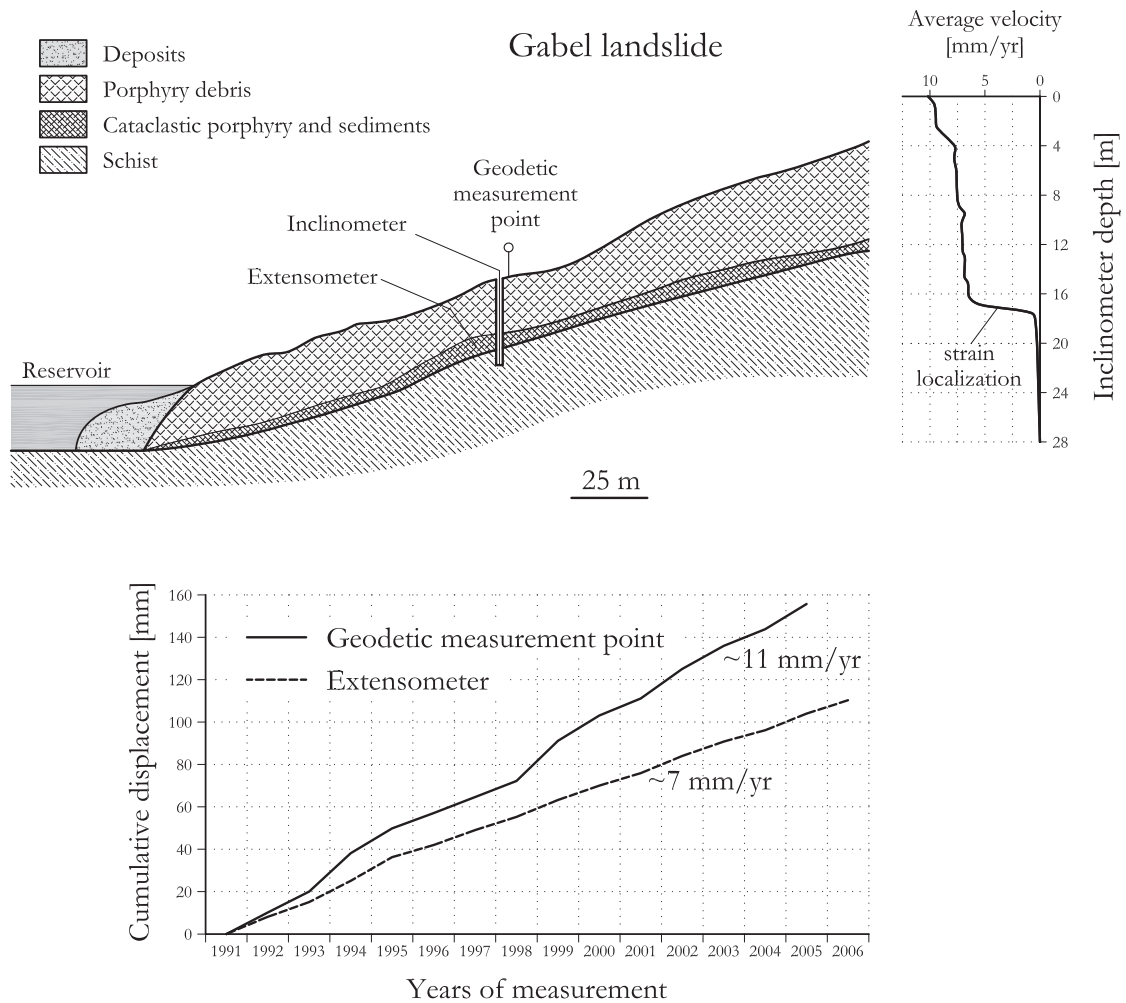
Figure 1.1

Gabel landslide at the Schönbrunn reservoir (Thüringen, Germany) (modified after Thüringer Fernwasserversorgung 2007)

Top left : Geological cross-section of the landslide mass, indicating the location of inclinometer, extensometer and geodetic measurement point. Top right: Vertical velocity profile deduced from inclinometer data. Inclinometer measurements indicate a strong strain localization in a distinct zone between 16.5-17.5 m depth.

Bottom: Cumulative displacement at the geodetic measurement point on the slope surface and the extensometer at the landslide base. The slope velocity is approximately constant in time.

Creep deformation of shear zone material therefore induces slope movements, even when the stress state within the slope is more favorable than that required for the traditional limit equilibrium (failure) condition (Leroueil 2001). This state is concisely pointed out by Vulliet & Hutter 1988b with the statement: "The slope is neither still nor ruptured but simply moves".

Accordingly, the landslide velocity does not abruptly vary from zero when the Factor of Safety is larger than or equal to 1, to infinity when it becomes less than 1, but progressively increases when the slope evolves from a stable state towards a limit equilibrium state (Fell et al. 2000; Tavenas & Leroueil 1981). This inverse correlation of the Factor of Safety and slope velocity was noted by many authors, e.g. Eshraghian et al. 2008b; Hutchinson 1988; Leroueil 2001; Morgenstern 1995; Vulliet & Hutter 1988b.

1.3 Socio-economic effects of creeping landslides

Case studies of creeping landslides are numerously reported in literature (amongst others: Bonzanigo et al. 2007; Chigira 1992; Glastonbury & Fell 2008a,b; Mansour et al. 2011; Schneider-Muntau 2012; Tavenas & Leroueil 1981). They are found in all types of environments, in various types of rock and soil, and with a wide range of sizes and volumes, from small-scale to large-scale and shallow-seated to deep-seated.

The comprehensive description and investigation of creeping landslides originates in their common interaction with urban areas, roads, railway lines, hydropower reservoirs, etc. (e.g. Barla et al. 2005, 2006, 2010c; Bonzanigo et al. 2007; Cascini et al. 2005; Eshraghian et al. 2008a,b; Francois et al. 2007; Massey 2010; Puzrin & Schmid 2011; Schneider-Muntau 2012; Zangerl et al. 2010a). The majority of these slopes exhibit displacement rates in the range of millimetres to metres per year. For constant slope conditions, the velocities are usually quasi-continuous, indicating that the respective system is in a steady-state regime. Changing boundary conditions, e.g. groundwater level drops or rises and/or loading/unloading of the slope surface, modify the stress regime in the slope and are, thus, usually accompanied by observable changes in the slope displacement rate (e.g. Calvello et al. 2008; Corominas et al. 2005; Glastonbury & Fell 2008b; Mansour et al. 2011; Massey 2010; Picarelli et al. 2004; Schneider-Muntau 2012).

Table 1.1 summarizes a selection of well-investigated creeping slides and gives insight in the geological setting, the creep velocity range and the socio-economic relevance. The list is however far from being exhaustive.

Table 1.1
A selection of creeping slides and their geological setting, velocity range and socio-economic relevance.

Name (Location)	Geological setting	Velocity range	Relevance	Reference(s)
Åknes rockslide (Norway)	Orthogneiss	50-60 mm/yr	Potential tsunami	Grøneng el al. (2010)
Beauregard rockslide (Italy)	Mica schist and paragneiss	3-5 mm/yr	Hydropower reservoir	Barla et al. (2010c)
Ca' Lita landslide (Italy)	Flysch (arenites and pelites)	up to several m/d	Urban area nearby	Borgatti et al. (2006)
Campo Vallemaggia (Switzerland)	Gneisses, mica schists, carbonates	50 mm/yr	Urban area	Bonzanigo et al. (2007)
Downie rockslide (Canada)	Schists, gneisses, quartzites	5-25 mm/yr	Hydropower reservoir	Kalenchuk (2010)
Hochmais landslide (Austria)	Paragneiss debris on moraine	20-30 mm/yr	Hydropower reservoir	Schneider-Muntau (2012), Zangerl et al. (2010a)
Panagopoula landslide (Greece)	Flysch	5-12 mm/yr	Highway and rail line	Koukis et al. (2009)
Gabel landslide (Germany)	Boundary metamorph basement /porphyry cover	3-15 mm/yr	Drinking water reservoir	Thüringer Fernwasserversorgung (2007)
Taihape landslide (New Zealand)	Siltstone with thin clay seams	15 mm /yr	Urban area	Massey (2010)
Tessina landslide, Pian de Cice (Italy)	Flysch	30-60 mm/yr	Urban area nearby	Marcato et al. (2009)
Triesenberg landslide (Liechtenstein)	Schists, limestones, sandstones, flysch	0-30 mm/yr	Various infrastructure	Francois et al. (2007)
Vallcebre landslide (Spain)	Siltstones and shales	3-14 mm/d	Urban area nearby	Ferrari et al. (2011)
Utiku landslide (New Zealand)	Siltstone with thin clay seams	up to 15 mm/d	Highway and railway line	Massey (in press)

In many cases, slight changes in the slope effective stress conditions induce significant slope velocity increases or decreases (e.g. Eshraghian et al. 2008b; Massey et al. in press, see also Section 6.3). The latter reflect the nonlinear creep behaviour of shear zone materials as observed on the laboratory scale (e.g. Schneider-Muntau 2012; Vulliet & Hutter 1988a).

Whenever such creeping landslides interfere with human settlements and infrastructure, damage and disturbance are common. The slow but progressive slope movements may result in an enormous socio-economic significance for the individual, private enterprises and public authorities (e.g. Barla et al. 2005, 2006, 2010c; Cascini et al. 2005; Puzrin & Schmid 2011; Thuro et al. 2004). Differential ground movements can lead to visible damages on buildings, traffic and transportation routes as well as supply lines, and cause high maintenance costs for these structures (e.g. Francois et al. 2007; Gündogdu 2011; Koukis et al. 2009). When highly sensitive systems, as e.g. railway lines, are involved, even small slope movements can bear an enormous risk (e.g. Eshraghian et al. 2008a; Koukis et al. 2009; Massey et al. in press). Slow slope deformation may further be a crucial aspect in the design and operation of oil and gas pipelines, which run over large distances and often unavoidably cross mountainous areas with numerous creeping slopes (e.g. Chan 1999). In many cases, a sound understanding of the slope processes can assist in minimizing hazard and maintenance costs, extending the life span of the infrastructure, and avoiding supply breakdowns (e.g. Puzrin & Schmid 2011; Bonzanigo et al. 2007).

Numerous creeping landslides are known in the context of artificial water reservoirs for hydropower energy production and drinking water storage. The impacts are manifold and the relevance is usually high (e.g. Barla et al. 2005, 2006, 2010c; Kalenchuk 2010; Macfarlane 2009; Schneider-Muntau 2012; Thüringer Fernwasserversorgung 2007; Zangerl et al. 2010a). On one hand, slope movements can directly affect construction elements of reservoirs. Prominent examples are creeping abutment slopes, which impinge and subsequently damage dam structures (e.g. Barla et al. 2005, 2006, 2010c and Figure 1.2, see also Section 6.2); or adits, tunnels and pressure shafts which are deformed or sheared off by progressive slope movements (e.g. Thuro et al. 2004; Zangerl et al. 2010a and Figure 1.3).

Figure 1.2
Beauregard reservoir (Aosta Valley, Italy)
Top: The reservoir is kept at less than 10% of its capacity due to
instability concerns, as progressive creep of the left abutment slope
damaged the arch-gravity dam (inset in lower left corner).
Bottom: Open joints in the left abutment slope.
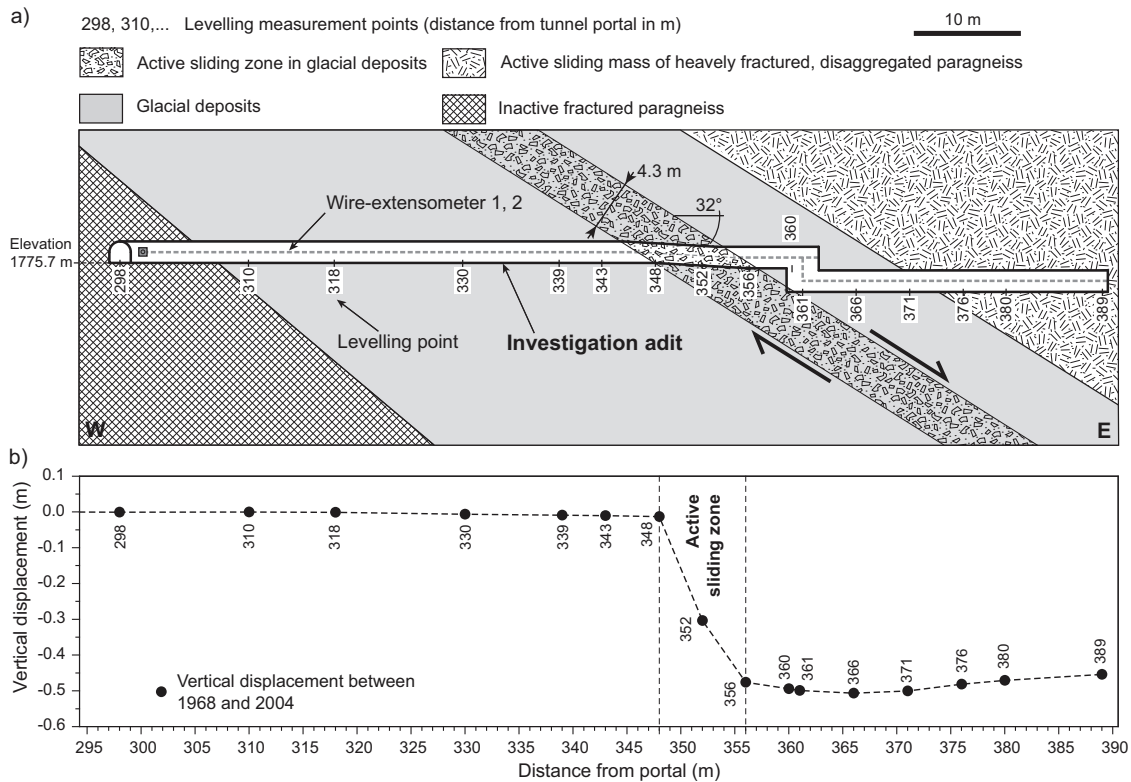
Figure 1.3
Hochmais landslide at the Gepatsch reservoir (Tyrol, Austria)
a) The investigation adit through the landslide mass was sheared off by
landslide movement b) Vertical displacement measured on levelling
points in the adit in the period 1968 – 2004 (from Zangerl et al. 2010a).

On the other hand, the reservoir management directly affects the stress conditions and, thus, the behaviour of the creeping slope (e.g. Barla et al. 2006; Schneider-Muntau 2012; Zangerl et al. 2010a and Figure 1.4). The slope response on the cyclic stress redistribution caused by the seasonal filling and emptying of the reservoir must be comprehensively understood in order to ensure a safe and sustainable reservoir management.
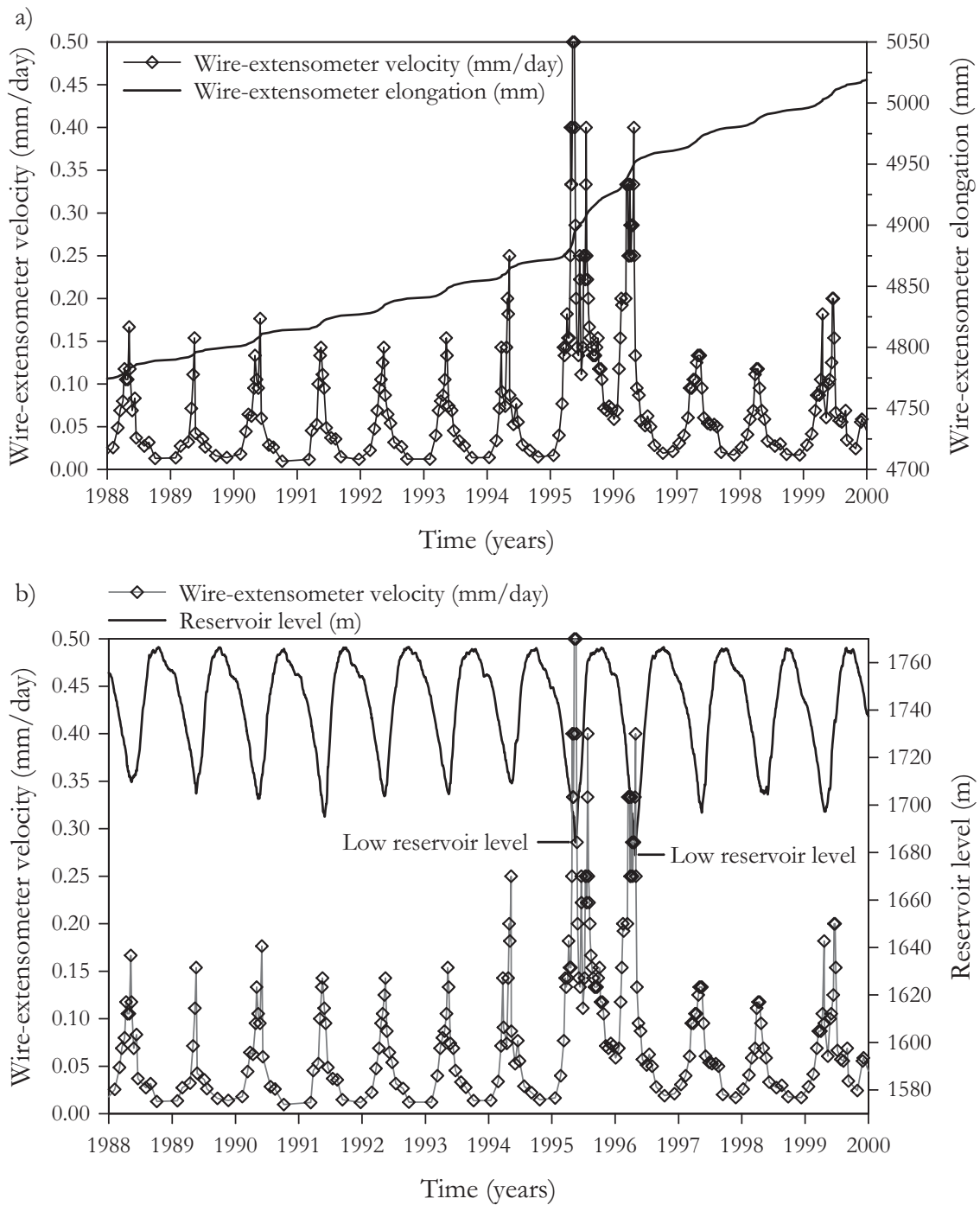
Figure 1.4
Hochmais landslide at the Gepatsch reservoir (Tyrol, Austria)
a) Measured elongation of a horizontal wire-extensometer installed in an investigation adit through the landslide, and deduced horizontal slope velocity b) Time dependent variation of horizontal slope velocity and reservoir level (from Zangerl et al. 2010a).

1.4 Motivation and vision

Our increasing need of space for civil, industrial and agricultural activities in mountainous regions fosters our endeavours to understand and potentially influence the behaviour of creeping slopes (e.g. Cascini et al. 2005). In many situations, this is feasable with acceptable efforts. In other cases, technical remedies against slope movement may be practically impossible, economically inefficient or environmentally intolerable (e.g. Mansour et al. 2011).

The thorough understanding of the present state of a creeping landslide facilitates to design potential mitigation measures, and evaluate them in terms of efficiency. Therefore, successfull replication of the present landslide behaviour can be the first step towards successfull mitigation in the future.

Having this in mind, a novel analytical analysis method for the investigation of creeping slide behaviour is developed and tested within the framework of this thesis. This is intended to provide practitioners and academics with a simple but valuable analysis tool.

1.5 Hypothesis

The focus of this work are creeping landslides which are characterised by
- strain localization within a basal viscous shear zone; and
- steady-state displacement behaviour

Figure 1.1 showed a representative example for this type of landslide.

The fundamental hypothesis of this work includes:
- Based on the strain localization, it is hypothesised that a rigid-element based modelling approach with viscous flow (creep) considerations within the basal shear zone is suitable for assessing the temporal deformation behaviour of these landslides.
- Based on the steady-state displacement behaviour, it is hypothesised that these landslides are in a state of quasi-static equilibrium and, therefore, equilibrium considerations are suitable to describe the slope system.

1.6   Research methods

The above hypothesis is investigatd by combining concepts of geotechnics and engineering geology in an innovative way.

Research methods include:

- Conception and elaboration of an analytical modelling approach for the analysis of creeping landslide behaviour, based on mechanical principles including rheology, statics and fluid statics, and kinematics

- Model algorithm development and programming

- Interpretation of exploration and monitoring data of case studies

- Analysis of laboratory creep experiments

- Modelling (forward and back analyses of creeping landslide behaviour)

1.7 Results

A new analysis tool referred to as CrEAM (Creep Equilibrium Analysis Method) is developed and tested within the framework of this research. This dissertation presents the theoretical background of CrEAM, and two case study applications.

CrEAM combines concepts of steady viscous flow (secondary creep), kinematics, and equilibrium of forces and moment within an analytical slice-based calculation scheme. Different CrEAM variants consider different sliding mechanisms, various constitutive relationships, and different assumptions for the action of interslice forces.

The case study results indicate that the analytical approach is capable of replicating the global displacement characteristics of creeping landslides (e.g. Figure 1.5). CrEAM requires relatively few input parameters and is characterised by a low calculation effort. It is therefore well suited for back calculations and comprehensive sensitivity analyses.
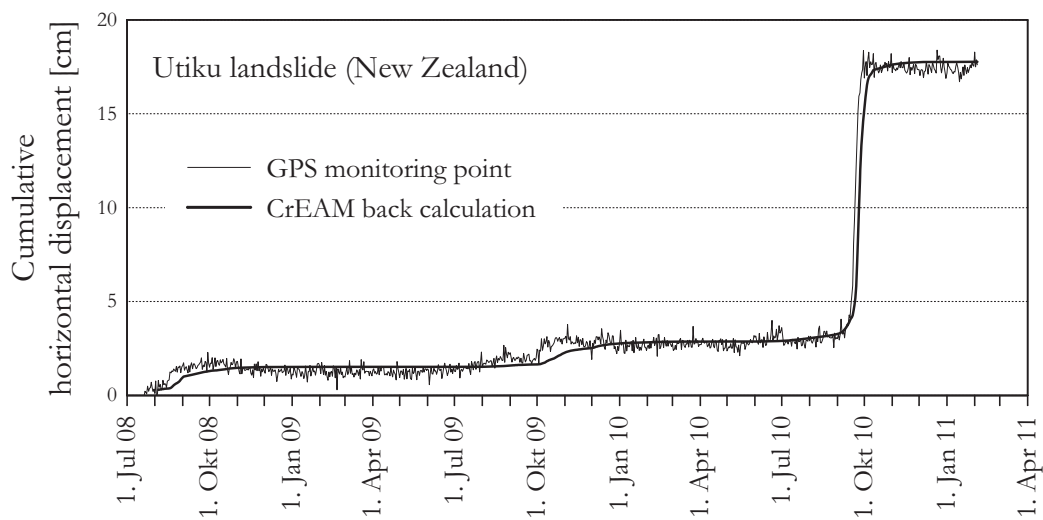
Figure 1.5
Monitored and back calculated displacement of the Utiku landslide.

1.8 Thesis structure

This thesis is subdivided into seven chapters.

After the general introduction to the topic in Chapter 1, the reader is inducted into the basic concepts of stress and viscous deformation in Chapter 2. The principles of stress and strain decomposition are presented since they are highly relevant for the constitutive relationships in Chapter 3. Furthermore, creep behaviour is identified as a multi-stage process. It is highlighted why the long-lasting intermediate stage i.e. the steady-state creep process is of special interest for this work.

Chapter 3 presents different constitutive models, which aim to establish a relationship between stress state and resulting time dependent deformation in terms of mathematical formulations. Two basic approaches are distinguished, i.e. deviatoric stress and effective stress based viscous formulations. Five viscous models are introduced in a general mathematical shape and subsequently developed towards plane strain formulations, which later are required for developing a two-dimensional analysis approach for creeping landslides.

Chapter 4 is dedicated to a review of conventional limit equilibrium stability analysis methods (LEAM's), as their principles will re-appear in the derivations in Chapter 5. Limit equilibrium stability analysis provides an index value i.e. the Factor of Safety, as a dimensionless measure of slope stability, and plays a strong role in the practice of slope failure prediction. However, limit equilibrium stability analysis is not able to account for time dependent effects of slope deformation.

Many landslides exhibit a Factor of Safety > 1 but nevertheless they move steadily due to time dependent material behaviour. In Chapter 5, an approach for calculating these "subcritical" slope deformations in time is presented. For this purpose, equilibrium requirements are merged with viscous constitutive relationships and kinematical constraints, yielding the novel analytical approach CrEAM (acronym for Creep Equilibrium Analysis Method). In contrast to the conventional limit equilibrium stability analysis, CrEAM is able to describe time dependent slope deformation by means of a physical measure i.e. the landslide creep velocity.

The theoretical framework of CrEAM in Chapter 5 is complemented with a selection of illustrative examples, which demonstrate the CrEAM application for the infinite slope condition. They aim to show the use and functionality of the formulas in a reproducible manner. Moreover, accompanying sensitivity analyses give the reader important insights to the characteristics of CrEAM modelling.

The application of CrEAM to two case studies, the Beauregard rockslide in Italy and the Utiku landslide in New Zealand, is comprehensively documented in Chapter 6. The case studies show the detailed analysis and interpretation of laboratory data and field measurements.

Modelling is subsequently performed in terms of both forward calculations using the material parameters as obtained by laboratory testing, and back calculations based on observed slope displacements. These practical case study analyses aim both to evaluate the novel methodology and to give stimulations how CrEAM can be applied for future landslide studies.

The concluding Chapter 7 summarizes the contribution of this thesis. Basic concepts and characteristics of CrEAM are reviewed, together with the limitations of the approach. The key findings from case studies are highlighted and proposals for further practical applications are presented. Finally, recommendations for future research questions aim to motivate further scientific work in the area of creeping slopes.

—

The author aimed to keep the main part of this thesis as slim as possible, in order to make it tractable for the reader to follow. Nevertheless, valuable details and background knowledge shall not be lost. The Appendix comprises additional information and derivations. They are not essential for understanding the central theme, but helpful for the interested reader, who wants to delve into the topic in more detail

CHAPTER 2

The concepts of stress and viscous behaviour

2.1 Preamble

This chapter introduces to appropriate mathematical formulations for stress and strain which later become essential for describing the relationship between the stress state and the viscous response of a material. The typical phenomenologic stages of creep behaviour are highlighted and their role in the context of this thesis specified. Moreover, concepts and laboratory observations pertaining to the micromechanical processes and scale effects of creep are presented.

2.2 Stress - strain - strain rate

In its most general form, the stress state inducing viscous deformation can be expressed as a three-dimensional Cauchy tensor $\boldsymbol{\sigma}$ composed of the normal stress components σ_{ii} and the shear stress components σ_{ij}

$$\boldsymbol{\sigma} = \begin{bmatrix} \sigma_{11} & \sigma_{12} & \sigma_{13} \\ \sigma_{21} & \sigma_{22} & \sigma_{23} \\ \sigma_{31} & \sigma_{32} & \sigma_{33} \end{bmatrix} \tag{2.1}$$

Satisfying the equilibrium of moment implies that the stress tensor is symmetric i.e. that the shear stresses on perpendicular planes are equal in magnitude, and perpendicularly point either towards to or away from the intersection line of the planes.

Therefore:

$$\sigma_{21} = \sigma_{12}, \qquad \sigma_{32} = \sigma_{23}, \qquad \sigma_{31} = \sigma_{13}^{1} \tag{2.2}$$

In terms of principal stresses (2.1) can be expressed as

$$\boldsymbol{\sigma}^P = \begin{bmatrix} \sigma_1 & 0 & 0 \\ 0 & \sigma_2 & 0 \\ 0 & 0 & \sigma_3 \end{bmatrix} \quad \text{with} \quad \sigma_1 \geq \sigma_2 \geq \sigma_3 \tag{2.3}$$

The strain associated with the stress state $\boldsymbol{\sigma}$ (2.1) at a time t can be expressed with a corresponding linearized strain tensor $\boldsymbol{\varepsilon}$ composed of the normal strain components ε_{ii} and the shear strain components ε_{ij}

$$\boldsymbol{\varepsilon} = \begin{bmatrix} \varepsilon_{11} & \varepsilon_{12} & \varepsilon_{13} \\ \varepsilon_{21} & \varepsilon_{22} & \varepsilon_{23} \\ \varepsilon_{31} & \varepsilon_{32} & \varepsilon_{33} \end{bmatrix} \tag{2.4}$$

Equivalent to (2.2), the symmetry of shear strains implicates

$$\varepsilon_{21} = \varepsilon_{12}, \qquad \varepsilon_{32} = \varepsilon_{23}, \qquad \varepsilon_{31} = \varepsilon_{13} \tag{2.5}$$

In terms of principal strains (2.4) can be expressed as

$$\boldsymbol{\varepsilon}^P = \begin{bmatrix} \varepsilon_1 & 0 & 0 \\ 0 & \varepsilon_2 & 0 \\ 0 & 0 & \varepsilon_3 \end{bmatrix} \tag{2.6}$$

The linearized strain $\boldsymbol{\varepsilon}$ is the symmetric part of the displacement gradient

$$\boldsymbol{\varepsilon} = sym \ grad\,(\mathbf{u}) \tag{2.7}$$

---

[1] The stress tensor symmetry satisfies the Boltzmann axiom, also referred to as the theorem of conjugate shear stresses. According Betten (2002, p. 44) the symmetry is not strictly applicable to damaged material.

where $\mathbf{u}$ is the displacement field and the components of $\boldsymbol{\varepsilon}$ are defined as

$$\varepsilon_{ij} = \frac{1}{2}\left(\frac{\partial u_i}{\partial x_j} + \frac{\partial u_j}{\partial x_i} \right) \tag{2.8}$$

The symmetric part of the velocity gradient is the stretching (stretch rate) $\mathbf{D}$

$$\mathbf{D} = sym\ grad(\mathbf{v}) \tag{2.9}$$

where $\mathbf{v}$ is the velocity field. Note, that the stretching $\mathbf{D}$ is generally not equal to the time derivative of the strain measurement. However, for small rotations the following simplification can be made

$$\mathbf{D} \approx \dot{\boldsymbol{\varepsilon}} = \frac{d\boldsymbol{\varepsilon}}{dt} = \frac{1}{dt} \cdot d \begin{bmatrix} \varepsilon_{11} & \varepsilon_{12} & \varepsilon_{13} \\ \varepsilon_{21} & \varepsilon_{22} & \varepsilon_{23} \\ \varepsilon_{31} & \varepsilon_{32} & \varepsilon_{33} \end{bmatrix} = \begin{bmatrix} \dot{\varepsilon}_{11} & \dot{\varepsilon}_{12} & \dot{\varepsilon}_{13} \\ \dot{\varepsilon}_{21} & \dot{\varepsilon}_{22} & \dot{\varepsilon}_{23} \\ \dot{\varepsilon}_{31} & \dot{\varepsilon}_{32} & \dot{\varepsilon}_{33} \end{bmatrix} \tag{2.10}$$

while for strictly rectilinear deformation $\mathbf{D}$ is equal to the time derivative of $\boldsymbol{\varepsilon}$

$$\mathbf{D} = \frac{d\boldsymbol{\varepsilon}}{dt} = \dot{\boldsymbol{\varepsilon}} \tag{2.11}$$

where $\boldsymbol{\varepsilon}$ here represents the logarithmic strain[2]. In particular, (2.11) holds for uniaxial and triaxial settings in geotechnical laboratory experiments.

Therefore, the rate of the logarithmic strain $\dot{\boldsymbol{\varepsilon}}$ is used instead of the stretching rate $\mathbf{D}$ in this thesis to describe the viscous deformation in time.

Depending on how viscous strain accumulates with time under a constant stress state $\boldsymbol{\sigma}$, three clearly specified stages of viscous deformation can be differentiated, i.e. primary, secondary and tertiary creep (see Section 2.5).

---

[2]   Strain is usually computed by comparing the final state with the initial state of a deforming body. This strain is commonly referred to as the engineering strain. However, when large deformations are encountered, the initial length cannot longer be taken as reference to determine the differential strain increments. Taking into account the continuous variation of length and, thus, the instantaneous length just before each strain increment, strain is denoted as the logarithmic strain. For small deformations the differences between engineering and logarithmic strain are small and can be neglected.

2.3 Stress decomposition

Determining the mean normal stress σ_m as the arithmetic mean of the normal stress components σ_{ii} in (2.1) and (2.3), respectively,[3]

$$\sigma_m = tr(\boldsymbol{\sigma}) = \frac{\sigma_{11} + \sigma_{22} + \sigma_{33}}{3} = \frac{\sigma_1 + \sigma_2 + \sigma_3}{3} \tag{2.12}$$

enables to decompose the stress tensor (2.1) into a hydrostatic (spherical) and deviatoric stress portion

$$\boldsymbol{\sigma} = \boldsymbol{\sigma}_{hyd} + \boldsymbol{\sigma}_{dev}$$

$$\begin{bmatrix} \sigma_{11} & \sigma_{12} & \sigma_{13} \\ \sigma_{21} & \sigma_{22} & \sigma_{23} \\ \sigma_{31} & \sigma_{32} & \sigma_{33} \end{bmatrix} = \underbrace{\begin{bmatrix} \sigma_m & 0 & 0 \\ 0 & \sigma_m & 0 \\ 0 & 0 & \sigma_m \end{bmatrix}}_{hydrostatic} + \underbrace{\begin{bmatrix} \sigma_{11} - \sigma_m & \sigma_{12} & \sigma_{13} \\ \sigma_{21} & \sigma_{22} - \sigma_m & \sigma_{23} \\ \sigma_{31} & \sigma_{32} & \sigma_{33} - \sigma_m \end{bmatrix}}_{deviatoric} \tag{2.13}$$

Introducing (2.12) into the first portion of the right hand side of (2.13) yields the hydrostatic component of the stress tensor as

$$\boldsymbol{\sigma}_{hyd} = \frac{\sigma_{11} + \sigma_{22} + \sigma_{33}}{3} \begin{bmatrix} 1 & 0 & 0 \\ 0 & 1 & 0 \\ 0 & 0 & 1 \end{bmatrix} = \frac{\sigma_1 + \sigma_2 + \sigma_3}{3} \begin{bmatrix} 1 & 0 & 0 \\ 0 & 1 & 0 \\ 0 & 0 & 1 \end{bmatrix} \tag{2.14}$$

Introducing (2.12) into the second portion of the right hand side of (2.13) yields the deviatoric component of the stress tensor as

$$\boldsymbol{\sigma}_{dev} = \frac{1}{3} \begin{bmatrix} 2\sigma_{11} - \sigma_{22} - \sigma_{33} & 3\sigma_{12} & 3\sigma_{13} \\ 3\sigma_{21} & 2\sigma_{22} - \sigma_{11} - \sigma_{33} & 3\sigma_{23} \\ 3\sigma_{31} & 3\sigma_{32} & 2\sigma_{33} - \sigma_{11} - \sigma_{22} \end{bmatrix} \tag{2.15}$$

For principal stresses the deviatoric stress tensor (2.15) reduces to

$$\boldsymbol{\sigma}_{dev}^p = \frac{1}{3} \begin{bmatrix} 2\sigma_1 - \sigma_2 - \sigma_3 & 0 & 0 \\ 0 & 2\sigma_2 - \sigma_1 - \sigma_3 & 0 \\ 0 & 0 & 2\sigma_3 - \sigma_1 - \sigma_2 \end{bmatrix} \tag{2.16}$$

---

[3] The mean stress is independent of the stress tensor orientation and therefore invariant.

2.4 From triaxial strain to plane strain

Many geotechnical problems can be approximated with plane strain conditions, provided that relevant boundary conditions are sufficiently remote. The three-dimensional stress state and strain rate may be reduced to two-dimensonal expressions in such cases.

Assuming plane strain conditions and, thus, suppressing all deformations in the third dimension (here defined as the x_2-coordinate axis) implies that all components of the strain rate tensor $\dot{\boldsymbol{\varepsilon}}$ relating to the x_2- direction are zero

$$\dot{\varepsilon}_{12} = \dot{\varepsilon}_{23} = \dot{\varepsilon}_{22} = 0 \tag{2.17}$$

which is a reasonable assumption for a system with a very large extension in the third coordinate direction. Considering the strain symmetry relationships (2.5), and introducing the requirements for plane strain given in (2.17) changes the triaxial strain rate tensor (2.10) to the plane strain rate tensor

$$\dot{\boldsymbol{\varepsilon}} = \begin{bmatrix} \dot{\varepsilon}_{11} & 0 & \dot{\varepsilon}_{13} \\ 0 & 0 & 0 \\ \dot{\varepsilon}_{13} & 0 & \dot{\varepsilon}_{33} \end{bmatrix} \tag{2.18}$$

In terms of principal strain rates, (2.18) can be expressed as

$$\dot{\boldsymbol{\varepsilon}}^p = \begin{bmatrix} \dot{\varepsilon}_{1} & 0 & 0 \\ 0 & 0 & 0 \\ 0 & 0 & \dot{\varepsilon}_{3} \end{bmatrix} \tag{2.19}$$

The overall volume change rate, $\dot{\varepsilon}_{vol}$, is determind by the sum of the normal strain components in (2.18) and (2.19), respectively, [4]

$$\dot{\varepsilon}_{vol} = tr(\dot{\boldsymbol{\varepsilon}}) = \dot{\varepsilon}_{11} + \dot{\varepsilon}_{33} = tr(\dot{\boldsymbol{\varepsilon}}^p) = \dot{\varepsilon}_{1} + \dot{\varepsilon}_{3} \tag{2.20}$$

For constant volume deformation, thus $\dot{\varepsilon}_{vol} = 0$, the normal strains in the plane are opposed in sign but equal in the absolute value, therefore $\dot{\varepsilon}_{33} = -\dot{\varepsilon}_{11}$ and $\dot{\varepsilon}_{3} = -\dot{\varepsilon}_{1}$.

---

[4]   The volumetric strain rate is independent of the strain tensor orientation and therefore invariant.

2.5 Primary, secondary, tertiary creep

By plotting the viscous strain observed during a constant stress setting versus time, a characteristic creep curve is obtained (Figure 2.1a). Based on morphological features, the creep curve can be subdivided into three sections referred to as the primary, secondary and tertiary creep stage. These terms were first introduced by Andrade (1910) and relate to a decreasing, constant and increasing strain rate, respectively (Figure 2.1b).
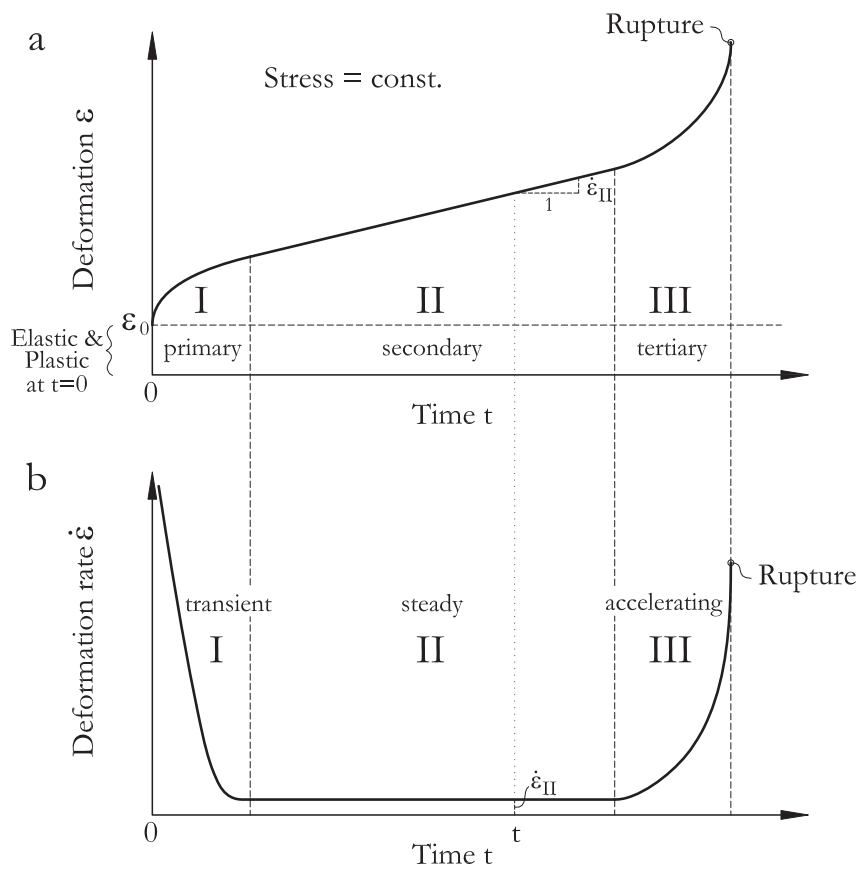
Figure 2.1
a) The characteristic creep curve in a deformation versus time diagram shows three distinct stages of creep (modified after Emery 1971). The slope of the creep curve represents the creep rate at the respective instant of time b) Plotting the creep rates versus time shows the transient (I), steady (II) and accelerated (III) deformation behaviour.

The primary (transient) creep stage is characterised by initially high viscous strains with strain accumulation subsequently gradually decreasing with time, displaying a monotonic decreasing strain rate and, therefore, a kind of strain hardening material behaviour (Figure 2.1, stage I). Primary creep commonly goes along with a significant volume reduction which is attributed to the internal structural reorganisation of the material particles (Emery 1971; see also Section 2.6).

As soon as a specific minimum value is achieved, the strain rate persists, causing viscous deformation to accumulate proportional to time. This constant viscous deformation is referred to as material flow or secondary (steady) creep (Figure 2.1, stage II). During this stage the volume of the specimen usually remains constant or slightly decreases. Creep deformations of the secondary stage usually are large and of a similar character to "pure" plastic deformations (Betten 2002). For constant stress conditions strain accumulates linearly with time. The strain rate $\dot{\varepsilon}$ is constant and hence time independent, i.e.

$$\dot{\varepsilon} = \frac{\partial \varepsilon}{\partial t} = \text{const.} \quad \text{for} \quad \sigma = \text{const.} \tag{2.21}$$

After the stage of constant creep deformation the strain rate may increase, leading to accelerated strain accumulation (accelerated or tertiary creep) which may cause failure denoted as creep rupture (Figure 2.1, stage III). However, depending on the stress conditions, creep rupture is not always achieved. In general, loading close to the material strength facilitates failure after a certain amount of creep deformation. This creep rupture is a time dependent failure, in contrast to an instantaneous frictional failure. Creep rupture is usually accompanied by a pronounced volume increase due to progressive loosening of the material. Tertiary creep may thus be considered as a result of strain softening.

Many natural systems involving viscous materials exhibit constant deformation in time under stationary boundary conditions without developing any warning signs of rupture. They are hence supposed to have passed the primary creep stage and are presently subjected to a state of secondary (steady) creep lasting for extensive time spans and provoking extensive deformations. Based on this, in the further chapters of this thesis the term "creep" exclusively refers to the secondary (steady) creep stage. Tertiary creep rupture i.e. failure due to temporal material fatigue is not taken into account.

2.6 Micromechanical concepts of creep

In order to understand the micromechanics of creep, we have to consider the granular structure of soil or discrete structure of rock.

According Poirier (1985), creep deformation is attributed to three processes:

- Grain boundary sliding (particle slippage);
- Dislocation slip and climb (dislocation creep) [5]; and
- Diffusional flow (diffusion creep) [6]

The intensity of these mechanisms depends on the stress magnitude, the mineralogical composition and shape of the particles, and the temperature. While grain boundary sliding occurs at any temperature, dislocation and diffusion creep are high-temperature deformation modes (Poirier 1985).

In the soil and rock mechanics context, creep is usually attributed to two basic processes, i.e. slippage between particles (Figure 2.2) and fracture of grains (Lade & Liu 1998). Non-brittle intragranular deformations (i.e. dislocation and diffusion creep) are neglected.
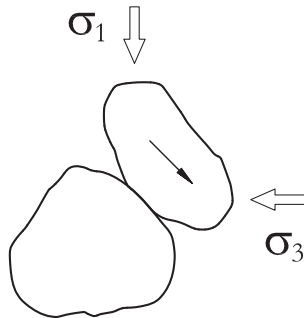
Figure 2.2
Simple mechanistic model of creep along a grain contact (particle slippage; after Lade & Liu 1998).

---

[5] Dislocations are line defects in the crystal lattice.
[6] Diffusion creep is attributed to diffusion of vacancies through the crystalline lattice.

Kuhn & Mitchell (1993) investigated this subcritical deformation of granular material by means of two-dimensional discrete element analyses, assuming an assembly of different-sized spherical particles and visco-frictional contact properties. The results showed that changes in the creep rate with time correlated with changes in the tangential and normal force ratio at the particle contacts, which resulted from particle rearrangement during deformation.

Bowman & Soga (2003) performed triaxial creep tests on dense natural sands and artificial granular material (glass beads) and investigated the changes in microstructure with optical microscopy on sections through the specimens. They revealed a complex microfabric evolution, with the progressive development of dense clusters on one hand, and dilatant microbands on the other hand. Based on these observations they concluded that particle contact slippage is not evenly distributed in the soil volume but is concentrated in less dense, and thus weak domains. Similar observations were also made by Kuhn & Mitchell (1993) in the numerical analyses.

These findings coincide partially with the idea of Mauri McSaveney (pers. comm.) that creep is an anastomosing process, with deformations changing their pathways through the material continuously, rather than deforming the volume homogeneously.

Besides interparticle slippage, particle breakage can considerably contribute to time dependent deformation (Leung et al. 1996; McDowell 2003). The latter is strongly dependent on the mineralogical composition (and thus material strength) of the particles, and promoted by high stress levels. Leung et al. (1996) compared the particle size distribution curves of sand before and after creep experiments and observed a significant grain size reduction. The effect increased with loading duration. Microscopic observations revealed that the asperities of the grains were grounded off and (to a minor extent) entire grains were crushed, producing fines which filled the voids between larger particles. The smoothening of the particle surfaces by asperity breakage significantly reduces the particle contact friction and therefore provokes more local slippages. The latter is associated with increasing creep rates and may eventually lead to creep failure.

On the macroscopic scale, the discrete micromechanical processes of creep exhibit as a relatively homogeneous deformation in time. The global creep strain accumulation commonly follows characteristic patterns in time, i.e. typical creep stages (compare with Section 2.5), that are essentially the same for soil and rock (e.g. Bowman & Soga 2003; Emery 1971; Lade & Liu 1998; Lomnitz 1955; Singh 1975). For well-defined conditions, constitutive equations can be used to reasonably describe the relationship between stress and creep rate (see Chapter 3).

2.7 Limitations of laboratory testing and scale effects

Several authors suppose that creep takes place at all levels of deviatoric stress (e.g. Bishop 1967; Singh & Mitchell 1968a,b; Vulliet & Hutter 1988a), while others argue for the existence of a material-specific stress threshold, at which creep deformation commences (e.g. Bath et al. 2011; Carey 2011; Morgenstern 1995).

Comprehensive creep test series indicate that the stress-creep rate relationship of soils can be extremely nonlinear (e.g. Malan et al. 1998; Schneider-Muntau 2012; Ewald Brückl pers. comm.). At low deviatoric stresses, creep rates are usually very small. This makes it difficult to decide whether a creep curve is tending towards a zero strain rate or some finite value after the primary creep, especially if the strain rate is decreasing at a slow rate (Singh 1975). Moreover, the precision of both the strain measurement equipment and the laboratory test itself is limited.
As the deviatoric stress regime of the experiment approximates the material strength of the specimen, strain rates become rapidly larger and signal that the stress state is close to the initiation of failure. These observations are accounted in nonlinear constitutive relationships (see Chapter 3).

In practice, small and large volumes of soil or rock may considerably differ in their physical properties, which eventually lead to different deformation behaviour. Significant scale effects have also been shown for viscous behaviour (e.g. Liu & Zhou 2000), emphasizing the difficulties in extrapolating laboratory creep parameters to the in situ scale.

Chapter summary

In this thesis, the stress state of a viscous material is described by a symmetric Cauchy stress tensor. The stress tensor can be decomposed in a hydrostatic and a deviatoric stress portion. The time dependent deformation is described by a symmetric logarithmic strain rate tensor. The strain rate of a creeping material is variable in time. In the secondary creep stage, the strain rate achieves a constant minimum value. During this stage, viscous strain accumulates linearly in time and constant in volume.

Viscous geomaterials are involved in many long-lived geological systems such as creeping landslides. These systems commonly exhibit constant deformation rates under stationary boundary conditions. They are therefore potentially in a steady-state secondary creep stage.

For the purpose of geotechnical analyses, three-dimensional landslides can described as a plane strain problem, on condition that the slope extends sufficiently with similar relief, internal structure and material composition in the third dimension.

CHAPTER 3

Constitutive models

for describing time dependent deformation

3.1 Preamble

The rheological reaction of a particular material to an applied load is formulated by means of equations which express the relationship between stresses and strains. These equations are referred to as constitutive equations, since they describe the macroscopic behaviour resulting from the internal constitution of a specific material. The formulation of a constitutive model is usually based on both the experimental investigation and the theoretical framework, where the latter is essential in order to devise suitable experiments and to interpret the experimental results[7] (Betten 2002).

Various constitutive models exist in literature for describing time dependent (viscous) material behaviour. Many approaches were originally developed for other disciplines (e.g. Newton for hydraulics, Bingham for the chemical industry, Norton for metallurgy) and have been subsequently adopted in soil mechanics.

The most common approach is to relate creep deformation to deviatoric stress (Betten 2002). Here, the hydrostatic stress level in the material is considered to have no impact on the creep behaviour. This is true for many fluids and metals since creep

---

[7] Avula (1987) stressed that "the validity of a model should not be judged by mathematical rationality alone, nor should it be judged purely by empirical validation at the cost of mathematical and scientific priniciples. A combination of rationality and empiricism (logic and pragmatism) should be used in the validation".

behaviour of these materials is generally unaffected if a hydrostatic pressure is superimposed. Based on this and the "pure plastic" similar deformation characteristics of secondary creep, many approaches use the "mathematical theory of plasticity", e.g. the theory of plastic potential after Van Mises (1928), for describing creep behaviour (Betten 2002).

For granular materials like soil and fractured rock masses the hydrostatic stress level is more meaningful in describing viscous creep since the shear strength of these materials is strongly related to the normal stress. This is clearly indicated by the strength criterions introduced by Mohr-Coulomb and Hoek-Brown. They postulate that the shear strength of soils and rocks gradually increases with rising normal stress level due to increasing friction between the particles. Consequently, creep deformation in granular materials like soil and rock may be primarily induced by deviatoric stress, but at the same time the behaviour may be significantly affected by the prevailing hydrostatic stress.

This chapter summarizes established deviatoric stress based and effective stress based constitutive models that are applicable to creep in granular materials. These models form the basis of the Creep Equilibrium Analysis Method (CrEAM) developed in this dissertation.

3.2 Deviatoric stress based viscous models

Deviatoric stress based viscous models presume that hydrostatic stress can cause finite volume changes in time (without distortion), and that deviatoric stress is able to produce large time dependent distortions. For a granular material that has achieved its critical density and deforms with constant volume, creep strain can be regarded as exclusively dependent on the deviatoric portion of the stress tensor.

(a) Newton

The simplest approach to describe viscous deformation is to relate time dependent deformation linearly to deviatoric stress. This approach is derived from the theory of elasticity. Appendix A.1 shows the derivation steps, starting with Hook's law, to obtain the linear viscous stress-strain rate relationship as proposed by Newton. The Newtonian constitutive model is applied to an infinite slope condition, as enumerated below.

Assuming infinite slope conditions, small strain rates and constant volume deformation in time, the angular shear strain rate $\dot{\gamma}$ is described as

$$\dot{\gamma} = \frac{\tau_{\dot{\gamma}}}{\overline{\mu}^{Newton}} \tag{3.1}$$

with the shear stress $\tau_{\dot{\gamma}}$[8] and the Newtonian shear viscosity $\overline{\mu}^{Newton}$. The shear viscosity represents the inherent resistance of the material to shear deformation in time[9], and has the unit of [stress × time] e.g. [Pascal·second; Pa·s].

Newton's viscous model indicates that a material deforms in time, as long as a deviatoric stress is present. The strain rate increases linearly with the prevailing shear stress, while the hydrostatic stress has no impact on the deformation behaviour.

---

[8] The index $\dot{\gamma}$ is introduced in order to distinguish stresses relating to a viscous constitutive model from calculative stresses associated with a Factor of Safety determination treated later in this thesis.

[9] In the "Handbuch of Physik" Reiner (1958, p. 450) describes Newton's law as following: "The resistance which arises from the lack of slipperiness of the parts of the liquid is proportional to the gradient of the velocity with which the parts … are separated" (cited from Feda 1992, p. 151). The "resistance" is here represented by the shear stress $\tau_{\dot{\gamma}}$, the "velocity" is expressed by the angular shear stain rate $\dot{\gamma}$, while the amount of "lack of viscosity" is reflected by the shear viscosity as a proportionality factor.

(b) Bingham

In contrast to Newton's model which predicts that any shear stress results in a creep deformation, some viscous materials exhibit a specific yield shear stress which has to be overcome for viscous deformation to commence (Figure 3.1a).
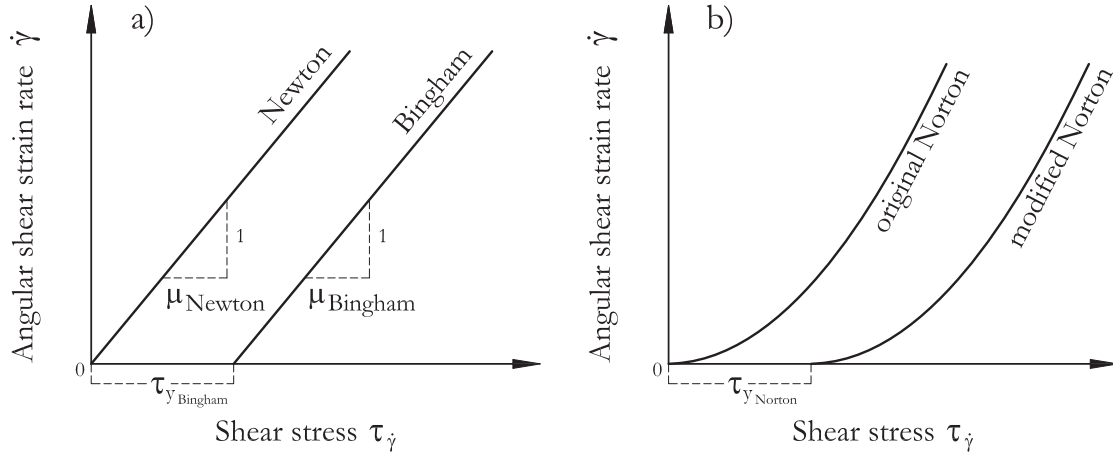
Figure 3.1
a) Linear and b) nonlinear deviatoric stress based models.

This is accounted in Bingham's viscous model

$$\dot{\gamma} = 0 \qquad for \qquad \tau_{\dot{\gamma}} < \tau_y^{Bingham}$$

$$\dot{\gamma} = \frac{\tau_{\dot{\gamma}} - \tau_y^{Bingham}}{\bar{\mu}^{Bingham}} \qquad for \qquad \tau_{\dot{\gamma}} \geq \tau_y^{Bingham} \tag{3.2}$$

where $\bar{\mu}^{Bingham}$ is the Bingham shear viscosity, and $\tau_y^{Bingham}$ is a yield shear stress.

Bingham's viscous model predicts creep deformation for all shear stresses larger than the yield shear stress. Once the yield stress is exceeded, the shear strain rate increases linearly with increasing shear loading. Similar to Newton's model, the hydrostatic stress does not affect the creep rate.

(c) Norton

Both Newton's and Bingham's model assume that the creep strain rate is directly proportional to the loading. However, many materials display a nonlinearly increasing deformation rate when loading is increased. This nonlinearity can be better described by a power law, also referred to as the Norton's power law (Norton 1929)

$$\dot{\gamma} = \frac{\tau_{\dot{\gamma}}^{m^{Norton}}}{\overline{\mu}^{Norton}} \tag{3.3}$$

with $\overline{\mu}^{Norton}$ being the Norton shear viscosity with the unit [stress$^m \times$ time] e.g. [Pascal$^m \cdot$ second; Pa$^m \cdot$ s]., and m^{Norton} being a dimensionless exponent which expresses the nonlinearity of the stress-strain rate relationship.

Similar to Bingham's model, a yield shear stress can be introduced, leading to an extended form of Norton's power law

$$\dot{\gamma} = 0 \qquad\qquad for \quad \tau_{\dot{\gamma}} < \tau_y^{Norton}$$

$$\dot{\gamma} = \frac{\left(\tau_{\dot{\gamma}} - \tau_y^{Norton}\right)^{m^{Norton}}}{\overline{\mu}^{Norton}} \qquad for \quad \tau_{\dot{\gamma}} \geq \tau_y^{Norton} \tag{3.4}$$

where τ_y^{Norton} represents a yield shear stress.

In the subsequent chapters, the expression (3.3) is referred to as the original Norton model while the formulation (3.4) is denoted as the modified Norton model. Both approaches are depicted in Figure 3.1b.

3.3 Effective stress based viscous models

(d+e) Vulliet-Hutter

Vulliet & Hutter (1988a) introduced an effective stress dependent creep model, including deviatoric and hydrostatic stress terms, in the form of

$$\dot{\boldsymbol{\varepsilon}} = A^{VH} \cdot \boldsymbol{\sigma}_{dev} \sqrt{\frac{\sigma_{devII}^{m^{VH}-1}}{\sigma_{devII,f}^{m^{VH}}}} \tag{3.5}$$

with $\dot{\boldsymbol{\varepsilon}}$ and $\boldsymbol{\sigma}_{dev}$ being the strain rate tensor and the deviatoric stress tensor, respectively, A^{VH} is a material-specific rate factor with the unit [time^{-1}] e.g. [s^{-1}], m^{VH} is a dimensionless exponent, σ_{devII} is the second invariant of the deviatoric stress tensor, and $\sigma_{devII,f}$ is the second invariant of the deviatoric stress tensor at failure.

The deviatoric stress at failure is a function of the hydrostatic stress level. Therefore, its second invariant $\sigma_{devII,f}$ includes the hydrostatic stress dependence in the Vulliet-Hutter constitutive relationship (3.5).

Material normal response, i.e. contraction or dilatation, are a priori not considered in the Vulliet-Hutter model. The relationship thus describes constant volume deformation which is reasonable for the secondary creep stage.

Two variants of the Vulliet-Hutter viscous relationship are summarized below, which differ only in the adopted failure criterion. Vulliet & Hutter (1988a) originally employed the Drucker-Prager failure criterion in order to describe the second invariant of the deviatoric stress tensor at failure, $\sigma_{devII,f}$. This approach is subsequently denoted as the original Vulliet-Hutter model. Schneider-Muntau (2012) used a modified approach, by substituting the Drucker-Prager with the Mohr-Coulomb failure criterion. This approach is here referred to as the modified Vulliet-Hutter model.

For this work, the original and modified Vulliet-Hutter approaches are adapted for infinite slope considerations. The respective derivation steps are summarized in Appendix A.1. The final formulations as applied later in this thesis are enumerated below.

(d) Original Vulliet-Hutter

In accordance with Vulliet & Hutter (1988a), the second invariant of the deviatoric stress tensor at failure is expressed by means of the Drucker-Prager failure criterion. The failure criterion can also be formulated by means of the Mohr-Coulomb strength parameters (friction angle and cohesion).

For infinite slope conditions, the angular shear strain rate $\dot{\gamma}$ is given as:

$$\dot{\gamma} = 2A^{VH_{DP}} \cdot \left\{ \frac{\tau_{\dot{\gamma}}\left(3 - \sin\varphi\right)}{\sqrt{12}\left[c\cos\varphi + \left(\sigma_{\dot{\gamma}} - u\right)\sin\varphi\right]} \right\}^{m^{VH_{DP}}} \tag{3.6}$$

where $A^{VH_{DP}}$ and $m^{VH_{DP}}$ are the rate factor and exponent associated with the original Vulliet-Hutter formulation, φ and c are the friction angle and cohesion of the viscous layer, $\sigma_{\dot{\gamma}}$ and $\tau_{\dot{\gamma}}$ are the normal stress and shear stress, and u is the hydrostatic porewater pressure.

(e) Modified Vulliet-Hutter

In the modified Vulliet-Hutter approach, the deviatoric stress required for failure is formulated in terms of the Mohr-Coulomb criterion. For infinite slope conditions we obtain:

$$\dot{\gamma} = 2A^{VH_{MC}} \cdot \left[\frac{\tau_{\dot{\gamma}}}{c\cos\varphi + \left(\sigma_{\dot{\gamma}} - u\right)\sin\varphi} \right]^{m^{VH_{MC}}} \tag{3.7}$$

where $A^{VH_{MC}}$ and $m^{VH_{MC}}$ are the rate factor and exponent associated with the modified Vulliet-Hutter formulation, and φ, c, $\sigma_{\dot{\gamma}}$, $\tau_{\dot{\gamma}}$ and u are defined as previously in the original formulation (3.6).

Generic comparison of the original and modified Vulliet-Hutter model

In principal stress space, the Drucker-Prager failure surface represents a smooth (conus-shaped) variant of the pyramid-shaped Mohr-Coulomb failure surface. Applying the Drucker-Prager parameters as used in Vulliet-Hutter (1988a), the Drucker-Prager surface circumscribes the Mohr-Coulomb surface (Figure 3.2).
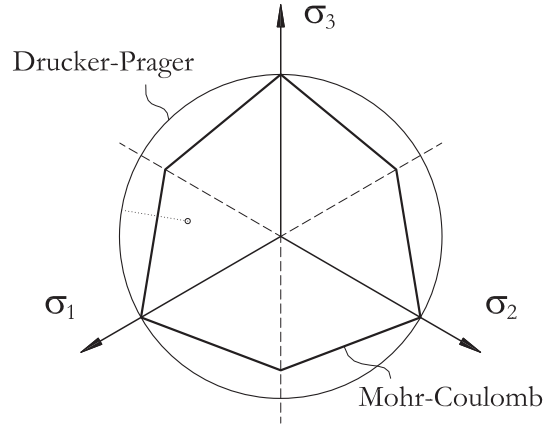
Figure 3.2
Mohr-Coulomb and Drucker-Prager failure surfaces in the space of
principal stresses. The doted line indicates the different distances of an
arbitrary stress point to the failure surfaces (modified after Mang &
Hofstetter 2008).

Therefore, in this definition, the Drucker-Prager deviatoric stress at failure is either
equal or larger than the Mohr-Coulomb deviatoric stress at failure.

For plane strain considerations applies

$$\left(\frac{\sigma_1-\sigma_3}{2}\right)_f^{DP} = \frac{\sqrt{12}}{3-\sin\varphi}\left(\frac{\sigma_1-\sigma_3}{2}\right)_f^{MC} \tag{3.8}$$

This indicates that the deviation between the Mohr-Coulomb and the Drucker-
Prager failure surface increases with increasing friction angle.

For equal rate factors and exponents (i.e. $A^{VH_{DP}} = A^{VH_{MC}}$ and $m^{VH_{DP}} = m^{VH_{MC}}$), the
original Vulliet-Hutter approach provides smaller strain rates than the modified ap-
proach, since the stress point is located farther from the failure surface (compare
with Figure 3.2).

Figure 3.3 shows a comparison of the original and modified Vulliet-Hutter model
for infinite slope conditions using constant rate factors and strength properties, and
variable exponents.
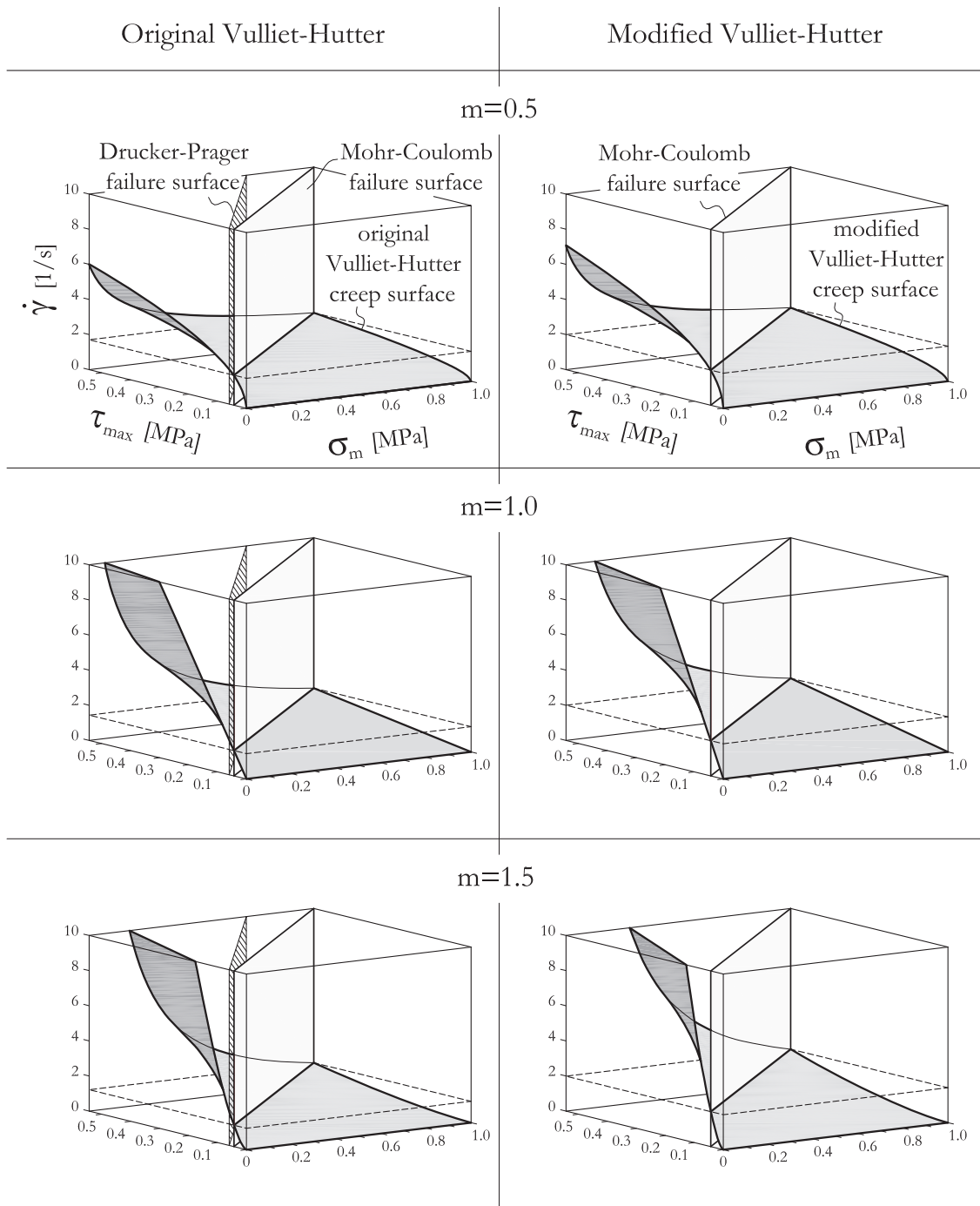
Figure 3.3
Comparison of the original and modified Vulliet-Hutter model for infinite slope conditions using constant parameters $A = 1$ s^{-1}, $\varphi = 30°$, $c = 0.05$ MPa and variable exponents $m = \{0.5; 1.0; 1.5\}$. The gray plane indicates the Mohr-Coulomb failure criterion, the hatched plane (only in left column) denotes the Drucker-Prager failure criterion.

Chapter summary

This chapter summarized the theoretical framework of six constitutive models which aim to mathematically describe the stress-strain rate relationship of a viscous material in the secondary (steady state) creep stage. The constitutive models can be separated into two classes:

- deviatoric stress based models (Newton, Bingham, original and modified Norton)
- effective stress based models (original and modified Vulliet-Hutter)

The deviatoric stress based approaches relate the distortional strain rate directly and exclusively to deviatoric stresses. In contrast, the effective stress based relationships include the hydrostatic stress level as an additional influencing factor. The latter is significant for describing viscous behaviour of soil and rock, since the strength of these materials is strongly related to normal stress conditions.

Deviatoric stress based constitutive models are easy in use and commonly applied in geomechanics. The effective stress based constitutive models are more complex but are considered more suitable for representing creep processes over a broad range of effective normal stress.

The constitutive relationship between stress and creep strain rate is described by either a linear formulation (Newton and Bingham) or a power law formulation (original and modified Norton, original and modified Vulliet-Hutter). Additionally, the Bingham and the modified Norton model include a yield stress component, below which viscous deformation can not occur.

All presented constitutive models were adapted for infinite slope considerations. These infinite slope constitutive equations will be applied in Chapter 5, in developing algorithms of the Creep Equilibrium Analysis Method (CrEAM).

CHAPTER 4

Limit Equilibrium Analysis Methods (LEAM's)

4.1 Preamble

The first reported application of a stability analysis using the method of slices and a simple limit equilibrium assumption was conducted by Petterson in the year 1916 for rotational slides which had occurred in the marine clays of the Stigberg Quay in Gothenburg/Sweden (Petterson 1955; Duncan & Wright 2005). About two decades later, the basic concepts of slice analysis were formalized by Fellenius (1936) in the "Ordinary" or "Swedish" method of slices for rotational sliding along a circular slip surface (also referred to as "Fellenius' method"). Janbu (1954) developed a slice analysis method for irregular (thus non-circular) slip surfaces ("Simplified Janbu method"), and Bishop (1955) developed a more rigorous approach for the analysis of rotational slides (i.e. the "Simplified Bishop method"). In contrast to the Fellenius method which provides a linear Factor of Safety equation, the approaches of Janbu and Bishop require an iterative procedure for obtaining a solution. Later, computer-based calculations enabled complex LEAM's with iterative solution procedures, such as the Morgenstern & Price (1965) and Spencer (1967) methods. Various refinements and improvements as well as new ideas were developed by numerous other authors e.g. Lowe & Karafiath (1959), the U.S. Army Corps of Engineers (1970 & 2003), Sarma (1973), Chen & Morgenstern (1983).

Key aspects of these methods are enumerated below.

4.2   Principles of limit equilibrium analysis

Limit Equilibrium Analysis Methods (LEAM's) are based on the third Newtonian axiom *"actio est reactio"*, stating that all active and passive forces acting in a closed system have to be in balance. Such a closed system can be represented by a distinct slope failure mechanism. Limit equilibrium methods are therefore traditionally applied for the stability assessment of both natural slopes and artificial embankments. Therein, the stability of a slope is expressed by a dimensionless index value referred to as the Factor of Safety (commonly indicated by the greec symbol η, or by the abbreviations *FoS*, *SF*, or simply *F*). The failure surface with the lowest η is considered the most critical.

Various assumptions have been made regarding potential failure modes and the associated mechanics, and regarding the definition of η.

4.2.1   Mechanical models

Mechanical models aim to represent the critical potential failure mode by accounting for forces acting in a slope system. They typically consider:

- the shape of the basal slip surface (planar, circular, irregular);
- geometry and interaction of the virtual rigid sub-elements (slices, wedges);
- magnitudes, orientations and locations of active and reactive forces; and
- equilibrium conditions

Assuming a sliding mass along a planar slip surface, LEAM considers a single block, and the reactive forces (shear and normal force) acting on the slip surface are statically determined. In contrast, a non-planar (circular or irregular) slip surface is more complex and statically indeterminate. In this case, the potential sliding mass is subdivided into an arbitrary number of rigid elements. This subdivision has no physical meaning but aims to represent the sliding mass by an assembly of mechanically interacting rigid bodies. Determination of reactive forces is achieved by solving equilibrium equations for each internal element, and for the overall mass.

Various assumptions are employed for the interslice force action. While the Fellenius method completely neglects the action of interslice forces, both the Simplified Bishop method and Simplified Janbu method disregard the shear force component,

thus, assuming only horizontal earth pressure at the slice interfaces. In contrast, many advanced methods assume inclined interslice forces and, hence, implicitly include shear resistance between the elements (e.g. Lowe & Karafiath 1959; Morgenstern & Price 1965; Spencer 1967).

4.2.2 Factor of Safety

The dimensionless Factor of Safety, η, is employed in all limit equilibrium methods for expressing the relation between stabilizing and destabilizing forces and/or moments. A Factor of Safety equal to unity, $\eta = 1$, characterises a slope in a state of limit equilibrium, indicating that the resisting forces (normally provided by material strength) are just able to counterbalance the destabilizing forces (e.g. material weight and unfavourable additional loads). In contrast, $\eta > 1$ denotes a stable slope with a distinct measure of strength reserves, while $\eta < 1$ indicates that the slope is denoted as unstable and is expected to fail (or has already failed). The η value is thus an index of stability.

Several ways have been proposed, in order to estimate the condition $\eta = 1$. Those most commonly applied are (Fellin 2004; Morgenstern & Sangrey 1978):

- decrease of shear strength (e.g. by using uniformly or individually reduced shear strength parameters);
- increase of destabilizing loads (e.g. increasing gravity, punctual load supplement); or
- the ratio of driving and resisting forces along the failure surface

All definitions provide the same result for the limit equilibrium state ($\eta = 1$). For conditions beyond limit equilibrium ($\eta \neq 1$), the η values depend on the approach and thus can diverge. Some discrepancies arising from different definitions are demonstrated in Fellin (2004).

The by far most frequently employed safety definition is the uniform strength parameter reduction also referred to as the Fellenius rule.[10]

---

[10] Fellenius (1927) proposed this formulation for the first time.

In this formulation, the Factor of Safety is that coefficient by which the strength parameters (e.g. the Mohr-Coulomb parameters cohesion and friction coefficient) must be reduced in order to force the slope into a state of limit equilibrium along a predetermined slip surface. Consequently, in this definition the Factor of Safety is an expression of the magnitude of strength mobilization. The merits as well as some limitations of this formulation are summarized in Morgenstern & Sangrey (1978).

All limit equilibrium procedures in this chapter employ the same safety definition i.e. the uniform strength parameter reduction (Fellenius rule). Hence, they express the resisting shear stress along the slip surface as a mobilized shear stress using the Mohr-Coulomb failure criterion.

Assuming τ_f is the shear stress at failure at the effective stress $(\sigma - u)$

$$\tau_f = c + (\sigma - u)\tan\varphi \tag{4.1}$$

the mobilized shear stress can be defined according the Fellenius rule as

$$\tau_\eta = \frac{\tau_f}{\eta} = \frac{c + (\sigma_\eta - u)\tan\varphi}{\eta} \tag{4.2}$$

where τ_η denotes the mobilized shear stress, and $\sigma_\eta = \sigma$ is the associated total normal stress. The index η indicates that both the shear and total normal stress refer to the stability analysis i.e. the Factor of Safety determination. [11]

Assuming a uniform stress distribution along the base of a slice, the mobilized shear force per unit width of the slope can be formulated

$$T_\eta = \frac{b\tau_\eta}{\cos\alpha} = \frac{b}{\cos\alpha}\left[\frac{c + (\sigma_\eta - u)\tan\varphi}{\eta}\right] \tag{4.3}$$

---

[11] The index is introduced to distinguish shear and normal stresses related to limit equilibrium stability analysis from shear and normal stresses referring to the Creep Equilibrium Analysis Method.

Analogously, the cohesion force C, the total normal force N_η, and the water pressure force U are defined as

$$C = \frac{bc}{\cos\alpha} \qquad N_\eta = \frac{b\sigma_\eta}{\cos\alpha} \qquad U = \frac{bu}{\cos\alpha} \qquad (4.4)$$

Implementing the formulations (4.4) in (4.3) yields the mobilized shear force T_η as used in the subsequent sections, i.e.

$$T_\eta = \frac{C + \left(N_\eta - U\right)\tan\varphi}{\eta} \qquad (4.5)$$

4.3 Selected stability analysis procedures

Commonly applied limit equilibrium stability analysis procedures are summarized below. They include considerations of:
- the infinite slope model;
- rotational mechanisms with circular slip surface; and
- translational mechanisms with irregular slip surface

4.3.1 Infinite slope model

The following forces operate at an arbitrary slice of an infinite slope with a slope-parallel groundwater flow (Figure 4.1):

- the weight force W determined as

$$W = \gamma b\left(h - h_w\right) + \gamma_r b h_w = b\left[\gamma h + h_w\left(\gamma_r - \gamma\right)\right] \qquad (4.6)$$

with γ and γ_r being the wet (unsaturated) and saturated specific weight of the soil or rock, h and h_w being the overall and water saturated height of the slice, and b being the width of the slice

- an optional external vertical and horizontal load P_v and P_h defined as

$$P_v = p_v b \qquad P_h = p_h b \tan\alpha \qquad (4.7)$$
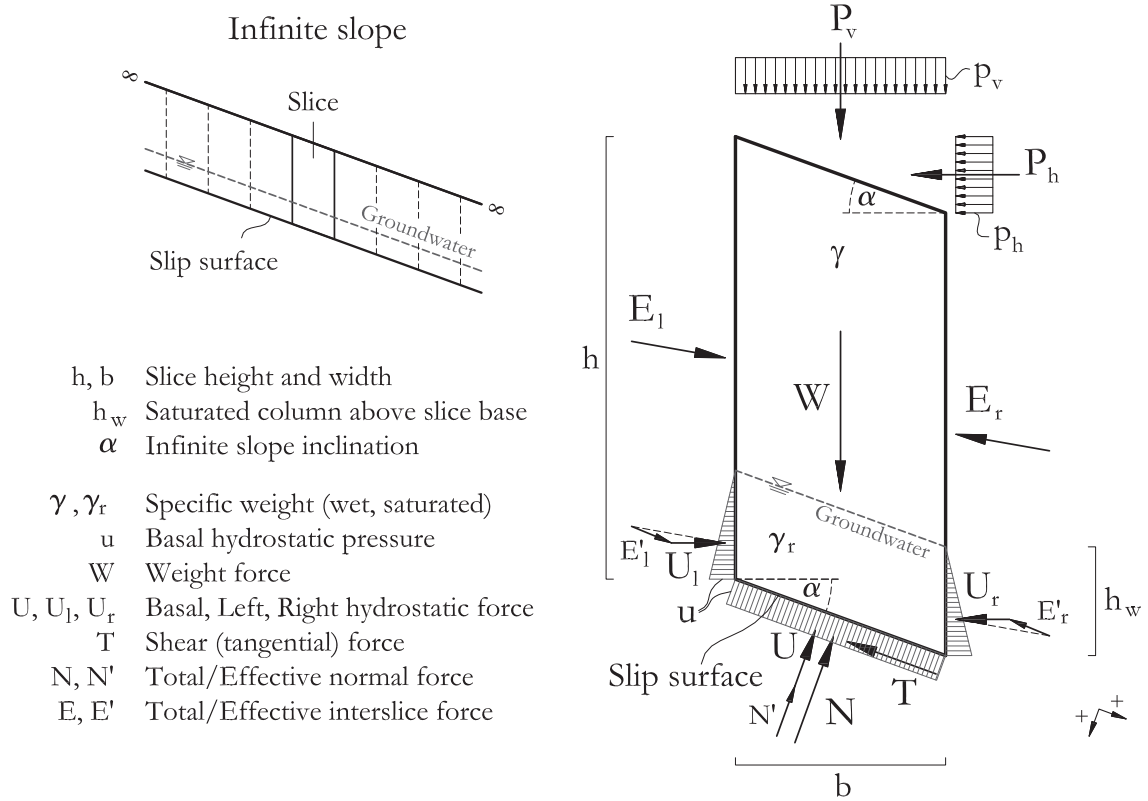
Figure 4.1
Active and passive forces acting on an arbitrary slice of an infinite slope.

- The water pressure u at the base of the slice is determined as (Figure 4.2)

$$u = \gamma_w h_u = \gamma_w h_w \cos^2 \alpha \tag{4.8}$$

with γ_w being the specific weight of water, and α being the inclination angle of the infinite slope. Assuming a constant water pressure u along the slice base, the hydrostatic normal forces at the slice base (U) and the lateral slice boundaries (U_l and U_r) can be expressed as

$$U = \frac{ub}{\cos \alpha} = \gamma_w h_w b \cos \alpha \tag{4.9}$$

$$U_l = \frac{u h_w}{2} = \frac{\gamma_w \left(h_w \cos \alpha \right)^2}{2} = U_r \tag{4.10}$$

44

Hydraulic head h_{hyd} = Elevation head z + Pressure head h_u

Infinite slope surface

Groundwater table

γ_r

Equipotential line

Sliding mass

γ_d (γ_m)

1

$h_{u,2}$

Shear zone

h_w

Equipotential line

h

Stable base

2

Equipotential line

z_1

α

Constant hydraulic head
along equipotential line

z_2

$z = 0$

$h_{hyd,1} = z_1 \,(+\,0)$

$h_{hyd,2} = z_2 + h_{u,2}$

$h_{hyd,1} = h_{hyd,2}$

$\rightarrow h_{u,2} = z_1 - z_2$

$= h_w \cos^2\alpha$
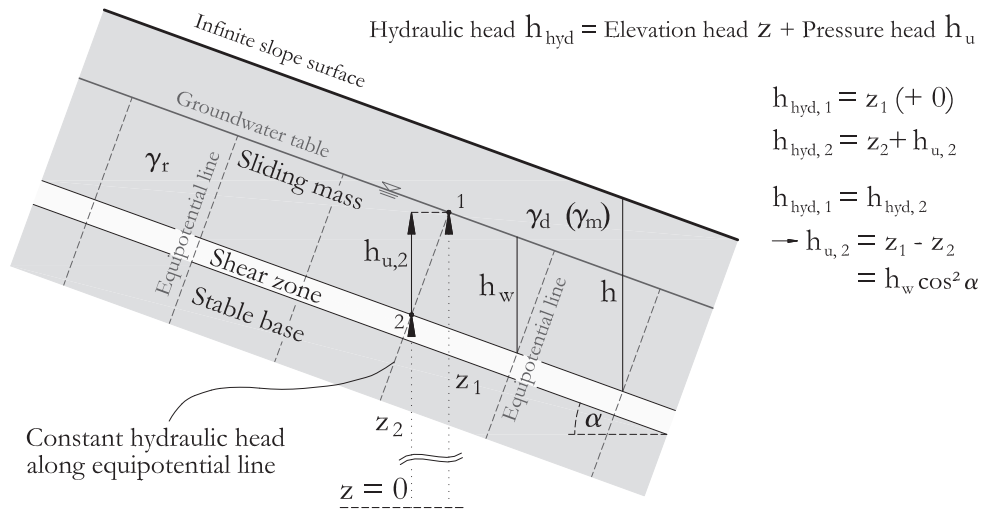
Figure 4.2
Determination of the pressure heads and porewater pressures in an
infinite slope by applying the flownet principle.

- the left- and right-lateral effective interslice forces E_l' and E_r'

- the total normal force N and the shear (tangential) force T, both acting at the
  slice base

While the active forces induced by the slice self-weight, external loading and water
pressure (W, P_v, P_h, U, U_l, U_r) are determined by the individual problem specifi-
cations, the reactive forces N, T, E_l' and E_r' are not known beforehand but have
to be solved by means of force equilibrium considerations.

Although there exist four unknown variables, the problem is rendered statically de-
terminate by recognizing that

$$\left|\vec{U}_l\right| = \left|\vec{U}_r\right| \qquad \left|\vec{E}_l'\right| = \left|\vec{E}_r'\right| \tag{4.11}$$

Consequently, the force equilibrium parallel and perpendicular to to infinite slope
inclination, respectively, is given as

$$\left(W + P_v\right)\sin\alpha - P_h\cos\alpha - T = 0 \tag{4.12}$$

$$\left(W + P_v\right)\cos\alpha + P_h\sin\alpha - N = 0 \tag{4.13}$$

Substituting expression (4.5) for $T = T_\eta$ in (4.12) and solving the equilibrium equation system yields the Factor of Safety η of the infinite slope as

$$\eta = \frac{C + (W + P_v)\cos\alpha\tan\varphi + (P_h\sin\alpha - U)\tan\varphi}{(W + P_v)\sin\alpha - P_h\cos\alpha} \tag{4.14}$$

By replacing the forces W, P_v, P_h, U and C in (4.14) by the formulations in (4.6), (4.7), (4.9) and (4.4), and subsequently simplifying the expression, we get

$$\eta = \frac{\dfrac{c}{\cos^2\alpha} + \tan\varphi\left[\gamma h + h_w(\gamma_r - \gamma - \gamma_w) + p_v + p_h\tan^2\alpha\right]}{\tan\alpha\left[\gamma h + h_w(\gamma_r - \gamma) + p_v - p_h\right]} \tag{4.15}$$

The detailed derivation steps are shown in Appendix Section A.2.1.

4.3.2 Rotational mechanism with circular slip surface

For landslides delimited by a circular (cylindrical) basal slip surface (Figure 4.3), the failure mechanism is rotational sliding. For calculation purposes the sliding mass is subdivided into a finite number (n) of imaginary slices. The slice bases are formed by linear circle segments which approximate the circular surface.

Commonly applied calculation procedures for the stability analysis of rotational slides include the Swedish circle method, the Fellenius method, and the Simplified Bishop method.

These approaches satisfy the equilibrium of moment while they differ in the treatment of interslice forces. The Fellenius approach neglects the principle of "*actio est reactio*" between the slices, leading to a straightforward calculation scheme. The Simplified Bishop method accounts for the horizontal component of the interslice forces while neglecting the vertical components. In contrast, the Swedish circle method implicitly accounts for full slice interaction, but is very restricted in the application (i.e for frictionless material only).
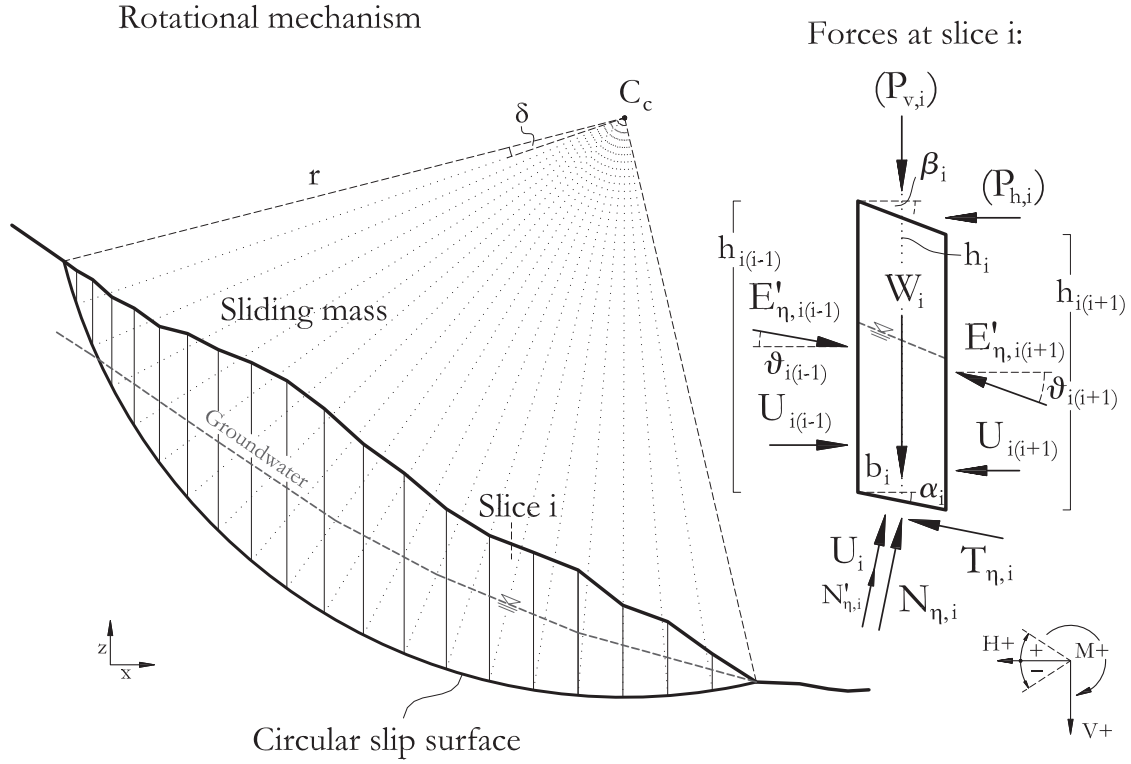
Figure 4.3
Left: Rotational sliding mass with internal slices. Right: Example slice showing geometry and all active and passive forces. The coordinate system in the lower right corner denotes the sign convention.

For rotational slides, the moment exerted on an arbitrary slice i due to rotation about the slip circle centre C_c is given by

$$M_i = \begin{bmatrix} -r\sin\alpha_i\left(W_i + P_{v,i}\right) + P_{h,i}\cos\alpha_i\left(r - h_i\cos\alpha_i\right) + rT_{\eta,i} \\ -a_{U,i(i-1)}U_{i(i-1)} - a_{E'_\eta,i(i-1)}E'_{\eta,i(i-1)} + a_{U,i(i+1)}U_{i(i+1)} + a_{E'_\eta,i(i+1)}E'_{\eta,i(i+1)} \end{bmatrix} \qquad (4.16)$$

where $a_{U,i(i-1)}$, $a_{U,i(i+1)}$, $a_{E'_\eta,i(i-1)}$ and $a_{E'_\eta,i(i+1)}$ are the lever arms of the water pressure forces $U_{i(i-1)}$ and $U_{i(i+1)}$ and the effective interslice forces $E'_{\eta,i(i-1)}$ and $E'_{\eta,i(i+1)}$, respectively.

47

Further supposing that:

- the vertical and horizontal surcharge loads $P_{v,i}$ and $P_{h,i}$ are acting in the middle of the slice tops;

- the basal normal forces $N_{\eta,i}$ act in the middle of the slice bases, thus, do not contribute in the moment since they have no lever arms; and

- no forces act at the lateral boundaries of the sliding mass i.e.

$$U_{1(1-1=0)} = E'_{\eta,1(1-1=0)} = 0 \quad \text{and} \quad U_{n(n+1)} = E'_{\eta,n(n+1)} = 0 \tag{4.17}$$

Satisfying the equilibrium of moment implies:

$$\sum_{i=1}^{n} M_i = r \sum_{i=1}^{n} \left[T_{\eta,i} - \left(W_i + P_{v,i} \right) \sin \alpha_i \right] + \sum_{i=1}^{n} \left[P_{h,i} \cos \alpha_i \left(r - h_i \cos \alpha_i \right) \right] = 0 \tag{4.18}$$

The moments induced by the interslice forces cancel out due to the principle of "*actio est reactio*". Substituting (4.5) for $T_{\eta,i}$ in (4.18) yields the overall moment equilibrium equation for the Factor of Safety determination

$$\sum_{i=1}^{n} M_i = r \sum_{i=1}^{n} \left[\begin{array}{c} \dfrac{C_i + \left(N_{\eta,i} - U_i \right) \tan \varphi_i}{\eta} - \left(W_i + P_{v,i} \right) \sin \alpha_i ... \\[2mm] ... + P_{h,i} \cos \alpha_i \left(1 - \dfrac{h_i}{r} \cos \alpha_i \right) \end{array} \right] = 0 \tag{4.19}$$

The n total normal forces $N_{\eta,i}$ in (4.19) are unknown. Different assumptions can be applied, leading to the approaches according Fellenius and Bishop, respectively. For the Swedish circle method $N_{\eta,i}$ does not appear in the moment equilibrium equation.

4.3.2.1 Swedish circle $(\varphi = 0)$ method

In absence of friction along the entire slip surface (e.g. for undrained conditions) the resisting forces include only a cohesional component. Accordingly, the term $\left(N_{\eta,i} - U_i \right) \tan \varphi_i$ in the moment equilibrium equation (4.19) does not appear, and the global Factor of Safety η can be obtained by rearranging (4.19) to

$$\eta = \frac{\sum\limits_{i=1}^{n} C_i}{\sum\limits_{i=1}^{n} \left[\left(W_i + P_{v,i} \right) \sin \alpha_i - P_{h,i} \cos \alpha_i \left(1 - \frac{h_i}{r} \cos \alpha_i \right) \right]} \tag{4.20}$$

4.3.2.2 Fellenius method

In the Fellenius approach, the total normal forces $N_{\eta,i}$ are directly calculated from the active forces, i.e. weight forces, external loads and water pressure forces in the slice interfaces, without considering the interslice forces, and therefore, violating the principle of "*actio est reactio*" in between the slices

$$N_{\eta,i} = N'_{\eta,i} + U_i = \left(W_i + P_{v,i} \right) \cos \alpha_i + P_{h,i} \sin \alpha_i + \left(U_{i(i+1)} - U_{i(i-1)} \right) \sin \alpha_i \tag{4.21}$$

Equation (4.21) provides a reasonable approximation for the normal forces, and thereby $N_{\eta,i}$ are known quantities in the moment equilibrium equation (4.19).

Consequently, the problem is mathematically reduced to one unknown i.e. the global Factor of Safety η which is obtained as

$$\eta = \frac{\sum\limits_{i=1}^{n} \left\{ C_i + \left[\left(W_i + P_{v,i} \right) \cos \alpha_i + P_{h,i} \sin \alpha_i + \left(U_{i(i+1)} - U_{i(i-1)} \right) \sin \alpha_i - U_i \right] \cdot \tan \varphi_i \right\}}{\sum\limits_{i=1}^{n} \left[\left(W_i + P_{v,i} \right) \sin \alpha_i - P_{h,i} \cos \alpha_i \left(1 - \frac{h_i}{r} \cos \alpha_i \right) \right]} \tag{4.22}$$

For derivation steps see Appendix Section A.2.2.2.

4.3.2.3 Simplified Bishop method

The total normal force $N_{\eta,i}$ can be derived more rigorously than in the Fellenius approach by means of the slice vertical force equilibrium, which is given as

$$W_i + P_{v,i} - N_{\eta,i}\cos\alpha_i - T_{\eta,i}\sin\alpha_i + E'_{\eta,i(i-1)}\sin\vartheta_{i(i-1)} - E'_{\eta,i(i+1)}\sin\vartheta_{i(i+1)} = 0 \tag{4.23}$$

where the index η referes to the Factor of Safety solution, and the angles $\vartheta_{i(i-1)}$ and $\vartheta_{i(i+1)}$ denote the inclination angles of the interslice forces E'. Assuming that the vertical components of the interslice forces are negligible and can be neglected, thus,

$$E'_{\eta,i(i-1)}\sin\vartheta_{i(i-1)} - E'_{\eta,i(i+1)}\sin\vartheta_{i(i+1)} = 0 \tag{4.24}$$

the total normal forces $N_{\eta,i}$ can be obtained by rearranging (4.23) as

$$N_{\eta,i} = N'_{\eta,i} + U_i = \frac{W_i + P_{v,i}}{\cos\alpha_i} - T_{\eta,i}\tan\alpha_i \tag{4.25}$$

Equation (4.25) provides a good approximation for the normal forces in the slip surface but in contrast to the Fellenius method, $N_{\eta,i}$ depend on the mobilized shear forces $T_{\eta,i}$, thus, remain unknown quantities.

Replacing $T_{\eta,i}$ in (4.25) by (4.5) and rearranging the equation enables to express the total normal force as a function of the Factor of Safety, i.e.

$$N_{\eta,i} = \frac{\eta\left(W_i + P_{v,i}\right) - \left(C_i - U_i\tan\varphi_i\right)\sin\alpha_i}{\eta\cos\alpha_i + \sin\alpha_i\tan\varphi_i} \tag{4.26}$$

Introducing (4.26) for $N_{\eta,i}$ in the moment equilibrium equation (4.19) allows to extract the last unknown i.e. the Factor of Safety η in terms of an implicit equation

$$\eta = \frac{\displaystyle\sum_{i=1}^{n}\left[\frac{\eta\tan\varphi_i\left(W_i + P_{v,i}\right)}{\eta\cos\alpha_i + \sin\alpha_i\tan\varphi_i} + \left(C_i - U_i\tan\varphi_i\right)\left(1 - \frac{\sin\alpha_i\tan\varphi_i}{\eta\cos\alpha_i + \sin\alpha_i\tan\varphi_i}\right)\right]}{\displaystyle\sum_{i=1}^{n}\left[\left(W_i + P_{v,i}\right)\sin\alpha_i - P_{h,i}\cos\alpha_i\left(1 - \frac{h_i}{r}\cos\alpha_i\right)\right]} \tag{4.27}$$

For derivation steps see Appendix Section A.2.2.3.

4.3.3 Translational mechanism with irregular slip surface

This approach is applicable for sliding masses delimited by a polygonal (prismatic) basal slip surface (Figure 4.4). The mechanism is translational sliding. Similar to the previous rotational mechanism, the sliding mass is subdivided into slices.

A commonly applied approach for the analysis of slides with irregular slip surface, i.e. the simplified procedure of Janbu (1954, 1973) is summarized below.
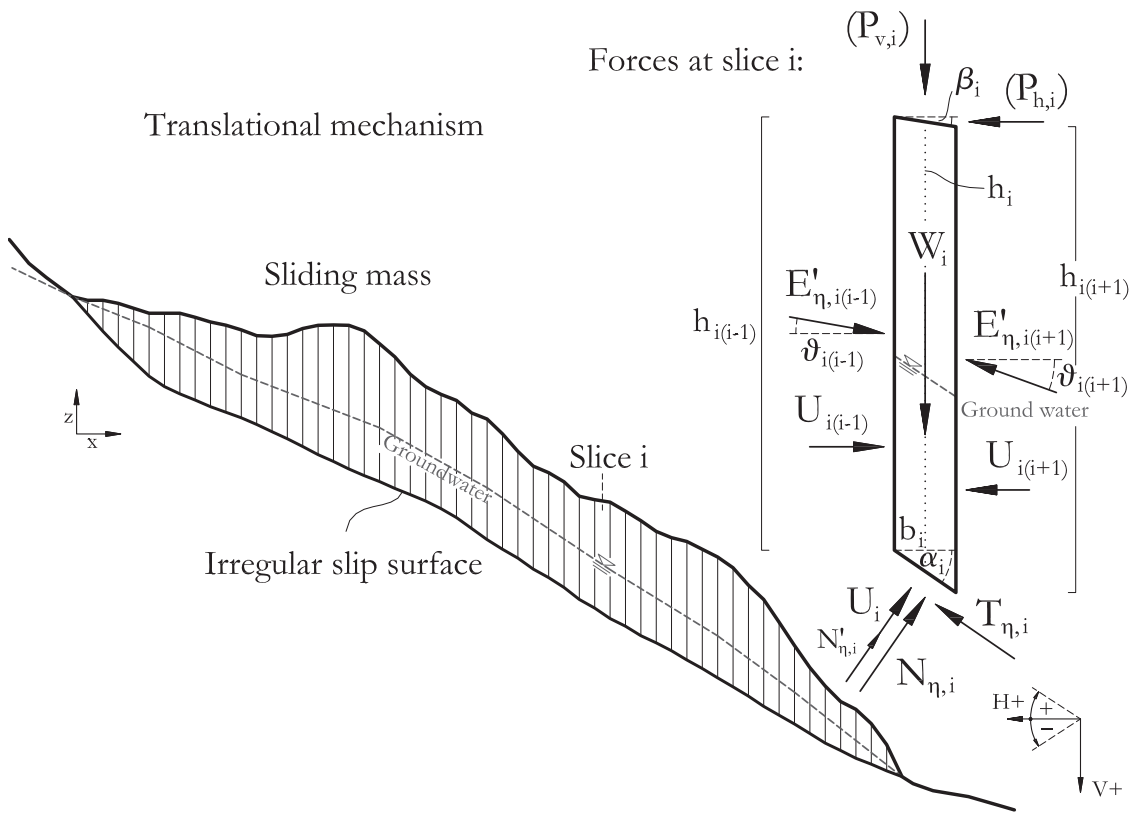
Figure 4.4
Left: Translational sliding mass on an irregular slip surface.
Right: Example slice showing the active and reactive forces.
The coordinate system in the lower right corner denotes the sign convention.

4.3.3.1 Simplified Janbu method

The horizontal force equilibrium for an arbitrary slice i in Figure 4.4 is given as

$$\begin{bmatrix} P_{h,i} - N_{\eta,i}\sin\alpha_i + T_{\eta,i}\cos\alpha_i - E'_{\eta,i(i-1)}\cos\vartheta_{i(i-1)}\ldots \\ \ldots - U_{i(i-1)} + E'_{\eta,i(i+1)}\cos\vartheta_{i(i+1)} + U_{i(i+1)} \end{bmatrix} = 0 \qquad (4.28)$$

where the index η refers to the Factor of Safety solution, and the angles $\vartheta_{i(i-1)}$ and $\vartheta_{i(i+1)}$ denote the inclination angles of the effective interslice forces E'. The corresponding vertical force equilibrium equation is given in expression (4.23).

Similar to the Simplified Bishop method, the Simplified Janbu approach neglects the vertical components of the interslice forces, assuming their difference to be zero (see equation (4.24)). Applying this supposition on the vertical force equilibrium requirement enables to express the total normal forces $N_{\eta,i}$ as a function of the Factor of Safety, i.e. expression (4.26), while the interslice forces discard in the relationship.

Furthermore, the interslice forces cancel out in the summation of all horizontal force equilibrium equations, leading to

$$\sum_{i=1}^{n}\left(P_{h,i} - N_{\eta,i}\sin\alpha_i + T_{\eta,i}\cos\alpha_i \right) = 0 \qquad (4.29)$$

Combining the above expression with (4.5) and (4.26) allows to rearrange the expression to the final formula for the Factor of Saftey η, i.e.

$$\eta = \frac{\left\{ \begin{matrix} \sum_{i=1}^{n}\left[P_{h,i} + \dfrac{(W_i + P_{v,i})\tan\varphi_i}{\tan\alpha_i\,\tan\varphi_i + \eta} \right]\ldots \\ \ldots + \sum_{i=1}^{n}\left[\left(\dfrac{C_i - U_i\tan\varphi_i}{\eta} \right)\left(\cos\alpha_i + \dfrac{\eta\tan\alpha_i - \tan\varphi_i}{\tan\alpha_i\,\tan\varphi_i + \eta}\cdot\sin\alpha_i \right) \right] \end{matrix} \right\}}{\sum_{i=1}^{n}\left[\dfrac{(W_i + P_{v,i})\tan\alpha_i}{\tan\alpha_i\,\tan\varphi_i + \eta} \right]} \qquad (4.30)$$

For detailed derivation steps see Appendix Section A.2.3.1.

Table 4.1

Overview of mechanical models for limit equilibrium analysis of slopes
(modified after Duncan & Wright 2005)

Infinite slope	Swedish circle	Fellenius	Simplified Bishop	Simplified Janbu
Geometry / Mechanism				
slope with infinite extent, slip surface parallel to slope	circular (cylindrical) slip surface; rotational mechanism			polygonal (prismatic) slip surface; translational mechanism
Assumptions for interslice forces				
all slices are self-similar, thus resultant of interslice forces is zero	interslice forces considered (but cancel out in the moment equilibrium)	interslice forces considered in moment equilibrium but neglected for the calculation of normal forces	horizontal components of interslice forces are accounted, vertical components are neglected (only horizontal earth pressure, no shear resistance between the slices considered)	
Equilibrium equations satisfied				
1 Σ forces perpendicular to slope 1 Σ forces parallel to slope 2 total equations*	1 Σ moment in circle centre 1 total equation (* equilibrium of moment is implicitly satisfied)		1 Σ moment in circle centre n Σ forces in vertical direction n+1 total equations	n Σ forces in vertical direction n Σ forces in horizontal direction 2n total equations
Constitutive equations				
n mobilized shear forces accord. Mohr-Coulomb failure criterion with uniform strength reduction				
c, φ	$c, \varphi = 0$	c, φ	c, φ	c, φ
Unknowns solved for				
1 Safety Factor 1 mobilized shear force in slip surface 2 total unkowns	1 Safety Factor n mobilized shear forces at the slice bases n+1 total unkown		1 Safety Factor 2n normal and mob. shear forces at the slice bases 2n+1 total unkowns	1 Safety Factor 2n normal and mob. shear forces at the slice bases n-1 horizontal interslice forces 3n total unkowns

Chapter summary

This chapter reviewed the basic forms of limit equilibrium stability analysis. Three different mechanisms were addressed i.e. translational sliding on an irregular slip surface, rotational sliding on a circular slip surface, and the general infinite slope model. All approaches employ the same constitutive relationship i.e. the Mohr-Coulomb criterion, and the same safety definition i.e. the uniform strength parameter reduction. Different solutions for the rotational geometry (i.e. the Swedish, Fellenius and Simplified Bishop method, respectively) arise from different equilibrium assumptions.

An overview of the mechanical assumptions of the presented methods is given in Table 4.1.

Similar considerations as reviewed in this chapter are adopted for the development of the Creep Equilibrium Analysis Method in Chapter 5.

CHAPTER 5

The Creep Equilibrium Analysis Method (CrEAM) - Theoretical framework

5.1 Preamble

Many landslides exhibit continual surface displacements, with velocities in the range of millimetres to metres per year. Typically, these displacements strongly localize within a basal shear zone of weak soil, or highly disintegrated and crushed rock with soil-like character (Noverraz 1996). These materials commonly show a pronounced tendency to creep (e.g. Martinotti 2010; Schneider-Muntau 2012).

Creep within the basal shear zone of a landslide is induced by the load of the hanging wall landslide mass. The shear zone thickness plays a prominent role. Inclinometer profiles of creeping landslides and laboratory creep tests on filled joints show that the creep strain increases approximately linearly with the shear zone thickness (Höwing & Kutter 1985; Malan et al. 1998; Van Asch & Van Genuchten 1990; Vulliet & Hutter 1988b).

The commonly observed steady-state deformation behaviour of creeping landslides suggests that they have reached a quasi-static equilibrium under current conditions. They are therefore considered to be in the stage of secondary (steady) creep.

This chapter introduces to a novel analytical approach for the analysis of creeping landslides. The method is rigid-element based and aims to describe the essential mechanics of creeping landslides with steady-state deformation behaviour. The new methodology merges concepts of viscous flow, kinematics and force equilibrium, and is referred to as the "Creep Equilibrium Analysis Method", with the acronym CrEAM.

5.2   Shear zone creep deformation

Assuming a viscous layer deforming in simple shear and exhibiting a linear creep displacement profile across the layer thickness, the angular shear strain is given as (Figure 5.1)

$$\tan \gamma = \frac{s_v}{d} \tag{5.1}$$

where s_v is the cumulative creep displacement at the top of the layer, and d is the layer thickness.
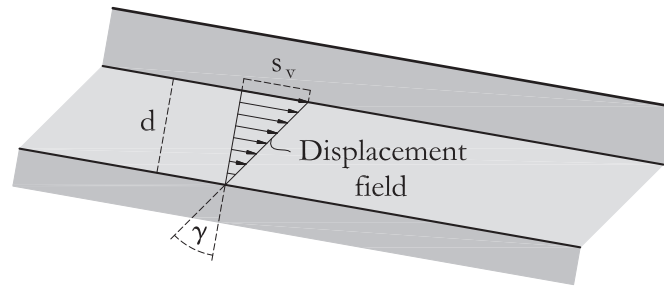
Figure 5.1
Linear velocity profile in a homogeneously deforming layer.

For small angles $\tan \gamma \approx \gamma$, (5.1) simplifies to

$$\gamma = \frac{s_v}{d} \tag{5.2}$$

where the angular shear strain γ has the unit of radian.

Differentiating (5.2) with respect to the time t changes the angular shear strain γ to the angular shear strain rate $\dot{\gamma}$, and the cumulative creep displacement s_v to the creep velocity v

$$\dot{\gamma} = \frac{d\gamma}{dt} = \frac{ds_v}{d \cdot dt} = \frac{v}{d} \tag{5.3}$$

The relationship between stress state and associated creep deformation of a viscous layer is established by equating (5.3) with the constitutive models of Chapter 3.

The coupling of the equations is shown below for the Newton constitutive relationship. The equivalent procedure for the other viscous models is documented in the Appendix A.3. The final expressions are listed below.

(a) Newton

Equating the angular shear strain rate $\dot{\gamma}$ in equation (5.3) with the Newtonian constitutive equation (3.1) and, subsequently, isolating $\tau_{\dot{\gamma}}$ yields

$$\tau_{\dot{\gamma}} = \bar{\mu}^{Newton} \cdot \frac{v}{d} \tag{5.4}$$

Assuming a uniform stress distribution at the bottom of the slice, the shear stress can be expressed in terms of the shear force and the area of the slice per unit width

$$\tau_{\dot{\gamma}} = \frac{T_{\dot{\gamma}} \cos\alpha}{b} \tag{5.5}$$

Equating (5.4) and (5.5) and isolating the shear force $T_{\dot{\gamma}}$ gives

$$T_{\dot{\gamma}} = \bar{\mu}^{Newton} \cdot \frac{bv}{\cos\alpha d} \tag{5.6}$$

(b) Bingham

Employing Bingham's model (3.2) yields

$$T_{\dot{\gamma}} = \frac{b}{\cos\alpha}\left(\tau_y^{Bingham} + \bar{\mu}^{Bingham} \cdot \frac{v}{d}\right) \tag{5.7}$$

(c) Norton

By introducing the constitutive equation of the modified Norton approach (3.4) we obtain

$$T_{\dot{\gamma}} = \frac{b}{\cos\alpha}\left(\tau_y^{Norton} + \sqrt[\langle m^{Norton}\rangle]{\frac{v\bar{\mu}^{Norton}}{d}}\right) \tag{5.8}$$

(d) Original Vulliet-Hutter

Using the constitutive equation of the original Vulliet-Hutter model (3.6) yields

$$T_{\dot{\gamma}} = \frac{\sqrt{12}\left[C\cos\varphi + \left(N_{\dot{\gamma}} - U\right)\sin\varphi\right]}{3-\sin\varphi} \cdot {}^{\langle m^{VH_{DP}}\rangle}\sqrt{\frac{v}{2dA^{VH_{DP}}}} \qquad (5.9)$$

(e) Modified Vulliet-Hutter

For the modified Vulliet-Hutter approach (3.7) we get

$$T_{\dot{\gamma}} = \left[C\cos\varphi + \left(N_{\dot{\gamma}} - U\right)\sin\varphi\right] \cdot {}^{\langle m^{VH_{MC}}\rangle}\sqrt{\frac{v}{2dA^{VH_{MC}}}} \qquad (5.10)$$

Remarks

The formulations (5.6) to (5.10) are valid for:

- infinite slope situations since the constitutive equations were developed for plane strain and constant volume deformation; and
- very thin creep layers since its self-weight is neglected

Nevertheless, the above formulations lead to a good approximation if

- the shear zone thickness is relatively small in comparison to its longitudinal extent; and
- the self-weight of the shear zone is small in comparison to the overburden

5.3 Kinematic constraints

The shape of the interface between the (rigid) landslide mass and the deforming layer fundamentally controls the kinematic behaviour of the landslide. While pure planar und circular surfaces allow a displacement without any internal deformation, an irregular interface inevitably demands a distortion of the sliding mass. Landslide displacement along an irregular basal boundary requires therefore appropriate assumptions in terms of the internal distortion mechanism (e.g. internal shear planes).

The kinematic conditions for planar, circular and irregular sliding surfaces are enumerated below and based on:
- rigid body idealisation for the elements of the sliding mass; and
- constant volume deformation of the creeping layer such that the creep vector direction corresponds to the interface inclination

5.3.1 Planar interface

For a mass moving on a perfectly planar surface no internal defomation is required in order to accommodate the displacement. The (virtual) elements behave kinematically as a single block (Figure 5.2).

Hence, the velocity vectors of all elements $\vec{v}_i$ are equal in magnitude and direction

$$\vec{v}_i = \vec{v} \tag{5.11}$$

Planar interface between rigid mass and deforming shear zone
(no curvature)

Velocity scheme
for block translation

$\vec{v} = \text{const.}$
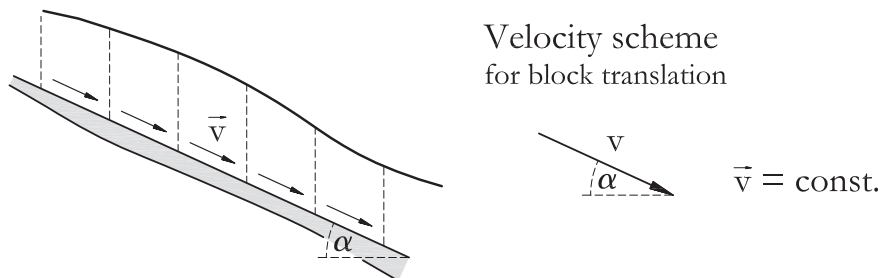
Figure 5.2
Schematic cross-section of a rigid mass with a planar interface to a basal shear zone (shaded).

5.3.2 Circular interface

Assuming a perfectly circular interface, the hanging wall sliding mass behaves like a single body rotating around the circle centre. All (virtual) elements thus displace with the same angular velocity ω

$$\omega_i = \omega \tag{5.12}$$

Since all points at the sliding mass base are equidistant to the circle centre, the velocity vectors along the base $\vec{v}_i$ are equal in magnitude (Figure 5.3)

$$\left|\vec{v}_i\right| = \left|\vec{v}\right| = v \tag{5.13}$$

while the creep vector direction depends on the local interface inclination.

The velocity at the slide base is related to the angular creep velocity by

$$v = \omega r \tag{5.14}$$

where r denotes the radius of the slip circle. The velocity of an arbitrary point P_x in or upon the rotational sliding mass depends both on the angular creep velocity ω, and the distance $a_{P_x C_c}$ to the circle centre C_c

$$v_{P_x} = \omega a_{P_x C_c} \tag{5.15}$$

Circular interface between rigid mass and deforming shear zone
(constant curvature)

Velocity scheme
for block rotation
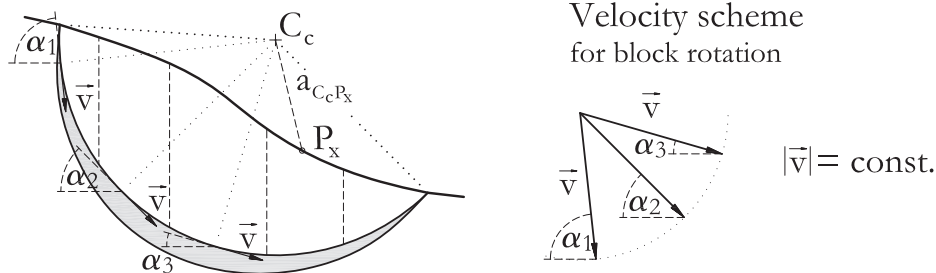
$\left|\vec{v}\right| = $ const.

Figure 5.3
Rigid mass with circular interface to a basal shear zone (left) and associated velocity scheme (right). The rotational deformation is characterised by constant displacement rates along the interface.

5.3.3 Irregular interface

For an irregular (polygonal) shaped interface between rigid slices and deforming layer, the individual element displacements are determined by a kinematic chain. In this way, coherent displacement of all elements is ensured. Assuming vertical interfaces between the rigid elements implies that relative displacements between the elements (slices) are solely vertical.

Therefore, the horizontal velocity vector component of all slices is equal (Figure 5.4)

$$v_h = |\vec{v}_1| \cos \alpha_1 = |\vec{v}_2| \cos \alpha_2 = ... |\vec{v}_i| \cos \alpha_i \qquad (5.16)$$

By rearranging (5.16), $|\vec{v}_i| = v_i$ can be formulated by means of $|\vec{v}_1| = v_1$ as

$$v_i = v_1 \cdot \frac{\cos \alpha_1}{\cos \alpha_i} \qquad (5.17)$$

Equation (5.17) indicates that all slice velocities v_i are coupled to each other. Once the velocity of one element in the system (e.g. v_1) is preset or known, all other element velocities are determined by kinematic relationships.

Irregular interface between rigid mass and deforming shear zone
(variable curvature)
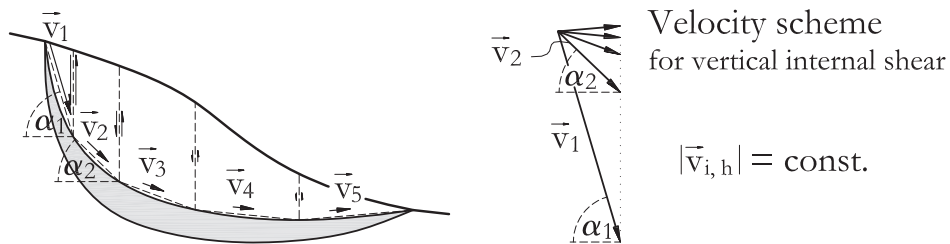
Figure 5.4
Cross-section of an assembly of rigid slices with an irregular interface to a basal deformation layer (left) and associated velocity scheme (right). The deformation is characterised by internal vertical shear and a kinematic chain with constant horizontal displacement rates.

61

5.4 CrEAM algorithms

Several approaches for the analysis of creeping landslides are presented below. In all approaches, the problem is rendered determinate by including

- constitutive equations;
- kinematic equations; and
- equilibrium equations

Three geometry classes include the infinite slope model as well as rotational and translational slides. Different CrEAM algorithms are developed, based on different mechanical assumptions and different constitutive models. The aim of each algorithm is to find the reactive forces and the associated creep deformation rates, which simultaneously satisfy the equilibrium requirements, kinematic constraints, and constitutive relationships. In general, solutions are obtained by an iterative calculation procedure. For some cases linear solutions exist.

5.4.1 Infinite slope model

A slope model consisting of an infinite rigid panel lying on a likewise infinite viscous layer represents the easiest geometry for creep analysis (Figure 5.5). Although this situation is theoretical, the infinite slope model provides valuable insights in the fundamental concepts and behaviour of CrEAM.

The problem is rendered statically determinate by recognizing that:

$$\left|\vec{U}_l\right| = \left|\vec{U}_r\right| \qquad \left|\vec{E}_l'\right| = \left|\vec{E}_r'\right| \tag{5.18}$$

The reactive forces at the base of a slice in the infinite slope can thus be determined from equilibrium requirements. Based on force equilibrium equations parallel and perpendicular to the slope inclination, the resulting shear force and total normal force are given as

$$T = \left(W + P_v\right)\sin\alpha - P_h\cos\alpha \tag{5.19}$$

$$N = \left(W + P_v\right)\cos\alpha + P_h\sin\alpha \tag{5.20}$$

Infinite slope

h, b   Slice height and width
h_w Saturated column above slice base
d   Shear zone thickness
α Infinite slope inclination

γ, γ_r Specific weight (wet, saturated)
u   Basal hydrostatic pressure
W   Weight force
U, U_l, U_r Basal, Left, Right hydrostatic force
T   Shear (tangential) force
N, N'   Total/Effective normal force
E, E'   Total/Effective interslice force
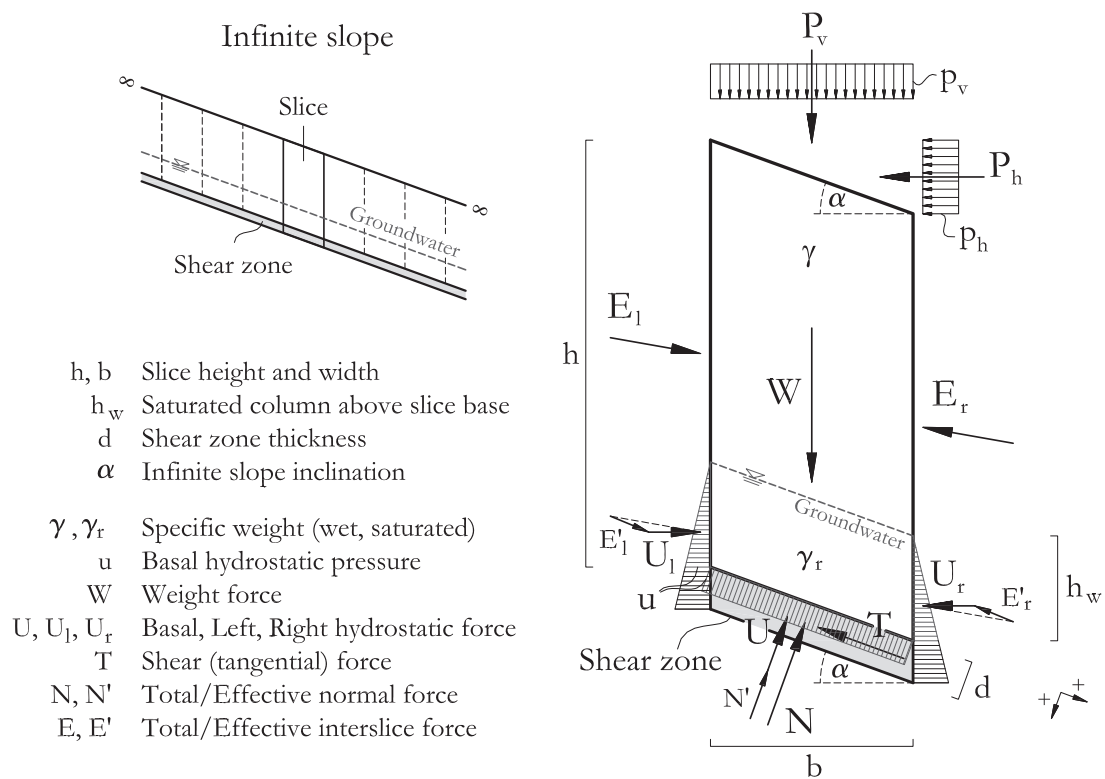
Figure 5.5
Active and passive forces operating at a slice of an infinite slope with a basal viscous shear zone.

Combining the above equilibrium equations with a viscous relationship allows the creep velocity of the infinite slope to be determined as a function of overburden self-weight, external loads, viscous parameters, and shear zone thickness.

Table 5.1 provides an overview of the boundary conditions and the unknown variables of the infinite slope problem. The ratio of equations to unknowns is 3:3. Solutions with different constitutive models are presented in the following subsections.

Table 5.1

Aspects of CrEAM for an infinite slope model (CrEAM^{inf}).

Geometry / Mechanism

Slope with infinite extent, slip surface parallel to slope surface

---

Assumptions for interslice forces

All slices are self-similar, resultant of interslice forces is zero

---

(Number of) Equilibrium equations satisfied

(1)	Σ Forces perpendicular to slope	$\left(W + P_v\right)\cos\alpha + P_h \sin\alpha - N_{\dot\gamma} = 0$
(1)	Σ Forces parallel to slope	$\left(W + P_v\right)\sin\alpha - P_h \cos\alpha - T_{\dot\gamma} = 0$

(Number of) Constitutive equation satisfied (options a-e)

	a. Newton, eq. (5.6)	$T_{\dot\gamma} = \bar\mu^{Newton} \cdot \dfrac{bv}{d\cos\alpha}$
	b. Bingham, eq. (5.7)	$T_{\dot\gamma} = \dfrac{b}{\cos\alpha}\left(\tau_y^{Bingham} + \bar\mu^{Bingham} \cdot \dfrac{v}{d}\right)$
(1)	c. Modified Norton, eq. (5.8)	$T_{\dot\gamma} = \dfrac{b}{\cos\alpha}\left(\tau_y^{Norton} + \sqrt[\langle m^{Norton}\rangle]{\dfrac{v \cdot \bar\mu^{Norton}}{d}}\right)$
	d. Original Vulliet-Hutter, eq. (5.9)	$T_{\dot\gamma} = \sqrt[\langle m^{VH_{DP}}\rangle]{\dfrac{v}{2dA^{VH_{DP}}}} \cdot \dfrac{\sqrt{12}\left[C\cos\varphi + \left(N_{\dot\gamma} - U\right)\sin\varphi\right]}{3 - \sin\varphi}$
	e. Modified Vulliet-Hutter, eq. (5.10)	$T_{\dot\gamma} = \sqrt[\langle m^{VH_{MC}}\rangle]{\dfrac{v}{2dA^{VH_{MC}}}} \cdot \left[C\cos\varphi + \left(N_{\dot\gamma} - U\right)\sin\varphi\right]$

Kinematic equations satisfied

Not required (self-similar system)

(Number of) Unknowns solved for

(3)   1 shear force $T_{\dot\gamma}$, 1 total normal force $N_{\dot\gamma}$, 1 creep velocity v

5.4.1.1 Deviatoric stress based creep analysis for infinite slopes (D-CrEAM^{inf})

(a) Newton

Equating (5.19) and the Newtonian creep model (5.6) yields

$$\left(W + P_v\right)\sin\alpha - P_h\cos\alpha = \bar{\mu}^{Newton}\cdot\frac{bv}{d\cos\alpha} \tag{5.21}$$

The creep velocity v is expressed as

$$v = \frac{d}{b}\sin\alpha\cos\alpha\cdot\left[\frac{W + P_v - P_h\cot\alpha}{\bar{\mu}^{Newton}}\right] \tag{5.22}$$

By replacing the forces W, P_v and P_h in (5.22) with the formulations in (4.6) and (4.7) we obtain

$$v = d\sin\alpha\cos\alpha\cdot\frac{\gamma h + h_w\left(\gamma_r - \gamma\right) + p_v - p_h}{\bar{\mu}^{Newton}} \tag{5.23}$$

(b) Bingham

Equating (5.19) with the Bingham relationship (5.7) and, subsequently, isolating the creep velocity v gives

$$v = \frac{d}{\bar{\mu}^{Bingham}}\left[\frac{\left(W + P_v\right)\sin\alpha\cos\alpha - P_h\cos^2\alpha}{b} - \tau_y^{Bingham}\right] \tag{5.24}$$

By replacing the forces W, P_v and P_h in (5.24) with the formulations in (4.6) and (4.7) we obtain

$$v = d\cdot\frac{\left[\gamma h + h_w\left(\gamma_r - \gamma\right) + p_v - p_h\right]\sin\alpha\cos\alpha - \tau_y^{Bingham}}{\bar{\mu}^{Bingham}} \tag{5.25}$$

(c) Norton

Equating (5.19) with the modified Norton relationship (5.8) and, subsequently, isolating the creep velocity v gives

$$v = \frac{d}{\overline{\mu}^{Norton}} \cdot \left[\frac{(W + P_v)\sin\alpha\cos\alpha - P_h\cos^2\alpha}{b} - \tau_y^{Norton} \right]^{m^{Norton}} \tag{5.26}$$

By replacing the forces W, P_v and P_h in the latter equation with the formulations in (4.6) and (4.7) we get

$$v = d \cdot \frac{\left\{ \left[\gamma h + h_w(\gamma_r - \gamma) + p_v - p_h \right]\sin\alpha\cos\alpha - \tau_y^{Norton} \right\}^{m^{Norton}}}{\overline{\mu}^{Norton}} \tag{5.27}$$

5.4.1.2 Effective stress based creep analysis for infinite slopes (E-CrEAM^{inf})

(d) Original Vulliet-Hutter

Equating the terms for the shear force T according the equilibrium requirement (5.19) with the original Vulliet-Hutter relationship (5.9) yields

$$(W + P_v)\sin\alpha - P_h\cos\alpha = \frac{\sqrt{12}\left[C\cos\varphi + (N_{\dot\gamma} - U)\sin\varphi \right]}{3 - \sin\varphi} \cdot \left\langle m^{VH_{DP}} \right\rangle \sqrt{\frac{v}{2dA^{VH_{DP}}}} \tag{5.28}$$

Expressing $N_{\dot\gamma}$ in (5.28) by the equilibrium requirement given in (5.20) and isolating v yields the creep velocity as

$$v = 2dA^{VH_{DP}} \cdot \left\{ \frac{3 - \sin\varphi}{\sqrt{12}} \cdot \frac{(W + P_v)\tan\alpha - P_h}{C \cdot \frac{\cos\varphi}{\cos\alpha} + \left[W + P_v + \tan\alpha P_h - \frac{U}{\cos\alpha} \right] \cdot \sin\varphi} \right\}^{m^{VH_{DP}}} \tag{5.29}$$

By replacing the forces W, P_v, P_h, U and C in the latter equation by the formulations (4.6), (4.7), (4.9) and (4.4), and subsequently cancelling out the constant slice width b, we obtain

$$v = 2dA^{VH_{DP}} \cdot \left\{ \frac{3 - \sin\varphi}{\sqrt{12}} \cdot \frac{\left[\gamma h + h_w (\gamma_r - \gamma) + p_v - p_h \right] \tan\alpha}{\frac{c\cos\varphi}{\cos^2\alpha} + \left[\begin{array}{l} \gamma h + h_w (\gamma_r - \gamma) ... \\ ... + p_v + p_h \tan^2\alpha - \gamma_w h_w \end{array} \right] \cdot \sin\varphi} \right\}^{m^{VH_{DP}}} \tag{5.30}$$

(e) Modified Vulliet-Hutter

Equating (5.19) with the modified Vulliet-Hutter relationship (5.10), and subsequently introducing (5.20) for the total normal force $N_{\hat{\gamma}}$, the creep velocity v can be expressed as

$$v = 2dA^{VH_{MC}} \cdot \left\{ \frac{(W + P_v)\tan\alpha - P_h}{C \cdot \frac{\cos\varphi}{\cos\alpha} + \left[W + P_v + \tan\alpha P_h - \frac{U}{\cos\alpha} \right] \cdot \sin\varphi} \right\}^{m^{VH_{MC}}} \tag{5.31}$$

By replacing the forces W, P_v, P_h, U and C in the latter equation by the formulations in (4.6), (4.7), (4.9) and (4.4), and discarding the constant slice width b, we get

$$v = 2dA^{VH_{MC}} \cdot \left\{ \frac{\left[\gamma h + h_w (\gamma_r - \gamma) + p_v - p_h \right] \tan\alpha}{\frac{c\cos\varphi}{\cos^2\alpha} + \left[\gamma h + h_w (\gamma_r - \gamma) + p_v + p_h \tan^2\alpha - \gamma_w h_w \right] \sin\varphi} \right\}^{m^{VH_{MC}}} \tag{5.32}$$

Section 5.5 demonstrates the application of the above CrEAM variants for infinite slopes. The examples give important insights to the behaviour of the constitutive models, and to the sensitivity of the CrEAM algorithms to the input parameters.

5.4.2 Rotational mechanism with circular creep interface

The approaches introduced in this section are designed for landslides with circular (cylindical) basal shear zones (Figure 5.6). The mechanism is rotational.

Different calculation procedures are enumerated below. From the kinematic point of view, all methods suppose a uniform cumulative creep deformation along the top of the viscous shear zone and, thus, a constant velocity along the bottom of the rigid mass. Furthermore, all methods share the requirement of moment equilibrium. Differences between the methods primarily relate to the constituitive models employed, and from assumptions regarding the interslice forces.

Figure 5.6
Left: Rotational landslide mass moving on a viscous shear zone.
Right: Example slice. The coordinate system in the lower right corner denotes the sign convention.

The moment exerted on an arbitrary slice i due to rotation about the slip circle centre C_c is given by

$$M_i = \begin{bmatrix} rT_{\dot{\gamma},i} - r\sin\alpha_i\left(W_i + P_{v,i}\right) + P_{h,i}\cos\alpha_i\left(r - h_i\cos\alpha_i\right)... \\ ... - a_{U,i(i-1)}U_{i(i-1)} - a_{E'_{\dot{\gamma}},i(i-1)}E'_{\dot{\gamma},i(i-1)} + a_{U,i(i+1)}U_{i(i+1)} + a_{E'_{\dot{\gamma}},i(i+1)}E'_{\dot{\gamma},i(i+1)} \end{bmatrix} \qquad (5.33)$$

where:

- $a_{U,i(i-1)}$, $a_{U,i(i+1)}$, $a_{E'_{\dot{\gamma}},i(i-1)}$ and $a_{E'_{\dot{\gamma}},i(i+1)}$ are the lever arms of the water pressure forces $U_{i(i-1)}$ and $U_{i(i+1)}$ and the effective interslice forces $E'_{\dot{\gamma},i(i-1)}$ and $E'_{\dot{\gamma},i(i+1)}$, respectively

Further supposing that:

- the vertical and horizontal surcharge loads $P_{v,i}$ and $P_{h,i}$ act at the middle of the slice tops

- the basal normal forces $N_{\dot{\gamma},i}$ act at the middle of the slice bases and, thus, have no lever arm, and consequently do not contribute to the moment

- no forces act at the lateral boundaries of the sliding mass i.e. $U_{1(1-1=0)} = E'_{\dot{\gamma},1(1-1=0)} = 0$ and $U_{n(n+1)} = E'_{\dot{\gamma},n(n+1)} = 0$

Satisfying the equilibrium of moment for the overall system implies that the summation of the moments of all n slices is equal to zero

$$\sum_{i=1}^{n} M_i = r\sum_{i=1}^{n}\left[T_{\dot{\gamma},i} - \left(W_i + P_{v,i}\right)\sin\alpha_i\right] + \sum_{i=1}^{n}\left[P_{h,i}\cos\alpha_i\left(r - h_i\cos\alpha_i\right)\right] = 0 \qquad (5.34)$$

The moments induced by the interslice forces cancel out due to the principle of "*actio est reactio*".

Introducing for $T_{\dot{\gamma},i}$ in (5.34) the diverse constitutive relationsships developed in Section 5.2 yields different approaches which are grouped in the subsequent sections.

5.4.2.1 Deviatoric stress based creep analysis for rotational slides (D-CrEAM^{rot})

This method is established for the creep analysis of rotational slides on the basis of deviatoric stress based viscous models. It is assumed that the creep deformation in the viscous layer is purely attributed to the basal shear forces $T_{\dot{\gamma},i}$. The total normal forces at the slice base $N_{\dot{\gamma},i}$ do neither take part of the various constitutive relationships (see Newton eq.(5.6), Bingham eq.(5.7), modified Norton, eq. (5.8)) nor contribute in the overall moment (see eq. (5.34)). Therefore, $N_{\dot{\gamma},i}$ can be disregarded in the solution of the equation system.

Mathematically, the problem is characterised by $n+1$ unknowns (n basal shear forces $T_{\dot{\gamma},i}$ and the basal creep velocity v), and $n+1$ equations (n constitutive equations and the overall moment equilibrium equation). The equations used in this approach and the associated unknown quantities are summarized in Table 5.2.

The detailed solution of D-CrEAM^{rot} is documented in Appendix Section A.4.2.1. The final formulas for the Newton, Bingham and Norton constitutive models are presented subsequently.

(a) Newton

Using the Newtonian constitutive relationship (5.6) and solving the equation system for the creep velocity v yields the solution:

$$v = \frac{\sum_{i=1}^{n}\left[\left(W_i + P_{v,i}\right)\sin\alpha_i - P_{h,i}\cos\alpha_i\left(1 - \cos\alpha_i\frac{h_i}{r}\right)\right]}{\sum_{i=1}^{n}\left(\frac{b_i\bar{\mu}_i^{Newton}}{d_i\cos\alpha_i}\right)} \tag{5.35}$$

(b) Bingham

Applying the Bingham constitutive relationship (5.7) yields

$$v = \frac{\sum_{i=1}^{n}\left[\left(W_i + P_{v,i}\right)\sin\alpha_i - \frac{b_i\tau_{y,i}^{Bingham}}{\cos\alpha_i} - P_{h,i}\cos\alpha_i\left(1 - \cos\alpha_i\frac{h_i}{r}\right)\right]}{\sum_{i=1}^{n}\left(\frac{b_i\bar{\mu}_i^{Bingham}}{d_i\cos\alpha_i}\right)} \tag{5.36}$$

Table 5.2
Aspects of CrEAM for rotational slides using deviatoric stress based viscous models (D-CrEAM^{rot}).

Geometry / Mechanism

Circular (cylindrical) slip surface / rotational mechanism

Assumptions for interslice forces

No assumptions (actio=reactio implicitly satisfied)

(Number of) Equilibrium equations satisfied

(1) Σ Moments of slices about centre of circle, eq. (5.34)

$$\sum_{i=1}^{n} M_i = r \sum_{i=1}^{n} \left[T_{\dot{\gamma},i} - \left(W_i + P_{v,i} \right) \sin\alpha_i + P_{h,i} \cos\alpha_i \left(1 - \cos\alpha_i \frac{h_i}{r} \right) \right] = 0$$

(Number of) Constitutive equation satisfied (options a-c)

(n)

a. Newton, eq. (5.6)

$$T_{\dot{\gamma},i} = \bar{\mu}_i^{Newton} \cdot \frac{b_i v}{d_i \cos\alpha_i}$$

b. Bingham, eq. (5.7)

$$T_{\dot{\gamma},i} = \frac{b_i}{\cos\alpha_i} \left(\tau_{y,i}^{Bingham} + \bar{\mu}_i^{Bingham} \cdot \frac{v}{d_i} \right)$$

c. Modified Norton, eq. (5.8)

$$T_{\dot{\gamma},i} = \frac{b_i}{\cos\alpha_i} \left(\tau_{y,i}^{Norton} + \langle m_i^{Norton} \rangle \sqrt{\frac{v \cdot \bar{\mu}_i^{Norton}}{d_i}} \right)$$

Kinematic equations satisfied

Constant creep velocity along base of rotational sliding mass, eq.(5.13) $\left| \vec{v}_i \right| = \left| \vec{v} \right| = v$

(Number of) Unknowns solved for

(n+1)   n shear forces $T_{\dot{\gamma},i}$, 1 constant creep velocity v

(c) Norton

For the modified Norton constitutive relationship (5.8) we obtain an iteration equation for the creep velocity v :

$$v = \frac{\sum_{i=1}^{n}\left[\left(W_i + P_{v,i}\right)\sin\alpha_i - \frac{b_i \tau_{y,i}^{Norton}}{\cos\alpha_i} - P_{h,i}\cos\alpha_i\left(1 - \cos\alpha_i\frac{h_i}{r}\right)\right]}{\sum_{i=1}^{n}\left[\frac{b_i}{\cos\alpha_i}\cdot\left\langle m_i^{Norton}\right\rangle\sqrt{\frac{v^{\left(1-m_i^{Norton}\right)}\bar{\mu}_i^{Norton}}{d_i}}\right]}$$

(5.37)

Assuming a constant exponent for all slices $m_i^{Norton} = m^{Norton}$ leads to a simplified solution of the form

$$v = \left\{\frac{\sum_{i=1}^{n}\left[\left(W_i + P_{v,i}\right)\sin\alpha_i - \frac{b_i \tau_{y,i}^{Norton}}{\cos\alpha_i} - P_{h,i}\cos\alpha_i\left(1 - \cos\alpha_i\frac{h_i}{r}\right)\right]}{\sum_{i=1}^{n}\left(\frac{b_i}{\cos\alpha_i}\cdot\left\langle m^{Norton}\right\rangle\sqrt{\frac{\bar{\mu}_i^{Norton}}{d_i}}\right)}\right\}^{m^{Norton}}$$

(5.38)

5.4.2.2 Simplified effective stress based creep analysis for rotational slides (Simplified E-CrEAM*rot*)

This method is established for the simplified creep analysis of rotational slides on the basis of effective stress based viscous models, which suppose that the creep deformation in the viscous layer is attributed to the basal shear forces $T_{\dot{\gamma},i}$ and the effective normal forces $N'_{\dot{\gamma},i} = N_{\dot{\gamma},i} - U_i$. In analogy to the Fellenius approach in the limit equilibrium stability analysis, the total normal forces $N_{\dot{\gamma},i}$ are directly calculated from the active forces without considering the effective interslice forces:

$$N_{\dot{\gamma},i} = N'_{\dot{\gamma},i} + U_i = \left(W_i + P_{v,i}\right)\cos\alpha_i + P_{h,i}\sin\alpha_i + \left(U_{i(i+1)} - U_{i(i-1)}\right)\sin\alpha_i$$

(5.39)

Equation (5.39) provides a reasonable approximation for the normal forces, which is significant since in this way $N_{\dot{\gamma},i}$ are known quantities.

Mathematically, the problem is characterised by $n+1$ unknowns (n basal shear forces $T_{\dot\gamma,i}$ and the basal creep velocity v), and $n+1$ equations (n constitutive equations and the overall moment equilibrium equation). An overview of the equations used in this approach and the associated unknown is summarized in Table 5.3.

The detailed solution of the Simplified E-CrEAM^{rot} is shown in Appendix Section A.4.2.2. The final formulas for the original and modified Vulliet-Hutter constitutive models are presented subsequently.

Table 5.3
Aspects of CrEAM for rotational slides with implemented effective stress based viscous models and neglected interslice forces (Simplified E-CrEAM^{rot}).

Geometry / Mechanism

Circular (cylindrical) slip surface / rotational mechanism

Assumptions for interslice forces

Interslice forces neglected, principle of actio=reactio between slices is not satiesfied

(Number of) Equilibrium equations satisfied

(1) Σ Moments of slices about centre of circle, eq. (5.34)

$$\sum_{i=1}^{n} M_i = r \sum_{i=1}^{n}\left[T_{\dot\gamma,i} - \left(W_i + P_{v,i}\right)\sin\alpha_i + P_{h,i}\cos\alpha_i\left(1 - \cos\alpha_i\frac{h_i}{r}\right)\right] = 0$$

(Number of) Constitutive equation satisfied for n slices (options d+e)

(n)

d. Original Vulliet-Hutter, eq. (5.9)

$$T_{\dot\gamma,i} = \langle m_i^{VH_{DP}}\rangle\sqrt{\frac{v}{2d_i A_i^{VH_{DP}}}}\cdot\frac{\sqrt{12}\left[C_i\cos\varphi_i + \left(N_{\dot\gamma,i} - U_i\right)\sin\varphi_i\right]}{3 - \sin\varphi_i}\,*$$

e. Modified Vulliet-Hutter, eq. (5.10)

$$T_{\dot\gamma,i} = \langle m_i^{VH_{MC}}\rangle\sqrt{\frac{v}{2d_i A_i^{VH_{MC}}}}\cdot\left[C_i\cos\varphi_i + \left(N_{\dot\gamma,i} - U_i\right)\sin\varphi_i\right]*$$

* the total normal force $N_{\dot\gamma,i}$ is directly derived by the weight of the slice, the external loads and the water pressure forces in the slice interfaces. The effective interslice forces are neglected.

Kinematic equations satisfied

Constant creep velocity along base of rotational sliding mass, eq.(5.13) $\left|\vec{v}_i\right| = \left|\vec{v}\right| = v$

(Number of) Unknowns solved for

(n+1) n shear forces $T_{\dot\gamma,i}$, 1 constant creep velocity v

(d) Original Vulliet-Hutter

Using the original Vulliet-Hutter constitutive relationship (5.9) and solving for the creep velocity v yields the iterative expression

$$v = \frac{\sum_{i=1}^{n}\left[\left(W_i + P_{v,i}\right)\sin\alpha_i - P_{h,i}\cos\alpha_i\left(1 - \cos\alpha_i\frac{h_i}{r}\right)\right]}{\sum_{i=1}^{n}\left\{\frac{\sqrt{12}\sin\varphi_i}{3-\sin\varphi_i}\cdot\left\langle m_i^{VH_{DP}}\right\rangle\sqrt{\frac{v^{\left(1-m_i^{VH_{DP}}\right)}}{2d_i A_i^{VH_{DP}}}}\cdot\begin{bmatrix}\left(W_i + P_{v,i}\right)\cos\alpha_i + C_i\cot\varphi_i + P_{h,i}\sin\alpha_i ...\\ ...+\left(U_{i(i+1)} - U_{i(i-1)}\right)\sin\alpha_i - U_i\end{bmatrix}\right\}} \quad (5.40)$$

A constant exponent for all slices $m_i^{VH_{DP}} = m^{VH_{DP}}$ leads to the simplified form

$$v = \left\{\frac{\sum_{i=1}^{n}\left[\left(W_i + P_{v,i}\right)\sin\alpha_i - P_{h,i}\cos\alpha_i\left(1 - \cos\alpha_i\frac{h_i}{r}\right)\right]}{\sum_{i=1}^{n}\left\{\frac{\sqrt{12}\sin\varphi_i}{3-\sin\varphi_i}\cdot\left(2d_i A_i^{VH_{DP}}\right)^{\left(\frac{-1}{m_i^{VH_{DP}}}\right)}\cdot\begin{bmatrix}\left(W_i + P_{v,i}\right)\cos\alpha_i + C_i\cot\varphi_i ...\\ ...+ P_{h,i}\sin\alpha_i - U_i ...\\ ...+\left(U_{i(i+1)} - U_{i(i-1)}\right)\sin\alpha_i\end{bmatrix}\right\}}\right\}^{m^{VH_{DP}}} \quad (5.41)$$

(e) Modified Vulliet-Hutter

For the modified Vulliet-Hutter constitutive relationship (5.10), the solution for the creep velocity v is

$$v = \frac{\sum_{i=1}^{n}\left[\left(W_i + P_{v,i}\right)\sin\alpha_i - P_{h,i}\cos\alpha_i\left(1 - \cos\alpha_i\frac{h_i}{r}\right)\right]}{\sum_{i=1}^{n}\left\{\sin\varphi_i\cdot\left\langle m_i^{VH_{MC}}\right\rangle\sqrt{\frac{v^{\left(1-m_i^{VH_{MC}}\right)}}{2d_i A_i^{VH_{MC}}}}\cdot\begin{bmatrix}\left(W_i + P_{v,i}\right)\cos\alpha_i + C_i\cot\varphi_i + P_{h,i}\sin\alpha_i ...\\ ...+\left(U_{i(i+1)} - U_{i(i-1)}\right)\sin\alpha_i - U_i\end{bmatrix}\right\}} \quad (5.42)$$

74

For a constant exponent for all slices $m_i^{VH_{MC}} = m^{VH_{MC}}$ we get

$$v = \left\{ \dfrac{\displaystyle\sum_{i=1}^{n}\left[\left(W_i + P_{v,i}\right)\sin\alpha_i - P_{h,i}\cos\alpha_i\left(1 - \cos\alpha_i\dfrac{h_i}{r}\right)\right]}{\displaystyle\sum_{i=1}^{n}\left\{\sin\varphi_i \cdot \left(2d_i A_i^{VH_{MC}}\right)^{\left(\frac{-1}{m_i^{VH_{MC}}}\right)} \cdot \begin{bmatrix}\left(W_i + P_{v,i}\right)\cos\alpha_i + C_i\cot\varphi_i \ldots \\ \ldots + P_{h,i}\sin\alpha_i - U_i \ldots \\ \ldots + \left(U_{i(i+1)} - U_{i(i-1)}\right)\sin\alpha_i\end{bmatrix}\right\}} \right\}^{m^{VH_{MC}}} \tag{5.43}$$

5.4.2.3   Ordinary effective stress based creep analysis for rotational slides (Ordinary E-CrEAM*rot*)

The Ordinary E-CrEAM*rot* represents a more rigorous formulation for creeping rotational slides than the Simplified E-CrEAM*rot*, as it includes additional equilibrium constraints. In analogy to the Bishop approach in the limit equilibrium stability analysis, the slice normal forces $N_{\dot\gamma,i}$ can be derived by means of the vertical slice equilibrium

$$W_i + P_{v,i} - N_{\dot\gamma,i}\cos\alpha_i - T_{\dot\gamma,i}\sin\alpha_i + E'_{\dot\gamma,i(i-1)}\sin\vartheta_{i(i-1)} - E'_{\dot\gamma,i(i+1)}\sin\vartheta_{i(i+1)} = 0 \tag{5.44}$$

where the index $\dot\gamma$ refers to the creep solution, and the angles $\vartheta_{i(i-1)}$ and $\vartheta_{i(i+1)}$ denote the inclination angles of the effective interslice forces E'.

Assuming that the difference of the vertical components of the effective interslice forces are small and can be neglected

$$E'_{\dot\gamma,i(i-1)}\sin\vartheta_{i(i-1)} - E'_{\dot\gamma,i(i+1)}\sin\vartheta_{i(i+1)} = 0 \tag{5.45}$$

the total normal force $N_{\dot\gamma,i}$ can be obtained by rearranging (5.44) as

$$N_{\dot\gamma,i} = \frac{W_i + P_{v,i}}{\cos\alpha_i} - T_{\dot\gamma,i}\tan\alpha_i \tag{5.46}$$

Equation (5.46) gives a good approximation for the normal forces but in contrast to the prior approach, $N_{\dot\gamma,i}$ depend on the shear forces $T_{\dot\gamma,i}$, thus, remain unknown quantities.

Mathematically, the problem is characterised by $2n+1$ unknowns (n basal shear forces $T_{\dot\gamma,i}$, n basal total normal forces $N_{\dot\gamma,i}$, and the basal creep velocity v), and $2n+1$ equations (n constitutive equations, n simplified equations of vertical force equilibrium, and the overall moment equilibrium equation). An overview of the equations used in this approach and the associated unknown quantities is summarized in Table 5.4.

The detailed solution of the Ordinary E-CrEAM^{rot} is documented in Appendix Section A.4.2.3. The final formulas are presented subsequently.

(d) Original Vulliet-Hutter

Using the original Vulliet-Hutter constitutive relationship (5.9) and solving for the creep velocity v yields the solution:

$$v = \frac{\sum_{i=1}^{n}\left[\left(W_i + P_{v,i}\right)\sin\alpha_i - P_{h,i}\cos\alpha_i\left(1 - \cos\alpha_i\frac{h_i}{r}\right)\right]}{\sum_{i=1}^{n}\left[\left\langle m_i^{VH_{DP}}\right\rangle\sqrt{\frac{v^{\left(1-m_i^{VH_{DP}}\right)}}{2d_i A_i^{VH_{DP}}}}\cdot\frac{\dfrac{W_i + P_{v,i}}{\cos\alpha_i} + C_i\cot\varphi_i - U_i}{\dfrac{3-\sin\varphi_i}{\sqrt{12}\sin\varphi_i} + \tan\alpha_i\left\langle m_i^{VH_{DP}}\right\rangle\sqrt{\dfrac{v}{2d_i A_i^{VH_{DP}}}}}\right]}$$

(5.47)

(e) Modified Vulliet-Hutter

For the modified Vulliet-Hutter constitutive relationship (5.10) we get

$$v = \frac{\sum_{i=1}^{n}\left[\left(W_i + P_{v,i}\right)\sin\alpha_i - P_{h,i}\cos\alpha_i\left(1 - \cos\alpha_i\frac{h_i}{r}\right)\right]}{\sum_{i=1}^{n}\left[\left\langle m_i^{VH_{MC}}\right\rangle\sqrt{\frac{v^{\left(1-m_i^{VH_{MC}}\right)}}{2d_i A_i^{VH_{MC}}}}\cdot\frac{\dfrac{W_i + P_{v,i}}{\cos\alpha_i} + C_i\cot\varphi_i - U_i}{\dfrac{1}{\sin\varphi_i} + \tan\alpha_i\left\langle m_i^{VH_{MC}}\right\rangle\sqrt{\dfrac{v}{2d_i A_i^{VH_{MC}}}}}\right]}$$

(5.48)

Table 5.4

Aspects of CrEAM for rotational slides using effective stress based viscous models and simplified force equilibrium constraints (Ordinary E-CrEAM^{rot}).

Geometry / Mechanism

Circular (cylindrical) slip surface / rotational mechanism

Assumptions for interslice forces

Principle of action = reactio is satisfied for horizontal (normal) interslice force components, the vertical (tangential) interslice force components are neglected

---

(Number of) Equilibrium equations satisfied

(1)	Σ Moments of slices about centre of circle, eq. (5.34)	$\displaystyle\sum_{i=1}^{n} M_i = r\sum_{i=1}^{n}\left[T_{\dot{\gamma},i} - \left(W_i + P_{v,i}\right)\sin\alpha_i + P_{h,i}\cos\alpha_i\left(1-\cos\alpha_i\frac{h_i}{r}\right)\right]=0$
(n)	Σ Forces in vertical direction per slice (interslice components neglected)	$W_i + P_{v,i} - N_{\dot{\gamma},i}\cos\alpha_i - T_{\dot{\gamma},i}\sin\alpha_i = 0$

(Number of) Constitutive equation satisfied for n slices (options d+e)

(n)	d. Original Vulliet-Hutter, eq. (5.9)	$T_{\dot{\gamma},i} = \left\langle m_i^{VH_{DP}}\right\rangle\sqrt{\dfrac{v}{2d_i A_i^{VH_{DP}}}} \cdot \dfrac{\sqrt{12}\left[C_i\cos\varphi_i + \left(N_{\dot{\gamma},i}-U_i\right)\sin\varphi_i\right]}{3-\sin\varphi_i}$
	e. Modified Vulliet-Hutter, eq. (5.10)	$T_{\dot{\gamma},i} = \left\langle m_i^{VH_{MC}}\right\rangle\sqrt{\dfrac{v}{2d_i A_i^{VH_{MC}}}} \cdot \left[C_i\cos\varphi_i + \left(N_{\dot{\gamma},i}-U_i\right)\sin\varphi_i\right]$

Kinematic equations satisfied

Constant creep velocity along base of rotational sliding mass, eq.(5.13) $\qquad |\vec{v}_i| = |\vec{v}| = v$

(Number of) Unknowns solved for

(2n+1)   n shear forces $T_{\dot{\gamma},i}$, n total normal forces $N_{\dot{\gamma},i}$, 1 constant creep velocity v

5.4.3 Translational mechanism with irregular creep interface

The approaches introduced in this section are designed for landslides with an irregular interface between landslide mass and basal shear zone. The mechanism of movement is translational. For the analysis, the landslide mass is subdivided into imaginary slices whose bottom edges form the boundary between hanging wall landslide mass and shear zone (Figure 5.7). Due to the irregular curvature of the interface, the downslope movement causes internal deformation of the hanging wall landslide mass. Therefore, in contrast to the rotational mechanism, the interslice boundaries possess a physical meaning since they act as shear planes between the rigid elements.
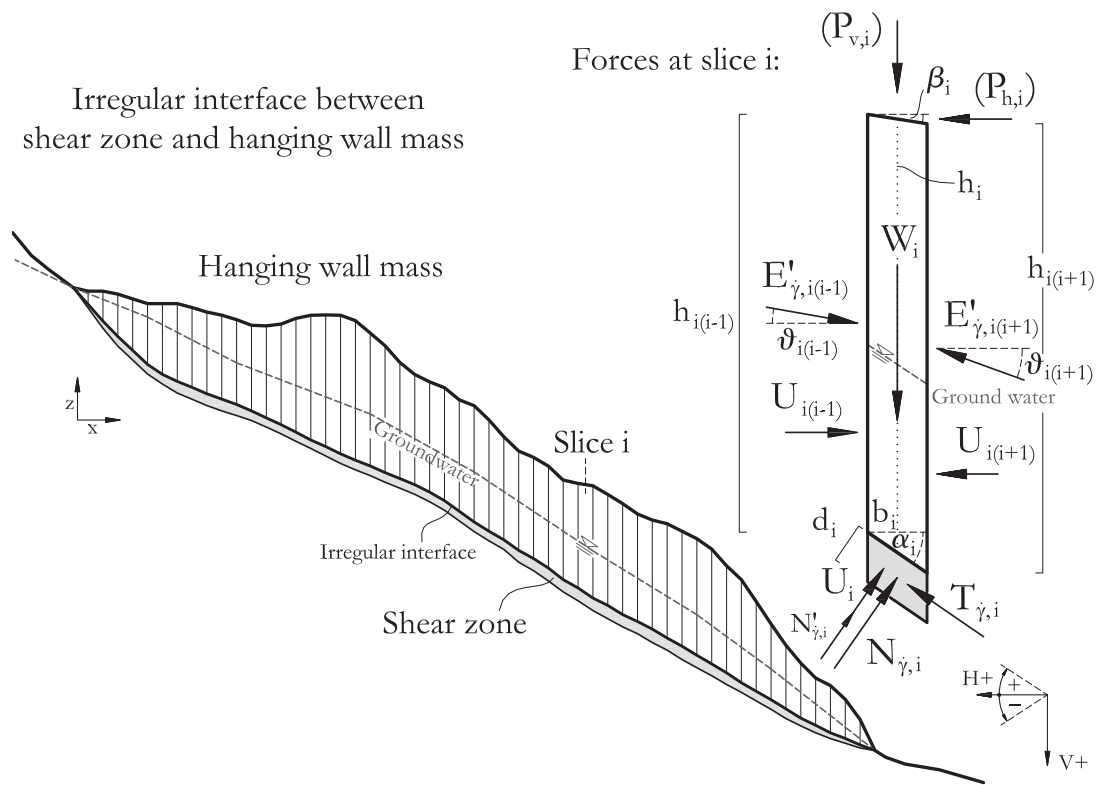
Figure 5.7
Left: Translational landslide mass moving on a viscous shear zone.
Right: Example slice. The coordinate system in the lower right corner denotes the sign convention.

Several calculation schemes based on different constitutive relationships are presented. All algorithms satisfy a simplified equilibrium of forces (corresponding to the Simplified Janbu equilibrium assumptions). Moreover, they assume kinematic compatibility of the slice creep displacements, and thus include a kinematic chain of creep velocities. Therefore, once the velocity of a single slice is known (e.g. v_1), the velocities v_i of all other slices can be determined by applying the kinematical equation (5.17).

The vertical and horizontal force equilibrium of an arbitrary slice i is given as:

$$W_i + P_{v,i} - N_{\dot\gamma,i} \cos\alpha_i - T_{\dot\gamma,i} \sin\alpha_i + E'_{\dot\gamma,i(i-1)} \sin\vartheta_{i(i-1)} - E'_{\dot\gamma,i(i+1)} \sin\vartheta_{i(i+1)} = 0 \qquad (5.49)$$

$$P_{h,i} - N_{\dot\gamma,i} \sin\alpha_i + T_{\dot\gamma,i} \cos\alpha_i - E'_{\dot\gamma,i(i-1)} \cos\vartheta_{i(i-1)} - U_{i(i-1)} + E'_{\dot\gamma,i(i+1)} \cos\vartheta_{i(i+1)} + U_{i(i+1)} = 0 \quad (5.50)$$

where the index $\dot\gamma$ refers to the creep analysis solution, and $\vartheta_{i(i-1)}$ and $\vartheta_{i(i+1)}$ denote the inclination angles of the effective interslice forces E'.

For the uppermost slice $i = 1$ the interslice forces $E'_{\dot\gamma,i(i-1)}$ and $U_{i(i-1)}$ are zero

$$E'_{\dot\gamma,i(i-1)} = U_{i(i-1)} = 0 \qquad (5.51)$$

Equivalently, for the lowermost slice $i = n$ applies

$$E'_{\dot\gamma,i(i+1)} = U_{i(i+1)} = 0 \qquad (5.52)$$

For the slices $i = \{2,...,n-1\}$ applies

$$\left|\vec{E}'_{\dot\gamma,i(i+1)}\right| = \left|\vec{E}'_{\dot\gamma,(i+1)i}\right| \qquad\qquad \left|\vec{E}'_{\dot\gamma,i(i-1)}\right| = \left|\vec{E}'_{\dot\gamma,(i-1)i}\right| \qquad (5.53)$$

In analogy to the Simplified Bishop and Simplified Janbu approaches in the stability analysis we can assume that the difference of the vertical components of the effective interslice forces acting on a slice i are small and can be neglected.

Mathematically, the problem is characterised by $(4n-1)$ unknowns (n basal shear forces $T_{\dot\gamma,i}$, n basal total normal forces $N_{\dot\gamma,i}$, $(n-1)$ horizontal components of the effective interslice forces $E'_{\dot\gamma,i(i+1)} \cos\vartheta_{i(i+1)} = E'_{\dot\gamma,(i+1)i} \cos\vartheta_{(i+1)i}$, and n basal creep velocities v_i defining the required kinematic chain), and $(4n-1)$ equations (n constitutive

equations, n simplified equations of vertical force equilibrium, n full equations of horizontal force equilibrium). An overview of the equations used for this approach and the associated unknowns is given in Table 5.5.

Detailed solutions are documented in Appendix Sections A.4.3.1 and A.4.3.2. Final formulas for the various constitutive models are shown subsequently.

5.4.3.1 Deviatoric stress based creep analysis for translational slides (D-CrEAM^{trans})

(a) Newton

Using the Newtonian constitutive relationship (5.6) and considering the kinematic chain requirement, the creep velocity v_1 is expressed as

$$v_1 = \frac{\sum_{i=1}^{n}\left[\left(W_i + P_{v,i}\right)\tan\alpha_i - P_{h,i}\right]}{\sum_{i=1}^{n}\left[\bar{\mu}_i^{Newton} \cdot \dfrac{b_i \cos\alpha_1}{d_i \cos\alpha_i}\left(1 + \tan^2\alpha_i\right)\right]} \tag{5.54}$$

(b) Bingham

Using the Bingham model (5.7) and the kinematic chain requirement yields the creep velocity v_1 as

$$v_1 = \frac{\sum_{i=1}^{n}\left[\left(W_i + P_{v,i}\right)\tan\alpha_i - P_{h,i} - b_i\tau_{y,i}^{Bingham}\left(1 + \tan^2\alpha_i\right)\right]}{\sum_{i=1}^{n}\left[\bar{\mu}_i^{Bingham} \cdot \dfrac{b_i \cos\alpha_1}{d_i \cos\alpha_i}\left(1 + \tan^2\alpha_i\right)\right]} \tag{5.55}$$

Table 5.5

Aspects of CrEAM for translational slides using a simplified equilibrium of forces (D-CrEAM^{trans} and E-CrEAM^{trans}).

Geometry / Mechanism

Polygonal (prismatic) slip surface / translational mechanism

Assumptions for interslice forces

Principle of action = reactio is satisfied for horizontal (normal) interslice force components, the vertical (tangential) interslice force components are neglected

(Number of) Equilibrium equations satisfied

(n)	Σ Forces in vertical direction per slice (interslice components neglected)	$W_i + P_{v,i} - N_{\dot\gamma,i}\cos\alpha_i - T_{\dot\gamma,i}\sin\alpha_i = 0$
(n)	Σ Forces in horizontal direction per slice	$\left\{\begin{array}{l} P_{h,i} - N_{\dot\gamma,i}\sin\alpha_i + T_{\dot\gamma,i}\cos\alpha_i - U_{i(i-1)} + U_{i(i+1)}\cdots \\ \cdots - E'_{\dot\gamma,i(i-1)}\cos\vartheta_{i(i-1)} + E'_{\dot\gamma,i(i+1)}\cos\vartheta_{i(i+1)} \end{array}\right\} = 0$

(Number of) Constitutive equation satisfied (options a-e)

(n)	a. Newton, eq. (5.6)	$T_{\dot\gamma,i} = \bar\mu_i^{Newton} \cdot \dfrac{b_i v_i}{d_i \cos\alpha_i}$
	b. Bingham, eq. (5.7)	$T_{\dot\gamma,i} = \dfrac{b_i}{\cos\alpha_i}\left(\tau_{y,i}^{Bingham} + \bar\mu_i^{Bingham}\cdot\dfrac{v_i}{d_i}\right)$
	c. Modified Norton, eq. (5.8)	$T_{\dot\gamma,i} = \dfrac{b_i}{\cos\alpha_i}\left(\tau_{y,i}^{Norton} + \langle m_i^{Norton}\rangle\sqrt{\dfrac{v_i\cdot\bar\mu_i^{Norton}}{d_i}}\right)$
	d. Original Vulliet-Hutter, eq. (5.9)	$T_{\dot\gamma,i} = \langle m_i^{VH_{DP}}\rangle\sqrt{\dfrac{v_i}{2d_iA_i^{VH_{DP}}}}\cdot\dfrac{\sqrt{12}\left[C_i\cos\varphi_i + \left(N_{\dot\gamma,i}-U_i\right)\sin\varphi_i\right]}{3-\sin\varphi_i}$
	e. Modified Vulliet- Hutter, eq. (5.10)	$T_{\dot\gamma,i} = \langle m_i^{VH_{MC}}\rangle\sqrt{\dfrac{v_i}{2d_iA_i^{VH_{MC}}}}\cdot\left[C_i\cos\varphi_i + \left(N_{\dot\gamma,i}-U_i\right)\sin\varphi_i\right]$

(Number of) Kinematic equations satisfied

(n-1)	Kinematic chain of creep velocities assuming shearing along slice boundaries, eq. (5.17)	$v_i = v_1\cdot\dfrac{\cos\alpha_1}{\cos\alpha_i}$

(Number of) Unknowns solved for

(4n-1)	n shear forces $T_{\dot\gamma,i}$, n total normal forces $N_{\dot\gamma,i}$, n creep velocities v_i, (n-1) horizontal components of eff. interslice forces $E'_{\dot\gamma,i(i+1)}\cos\vartheta_{i(i+1)} = E'_{\dot\gamma,(i+1)i}\cos\vartheta_{(i+1)i}$

(c) Norton

Using the modified Norton constitutive relationship (5.8) and considering the kinematic chain requirement allows to solve the equation system for the creep velocity v_1 by the expression

$$v_1 = \frac{\sum\limits_{i=1}^{n}\left[\left(W_i + P_{v,i}\right)\tan\alpha_i - P_{h,i} - b_i\tau_{y,i}^{Norton}\left(1+\tan^2\alpha_i\right)\right]}{\sum\limits_{i=1}^{n}\left[v_1^{\left(\frac{1-m_i^{Norton}}{m_i^{Norton}}\right)}\cdot b_i\left(1+\tan^2\alpha_i\right)\cdot\sqrt[\langle m_i^{Norton}\rangle]{\frac{\overline{\mu}_i^{Norton}}{d_i}\cdot\frac{\cos\alpha_1}{\cos\alpha_i}}\right]}$$

(5.56)

A constant exponent for all slices $m_i^{Norton} = m^{Norton}$ leads to the solution of the form

$$v_1 = \left\{\frac{\sum\limits_{i=1}^{n}\left[\left(W_i + P_{v,i}\right)\tan\alpha_i - P_{h,i} - b_i\tau_{y,i}^{Norton}\left(1+\tan^2\alpha_i\right)\right]}{\sum\limits_{i=1}^{n}\left[b_i\left(1+\tan^2\alpha_i\right)\cdot\sqrt[\langle m^{Norton}\rangle]{\frac{\overline{\mu}_i^{Norton}}{d_i}\cdot\frac{\cos\alpha_1}{\cos\alpha_i}}\right]}\right\}^{m^{Norton}}$$

(5.57)

5.4.3.2 Effective stress based creep analysis for translational slides (E-CrEAM^{trans})

(d) Original Vulliet-Hutter

Using the original Vulliet-Hutter constitutive relationship (5.9) and considering the kinematic chain requirement gives the creep velocity v_1 with the iterative equation:

$$
v_1 = \frac{\displaystyle\sum_{i=1}^{n}\left[\frac{W_i + P_{v,i} - \dfrac{\Lambda_i \sin\alpha_i}{\mathrm{I}_i^{DP}}\cdot\left\langle m_i^{VH_{DP}}\right\rangle\sqrt{\dfrac{v_1}{k_i^{\alpha VH_{DP}}}}}{\dfrac{1}{\tan\alpha_i} + \dfrac{\sin\varphi_i}{\mathrm{I}_i^{DP}}\cdot\left\langle m_i^{VH_{DP}}\right\rangle\sqrt{\dfrac{v_1}{k_i^{\alpha VH_{DP}}}}} - P_{h,i}\right]}{\displaystyle\sum_{i=1}^{n}\left[\left\langle m_i^{VH_{DP}}\right\rangle\sqrt{\dfrac{v_1^{1-m_i^{VH_{DP}}}}{k_i^{\alpha VH_{DP}}}}\cdot\left(\dfrac{\Lambda_i \cos\alpha_i}{\mathrm{I}_i^{DP}} + \dfrac{W_i + P_{v,i} - \dfrac{\Lambda_i \sin\alpha_i}{\mathrm{I}_i^{DP}}\cdot\left\langle m_i^{VH_{DP}}\right\rangle\sqrt{\dfrac{v_1}{k_i^{\alpha VH_{DP}}}}}{\dfrac{\mathrm{I}_i^{DP}}{\sin\varphi_i} + \tan\alpha_i \cdot\left\langle m_i^{VH_{DP}}\right\rangle\sqrt{\dfrac{v_1}{k_i^{\alpha VH_{DP}}}}}\right)\right]}
\tag{5.58}
$$

where the variables Λ_i, I_i^{DP} and $k_i^{\alpha VH_{DP}}$ are substitutions for

$$
\Lambda_i = C_i \cos\varphi_i - U_i \sin\varphi_i
\tag{5.59}
$$

$$
\mathrm{I}_i^{DP} = \frac{3 - \sin\varphi_i}{\sqrt{12}}
\tag{5.60}
$$

$$
k_i^{\alpha VH_{DP}} = 2 d_i A_i^{VH_{DP}} \cdot \frac{\cos\alpha_1}{\cos\alpha_i}
\tag{5.61}
$$

(e) Modified Vulliet-Hutter

With the modified Vulliet-Hutter model (5.10) and the kinematic chain requirement the iterative equation for the creep velocity v_1 is

$$v_1 = \frac{\displaystyle\sum_{i=1}^{n}\left[\frac{W_i + P_{v,i} - \Lambda_i \sin\alpha_i \cdot \sqrt[\langle m_i^{VH_{MC}}\rangle]{\dfrac{v_1}{k_i^{\alpha VH_{MC}}}}}{\dfrac{1}{\tan\alpha_i} + \sin\varphi_i \cdot \sqrt[\langle m_i^{VH_{MC}}\rangle]{\dfrac{v_1}{k_i^{\alpha VH_{MC}}}}} - P_{h,i}\right]}{\displaystyle\sum_{i=1}^{n}\left[\sqrt[\langle m_i^{VH_{MC}}\rangle]{\dfrac{v_1^{1-m_i^{VH_{MC}}}}{k_i^{\alpha VH_{MC}}}} \cdot \left(\Lambda_i \cos\alpha_i + \frac{W_i + P_{v,i} - \Lambda_i \sin\alpha_i \cdot \sqrt[\langle m_i^{VH_{MC}}\rangle]{\dfrac{v_1}{k_i^{\alpha VH_{MC}}}}}{\dfrac{1}{\sin\varphi_i} + \tan\alpha_i \cdot \sqrt[\langle m_i^{VH_{MC}}\rangle]{\dfrac{v_1}{k_i^{\alpha VH_{MC}}}}}\right)\right]} \tag{5.62}$$

with the substitutions Λ_i as defined in (5.59), and $k_i^{\alpha VH_{MC}}$ given by

$$k_i^{\alpha VH_{MC}} = 2 d_i A_i^{VH_{MC}} \cdot \frac{\cos\alpha_1}{\cos\alpha_i} \tag{5.63}$$

5.5 Illustrative examples of CrEAM applied to infinite slopes

This section presents examples which demonstrate the application of CrEAM algorithms for infinite slopes. The simple geometry provides insight to the characteristic properties of the various constitutive relationships. A special focus is given on comprehensive sensitivity analyses regarding the model input parameters. These sensitivity analyses aim to emphasize the effects of parameter variability.

For each situation presented in the following subsections, six different viscous materials are assumed, each being represented by a constitutive model. Table 5.6 summarizes the assumed parameters for these materials.

Table 5.6
Viscous materials and their parameters.

Material parameter		Material 1 "Newton"	Material 2 "Bingham"	Material 3 "Original Norton"	Material 4 "Modified Norton"	Material 5 "Original Vulliet & Hutter"	Material 6 "Modified Vulliet & Hutter"
Viscosity $\bar{\mu}$	[Pa·s]	10^{13}	10^{13}	10^{17}	10^{17}	-	-
Rate factor A	[s⁻¹]	-	-	-	-	10^{-9}	10^{-9}
Yield shear stress τ_y	[Pa]	-	20,000	-	20,000	-	-
Exponent m	[-]	-	-	2	2	2	2

The materials denoted as "Newton" and "Bingham" are characterised by the same viscosity value while the "Bingham" material features an additional yield shear stress. The same is valid for the materials named "original" and "modified Norton". While the materials "original Vulliet & Hutter" and "modified Vulliet & Hutter" exhibit identical parameters, the material behaviour is different.

Since the above parameter sets represent different materials, the respective model results are not absolutely comparable to each other. Attention should be paid rather to the relative trends which show the inherent properties of the constitutive models.
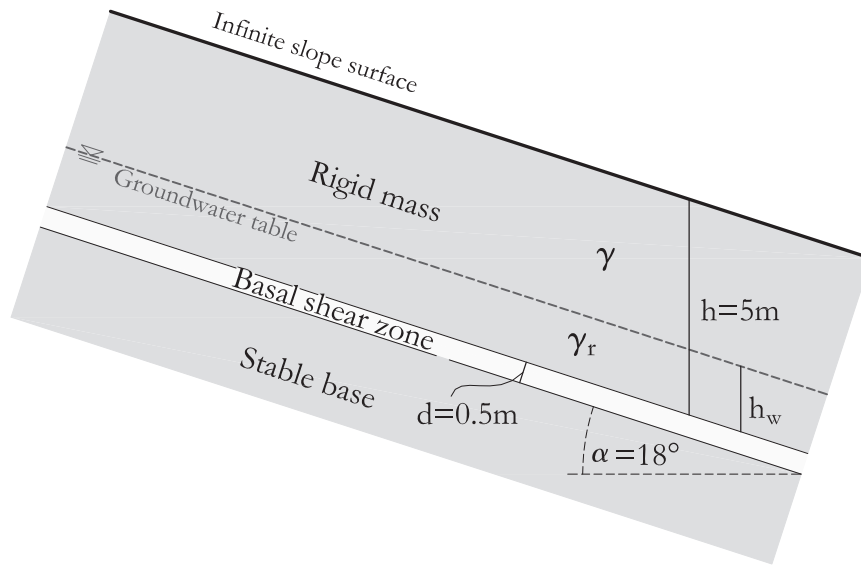
Figure 5.8
Infinite slope example used for the subsequent sensitivity analyses.

Figure 5.8 shows an infinite slope which is characterised by a rigid slab lying on a viscous layer. The slope inclination is $\alpha = 18°$. The vertical height of the rigid slab is $h = 5$ m, while the thickness of the viscous layer is $d = 0.5$ m. The slope is presently dry, and the specific weight of the hanging wall rigid mass is $\gamma = 20$ N/m³. Under saturated conditions, the latter increases to $\gamma_r = 25$ N/m³. The specific weight of water is assumed with $\gamma_w = 10$ N/m³.

As the viscous layer is thin in comparison with the rigid slab (about 10% of the thickness of the hanging wall mass), the self-weight of the viscous material is neglected in the calculations. The friction angle of the viscous layer is $\varphi = 30°$. The cohesion is supposed to has been completely degraded by preceding creep displacements and, thus, is assumed with $c = 0$.

In the following subsections, the geometrical and constitutive parameters characterizing the above system are individually varied in order to show their effect on the system behaviour.

5.5.1 Effect of viscous layer thickness

In a first analysis, the thickness of the viscous layer d is varied between 0 and 1 m (~20% of the thickness of the hanging wall mass). For all materials, and thus constitutive models, the creep velocities increase linearly with increasing viscous layer thickness (Figure 5.9). This linear relationship reflects the inherent assumption of the linear velocity profile within the viscous layer (see Figure 5.1), and is also directly recognizable from the CrEAM^{inf} formulas in Section 5.4.1.
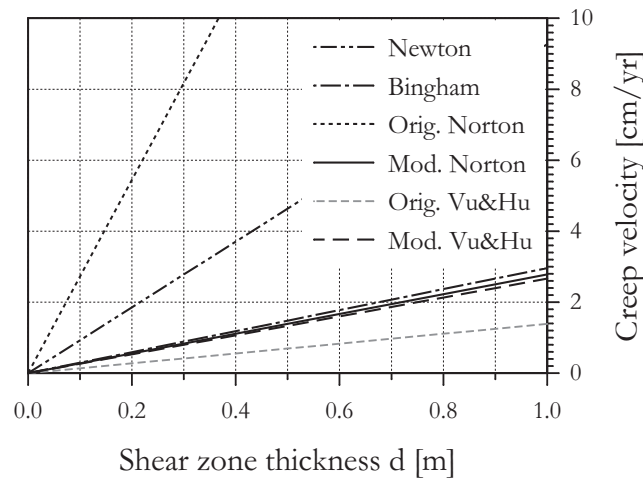
Figure 5.9
Effect of the viscous layer thickness d.

5.5.2 Effect of viscosity and rate factor

In this example, the shear viscosity values $\bar{\mu}$ and the rate factors A, respectively, are varied over one order of magnitude (thus, maximum deviation by factor 10). Figure 5.10 shows the results both in linear (left column) and double-logarithmic diagrams (right column).

For the deviatoric stress based constitutive models (Newton, Bingham, Norton) using a viscosity $\bar{\mu}$, the creep velocities decrease with increasing viscosity value. The velocity decrease is nonlinear (diagrams in left column). The same results plotted in a double-logarithmic diagram (right column) show a linear trend, indicating that a viscosity increase by the factor 10 results in a velocity decrease by the factor 0.1 (thus, a velocity drop of 90%).
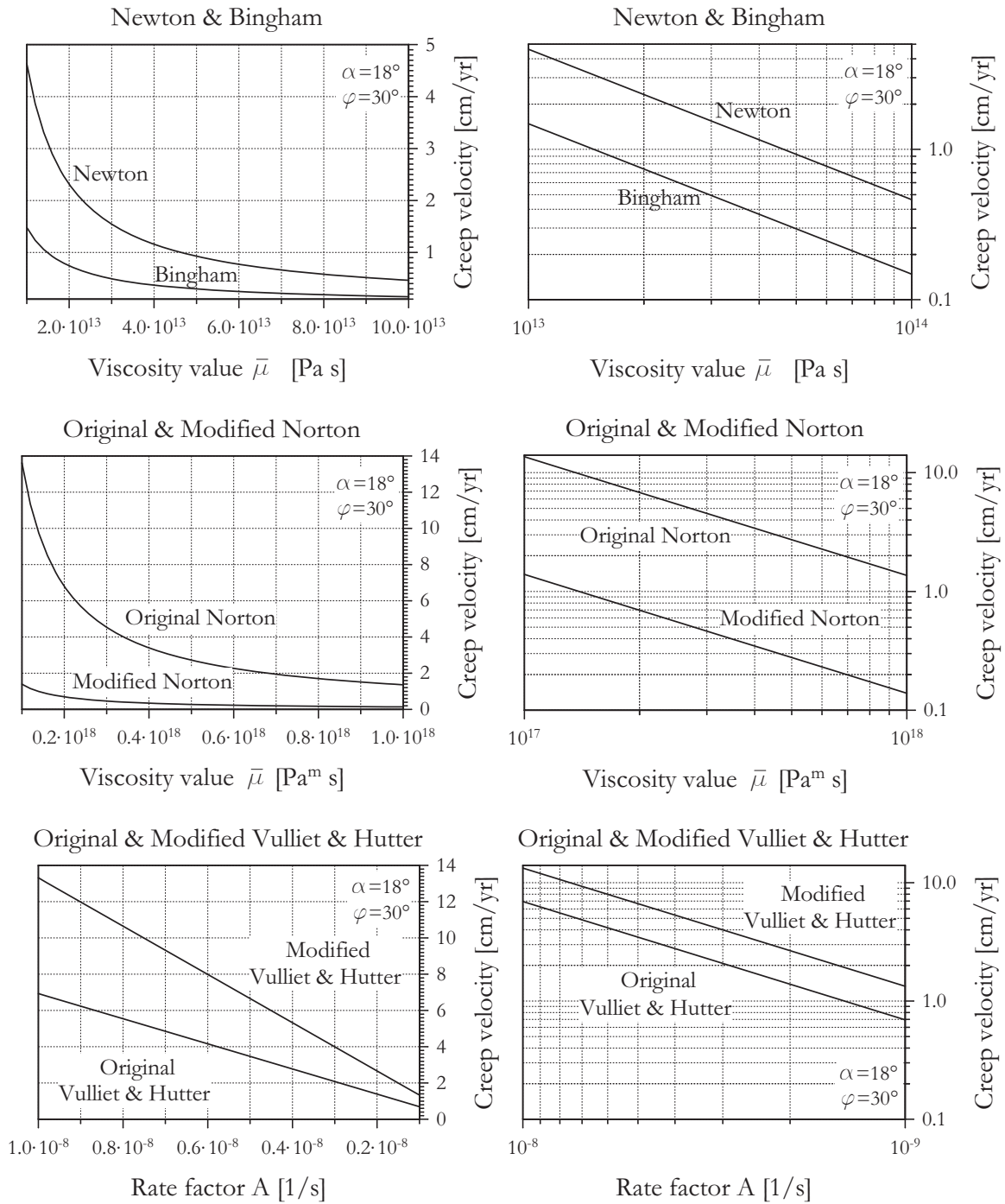
Figure 5.10

Effects of the shear viscosity $\bar{\mu}$ and the rate factor A. The dependencies are depicted on linear axes (left column) and on logarithmic axes (right column). Please note that the viscosities increase on the diagram abscissas from left to right (first two rows), while the rate factors decrease in the same direction (last row).

Materials with an additional constant yield shear stress (Bingham, modified Norton) yield lower creep velocities than the equivalents without creep threshold (Newton, original Norton).

For the effective stress based constitutive models (original and modified Vulliet-Hutter) which use the rate factor A, the creep velocities decrease with decreasing rate factor. In contrast to the deviatoric stress based models, here the velocity decrease is linear. The linear trend in the respective double-logarithmic diagram indicates that a rate factor decrease by the factor 0.1 (corresponding to a rate factor drop of 90%) results in a velocity decrease by the factor 0.1 (thus, a velocity drop of 90%).

5.5.3 Effect of yield shear stress

Figure 5.11 shows the impact of the yield shear stress both on the linear Bingham and the nonlinear modified Norton model. In this example, the yield shear stress τ_y is varied between 0 and 40,000 Pa. In Bingham's material, the creep velocity decreases linearly with increasing yield shear stress. For the modified Norton material the velocity decrease is nonlinear. Both models predict a maximum yield shear stress τ_y of about 30,000 Pa in order to initiate creep deformation.
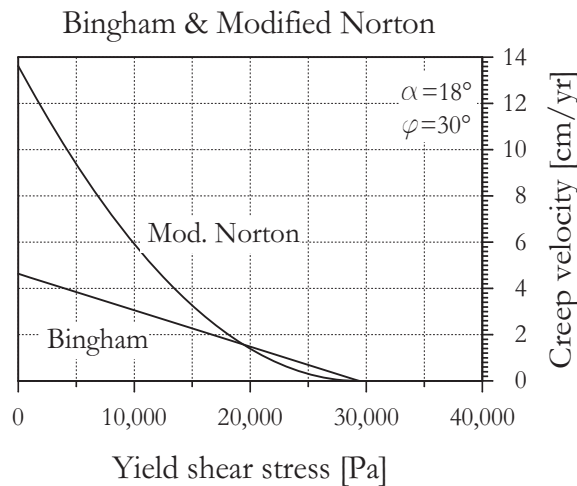
Figure 5.11
Effect of the yield shear stress τ_y.

5.5.4 Effect of the exponent *m*

The sensitivity analysis of the exponent m, used both in the original and modified Norton and Vulliet-Hutter models, demonstrates that a slight change of this parameter can influence creep velocities considerably. Figure 5.12 shows the results of a variation of m between 0 and 4.

For the deviatoric stress based original and modified Norton models, the creep velocities rapidly increase with rising exponent. The sensitivity of the modified Norton model in respect to the exponent depends on the magnitude of the yield shear stress (here held constant at 20 MPa).

For the original and modified Vulliet-Hutter approaches, a rising exponent causes decreasing velocities. Figure 5.12 further indicates that the original Vulliet-Hutter model is much more sensitive to the exponent than the modified approach.
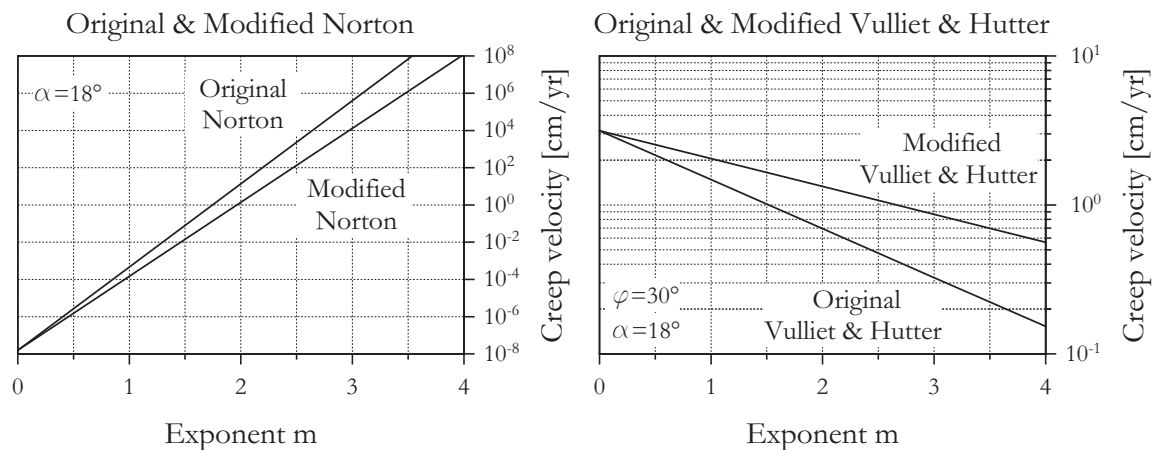
Figure 5.12
Effect of the exponent m. Note that the ordinate in the diagrams is scaled logarithmically.

5.5.5 Effect of slope inclination and friction angle

This section aims to demonstrate the influence of both the slope inclination α and the shear strength in the basal deformation zone (here represented by the friction angle φ while $c = 0$) on slope stability and creep velocity. The thickness of the rigid mass, $h\cos\alpha = 5$ m, is held constant for the calculations (thus, the vertical height h of the slab is changing with α).

Figure 5.13 and Figure 5.14 show the dependencies in terms of the Factor of Safety and the creep velocities, for both the deviatoric stress based and effective stress based constitutive models.
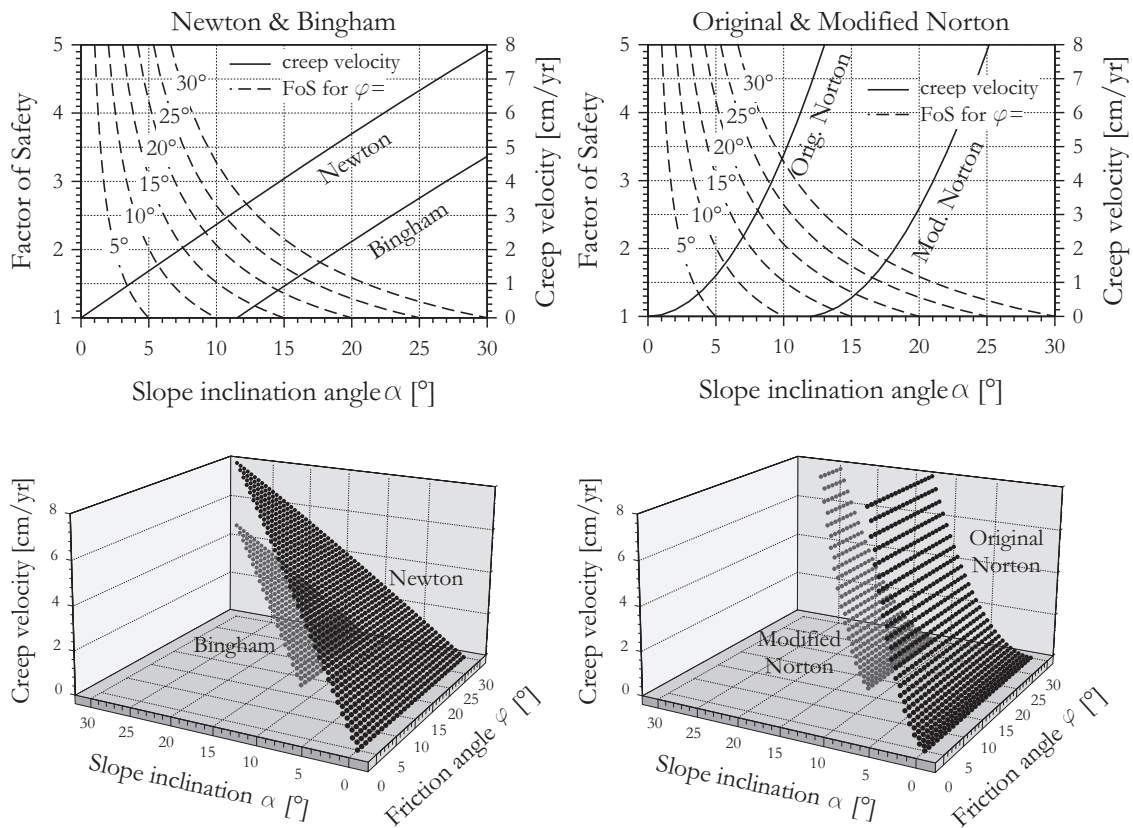
Figure 5.13
Effects of the slope inclination α and the friction angle φ on the Factor of Safety and creep velocity of an infinite slope, based on the deviatoric stress related models according Newton, Bingham and original and modified Norton.
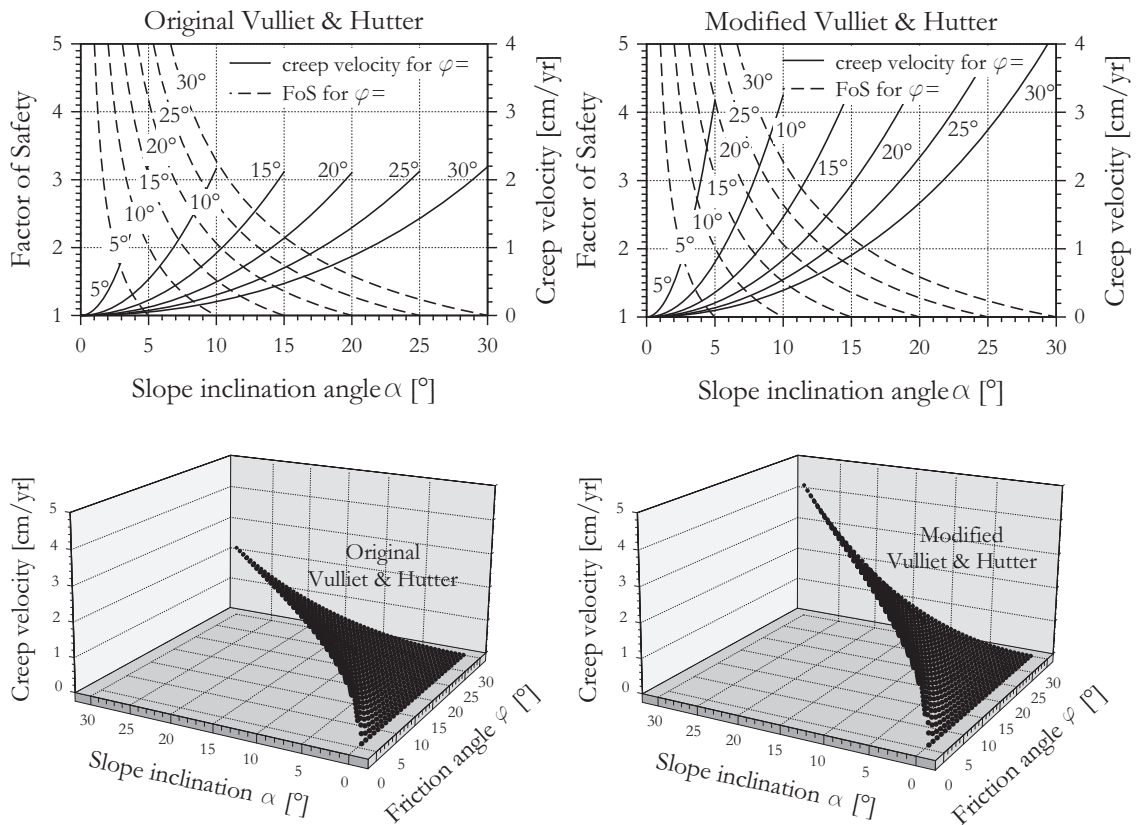
Figure 5.14
Effects of the slope inclination α and the friction angle φ on the Factor of Safety and the creep velocity of an infinite slope, based on the effective stress related original and modified Vulliet-Hutter models.

For all creep models, a drop of the Factor of Safety goes along with an increase of creep velocity.

For the deviatoric stress based models (Figure 5.13), the velocity increase is purely dependent on the slope inclination α while the friction angle only determines the upper cut-off of the creep curves, i.e. when $\alpha = \varphi$, thus, the infinite slope reaches limit equilibrium ($\eta = 1$).

For the effective stress based models (Figure 5.14), the creep curves depend on both α and φ. At a given slope inclination, a lower friction angle provokes higher creep velocities. The upper cut-off is again defined by $\alpha = \varphi$.

5.5.6 Effect of overburden

The sensitivity analysis in respect to the parameter h which is denoting the vertical height of the rigid slab reveals the effect of an increasing depth of the deformation layer. The behaviours according different constitutive models are depicted in Figure 5.15.
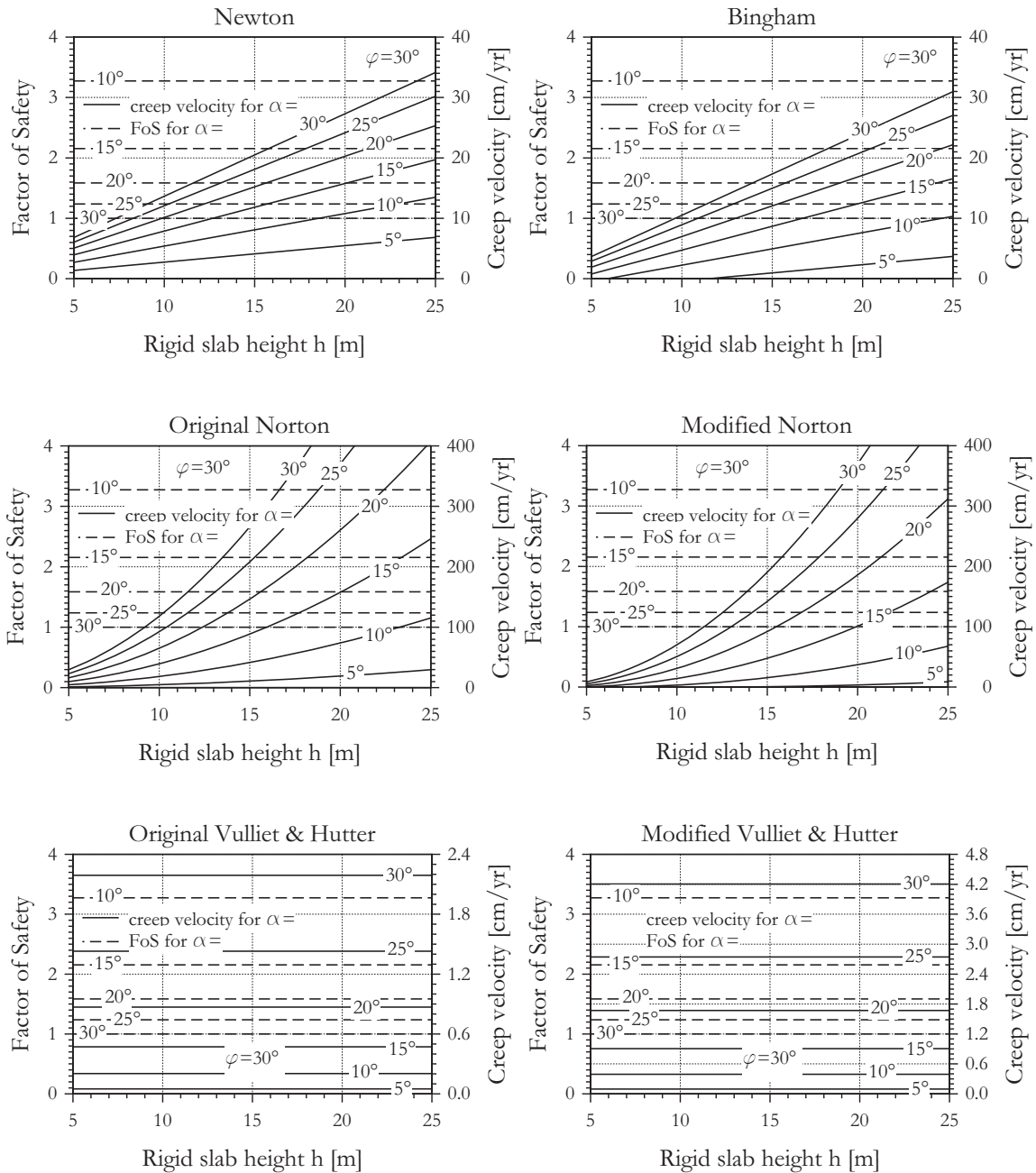
Figure 5.15
Effects of trigid slab height h and the slope inclination α.

Having no cohesion, the Factor of Saftey is inaffected by an increase in depth since η is purely governed by the ratio of the friction angle and the inclination angle.

An essentially different behaviour can be observed in terms of creep velocities derived from deviatoric stress based models on one hand and effective stress based models on the other hand. The effective stress based models predict no change in creep deformation due to an increasing overburden (which is congruent with the constant Factor of Safety) while the deviatoric stress based models predict a linear (Newton, Bingham) or nonlinear increase of the infinite slope creep velocity.

5.5.7 Effect of groundwater fluctuations

Groundwater in a porous soil or rock slope invokes changes in terms of i.) an increased overburden, and ii) by reducing the effective normal stresses. The deviatoric stress based creep models only account for the increasing shear stress in the deformation layer while the effective stress based models additionally consider the drop in effective normal stress due to the hydrostatic pressure.

Figure 5.16 shows the reaction of the infinite slope model on rising groundwater. For all creep models, a rising groundwater table causes a drop of the Factor of Safety and an increase of creep velocity. The velocity increase is either linear (Newton, Bingham) or nonlinear (original and modified Norton, original and modified Vulliet-Hutter). For the effective stress based models, the predicted velocity increase additionally depends of the friction angle. By contrast, the friction angle plays no role for the deviatoric stress based models.

Since the velocities of the different constitutive models at different groundwater levels in Figure 5.16 are not directly comparable, Figure 5.17 summarizes the relative velocities rises, exhibiting that the model responses show large deviations. The original and modified Vulliet-Hutter models predict the same relative velocity increase due to groundwater rise, independently of the shear strength in the deforming layer.
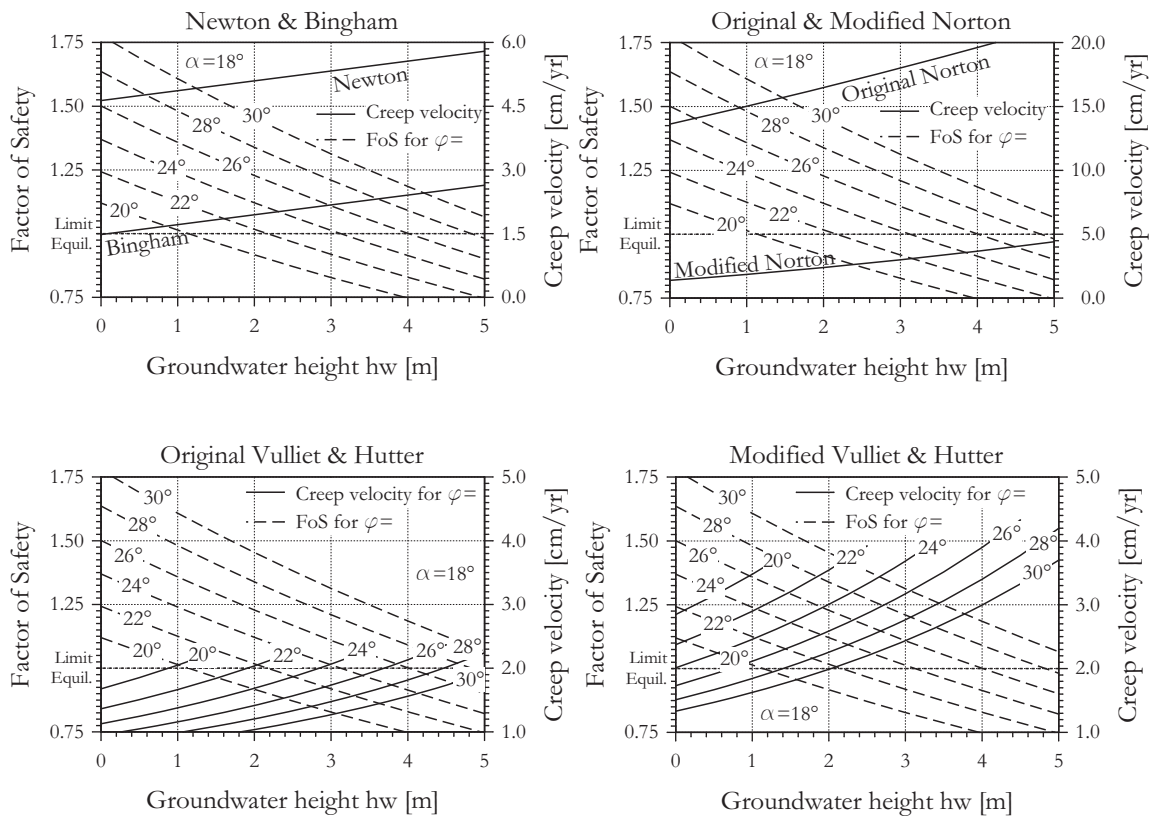
Figure 5.16

Effects of the vertical groundwater height h_w in an infinite slope with an inclination of $\alpha = 18°$ and different friction angles.
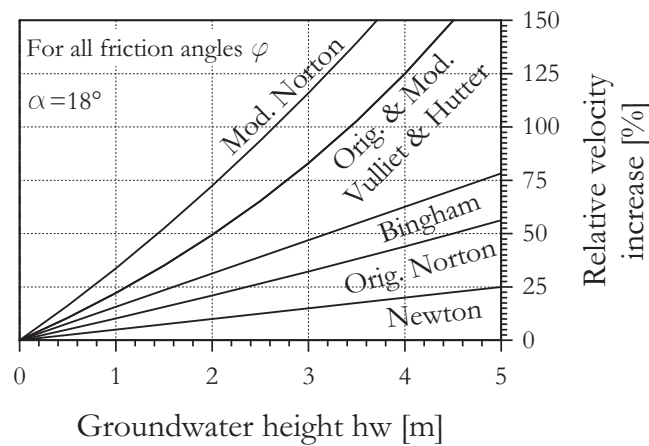
Figure 5.17

Relative creep velocity increase due to rising groundwater.

Chapter summary

This chapter presented the theoretical framework of CrEAM. The methodology is designed for landslides which show steady displacement behaviour under constant boundary conditions, with velocities in the range of millimetres to metres per year. Creep deformation is assumed to take place in a thin viscous shear zone while the hanging wall mass is assumed to behave rigid and is transported downslope.

CrEAM incorporates concepts of steady viscous flow (secondary creep), kinematics, and equilibrium of forces and moment. For calculation purposes, the hanging wall mass is discretized by an assembly of rigid sub-elements. CrEAM algorithms are developed for different sliding modes, various constitutive relationships, and different assumptions for the action of interslice forces between the rigid elements. The creep velocity of a slope system is determined with closed-form or iterative calculation procedures. The variants of CrEAM are listed in Table 5.7 and shown in Figure 5.18.

Illustrative examples demonstrated the application of CrEAM for infinite slopes. Moreover, comprehensive sensitivity analyses provided insight to the behaviour of different constitutive models and parameter input values.

Table 5.7
CrEAM variants for different deformation mechanisms. Two major groups are distinguished: 1. Deviatoric stress based methods using deviatoric stress based viscous models (Newton, Bingham, Norton) 2. Effective stress based methods using deviatoric and hydrostatic stress based viscous models (Vulliet-Hutter).

	Deviatoric stress based **Cr**eep **E**quilibrium **A**nalysis **M**ethods	**E**ffective stress based **C**reep **E**quilibrium **A**nalysis **M**ethods
Infinite slope model	D-CrEAM^{inf}	E-CrEAM^{inf}
Circular creep interface, rotational mechanism	D-CrEAM^{rot}	Simplified E-CrEAM^{rot} Ordinary E-CrEAM^{rot}
Irregular creep interface, translational mechanism	D-CrEAM^{trans}	E-CrEAM^{trans}
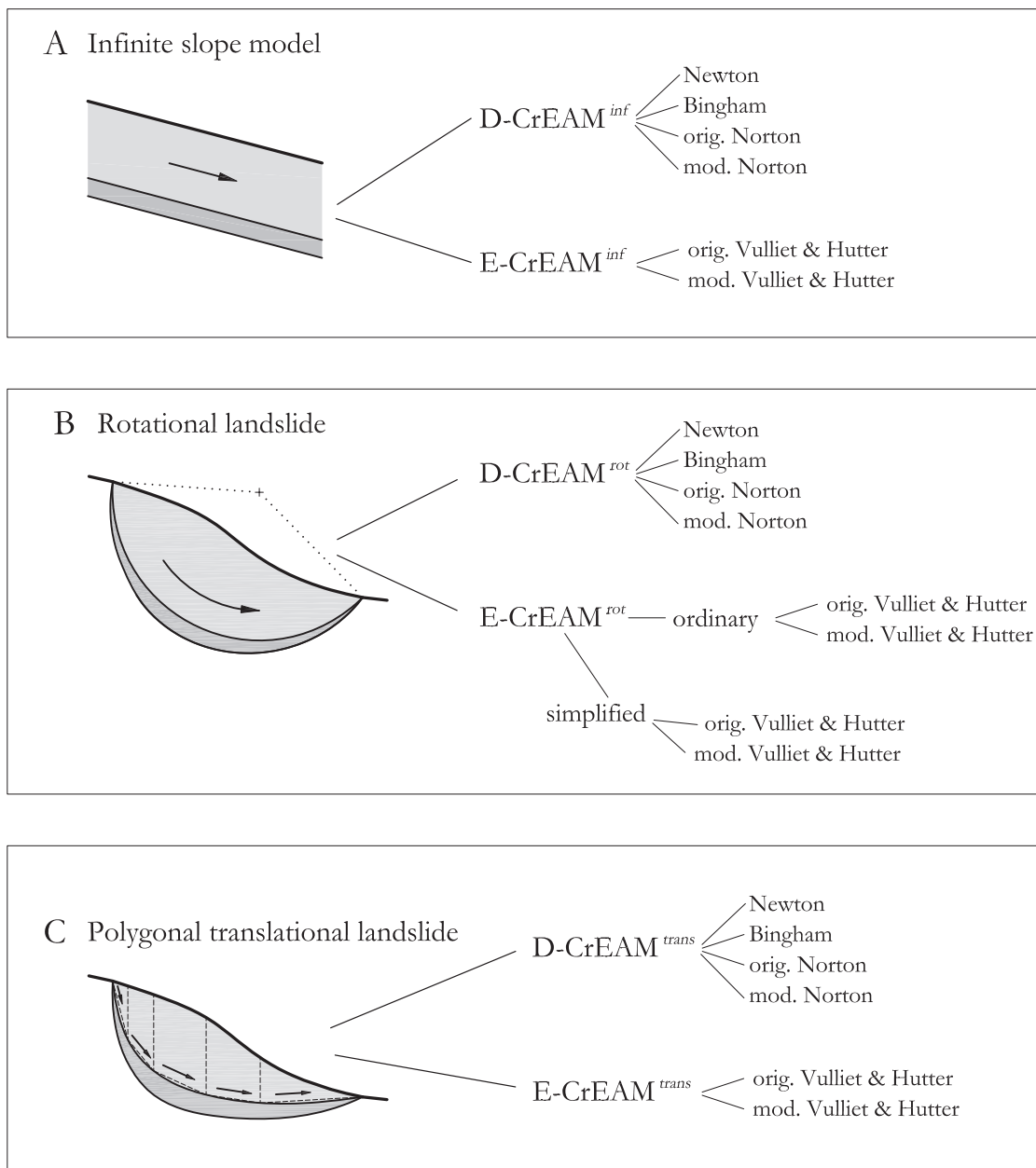
Figure 5.18
Overview of CrEAM variants. "D" denotes deviatoric stress based, "E" effective stress based formulations.

CHAPTER 6

Case Studies

6.1 Preamble

In this chapter, the Creep Equilibrium Analysis Method (CrEAM) developed previously in this work is applied on two case studies, i.e. the Beauregard rockslide in Italy and the Utiku landslide in New Zealand. Both landslides are characterised by an excellent data base in terms of exploration and monitoring while they differ completely in their geological setting. They are therefore considered well suited for examining and evaluating the novel CrEAM methodology.

The left abutment slope of the Beauregard reservoir (Aosta Valley, Italy) is a deep-seated rockslide in crystalline rock and exhibits a semi-rotational failure mechanism. The interaction of the creeping slope with the arch-gravity dam motivated a long-term monitoring program. The results show clear slope response to elevated piezometric conditions after snowmelt. Efforts to mitigate slope movement motivated comprehensive laboratory investigations of the intact rock and shear zone material. In this thesis, the Beauregard rockslide is investigated with CrEAM in terms of both a forward and back analysis, using laboratory material parameters and survey data, respectively. The focus of this case study relates to differences between laboratory and back calculated (in situ) creep parameters, and the impact of geometric uncertainties. Moreover, the applicability of different constitutive models implemented in CrEAM is discussed.

The Utiku landslide is a shallow-seated landslide in sedimentary rock in New Zealand. The landslide geometry is constrained, and the displacement rates have been documented with high-resolution monitoring. The landslide behaviour is highly sensitive to pore pressure variations in the slope. In the Utiku case study, CrEAM is used to replicate the seasonal deformation pattern over several years, based on the measured fluctuations of the hydrostatic pressure in the basal shear horizon.

For the analyses of the Beauregard and Utiku case studies, the different CrEAM variants presented in Chapter 5 are implemented in MATLAB (version 7.11), and the algorithms are subsequently solved therein. The calculation procedure takes only a few seconds, enabling time efficient back analyses.

6.2 The Beauregard rockslide (Italy)

6.2.1 Introduction

The Beauregard rockslide in the Aosta Valley (northwestern Italy, see inset in Figure 6.1) involves an area of about 1,700 m by 2,400 m (4 km²) at the left abutment slope of the Beauregard reservoir (Figure 6.2). The landslide toe impinges the concrete arch-gravity dam which was built between 1951 and 1960 in order to retain the Dora di Valgrisenche River for energy production.

The left abutment slope is an ancient rockslide. A sequence of overridden glaciofluvial deposits was found at the slope toe during excavation works in the 1950's (Barla et al. 2005). These sediments were completely removed before dam construction and replaced by concrete, due to concerns about dam stability and water flow control. Additionally, a vertical grout curtain reaching depths of 100 m below the original river bed was introduced along the entire dam in order to reduce the hydraulic conductivity of the foundation (Barla et al. 2005).

Since the initial reservoir filling in the 1960's, the slope experienced yearly deformations of 3-5 mm, leading to slow but progressive narrowing of the valley and, thus, bending and damaging of the dam structure. Continuous geodetic and piezometric monitoring of the slope adjacent to the reservoir over the last decades showed that the displacements correlate with both an elevated reservoir and groundwater level (Barla et al. 2006; Barla et al. 2010c). The latter is the result of snowmelt and subsequent water infiltration in the subground in spring. Slope movements mainly take place during spring and early summer, whereas hardly any slope deformation is observed during autumn and winter months (Barla et al. 2006).

The design lake level of 1,770 m a.s.l. (above sea level), corresponding to an impounded water volume of 70 million m³, was achieved during the first infilling; however this water level has never been achieved again due to the instability concerns (Barla et al. 2006). In 1969, the Italian Dam Authorities mandated a maximum reservoir level of 1,710 m a.s.l., reducing the reservoir capacity to about 10% of the design volume (6.8 million m³, Barla et al. 2006). In 1998, the authorities further reduced the permitted lake level to 1,705 m a.s.l. Since January 1997, the reservoir level has been kept between 1,700 and 1,705 m a.s.l., with an one-time temporary drowdown in spring 2005 (Barla et al. 2005; Miller et al. 2008).
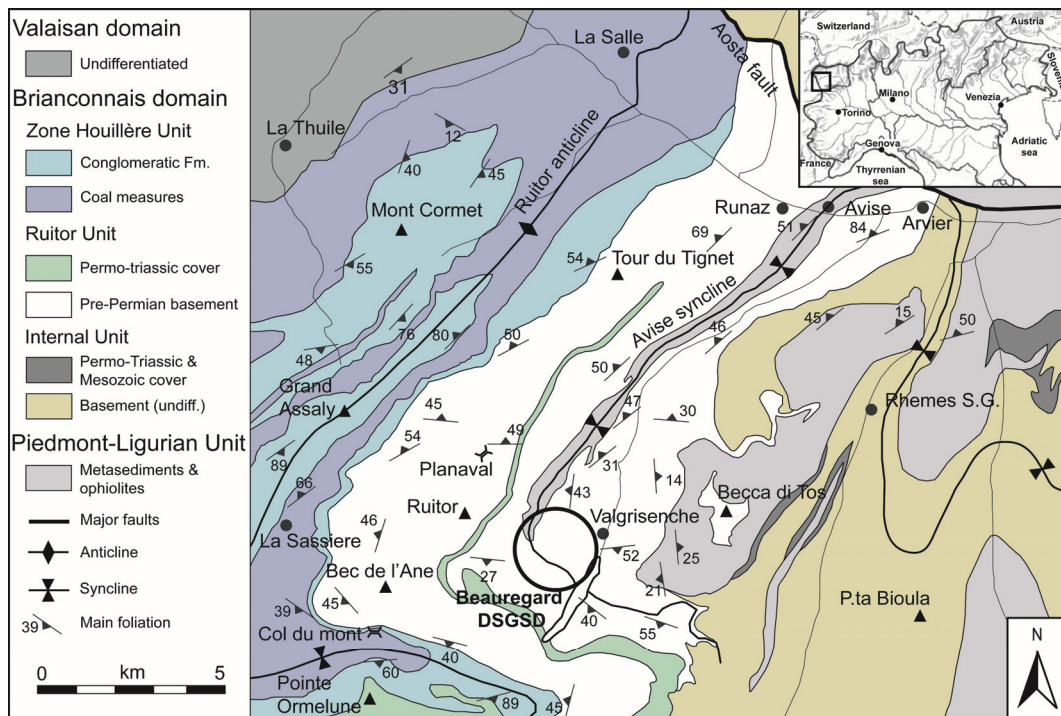
Figure 6.1
Geological map of the western Aosta Valley. The circle indicates the approximate location of the Beauregard rockslide (from Barla et al. 2010c, modified after Bucher et al. 2004).

Figure 6.2
Overview of the Beauregard rockslide and the concrete arch-gravity dam in the valley (red circle). View eastward from the top of the main scarp.

6.2.2 Geology and geomorphology

The slopes on either side of the Beauregard reservoir are dominantly comprised of mica schists and paragneisses interlayed with abundant metabasites (prasinites and amphibolites). The rocks represent the Pre-Permian basement of the Brianconnais domain and are tectonically overlain by Mesozoic calcschists with intercalations of marbles and metabasites (Bucher et al. 2004). The latter are mainly found in the crest region of the Valgrisenche valley. The complex structure in the Valgrisenche area indicates a polyphase ductile folding history followed by subsequent brittle faulting and fracturing of the rock units (Barla et al. 2010c, Figure 6.1).

In the area of the Beauregard reservoir, the schistosity planes of the paragneisses and mica schists strike approximately perpendicularly to the valley axis and dip in average 25-30° to the S and SW. The dominant discontinuities strike parallel to the slope (NE-SW to NNE-SSW), dipping steeply (70-80°) into the slope on the left valley side, and out of the slope on the right valley side. Perpendicular to the dominant joint set, minor ESE-WNW directed subvertical discontinuities and mylonitic shear zones are developed (Barla et al. 2010c).

Although the left and right abutment slopes exhibit a similar tectonic setting and the same lithologies, they show rather different characteristics. On the orographically right (south-eastern) valley side, the rock mass is of good to excellent quality while the orographically left (north-western) valley side is highly fractured and disintegrated (Barla et al. 2010c).

The overall geomorphology of the left slope suggests a fairly advanced deep seated-slope deformation, involving a relief of approximately 1,500 m (from 1,700 to 3,200 m a.s.l.). A headscarp forming a wide niche with a maximum relief of 250 m is interpreted as the day-lighting portion of the rupture surface in the upper slope portion (Barla et al. 2010c). In the lower slope portion, between 2,050 and 2,200 m a.s.l., the steep headscarp of a further rockslide mass is evident (Figure 6.3 and Figure 6.4). This rupture surface is interpreted as the morphological expression of the lowermost portion of the rockslide system moving towards the reservoir (Barla et al. 2010c). The steep scarp area passes into the Alpettaz flat with low slope inclinations (1,950-2,050 m a.s.l.). At lower elevations (1,800-1,950 m a.s.l.), the slope inclinations gradually increase towards the reservoir while the slope surface is dissected by numerous minor valley-parallel scarps and counterscarps.
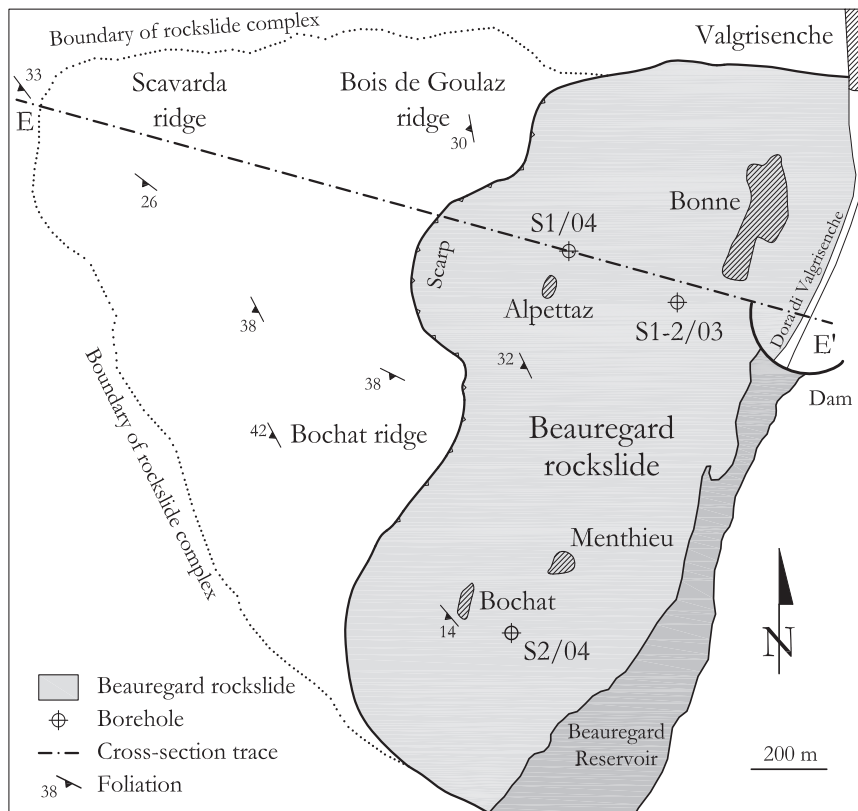
Figure 6.3
Map of the Beauregard left abutment slope (modified after Barla et al. 2010c). E-E' denotes the trace of the cross-section in Figure 6.4.
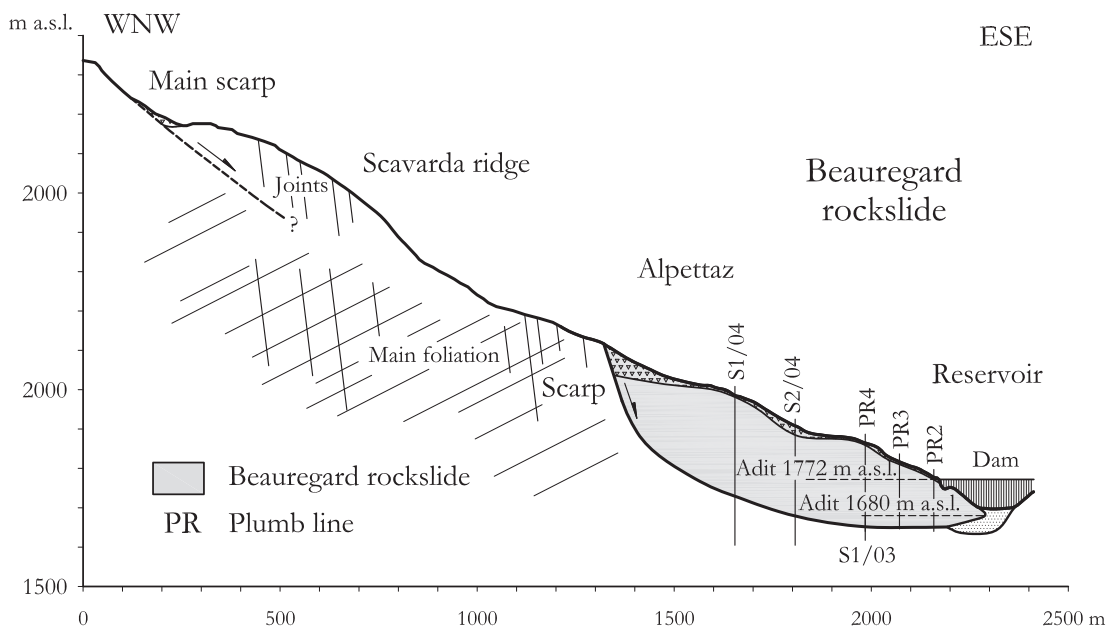
Figure 6.4
Cross-section E-E' of the Beauregard rockslide complex (modified after Barla et al. 2010d). The trace of the cross-section is shown in Figure 6.3.

Left abutment / Right abutment
WNW / ESE

Maximum reservoir level

M1

d

Dora di Valgrisenche river

a

d

M

M2

M

Foundations excavation

d - Debris and glacial deposits
a - Fine and coarse alluvial deposits
M - Compact micaschists
M1 - Fractured and mylonitic micaschists
M2 - Micaschists as M1 but very disjointed

0   50   100 m
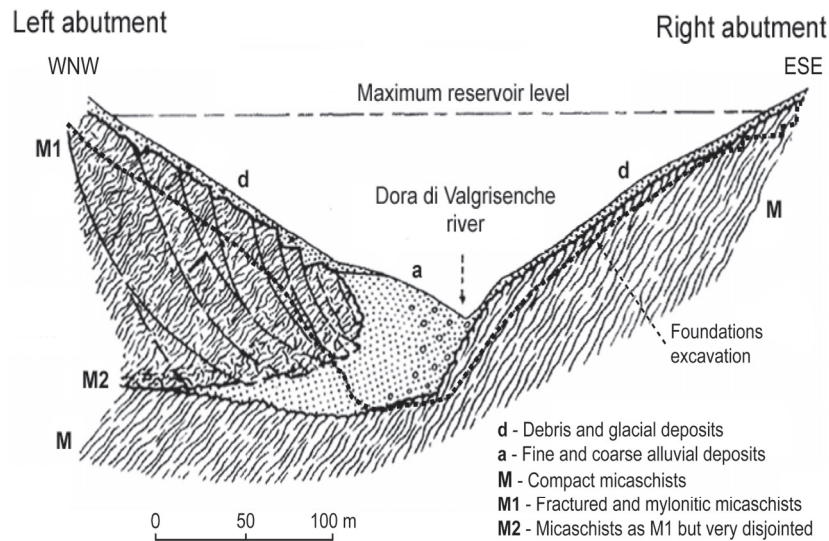
Figure 6.5
Geological cross-section of the dam site (from Barla et al. 2010c, modi-
fied after Desio 1973).

At the slope toe, the landslide impinges the concrete arch-gravity dam. Here, a thick sequence of glaciofluvial sediments was found burried underneath strongly disinte-grated paragneisses during the excavation works for the dam construction (Desio 1973; Barla et al. 2005, Figure 6.5). These overridden glaciofluvial deposits and the overall geomorphology of the reservoir slope indicate an ancient rockslide system.

Since the geodetic monitoring program was only started in the early days of reser-voir infilling in the 1960's, it is unknown whether the rockslide system was active before the time of dam construction, or whether the movements have been reacti-vated as a consequence of damming the Dora di Valgrinsenche River.

6.2.3 Exploration and monitoring

Since 1960, a comprehensive surface monitoring program and several subsurface exploration campaigns were undertaken at the Beauregard rockslide in order to gain insight into its deformation behaviour. Most attention was given to the lower rock-slide portion which is impinging the arch-gravity dam.

The surface displacements have been measured since 1967 until present. The first monitoring program concentrated mainly on the lower slope portion. In 1995, the geodetic network was supplemented with a wide-meshed GPS-network reaching up to the main scarp of the rockslide. In 2008 and 2009, a ground-based radar inferometry has been applied for an observation of the overall rockslide area (Antolini in prep.; Barla et al. 2010c; Barla et al. 2011).

Ten standpipe piezometers were installed in the lower slope portion during dam construction. Starting with 1968, five plumb line sequences were operated in the slope adjacent to the dam (Barla et al. 2010c).

Two investigation adits through the lower landslide mass were excavated at an elevation of 1,680 m a.s.l and 1,772 m a.s.l., respectively (compare with Figure 6.4). During drilling compaigns in the years 2003, 2004 and 2007, both from the surface and the adits, a distinct shear zone was encountered in several boreholes, which has been interpreted to represent the basal shear zone of the rockslide in the lower slope portion. This interpretation was supported by an accompanying geophysical exploration of the lower slope section. Subsequently, three boreholes as well as the existing standpipe piezometers were equipped with automated piezometers in order to monitor the groundwater conditions in the slope continuously (Barla et al. 2010c).

6.2.3.1 Geodetic monitoring

The first geodetic monitoring system was installed and commissioned in 1967, comprising 22 target points which were mostly placed at the lower slope section. The targets were manually observed twice a year (June-July and September-October) by means of a theodolite.

In 2003, a permanent automatic total station was installed at the right slope close to the dam guard house which included 19 target points. The point network covers the lower slope portion and partly coincides with the previous survey targets.

The automatic measurement takes place every 24 hours during the night in order to minimize the atmospheric impact. The survey data is transferred into a local cartesian coordinate system (x, y, z) with origin on the right abutment slope (point K24bis), in which the local x-axis is parallel to the Dora River and positively di-

rected upstream, the local y-axis is perpendicular to the Dora River (thus ~parallel to the mean slope dip direction) and positively directed uphill the left abutment slope, and the z-axis is vertical. The locations of the total station and the geodetic target points as well as the origin of the local coordinate system are depicted in Figure 6.6.

The daily measurements of the automatic total station capture the surface displacements of the left abutment slope in high resolution. Figure 6.7 shows the survey results of the target points K1, K3, K14 and PR1 situated near the dam, within the time period April 2003 - June 2010. The survey data confirm the slow movement of the slope towards the dam, as it was previously detected by the semi-annual geodetic measurements. Additionally, the high resolution time series reveal that the slope undergoes reversible cyclic (seasonal) deformation in an annual rhythm which overprints the small irreversible deformations.
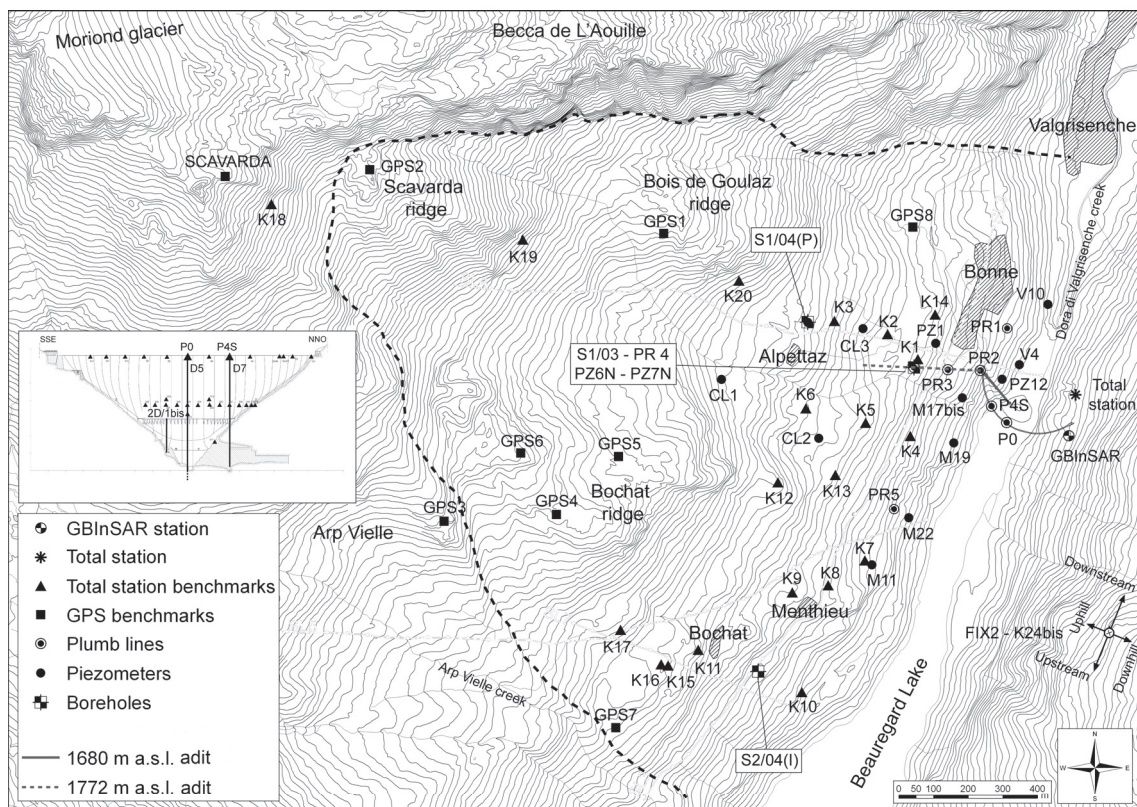
Figure 6.6
Map of the left abutment slope indicating the position of the monitoring elements within the rockslide mass (geodetic survey targets, GPS points, plumb lines and standpipe piezometers) as well as the adit and borehole locations (from Barla et al. 2010c).
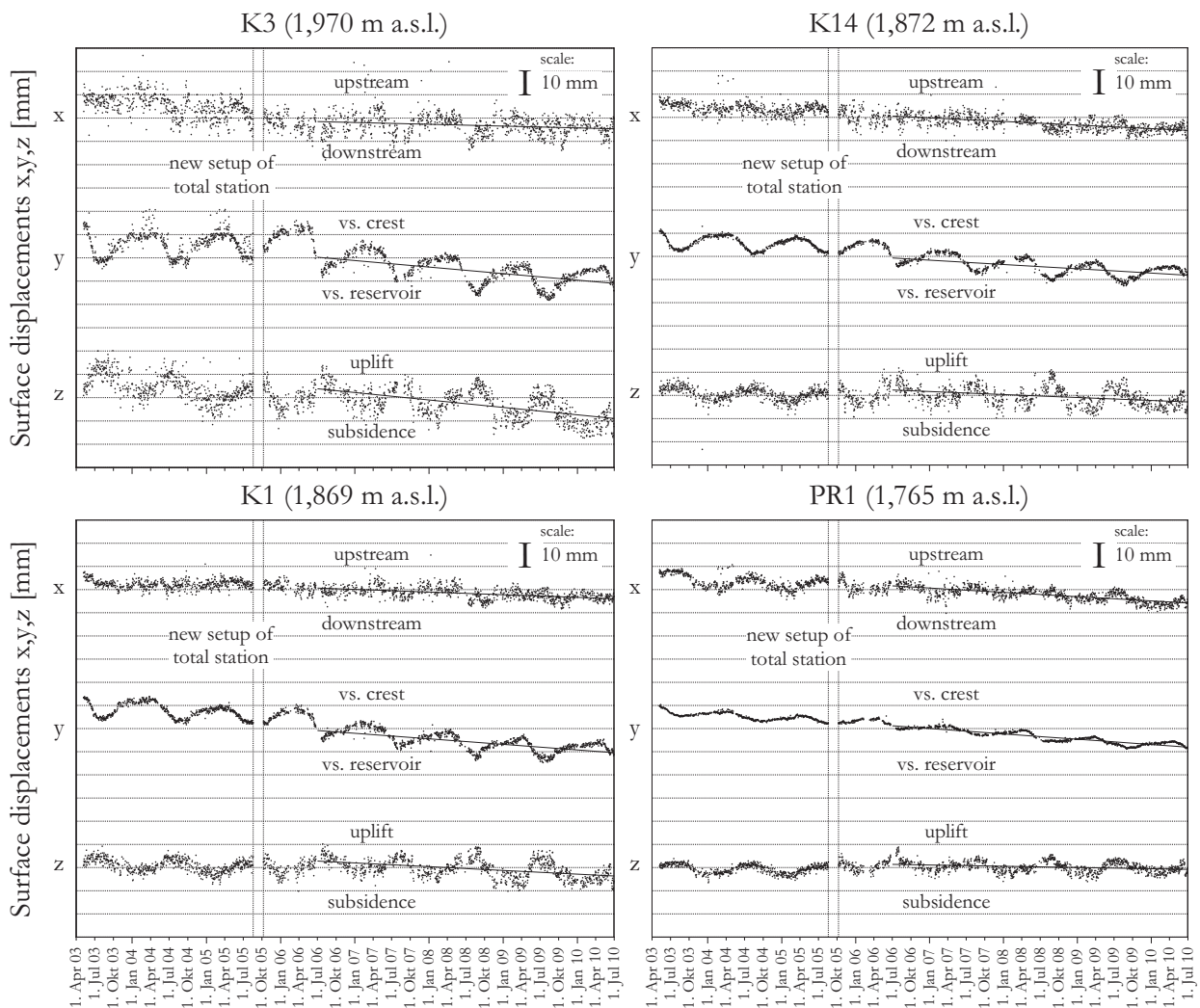
Figure 6.7
Overview of the geodetic survey data of four selected target points near and up-hill the dam (K1, K3, K14, PR1). The total station was newly installed in autumn 2005, causing a minor offset of the data. Bold black lines indicate the result of the regression analysis for the x, y and z-components of each point, considering a period of four years (July 1, 2006 – June 30, 2010).

Reversible cyclic displacements dominantly occur in the y- and z-component of the survey data and hence indicate deformation towards and away from the free space. By contrast, the x-component (corresponding to the strike direction of the slope) generally exhibits strongly attenuated cyclic deformation.

Furthermore, the intensities of the reversible cyclic deformations increase with elevation, with minor amplitudes at the slope foot (PR1; at 1,765 m a.s.l.), moderate amplitudes at middle elevations (K1/K14; at 1,869/1,872 m a.s.l.), and high amplitudes near the Alpettaz area (K3; at 1,970 m a.s.l.), respectively. The cyclic slope deformation is supposed to arise from buoyancy effects during elevated groundwater conditions as well as freeze-thaw processes and thermal rock expansion (compare with Barla et al. 2010c and Loew et al. 2007).

Beyond the reversible cyclic deformations, the geodetic survey data show a clear trend of permanent (irreversible) slope displacement in time. The mean annual irreversible displacement rates can be obtained by applying a linear regression analysis on the coordinate components x, y and z. The impact of seasonal (reversible) deformation is minimized by using a full number of cycles. Regression analyses are performed for the target points K1, K3, K14 and PR1 using a four year period (four cycles) of continuous measurements, from July 1, 2006 to June 30, 2010 (Figure 6.7).

The analysis results are listed in Table 6.1. The obtained values are considered to reflect the average permanent deformations in the slope in this four year period. The coordinate differences Δy and Δx indicate the horizontal displacement of the target points versus the reservoir and downstream, respectively. The associated ratio $\Delta x / \Delta y$ gives thus a rough measure about the obliquity of the movements with respect to the average slope dip direction. The mean annual horizontal displacement rate is calculated by dividing the horizontal displacement resultant by the number of years $t = 4$, i.e. $v_h = \frac{1}{t}\sqrt{\Delta x^2 + \Delta y^2}$. The variables v and α_v in Table 6.1 describe the magnitude and inclination of the total mean annual velocity vector.

The average horizontal displacement rate of the four survey points is equal in magnitude, ranging from 2.4-3.0 mm/yr. The displacement vector inclinations vary. Whereas the lowermost point PR1 exhibits a small vector dip (10.2°), the inclination values increase with increasing elevation, i.e. moderate inclinations of 28.0°-30.7° for K14 and K1, and a steep vector (47.4°) for K3.

Table 6.1
Results from the regression analysis in Figure 6.7. The coordinate differences $\Delta x, \Delta y, \Delta z$ show the relative displacements of the target points in a four year period. The value $\Delta x / \Delta y$ indicates the ratio of the respective downstream and versus reservoir directed components of slope movement. v_h is the horizontal mean annual displacement rate (velocity) of the slope, while v and α_v describe the total mean annual velocity vector.

| Target | Elevation | Displacements July 1, 2006 - June 30, 2010 | | | | Mean annual displacement rates | | |
| | | Δx | Δy | Δz | $\Delta x / \Delta y$ | v_h | v | α_v |
	[m a.s.l.]	[mm]	[mm]	[mm]	[-]	[mm/yr]	[mm/yr]	[°]
K3	1970	-3.1	-11.3	-12.7	0.3	2.9	4.3	47.4
K1	1869	-4.6	-9.7	-6.4	0.5	2.7	3.1	30.7
K14	1872	-6.2	-7.5	-5.2	0.8	2.4	2.7	28.0
PR1	1765	-7.4	-9.3	-2.1	0.8	3.0	3.0	10.2

6.2.3.2 Drilling

In the first core drilling campaign in 2003, a vertical borehole (S1/03) with a depth of 62.7 m was drilled starting from the lower adit at 1,680 m a.s.l. The drilling encountered highly fractured bedrock material and, at a depth of 24.5 to 28.5 m, a four metre thick horizon of clayey-silty fault gouge. Underneath this apparent shear horizon, the rock mass quality increased immediately, suggesting that the base of the rockslide has been reached. In 2004, a second borehole (S1/04) was drilled, starting from the surface at 1,985.4 m a.s.l. and achieving a depth of 380.8 m. Between drillmetre 234.0 and 255.6, a strongly sheared zone was reached (21.6 m in thickness), which was followed by good quality host rock up to 380.8 m in depth. A third borehole, S2/04, exhibited a similar shear zone between 147 to 159 m depth. The internal shear zone structure was very inhomogeneous, with boulders of various sizes floating in a fine-grained silty-sandy matrix (Martinotti 2010).

Figure 6.8 shows the drilling core records and RQD-profiles of the boreholes S1/03, S1/04 and S2/04.
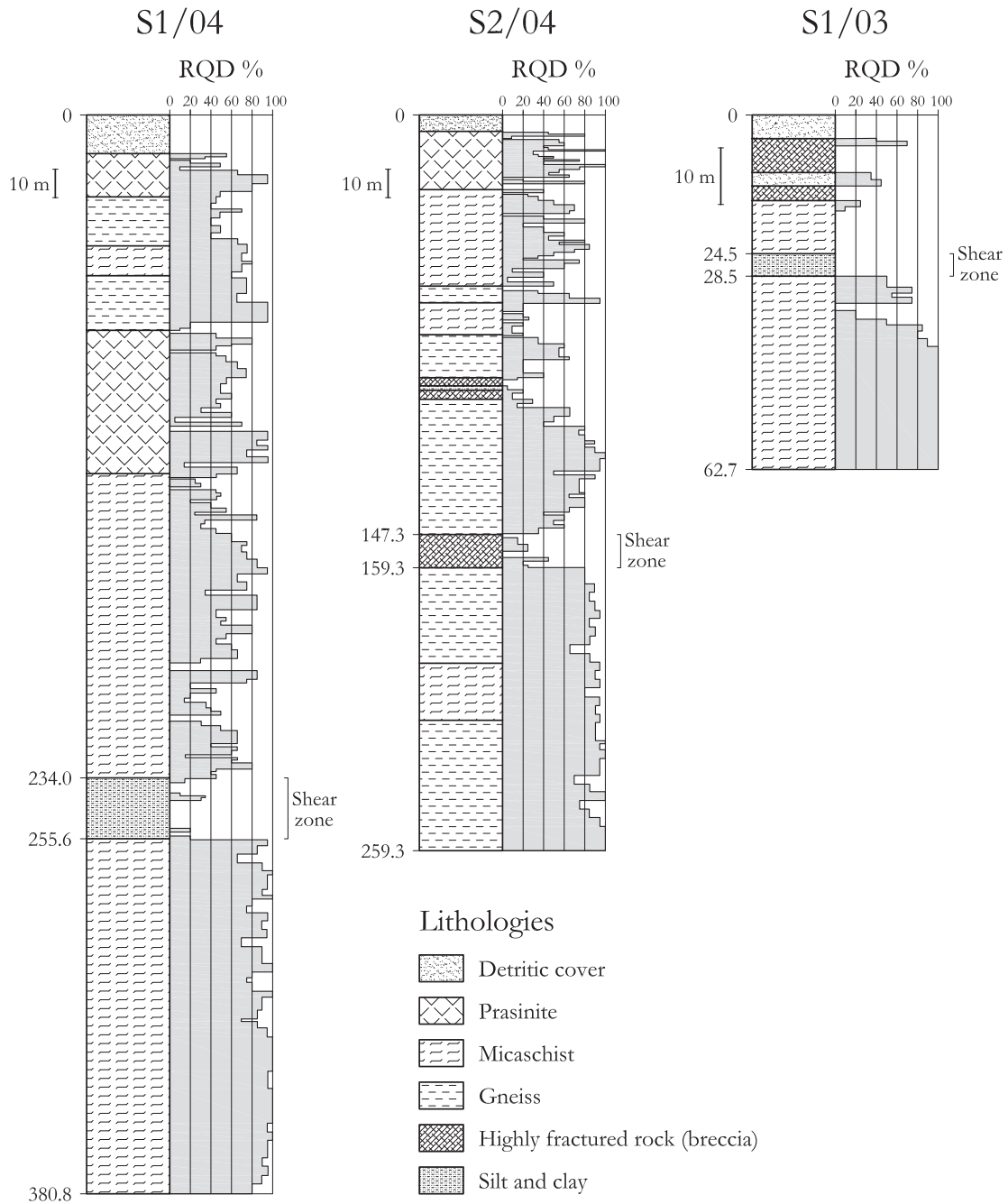
Figure 6.8
Dilling core records and RQD-profiles of the boreholes S1/03, S1/04 and S2/04 in the Beauregard rockslide with indication of the main shear zone (modified after Barla et al. 2010c).

Three main domains are recognizable in the drilling records:
(starting from the surface)

- moderately fractured bedrock with low RQD-values;
- a distinct zone up to 22 m thick with strongly disintegrated
  and comminuted bedrock (kakirites, fault gouges); and
- intact to hardly fractured bedrock

Similar to the drillings, seismic tomography data show a disturbed rock mass with a maximum thickness of 260 m, and a semi-circular basal boundary towards the unaffected bedrock (Barla et al. 2010c).

6.2.3.3   Plumb line monitoring

Five plumb line sequences (PR1, PR2, PR3, PR4, PR5) were installed at different positions adjacent to the dam in order to measure the horizontal displacements of vertical shafts. Each plumb line sequence includes a number of normal and inverted plumb lines acting at different depths. Each of them provides relative displacements which can be cumulatively summed to obtain absolute horizontal displacements along the depth. The lowermost monitoring point is represented by an inverse plumb line which is fixed in the stable bedrock underneath the shear zone. Horizontal displacements are measured on two orthogonal axes, i.e. towards the reservoir and in downstream direction, respectively (compare with the geodetic survey coordinate system in Figure 6.6). A detailed description of the plumb line setup is provided in Barla et al. 2010c.

Figure 6.9 depicts the data of the plumb line sequences PR2, PR3 and PR4 which are adjacent to the dam crest. The left-hand diagrams show the cumulative displacements at the different measurement depths, in the period from April 1, 2003 to July 1, 2010. In contrast to conventional inclinometer data, the number of measurement points is very limited (i.e. three for PR2, four for PR3 and five for PR4). The deformation gradient in depth is therefore obtained in low resolution.

The mean annual horizontal displacement rates with depth were determined by applying a linear regression on the cumulative plumb line data, considering a three years from period April 1, 2003 to April 1, 2006. The results are listed in Table 6.2.
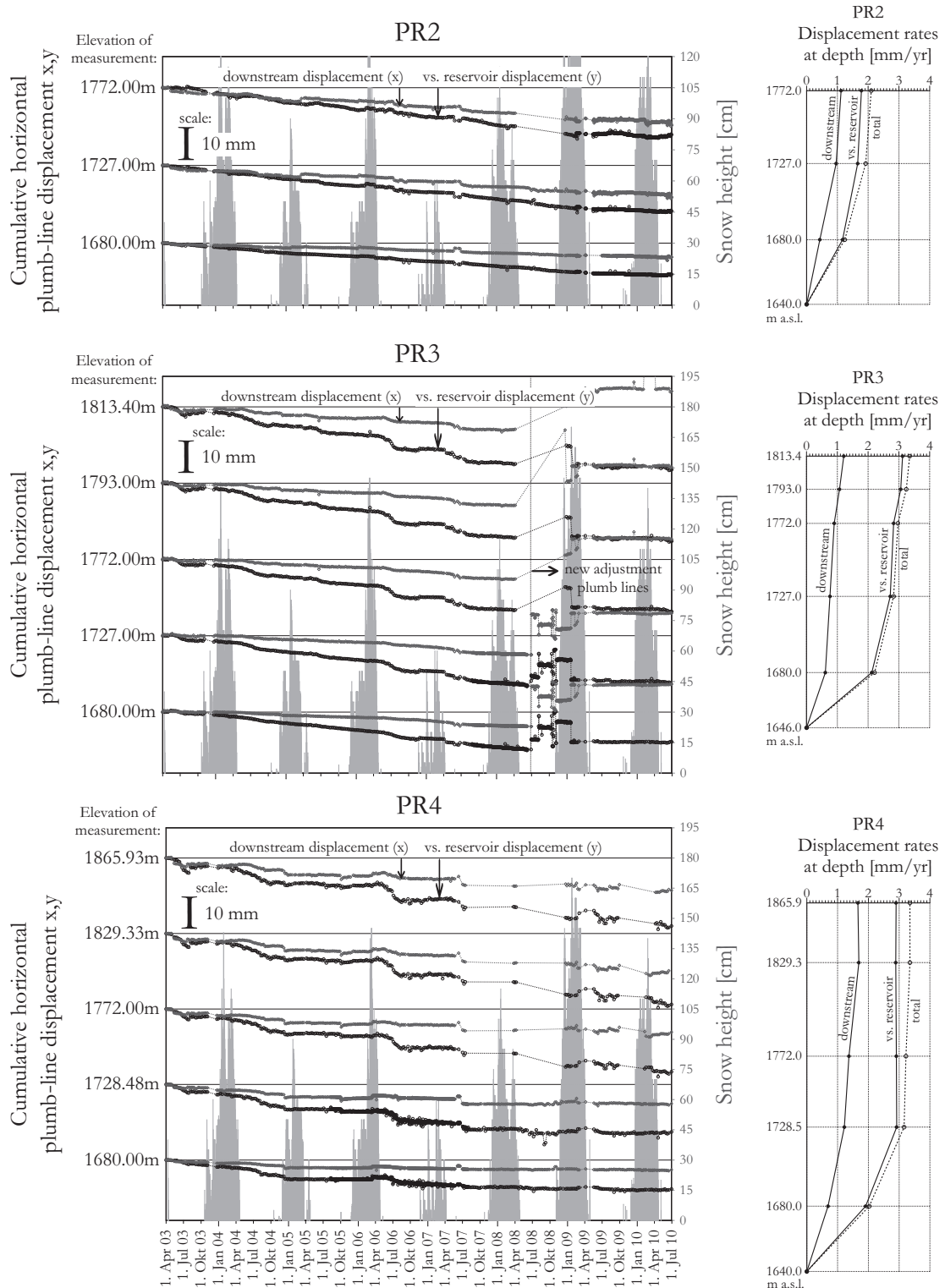
Figure 6.9

Left: Cumulative horizontal displacement at the plumb lines PR2, PR3 and PR4 (left axis) and snow height as a reference (grey, right axis).

Right: Mean annual horizontal displacement rates with depth. The curves can be interpreted as velocity profiles through the rockslide mass.

Table 6.2

Mean annual horizontal displacement rates at different depths of the plumb line sequences PR2, PR3 and PR4. The analyzed period is three years, from April 1, 2003 to April 1, 2006.

PR2		PR3		PR4	
Elevation	v_h	Elevation	v_h	Elevation	v_h
[m a.s.l.]	[mm/yr]	[m a.s.l.]	[mm/yr]	[m a.s.l.]	[mm/yr]
		1813.4	3.35	1865.9	3.35
		1793.0	3.24	1829.3	3.35
1772.0	2.10	1772.0	2.97	1772.0	3.22
1727.0	1.92	1727.0	2.83	1728.5	3.16
1680.0	1.24	1680.0	2.21	1680.0	2.03
1640.0	0*	1646.0	0*	1640.0	0*

* base of plumb line sequence assumed to be fix

The respective velocity profiles are depicted on the right-hand side of Figure 6.9. All plumb lines show a similar deformation pattern, characterised by small deformation gradients close to the slope surface and a strong gradient increase towards the lower end of the plumb line sequence. The data confirm that the rockslide displacement mainly localizes between the two lowermost measurements. These findings are in agreement with the drilling observations which exhibited a shear zone in this depth. The velocity profiles in Figure 6.9 show the linear connection of the data points and, consequently, give no information about the deformation gradients between the measurements. The precise thickness of the actively deforming layer is therefore not deducible from the plumb line data.

6.2.3.4 Groundwater monitoring

At the time of dam construction, ten standpipe piezometers with manual reading were installed in the left slope. In October 2003, the piezometers were equipped with automatic sensors in order to observe the piezometric conditions in the slope continuously. Three additional piezometers were installed in 2005 and 2006, respectively. Automatic measurements take place three times per day and provide time series of the piezometric situation in the slope.

The data of the piezometers S1/04, CL2, PZ1, M11 and the elevation of the reservoir level from January 2003 to June 2010 are shown in Figure 6.10. The locations of the piezometers are depicted in Figure 6.6. The measurements indicate distinct seasonal fluctuations, with piezometric levels rising up by at least 20 m after snowmelt in spring and early summer.
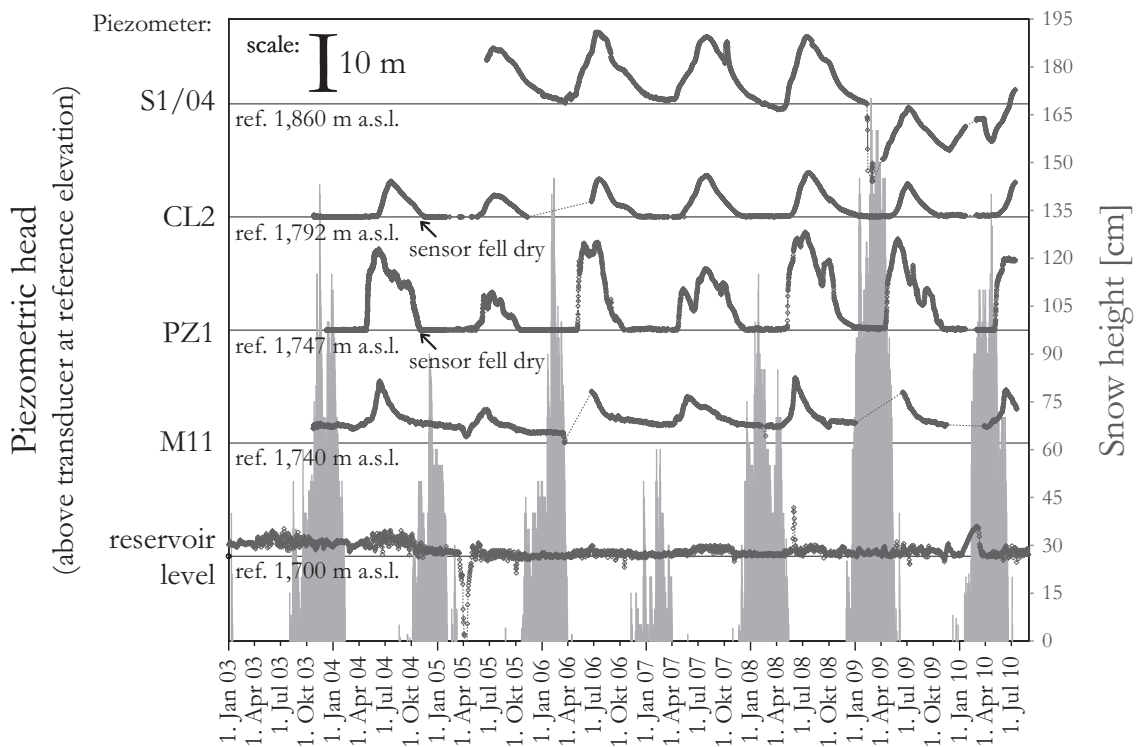
Figure 6.10
Reservoir level and piezometric heads in the slope over time (the scale of the fluctuations is indicated by the 10 m beam in the upper left corner). The grey columns and the associated scale on the right-hand diagram axis indicate the measured snow heights.

6.2.4 Laboratory testing

Samples of the basal shear zone were extracted from the drilling cores of the boreholes S1/03, S1/04 and S2/04 (Figure 6.6). Specimens which have been taken in one (intact) piece are in the following referred to as undisturbed samples.[12] Additionally, loose drilling material was used to prepare remoulded specimens. An upper grain size limit of 0.25 mm was applied, in order to avoid the impact of large particles in the shear band (Martinotti 2010).

Both undisturbed and remoulded samples were investigated with respect to strength and time dependent (creep) behaviour by Martinotti (2010) in direct shear, ring shear and triaxial test settings, i.e. the Casagrande Shear Apparatus, the High Pressure Back Pressure Direct Shear Apparatus (HPBPSA; Barla et al. 2010b), the Bromhead Ring Shear Apparatus, and the High Pressure Triaxial Apparatus (HPTA, Barla et al. 2010a). The experiments were performed either strain-controlled (thus with constant deformation rate) for strength experiments, or load-controlled (thus with constant load) for creep experiments.

6.2.4.1 Shear strength parameters

The peak shear resistance of the shear zone material was investigated by Martinotti (2010) with direct shear and triaxial tests; the residual shear strength was tested by means of ring shear experiments. The detailed experiment boundary conditions and data are shown in Appendix A.5.1.

Table 6.3 summarizes the strength parameters of the basal shear zone as obtained from laboratory testing.

The direct shear experiments yield a peak friction angle of $\varphi_{peak} = 29.7°$ while the triaxial experiments yield $\varphi_{peak} = 26.2°$. This difference in φ_{peak} can be attributed to the differing inherent constraints of the direct shear and triaxial test setups and data interpretations, respectively (compare with Fellin 2011). The residual friction angle obtained from the ring shear tests is $\varphi_{res} = 24.6°$.

---

[12] Strictly speaking, the samples are not undisturbed due to the mechanical impact of the drilling and the subsequent stress relaxation.

Table 6.3
Overview of the Mohr-Coulomb strength parameters of
undisturbed and remoulded samples of the Beauregard
basal shear zone (from Martinotti 2010).

Strength	Experiment type	Regression results		
		Friction angle	Cohesion	R^2 *
Peak	Direct shear test (Casagrande)	$\varphi_{peak} = 29.7°$	$c_{peak} = 0$	0.99
	Triaxial test (HPTA)	$\varphi_{peak} = 26.2°$	$c_{peak} = 0$	0.96
Residual	Ring shear test (Bromhead)	$\varphi_{res} = 24.6°$	$c_{res} = 0$	1.00

* Coefficient of determination

The values correlate well with laboratory strength parameters of similar crystalline shear zone materials (e.g. Engl et al. 2008; Linser 2009; Renk 2006; Strauhal 2009; Vogelhuber 2007).

6.2.4.2 Creep parameters

Martinotti (2010) performed several creep experiments with the material of the Beauregard shear zone using different equipment, i.e. the Casagrande Direct Shear Apparatus, the HPBPSA, and the HPTA. Creep experiments were performed under constant load and usually stopped when secondary (steady) creep was achieved. The detailed testing boundary conditions and regression results of the creep experiments are summarized in Appendix A.5.2.

For similar stress conditions, the creep deformation rates were generally lower in the triaxial mode than in the direct shear mode. The latter is supposed to arise from the enforced strain localization in the direct shear apparatus. The differences in the two experiment types might therefore be attributed to the differing inherent constraints of the test setups.

In this work, the creep experiment results of Martinotti (2010) are interpreted in terms of the viscous models presented in Chapter 3, in order to characterise the Beauregard shear zone material for the subsequent CrEAM modelling. The interpretations refer to the constant creep rates observed in the secondary creep stage.

Separate evaluations are performed for the direct shear and triaxial creep tests, respectively. The material strength required for the effective stress based Vulliet-Hutter models is assumed with laboratory parameters, which have been obtained by strain-controlled experiments in the same test setup. For the triaxial creep experiment interpretation, the triaxial peak friction angle is applied. For the direct shear creep experiment interpretation, the direct shear peak friction angle and the ring shear residual friction is applied, respectively. Details on the creep experiment interpretation are shown in Appendix A.5.2. The viscous parameter sets according different constitutive relationships are summarized in Table 6.4 .

As the number of data was very limited, the regression analysis quality is generally poor and the deduced creep parameters relatively unprecise. A larger number of creep experiments would be necessary in order to extract statistically significant results. Despite of these shortcomings, the analyses are supposed to indicate the order of magnitude of the viscous behaviour on the laboratory scale.

It is expected that the laboratory strength and viscous parameters are not directly transferable to the in situ problem since the tested specimens are hardly representative for the complex and inhomogeneous architecture of the shear zone in the slope.

Description of Table 6.4 (following page)
Viscous parameters of the Beauregard basal shear zone according to different viscous models, obtained from the regression analyses of the direct shear and triaxial creep experiments. For the Vulliet-Hutter models, the additional φ-values indicate the required strength assumption. The values correspond to the friction angles as obtained from the direct shear, ring shear and triaxial experiments (see Table 6.3). "n" is the number of data sets, "R²" denotes the regression coefficient.

Table 6.4 (description see previous page)

	Casagrande direct shear creep test DSc1-DSc3; n=3		Triaxial creep test two stages Br_Tx_001; n=2	
Newton	Newton-DSc: $\bar{\mu}_{\text{lab}}^{Newton} = 1.61 \cdot 10^{13}$ Pa·s	$\left(R^2 = 0.20 \right)$	Newton-TXc: $\bar{\mu}_{\text{lab}}^{Newton} = 2.61 \cdot 10^{16}$ Pa·s	$\left(R^2 = - \right)$ **
Bingham	Bingham-DSc: $\bar{\mu}_{\text{lab}}^{Bingham} = 1.84 \cdot 10^{12}$ Pa·s $\tau_{y,\text{lab}}^{Bingham} = 1.78 \cdot 10^{6}$ Pa	$\left(R^2 = 0.94 \right)$	not defined ***	
original Norton	orig. Norton-DSc: $\bar{\mu}_{\text{lab}}^{Norton} = 1.87 \cdot 10^{58}$ Pa$^{\text{m}}$·s $m_{\text{lab}}^{Norton} = 8.144$	$\left(R^2 = 0.90 \right)$	not defined ***	
modified Norton	mod. Norton-DSc: $\bar{\mu}_{\text{lab}}^{Norton} = 3.03 \cdot 10^{17}$ Pa$^{\text{m}}$·s $\tau_{y,\text{lab}}^{Norton} = 1.59 \cdot 10^{6}$ Pa $m_{\text{lab}}^{Norton} = 1.878$	$\left(R^2 = 0.91 \right)$	not defined ***	
original Vulliet-Hutter	orig.VH-DSc-DSφ: $A_{\text{lab}}^{VH_{DP}} = 1.87 \cdot 10^{-7}\text{s}^{-1}$ $m_{\text{lab}}^{VH_{DP}} = 1.5$ $\varphi_{peak} = 29.7°$ --- $\left(R^2 = 0 \right)$ * orig.VH-DSc-RSφ: $A_{\text{lab}}^{VH_{DP}} = 1.13 \cdot 10^{-7}\text{s}^{-1}$ $m_{\text{lab}}^{VH_{DP}} = 1.5$ $\varphi_{res} = 24.6°$ --- $\left(R^2 = 0 \right)$ *		orig.VH-TXc-TXφ: $A_{\text{lab}}^{VH_{DP}} = 5.17 \cdot 10^{-8}\text{s}^{-1}$ $m_{\text{lab}}^{VH_{DP}} = 30.8$ $\varphi_{peak} = 26.2°$	$\left(R^2 = - \right)$ ****
modified Vulliet-Hutter	mod.VH-DSc-DSφ: $A_{\text{lab}}^{VH_{MC}} = 8.83 \cdot 10^{-8}\text{s}^{-1}$ $m_{\text{lab}}^{VH_{MC}} = 1.5$ $\varphi_{peak} = 29.7°$ --- $\left(R^2 = 0 \right)$ * mod.VH-DSc-RSφ: $A_{\text{lab}}^{VH_{MC}} = 6.35 \cdot 10^{-8}\text{s}^{-1}$ $m_{\text{lab}}^{VH_{MC}} = 1.5$ $\varphi_{res} = 24.6°$ --- $\left(R^2 = 0 \right)$ *		mod.VH-TXc-TXφ: $A_{\text{lab}}^{VH_{MC}} = 4.67 \cdot 10^{-8}\text{s}^{-1}$ $m_{\text{lab}}^{VH_{MC}} = 35.0$ $\varphi_{peak} = 26.2°$	$\left(R^2 = - \right)$ ****

*   very poor regression, viscosity parameters indicate only an order of magnitude

** only one data point for the regression of the one-component Newton model

*** deviatoric stress was kept constant during the two triaxial creep stages, thus, no regression for the deviatoric stress based viscous models with two or more parameters possible

**** only two data points for the regression of the Vulliet-Hutter models

6.2.5   Rockslide geometry

The rockslide mass in the lower portion of the left abutment slope is defined by a smooth but extensive scarp plane between 2,050 and 2,200 m a.s.l. The surface morphology below this distinct scarp feature is characterised by the Alpettaz flat adjacent to the scarp and an oversteepened slope towards the reservoir and the dam. These morphological expressions suggest a deep-seated semi-rotational deformation mechanism in the lower slope portion.

Despite the limited resolution, the plumb line monitoring data indicate small deformation gradients close to the slope surface and a strong gradient increase towards the lower end of the plumb line sequences (see velocity profiles on the right-hand side of Figure 6.9). The hanging wall rock mass experiences a minor internal deformation. These observations suggest that the bulk displacement of the lower slope takes place in the soil like shear zone which was encountered in the boreholes S1/03, S1/04 and S2/04. It is however unknown, whether the deformations takes place in the entire sheared and disintegrated rock volume, or whether they localize in a more discrete zone.

A two-dimensional geomechanical model through the Beauregard rockslide mass adjacent to the reservoir is employed for the stability and creep calculations in the subsequent sections. The analysis cross-section is located close to the arch-gravity dam and orientated parallel to the mean direction of slope movements. The cross-section includes the depth and thickness of the encountered shear zone and the observed displacement vector inclinations on the rockslide surface. Figure 6.11 depicts three different interpretations (geometries "A", "B" and "C") which are subsequently analysed.

Geometry "A" denotes the cross-section as used by Barla (2010d) for the stability and deformation analysis of the rockslide with a Finite Element code. Therein, the basal shear layer is assumed as a polygonal zone, composed of four straight segments with a constant thickness of 20 m. The latter assumption is based on the findings in borehole S1/04, where the maximum shear zone thickness was observed (i.e. 21.6 m).
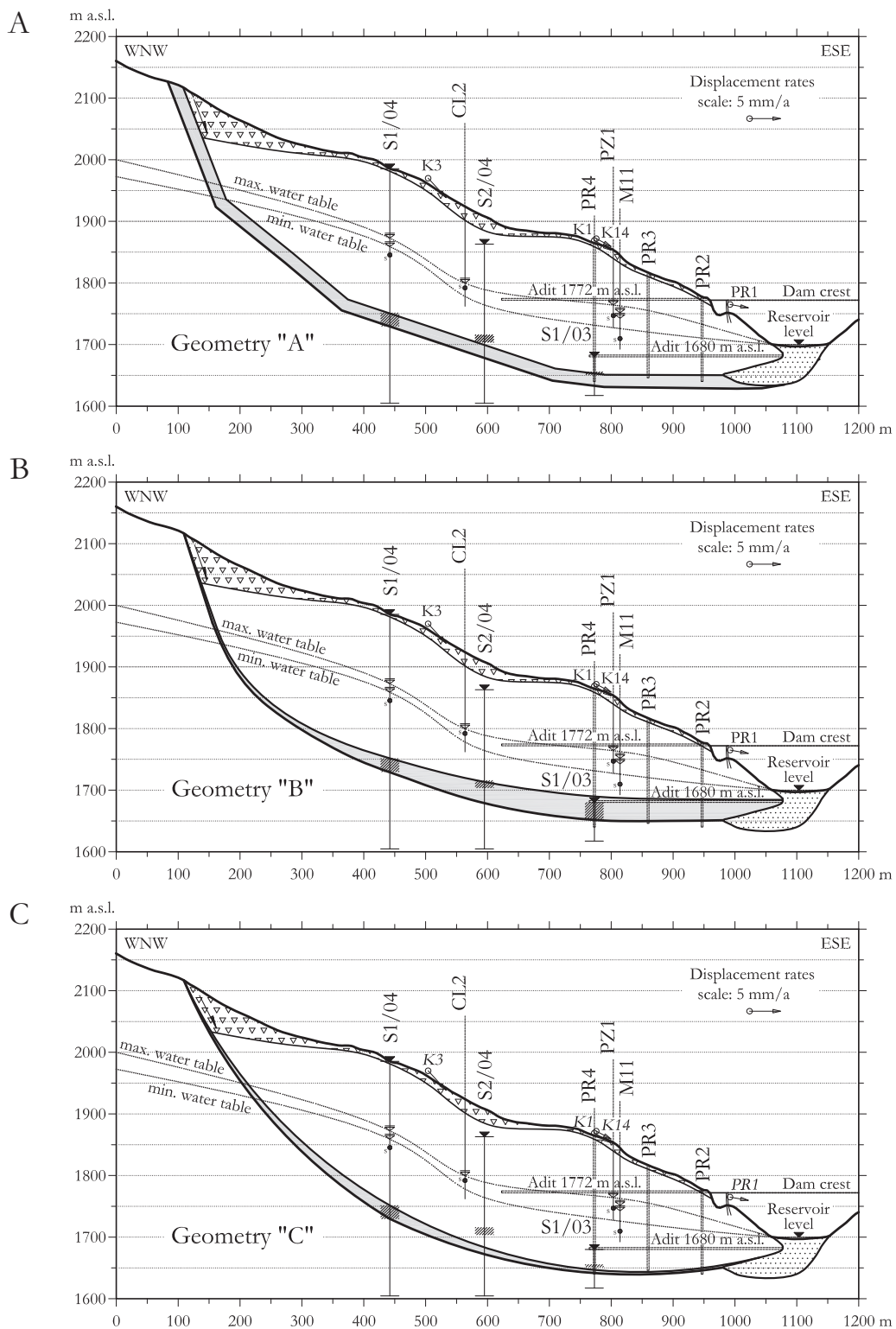
Figure 6.11

Cross-section E-E' of the Beauregard lower rockslide portion: Geometry variants "A", "B" and "C" (for cross-section trace see Figure 6.3)

By contrast, in geometry "B" the shear horizon along the rockslide base is assumed to be strongly variable in thickness, i.e. very thin in the scarp region and increasing in thickness towards the slope toe. This geomechanical model accounts for the findings in S1/04 and assumes further that the bulk disintegrated rock volume entcountered in the drilling S1/03 acts as a basal deformation zone of the rockslide.

In geometry "C", the rockslide mass is confined by a circular surface towards the basal deformation horizon and the geometry therefore implicates a rotational mechanism. This geomechanical model includes the shear zone location and thickness as encountered in the drilling S1/04 (21.6 m) and the four metres fault gouge horizon in S1/03.

Each geometry variant in Figure 6.11 show the minimum respective maximum groundwater level in the slope, reflecting the low piezometric conditions in autumn-winter and the elevated piezometric conditions after snowmelt in spring-early summer. Furthermore, all variants assume a constant reservoir level of 1,700 m a.s.l., based on operating conditions since January 1997.

In the following, the three different geometry variants are investigated by means of two-dimensional stability and creep analyses. The specific weights of the rock mass above the shear horizon as assigned for the calculations are listed in Table 6.5.

The assumptions for the strength and viscous properties of the shear zone material are introduced and discussed in the following sections.

Table 6.5
Overview of the paragneissic rock mass properties above the shear zone (after Barla et al. 2006).

Specific unsaturated weight γ (above groundwater level)	Specific saturated weight γ_r (below groundwater level)
24 KN/m³	25 KN/m³

6.2.6 Stability analysis

In a first step, the geometry variants "A", "B" and "C" are evaluated in terms of stability. For this purpose, standard two-dimensional limit equilibrium methods are applied. The mechanisms with polygonal (irregular) sliding bases, i.e. the geometries "A" and "B", are calculated with the Simplified Janbu method, while the rotational variant "C" is analysed with the Simplified Bishop approach. The analyses use the strength parameters as obtained by the different laboratory tests.

The detailed stability analysis results are listed in Table 6.6 and depicted in Figure 6.12. The minimum Factor of Safety values range between $\eta = 1.13\text{-}1.24$ for the low groundwater level in winter and drop to $\eta = 1.07\text{-}1.17$ for the high groundwater level in summer, based on the residual friction angle determined by ring shear testing. For the peak friction angle obtained from the direct shear tests, the Factor of Safety value rise to respective $\eta = 1.40\text{-}1.55$ for winter conditions and $\eta = 1.33\text{-}1.46$ for summer conditions.

Generally, the Factor of Saftey values of the mechanisms with the irregular sliding zone (geometries "A" and "B") are slightly less then the values of the rotational mechanism (geometry "C").

Table 6.6
Limit equilibrium stability analysis results for the geometry variants "A", "B" and "C" using different friction angles (the cohesion is zero in all calculations). The columns "Winter" and "Summer" denote the respective low and high groundwater level in the slope as shown in Figure 6.11.

		Factor of Safety					
Shear zone strength		Geometry A		Geometry B		Geometry C	
		Winter	Summer	Winter	Summer	Winter	Summer
Direct shear	$\varphi_{peak} = 29.7°$	1.40	1.33	1.48	1.39	1.55	1.46
Triaxial	$\varphi_{peak} = 26.2°$	1.21	1.14	1.28	1.20	1.33	1.26
Ring shear	$\varphi_{res} = 24.6°$	1.13	1.07	1.19	1.12	1.24	1.17
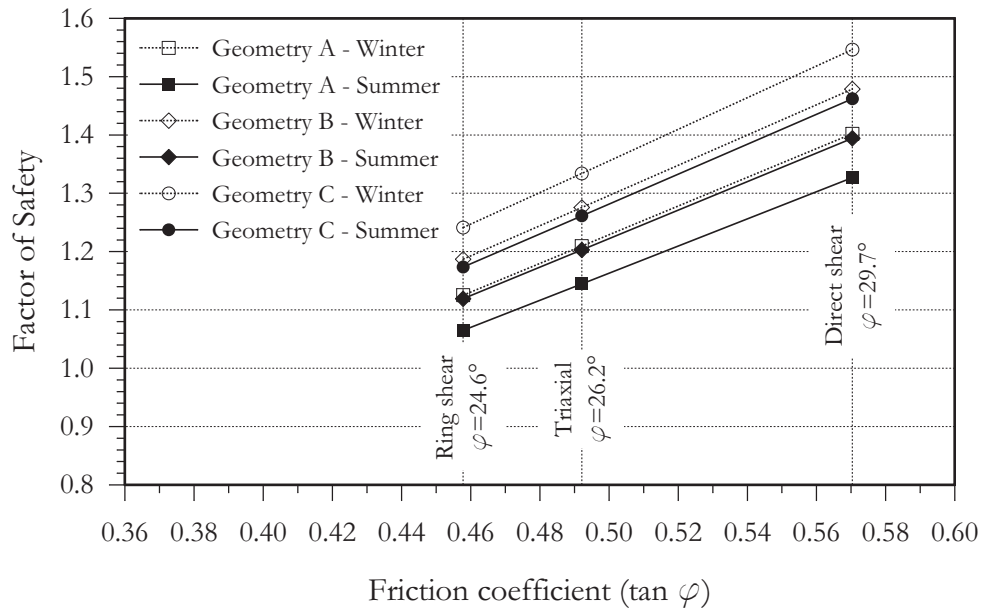
Figure 6.12
Factor of Safety results of the limit equilibrium stability analysis using the Simplified Janbu method (Geometry "A" and "B") and Simplified Bishop method (Geometry "C").

A friction angle of $\varphi = 22°$ ($c = 0$) yields for all geometries a state close to limit equilibrium, thus $\eta \approx 1$, which is in accordance with the findings of Barla (2010d).

6.2.7 Creep analysis using CrEAM

In this section, the geometry variants "A", "B" and "C" are investigated with the Creep Equilibrium Analysis Method (CrEAM). The calculations employ the various constitutive models presented in Chapter 3.

Different algorithms are applied, depending on both the mechanism (translational or rotational) and the constitutive model. The geometry variants "A" and "B" are investigated with the deviatoric stress based CrEAM for translational slides (D-CrEAM*trans*) using the viscous models Newton, Bingham and Norton, and with the effective stress based CrEAM for translational slides (E-CrEAM*trans*) using the original and modified Vulliet-Hutter relationships, respectively. Geometry "C" is calculated with D-CrEAM*rot* and the Ordinary E-CrEAM*rot*.

Two different modelling approaches are pursued. In the first step, a regular forward calculation based on laboratory material parameters is performed. Associated creep displacement rates are determined. In the second step, a back calculation is performed, by using the actually measured displacement rates on the surface and at the plumb lines as a reference. The in situ input material parameters required to fit the survey observations are back calculated by means of a heuristic (trial-and-error) process. The results of forward and back analyses are subsequently compared and discussed in Section 6.2.8.

6.2.7.1   Forward analysis of displacement rates based on laboratory parameters

In the following, the displacement rates of the Beauregard lower slope portion are calculated with CrEAM in a forward analysis, based on the laboratory creep testing results. For this purpose, the laboratory parameter sets derived for the different constitutive models are directly introduced in the model. Table 6.7 summarizes the forward analysis results.

Figure 6.13 shows an overview of the calculated displacement rates for all constitutive models and the three different geometries. Therein, the investigated viscous models and the associated laboratory parameter sets are arranged on the diagram abscissa. The diagam ordinate indicates the calculated horizontal displacement rate. The columns in the diagram show the velocity range between low and high groundwater conditions in the slope for the different geometry variants "A", "B" and "C".

A comparision of the different laboratory test based parameter sets shows a large scatter of the forward analysis outcome. Modelling results diverge in eight orders of magnitude. The original Vulliet-Hutter parameters deduced from the triaxial creep test yield velocities in the order of 10^{-1} to 10^{-3} mm/month while the direct shear creep tests DSc1-DSc3 (interpreted by the same viscous model) yield velocities in the range of 10^5 mm/month.

The two dashed horizontal lines shown in Figure 6.13 (0.1 and 0.7 mm/month, respectively) denote the winter and summer slope velocities used for the back analysis in the next section.

When taking these values as a reference, Figure 6.13 reveals that the viscous parameter sets based on the multi-stage triaxial creep experiment (i.e. Newton-TXc, orig.VH-TXc-$\text{TX}\varphi$ and mod.VH-TXc-$\text{TX}\varphi$), yield model velocities closer to the observed velocities than the direct shear creep test related parameter sets. Nevertheless, these parameter sets still underestimate and overestimate the observed velocity by 1-2 orders of magnitude, respectively.

Table 6.7
Results of the forward analysis with CrEAM based on laboratory creep parameters (Table 6.4), using different constitutive relationships and the three geometry variants "A", "B" and "C".

Viscous model	Laboratory parameter set code (see Table 6.4)	Horizontal slope velocity v_h [mm/month] at (low | high) groundwater level, based on laboratory creep parameters		
		Geometry "A"	Geometry "B"	Geometry "C"
Newton	Newton-DSc	[1] $\left(1.78 \mid 1.79\right)\cdot 10^3$	[1] $\left(1.54 \mid 1.55\right)\cdot 10^2$	[3] $\left(7.44 \mid 7.46\right)\cdot 10^3$
	Newton-TXc	[1] $\left(1.10 \mid 1.10\right)$	[1] $\left(9.53 \mid 9.56\right)\cdot 10^{-2}$	[3] $\left(4.59 \mid 4.60\right)$
Bingham	Bingham-DSc	no creep	no creep	no creep
original Norton	orig. Norton-DSc	[1] $\left(9.83 \mid 10.1\right)$	[1] $\left(1.60 \mid 1.64\right)$	[3] $\left(1.27 \mid 1.31\right)\cdot 10^2$
modified Norton	mod. Norton-DSc	no creep	no creep	no creep
original Vulliet-Hutter	orig.VH-DSc-$\text{DS}\varphi$	[2] $\left(1.32 \mid 1.44\right)\cdot 10^3$	[2] $\left(9.26 \mid 9.98\right)\cdot 10^2$	[4] $\left(6.61 \mid 7.14\right)\cdot 10^4$
	orig.VH-DSc-$\text{RS}\varphi$	[2] $\left(1.09 \mid 1.18\right)\cdot 10^3$	[2] $\left(7.62 \mid 8.20\right)\cdot 10^2$	[4] $\left(5.44 \mid 9.71\right)\cdot 10^4$
	orig.VH-TXc-$\text{TX}\varphi$	[2] $\left(5.74 \mid 31.25\right)\cdot 10^{-3}$	[2] $\left(9.08 \mid 54.18\right)\cdot 10^{-4}$	[4] $\left(1.68 \mid 9.36\right)\cdot 10^{-2}$
modified Vulliet-Hutter	mod.VH-DSc-$\text{DS}\varphi$	[2] $\left(1.02 \mid 1.10\right)\cdot 10^3$	[2] $\left(7.11 \mid 7.66\right)\cdot 10^2$	[4] $\left(5.08 \mid 5.48\right)\cdot 10^4$
	mod.VH-DSc-$\text{RS}\varphi$	[2] $\left(9.49 \mid 10.31\right)\cdot 10^2$	[2] $\left(6.64 \mid 7.16\right)\cdot 10^2$	[4] $\left(4.74 \mid 9.11\right)\cdot 10^4$
	mod.VH-TXc-$\text{TX}\varphi$	[2] $\left(4.14 \mid 28.53\right)\cdot 10^1$	[2] $\left(5.13 \mid 40.03\right)$	[4] $\left(8.01 \mid 56.85\right)\cdot 10^1$

Calculated with (1) D-CrEAM[trans]; (2) E-CrEAM[trans]; (3) D-CrEAM[rot] and (4) ord. E-CrEAM[rot]
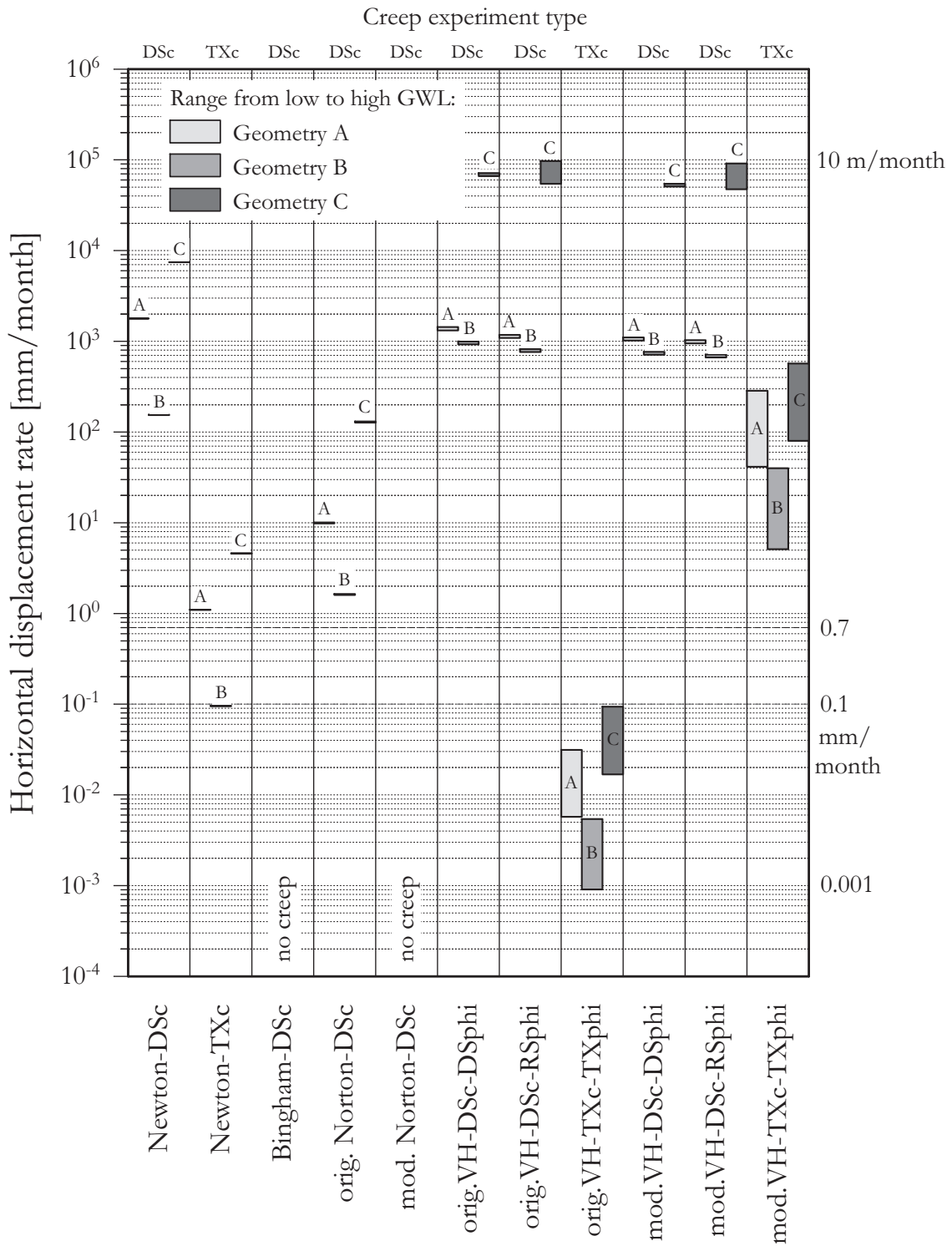
Figure 6.13
Results of the forward analysis of displacement rates using the viscous parameters from the laboratory creep tests. Please note the logarithmic scale of the velocity axis.

The characterization of the basal shear zone with direct shear creep test results interpreted with the Bingham and modified Norton viscous models, respectively, yield no creep displacements, both for low and high groundwater conditions. According these model results, the assigned yield shear stresses, i.e. 1.78 MPa for the Bingham model and 1.59 MPa for the modified Norton model (deduced from the direct shear creep tests) are too high to initiate creep deformation in the basal shear zone.

The increase of the slope displacement rate from the low winter to the high summer groundwater conditions is variable. Generally, the predicted velocity jump increases from the simple linear viscous model according Newton to the more sophisticated constitutive relationships proposed by Vulliet & Hutter (1988a). The original and modified Vulliet-Hutter parameter sets from the triaxial creep experiment (orig.VH-TXc-TXφ and mod.VH-TXc-TXφ) exhibit the highest sensitivity with respect to groundwater fluctuations. Both models predict a relative seasonal velocity jump by a factor 5.5 to 7.

The different geometry variants used for the modelling show a clear effect on the analysis results. For all viscous models, the geometry "B" which assumes an increasing shear zone thickness from the scarp to the toe of the rockslide yields the lowest creep velocities. In contrast, the geometry "C" characterised by a relatively thin shear zone yields the highest creep velocities. Geometry "A" with a constant shear zone thickness occupies an intermediate position.

6.2.7.2   Back analysis of in situ creep parameters based on measured displacement rates

The back analysis performed in this section seeks to reveal suitable constitutive relationships and the respective material parameters which are capable to replicate the observed seasonal displacement characteristics of the rockslide. For this purpose, the measured displacement rates are used as model input. Following the geodetic observations and the plumb line measurements, the overall irreversible horizontal displacement of the slope is about 3 mm per year. Furthermore, the detailed plumb line displacement curves evidence a constant slow slope movement during the months of autumn, winter and early spring while the slope accelerates every year in late spring. High displacement rates usually persist until the end of summer and correlate with enhanced piezometric heads in the slope after snow melt.

For the back calculation, two velocity states are defined which are correlated with the minimum (winter) and maximum (summer) groundwater level in the slope, respectively. Furthermore, the following assumption is made: Creep velocities during the high groundwater level are about seven times larger than during the low groundwater level, according the observations in the plumb line measurements.

$$
\begin{aligned}
v_{h,winter} &= 1.2 \text{ mm/yr} = 0.1 \text{ mm/month} \\
v_{h,summer} &= 8.4 \text{ mm/yr} = 0.7 \text{ mm/month}
\end{aligned}
\tag{6.1}
$$

The slope is analysed in terms of two hypothesised extreme states, i.e. a low groundwater level associated with a creep rate of 0.1 mm/month, and a high groundwater level associated with a creep rate of 0.7 mm/month.

In the back analysis, the viscous parameter sets which are suitable to fit the low displacement rates associated with the low groundwater level in the winter season (0.1 mm/month) are iterated for the different geometries "A", "B" and "C" and six different viscous models by means of a trial-and-error procedure. For the Newton, original Norton and original/modified Vulliet-Hutter models, only one parameter was varied during the calibration i.e. the viscosity values $\bar{\mu}$ (for Newton and original Norton) and the rate factor values A (for original and modified Vulliet-Hutter). The associated exponents m and friction angles φ $(c = 0)$ were kept constant at the values obtained from the triaxial creep and strength tests, respectively. This makes the back calculated viscosities and rate factors directly comparable with their laboratory equivalents.

Applying the Bingham and modified Norton viscous models and assigning the laboratory yield shear stress of 1.6-1.8 MPa (see Table 6.4) to the basal shear zone results in no creep displacements. Consequently, for the back calculation, the yield shear stress must be lowered in order to initiate creep. Several possible combinations of the viscosity value and the yield shear stress exist which yield the target velocity of 0.1 mm/month for the winter groundwater level. For this back calculation, the yield shear stress was arbitrarily fixed at 0.1 MPa and the viscosity varied.

Table 6.8 summarizes the back calculated viscous parameter sets of all six evaluated constitutive models which fit the horizontal slope displacement rate of 0.1 mm/month for low groundwater conditions.

Table 6.8

Back calculated in situ creep parameters using the velocity of 0.1 mm/month as a reference, for three different geometries and six viscous models. Values in parenthesis are assumed based on laboratory testing.

Viscous model	Material parameter	Back calculated in situ creep parameter values		
		Geometry "A"	Geometry "B"	Geometry "C"
Newton	$\overline{\mu}_{\text{in situ}}^{Newton} =$	$2.87 \cdot 10^{17}\,\text{Pa}\cdot\text{s}$ [1]	$2.49 \cdot 10^{16}\,\text{Pa}\cdot\text{s}$ [1]	$1.2 \cdot 10^{18}\,\text{Pa}\cdot\text{s}$ [3]
Bingham	$\overline{\mu}_{\text{in situ}}^{Bingham} =$ $\tau_{y,\text{in situ}}^{Bingham} =$	$2.57 \cdot 10^{15}\,\text{Pa}\cdot\text{s}$ [1] $10^{5}\,\text{Pa}$	$2.20 \cdot 10^{16}\,\text{Pa}\cdot\text{s}$ [1] $10^{5}\,\text{Pa}$	$1.08 \cdot 10^{18}\,\text{Pa}\cdot\text{s}$ [3] $10^{5}\,\text{Pa}$
original Norton	$\overline{\mu}_{\text{in situ}}^{Norton} =$ $m_{\text{lab}}^{Norton} =$	$1.84 \cdot 10^{60}\,\text{Pa}^{\text{m}}\cdot\text{s}$ [1] $\left(8.144\right)$	$2.99 \cdot 10^{59}\,\text{Pa}^{\text{m}}\cdot\text{s}$ [1] $\left(8.144\right)$	$2.38 \cdot 10^{61}\,\text{Pa}^{\text{m}}\cdot\text{s}$ [3] $\left(8.144\right)$
modified Norton	$\overline{\mu}_{\text{in situ}}^{Norton} =$ $\tau_{y,\text{in situ}}^{Norton} =$ $m_{\text{lab}}^{Norton} =$	$4.47 \cdot 10^{22}\,\text{Pa}^{\text{m}}\cdot\text{s}$ $10^{5}\,\text{Pa}$ [1] $\left(1.878\right)$	$6.77 \cdot 10^{21}\,\text{Pa}^{\text{m}}\cdot\text{s}$ $10^{5}\,\text{Pa}$ [1] $\left(1.878\right)$	$3.28 \cdot 10^{23}\,\text{Pa}^{\text{m}}\cdot\text{s}$ $10^{5}\,\text{Pa}$ [3] $\left(1.878\right)$
original Vulliet-Hutter	$A_{\text{in situ}}^{VH_{DP}} =$ $m_{\text{lab}}^{VH_{DP}} =$ $\varphi_{\text{peak, lab (TX)}} =$	$9.01 \cdot 10^{-7}\,\text{s}^{-1}$ $\left(30.8\right)$ [2] $\left(26.2°\right)$	$5.69 \cdot 10^{-6}\,\text{s}^{-1}$ $\left(30.8\right)$ [2] $\left(26.2°\right)$	$3.08 \cdot 10^{-7}\,\text{s}^{-1}$ $\left(30.8\right)$ [4] $\left(26.2°\right)$
modified Vulliet-Hutter	$A_{\text{in situ}}^{VH_{MC}} =$ $m_{\text{lab}}^{VH_{MC}} =$ $\varphi_{\text{peak, lab (TX)}} =$	$1.13 \cdot 10^{-10}\,\text{s}^{-1}$ $\left(35.0\right)$ [2] $\left(26.2°\right)$	$9.10 \cdot 10^{-10}\,\text{s}^{-1}$ $\left(35.0\right)$ [2] $\left(26.2°\right)$	$5.83 \cdot 10^{-11}\,\text{s}^{-1}$ $\left(35.0\right)$ [4] $\left(26.2°\right)$

Calculated with (1) D-CrEAM*trans*; (2) E-CrEAM*trans*; (3) D-CrEAM*rot* and (4) ord. E-CrEAM*rot*

Figure 6.14 shows a comparision of the laboratory and back calculated (in situ) viscous parameters. For the deviatoric stress based constitutive models, the back calculated viscosities $\overline{\mu}$ are higher than the laboratory value (one to three orders of magnitude for original Norton; three to five orders of magnitude for Newton). For the effective stress based constitutive models employing a rate factor A, the back calculated rate factor is by one to two orders of magnitude higher than the laboratory value for the original Vulliet-Hutter model, and by one to three orders of magnitude lower for the modified Vulliet-Hutter model.

Newton

Original Norton

Original Vulliet-Hutter

Modified Vulliet-Hutter
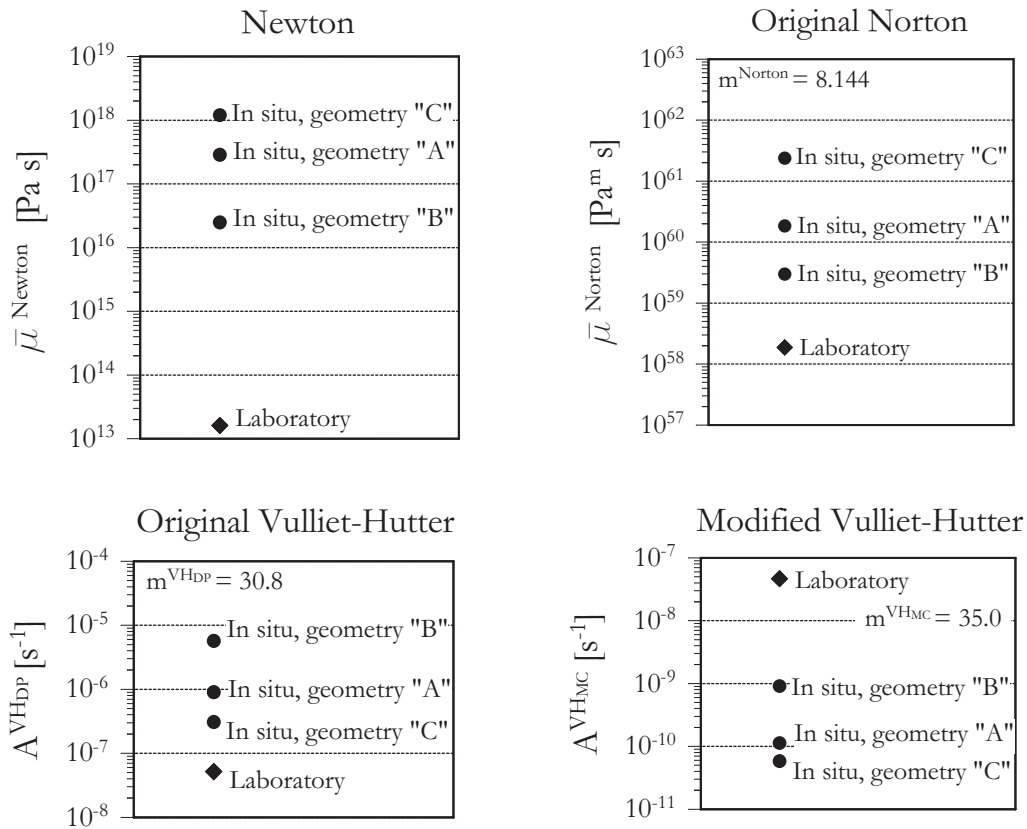
Figure 6.14

Comparision of laboratory and back calculated in situ creep parameters (viscosities $\overline{\mu}$ for Newton and Norton; rate factors A for original and modified Vulliet-Hutter, respectively). Note the logarithmic scale of the parameter axes.

In the next step, the back calculated in situ creep parameters are applied for the high groundwater level in the slope. Table 6.9 summarizes the predicted velocities for the different geometries and the six evaluated constitutive models.

All calculations predict an increase in creep velocity and, thus, a slope acceleration for elevated groundwater conditions. The magnitude of the predicted velocity increase is however strongly dependent on the applied constitutive model. By contrast, the geometry variants have a minor influence on the model results.

Table 6.9

Model prediction of the seasonal velocity fluctuation related to the low and high groundwater conditions in the slope, using the back calculated viscous parameters from Table 6.8.

Viscous model	Horizontal slope velocity v_h [mm/month] at (low ∣ high) groundwater level		
	Geometry "A"	Geometry "B"	Geometry "C"
Newton	[1]$(0.100 \mid 0.100)$	[1]$(0.100 \mid 0.100)$	[3]$(0.100 \mid 0.100)$
Bingham	[1]$(0.100 \mid 0.100)$	[1]$(0.100 \mid 0.100)$	[3]$(0.100 \mid 0.100)$
original Norton	[1]$(0.100 \mid 0.103)$	[1]$(0.100 \mid 0.103)$	[3]$(0.100 \mid 0.103)$
modified Norton	[1]$(0.100 \mid 0.101)$	[1]$(0.100 \mid 0.101)$	[3]$(0.100 \mid 0.100)$
orig. Vulliet-Hutter	[2]$(0.100 \mid 0.544)$	[2]$(0.100 \mid 0.594)$	[4]$(0.100 \mid 0.558)$
mod. Vulliet-Hutter	[2]$(0.100 \mid 0.689)$	[2]$(0.100 \mid 0.780)$	[4]$(0.100 \mid 0.709)$

Calculated with (1) D-CrEAM*trans*; (2) E-CrEAM*trans*; (3) D-CrEAM*rot* and (4) ord. E-CrEAM*rot*

Figure 6.15 depicts the modelled velocity ranges and clearly illustrates whether the different constitutive models are able to replicate the assumed velocity fluctuation of 0.1 to 0.7 mm/month.

Good modelling results are achieved with the effective stress based viscous models (i.e. original and modified Vulliet-Hutter). Both relationships approximate the target value of 0.7 mm/month for summer conditions, by using the rate factor A as previously calibrated for the low landslide activity in the winter months, and the exponent m as well as the friction angle φ as deduced from laboratory testing. The best fit is obtained with the modified Vulliet-Hutter model.

In contrast, the nonlinear deviatoric stress based constitutive relationships (i.e. original and modified Norton) predict a minor velocity increase when the groundwater in the slope rises from the winter to the summer level. The linear deviatoric stress based constitutive relationships Newton and Bingham predict an insignificant velocity increase.
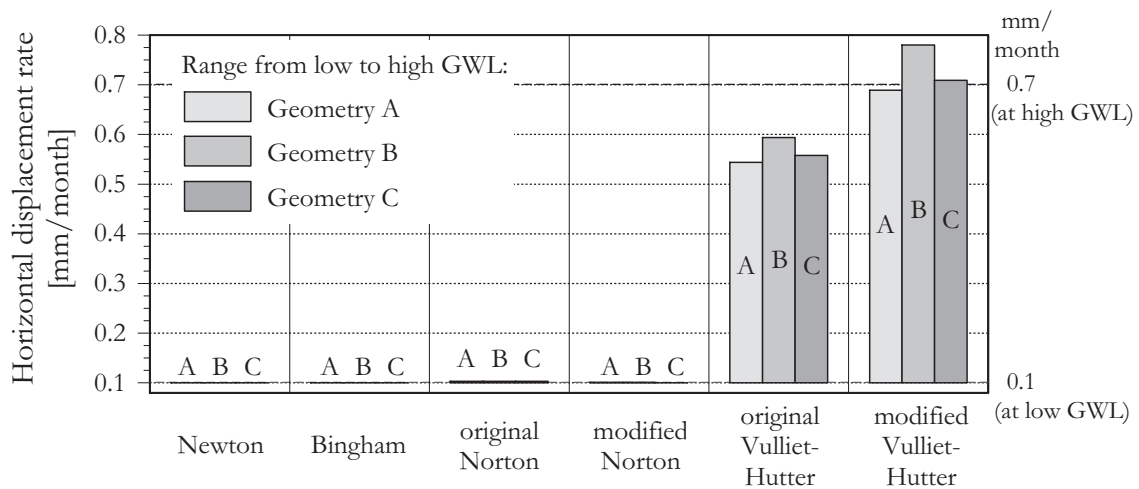
Figure 6.15
Modelled slope velocity ranges associated with the seasonal groundwater
level (GWL) fluctuation, for different constitutive models and geometries.
Calculations are based on the viscous parameter sets in Table 6.8 which
have been calibrated for the low groundwater level.

6.2.8   Case study discussion

The presented investigations with CrEAM are based on the analysis of two extreme
states and do not consider any transition phases. The investigated szenario repre-
sents therefore only a very simple approximation of both the groundwater condi-
tions and the velocity regime of the slope during the annual cycle.

The application of laboratory creep parameters in the forward analysis generally
overestimated the slope creep velocity in the range of several orders of magnitude,
i.e. up to three orders of magnitude using the triaxial creep test based parameters,
and up to five orders of magnitude using the direct shear creep test based parame-
ters. Similar findings have been made by other authors (e.g. Van Asch et al. 2007;
Schneider-Muntau 2012). A clear trend between triaxial creep test based parameters
and direct shear test based parameters is discernable: Triaxial test based parameters
approximated the actual slope behaviour better than the direct shear based parame-
ters. This suggests that i) the in situ creep processes are better reproduced in the tri-
axial cell than in the direct shear apparatus, or/and ii) the direct shear creep experi-
ment cannot be properly interpreted due to the various unknowns in the testing

setup (i.e. stress distribution along the sample, orientation of the principal stress axes, thickness of the deforming layer; compare with Thornton & Zhang 2003).

The back calculation concentrated on the variation of the viscosity value $\bar{\mu}$ (for Newton, Bingham, original and modified Norton) and the rate factor A (for original and modified Vulliet-Hutter), while the other model input material parameters (exponent m, friction angle φ and cohesion c) were constantly assigned with the triaxial laboratory values. The latter represents a strong simplification, since it is a priori presumed that these parameters (m, φ, c) are scale-independent and, thus, directly transferable to the in situ conditions.

In order to fit the predefined deformation rate of 0.1 mm/month at groundwater low stand, the back calculated viscosities in the Newton, Bingham and Norton models must be up to five orders of magnitude higher than determined in the laboratory. The rate factor used in the modified Vulliet-Hutter model must be up to three orders of magnitude lower than determined in the laboratory. Both higher viscosity values and lower rate factors indicate a higher creep resistance of the material than observed in the laboratory. This is reasonable, since the laboratory creep tests were conducted on very fine-grained shear zone material which is not representative for the inhomogeneous shear zone comprising also significant portions of gravel and boulder-sized components. Therefore, the bulk in situ creep resistance might be considerably higher than observed in the laboratory.

In contrast, the analysis results from the triaxial creep test based original Vulliet-Hutter parameters are inconsistent with this trend. They indicate, that the rate factor must be higher, thus, the in situ creep resistance must be lower than determined in the laboratory. This can be attributed to the high exponent $m = 35$. This exponent value is based on two creep stages and thus poorly determined. Since the original Vulliet-Hutter relationship is highly sensitive in respect to the exponent (compare with Section 5.5.4), parameter uncertainties can have significant effects.

The model response on an imposed groundwater rise in the slope and, thus, reduced effective normal stresses in the basal shear zone is strongly dependent on the employed constitutive relationship. While the effective stress based constitutive models predicted a significant velocity increase, the deviatoric stress based models exhibited hardly any change. Consequently, in both the forward and back analyses, the different underlying constitutive models showed a prominent impact on the modelling results. Similar findings are documented in Schneider-Muntau (2012).

The geometry variation in terms of the thickness of the viscous layer and different kinematic mechanisms played a minor role. The uncertainty with respect to the location and thickness of the actively deforming layer has therefore no major impact on the modelling results.

The velocity increase from low and high groundwater conditions was best reproduced with the modified Vulliet-Hutter constitutive model. This is in accordance with the results of Schneider-Muntau (2012) who used the modified Vulliet-Hutter constitutive relationship in a Finite Element environment.

A more advanced back calculation would require a multi-parameter-calibration of all model components i.e. rate factor, exponent and strength parameters. Furthermore, a more sophisticated szenario including the detailed piezometric trend in the slope during the year would be beneficial.

6.2.9   Case study conclusions

The key observations of the Beauregard rockslide analysis with CrEAM are:

▪ The CrEAM application with laboratory creep parameters generally overestimates the slope creep velocity up to five orders of magnitude. Accordingly, the creep resistance measured in the laboratory is too low. This can be attributed to the laboratory limitations (specimen size, maximum grain size). The tested material is therefore not representative for the complex and inhomogeneous architecture of the shear zone. In order to replicate the measured slope velocities, the in situ creep resistance must be up to five orders of magnitude higher than observed in laboratory testing.

▪ The rockslide geometry including the kinematic mechanism and the thickness of the viscous layer plays a minor role for the modelled slope velocity.

▪ The model response on an imposed groundwater rise in the slope is strongly dependent on the employed constitutive relationship. The effective stress based constitutive models (original and modified Vulliet-Hutter) predict a significant velocity increase while the deviatoric stress based models (Newton, Bingham, Norton) show hardly any change. The velocity increase from low and high groundwater conditions was best reproduced with the modified Vulliet-Hutter constitutive model.

6.3 The Utiku landslide (New Zealand)

6.3.1 Introduction

The Utiku landslide is located in the central North Island of New Zealand, about 7 km south of Taihape (Figure 6.16). The landslide is crossed by both the State Highway 1 (SH1) and the North Island Main Trunk Railway Line (NIMT), which are first-order transportation routes connecting Auckland in the north with the capital Wellington in the south.

The Utiku landslide affects an area of about 800,000 m² and consists of two parts: a historically active part, and a historically inactive part (Massey 2010; Figure 6.17). The active landslide portion is about 1,000 m long, extending from the headscarp along the State Highway 1 in the north to the Hautapu River in the south, and is about 400 m wide. The active landslide mass involves about 2.2 million m³ of weakly indurated marine sedimentary rocks (Massey et al. in press).

Massey (2010) describes the Utiku landslide as a complex, reactivated, translational rock slide-earth flow, following the classification of Cruden & Varnes (1996), and as a block slide following the classification of Panet (1969). Movements occur along a fully developed basal shear zone. The movement rates are typically extremely slow to very slow following Cruden & Varnes (1996).

The landslide has been under observation since the 1930's and was the subject of several detailed investigations after a major reactivation in 1964 (Belz 1967; Ker 1972; Stout 1977). Since then, the Utiku landslide has been intermittently active with resulting damage to the highway and railway lines.

6.3.2 Geology and geomorphology

The Utiku landslide developed in Tertiary-age marine sediments (early Pliocene, 3.6 to 5.3 million years ago), at the stratigraphic boundary between the Tarare Sandstone and the underlying Taihape Mudstone (Massey 2010). Both lithologies are characterised as extremely weak to weak.
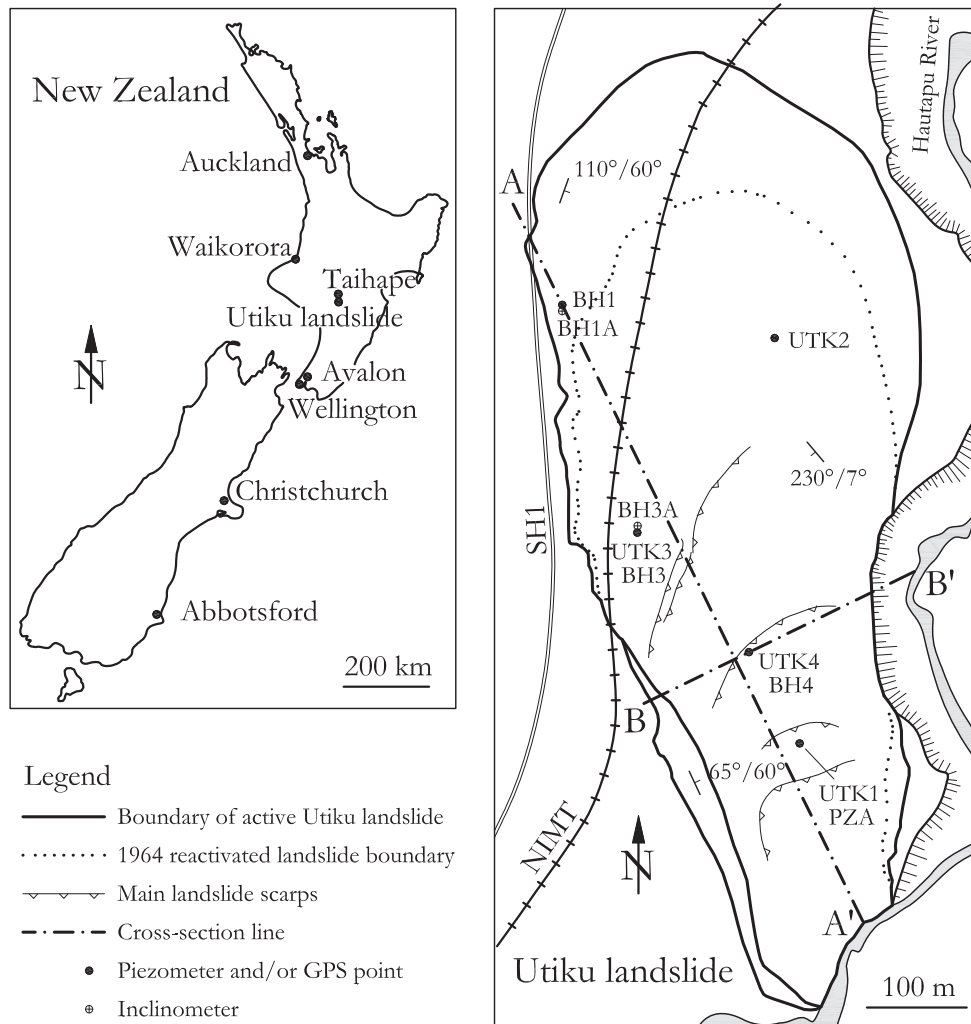
Figure 6.16
The location of the Utiku landslide in New Zealand (left) and a map
showing the extent of the active landslide mass, location of the GPS
monitoring points and piezometers, and inclinometer positions (right).
A-A' and B-B' denote the traces of the cross-sections in Figure 6.23.
(modified after Massey 2010)

The Tarare Sandstone is a massive, very fine-grained silty sandstone, with rare ovoid
cobble and boulder-sized calcareous concretions. The transition to the underlying
more silty Taihape Mudstone is characterised by several thin soft clay seams, which
are assumed to represent volcanic ash depositions. Detailed descriptions of the
lithologies are given in Massey (2010).
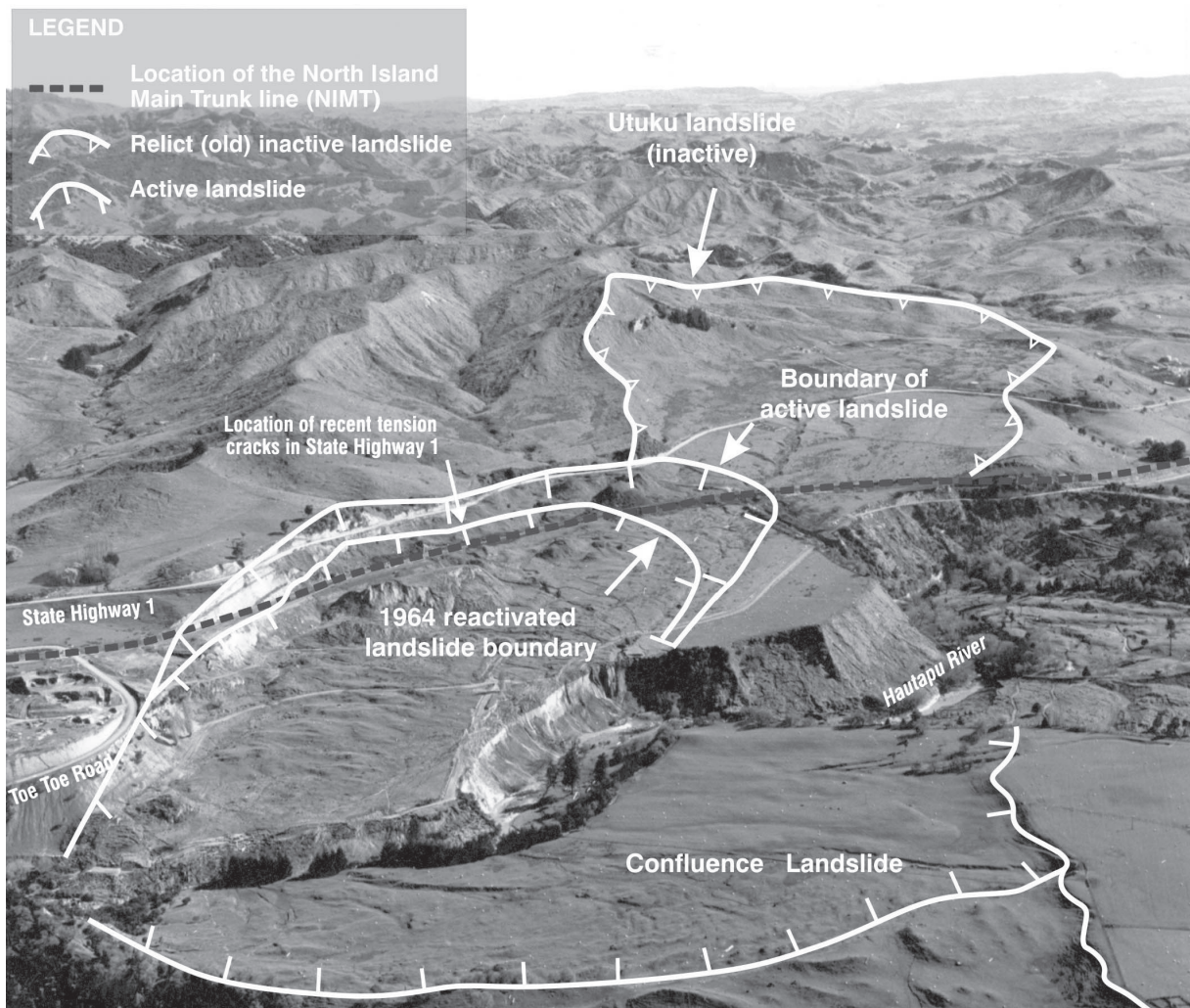
Figure 6.17
Aerial oblique view taken in 1965 with indicated boundaries of the active and passive Utiku landslide. The state Highway 1 and the Rail Trunk Line (denoted by the dashed line) cross the scarp region of the presently active part. A similar landslide (Confluence landslide) is developed on the opposite site of the Hautapu river (from Massey 2010; original photo source: GNS Science).

Due to east-west crustal compression and gentle folding, the bedding planes of the depositional succession are now found slightly inclined with a dip of approximately 3°-7° towards the south-southwest (230°). The weakly indurated marine sedimentary rocks are deeply incised by the Hautapu River and its tributaries.

In the Utiku area, the thickest of the clay layers (about 50 mm thick) at the stratigraphic boundary between Tarare Sandstone and Taihape Mudstone outcrops along the Hautapu River and acts as the major basal shear zone of the Utiku landslide mass, as shown by inclinometer measurements (Massey 2010).

The shear zone is at or near ground level along the eastern edge of the landslide and deepens westward. At the toe, the shear zone daylights at the Hautapu River on the eastern edge and dips below it in the west. The material can be described as a dark grey, soft (highly plastic), silty clay (Massey 2010). The layer was also found in six boreholes conducted in the landslide mass in 2008. Three-point solutions between the drillings BH1, BH2 and BH3 respective BH2, BH3 and BH4 indicate that the basal shear zone is planar, with a dip direction/dip of 230°/7° and very little variation across the landslide (Massey et al. in press).

On the western side, the landslide mass is confined by a steeply (45° to 60°) east-northeast (65°) dipping lateral scarp. Together with the landslide headscarp, orientated east-southeast (110°), the gently dipping clay layer and the steep lateral scarp release a wedge-shaped rock body. For deformations occurring on these bounding surfaces, the mass is kinematically constrained to move parallel to the intersection line formed by the lateral scarp and the bedding plane (dip direction/dip 154°/2°; see Figure 6.18).

Based on geomorphology and movement characteristics, Massey (2010) divided the active part of the Utiku landslide into two zones, i.e.

- an upper zone with displaced but relatively intact blocks of Tarare Sandstone; and

- a lower zone being composed of mainly remoulded material of Tarare Sandstone, dissected by numerous secondary scarps and tension cracks.

Mechanically, the larger volume of the landslide is characterised by slow translational block sliding on a thin clay layer (upper and middle parts), while the toe of the landslide close to the Hautapu River is a highly active zone which can be classified as an earth flow (Cruden & Varnes 1996).
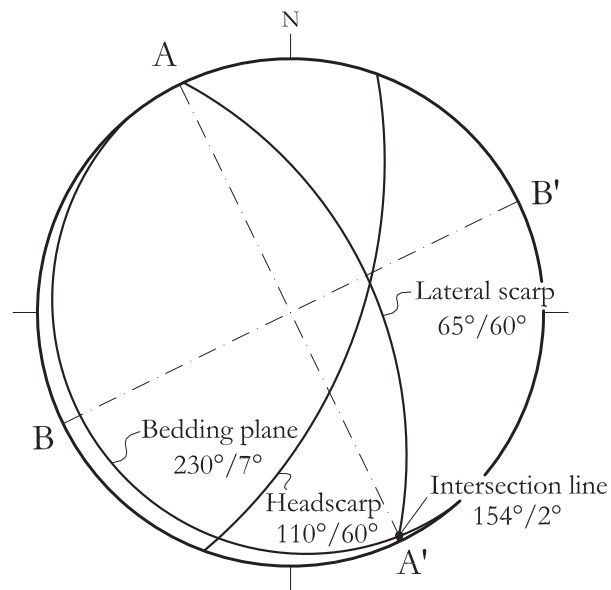
Figure 6.18
Main bounding surfaces of the Utiku landslide in the stereographic lower hemisphere projection. A-A' and B-B' denote the orientation of the cross-sections in Figure 6.23.

6.3.3 Monitoring

The Utiku landslide has a long history of monitoring (1930 until present) as it has continuously damaged the State Highway 1 and the North Island Main Trunk Line. Due to a major reactivation event in 1964, numerous detailed ground investigations (exploration drillings, piezometric measurements, and geodetic monitoring) were carried out. This reactivation was attributed to high pore pressures (Belz 1967). The landslide activity decreased between 1973 and 1990. Since 1991, subsidience of the State Highway has been documented (Massey 2010). A detailed monitoring program was setup by GNS Science in 2008, including surface monitoring via continuous GPS, subsurface monitoring via inclinometers, and piezometric monitoring of porewater pressures close to the basal shear zone. Detailed descriptions of the measurement equipment, data collection and processing is given in Massey (2010) and summarized below.

6.3.3.1 GPS monitoring

Since June 2008, four continuous GPS receivers have been operated on the Utiku landslide to monitor the surface movements. The measurements take place every 30 seconds and are averaged over 24 hours (Massey 2010). This high resolution monitoring enables detection of the spatial and temporal variability of slope deformation rates.

Massey (2010) determined the average horizontal motion bearings of the displacements vectors for each GPS station, using an observation period of 16 months, from July 2008 to October 2009. The bearings were found to be about 145° in the upper and middle landslide portion (UTK 2, UTK3 and UTK 4) and 155° in the lower landslide portion (UTK1). These directions coincide well with the bearing of the intersection line of the basal slip surface and the lateral western scarp, i.e. 154°.

In the monitoring period from July 17, 2008 to February 4, 2011, the largest displacement was recorded at the toe of the landslide, i.e. at GPS station UTK1 (27 cm in about 31 months). Smaller displacements were recorded in the upper and middle part of the landslide in the same period, i.e. 22 cm at UTK2, 18 cm at UTK3, and 20 cm at UTK4. The calculated average horizontal displacement rates for the monitoring period range between 0.30 mm/d (11 cm/yr) for the landslide toe and 0.19 - 0.24 mm/d (6.9 - 8.8 cm/yr) for the middle and upper part. This classifies the Utiku landslide as extremely slow to very slow according to the classification scheme of Cruden and Varnes (1996; 1.6 cm/yr < x < 1.67 m/yr). The different displacement behaviour of the toe and the higher slope portion reflects the composite nature of the landslide as highlighted in the previous section, i.e. a translational block slide in the upper and middle part, and a highly active earth flow in the lower part.

Figure 6.19 depicts the cumulative horizontal displacements of the four continuous GPS monitoring points on the landslide mass (UTK1 to UTK4). The high resolution measurement series reveal that the slope displacement rates fluctuate in time, indicated by the variable gradients of the cumulative displacement curves. The respective velocity plots in Figure 6.20 show that slope displacement rates range from negligibile to 15 mm/d.
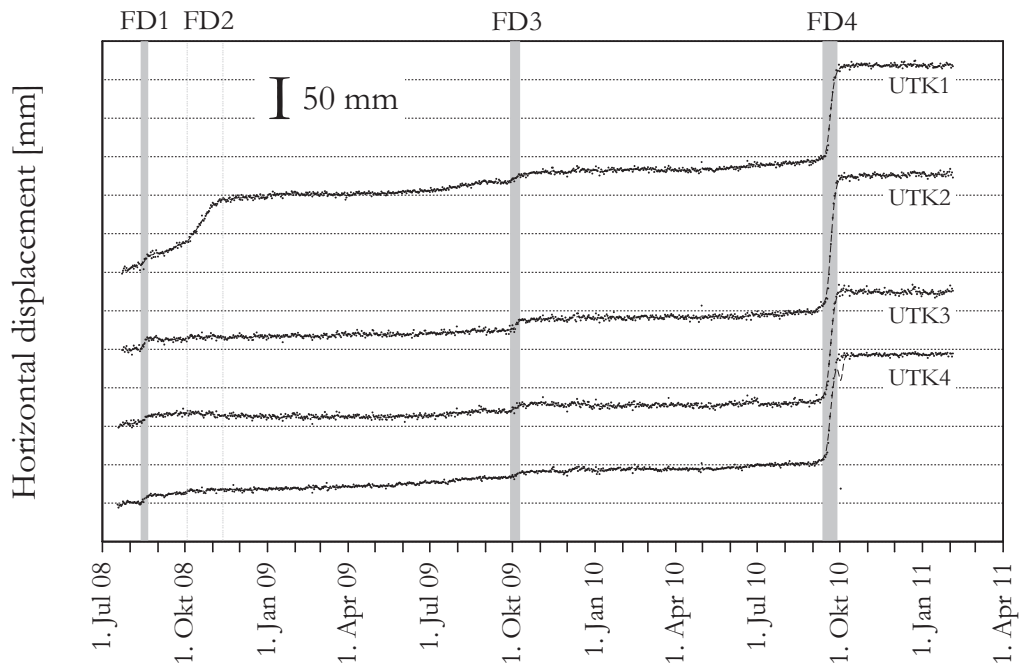
Figure 6.19
Cumulative horizontal displacements recorded at the Utiku landslide by continuous GPS measurements at the points UTK1, UTK2, UTK3 and UTK4 (from July 2008 to February 2011). Grey vertical lines indicate periods, when faster displacements were observed at all monitoring points.

Massey et al. (in press) performed a detailed analysis of the displacement data and interpreted three main types of motion:

- Faster displacement: short duration, relatively rapid motions, with typical duration of days to weeks, resulting from deformation in the basal clay seam as recorded by borehole deformation surveys;

- Slower displacement: longer duration slower motions typically lasting many months to years, involving both displacement in the basal clay layer and internal deformation of the landslide mass; and

- Seasonal cyclic displacement: Seasonal reversible deformations which correlate with the groundwater conditions in the slope; they are interpreted as downslope movements and upslope rebound due to swelling of the involved materials during the wetter winter months and shrinking during the dryer summer months, respectively.
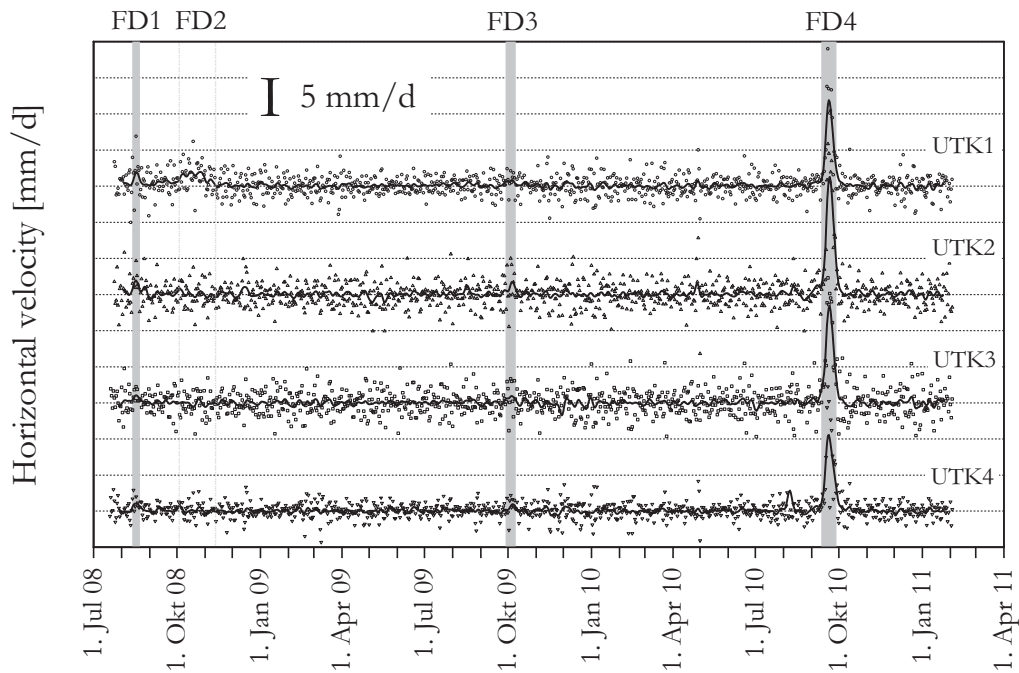
Figure 6.20
Horizontal displacement rates derived from the continuous GPS measurements. Markers show the raw time derivative of the cumulative displacements, bold lines indicate the smoothed data. Grey vertical lines indicate periods, when faster displacements were observed at all monitoring points.

At least four statistically significant periods of faster displacement (FD) are discernable on Figure 6.19 and Figure 6.20. Three of them were recorded at all GPS stations (events FD1, FD3 and FD4), while one event (FD2) was only observed by the GPS station at the landslide toe (UTK1). FD2 is hence interpreted as a local event at the landslide toe, and is thus not considered in the further considerations. The three faster displacement phases involving the entire landslide mass took place from:

- 15/08/2008 to 22/08/2008 (FD1)
- 30/09/2009 to 10/10/2009 (FD3)
- 15/09/2010 to 29/09/2010 (FD4)

For these events, the faster displacements were simultaneous in all measurement points. Generally, the landslide mass velocity increased relatively rapidly, then velocities became steady, followed by rapid velocity decrease.

The magnitudes of maximum velocity were similar for the events FD1 and FD3, while the last recorded faster displacement event FD4 showed significant higher velocities (Figure 6.20). It is further notable that faster displacement in all three cases occurred in early spring.

6.3.3.2 Inclinometer monitoring

Inclinometers were installed in two boreholes located in the upper and middle part of the Utiku landslide, on the western edge of the landslide, where the sliding mass reaches its maximum depth. Readings were started in July 2008 and conducted every three months, or when a significant movement had been noted. The cumulative deflection profiles detect the actual displacement characteristics of the landslide mass in depth. Moreover, the inclinometer data verify the results from GPS surface monitoring.

Figure 6.21 shows the data of the inclinometer BH3A from July 9 to November 11, 2008. The depicted monitoring period comprises the first observed faster displacement event (FD1). The deflection profiles show strain localisation in a 4 cm thick shear zone at 49.5 m depth from the top of the inclinometer, which correlates with the thickness and depth of the clay layer found in the drilling (Massey 2010).
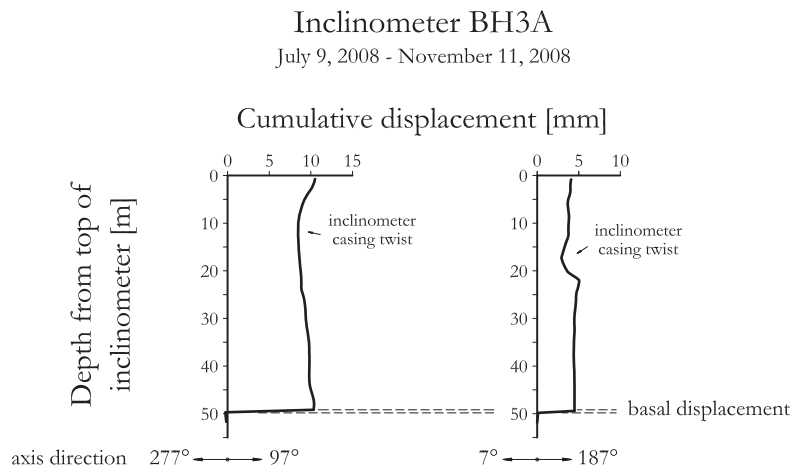
Figure 6.21
Cumulative deflection profiles along the two axes of measurement at the inclinometer BH3A. The sinusoidal-shaped gradients from 0-35 m are attributed to an casing twist as a result of movement. The inclinometer location is shown in Figure 6.16 (modified after Massey 2010).

6.3.3.3 Groundwater monitoring

The Taihape-Utiku area is characterised by low seasonal variations in precipitation, with mean monthly rainfalls of 70 mm in winter and 81 mm in summer. The average annual rainfall is 960 mm (Massey 2010). Nevertheless, the Utiku landslide was reported to be highly sensitive to changing groundwater conditions.

Standpipe piezometers were installed in five boreholes in the landslide mass (BH1, BH2, BH3, BH4 and PZA), with response zones located at the depth of the clayey shear zone. Measurements were taken automatically at 5-minute intervals, aiming to track the pore pressure changes in the basal shear layer following precipitation. The piezometers BH1, BH3, BH4 and PZA are located on the western (and thus deepest) part of the landslide, from the landslide scarp area to the lower landslide portion.

Figure 6.22 shows the pore pressures measured close to the basal shear zone for the monitoring period from August 3, 2008 to February 4, 2011. The data indicate that pore pressures vary in the range of maximum 30 kPa (Massey 2010), and exhibit a clear seasonal pattern, with maximum values in spring and minimum values in autumn.

The high temporal resolution of the piezometric data enables changes in the pore pressures to be correlated with landslide displacement. A comparison of piezometric and surface displacement data attest, that increased velocities in spring roughly coincide with pore pressure peaks. However, in more detail, Figure 6.22 reveals that movements take place slightly before the actual pore pressure peaks.

The level of the phreatic surface was not monitored and, therefore, no information about the degree of slope saturation in time is available. Periodical artesian spring phenomena within graben structures on the landslide surface however indicate confined groundwater conditions, in which the Tarare Sandstone block might act as the confining layer (pers. comm. Chris Massey).
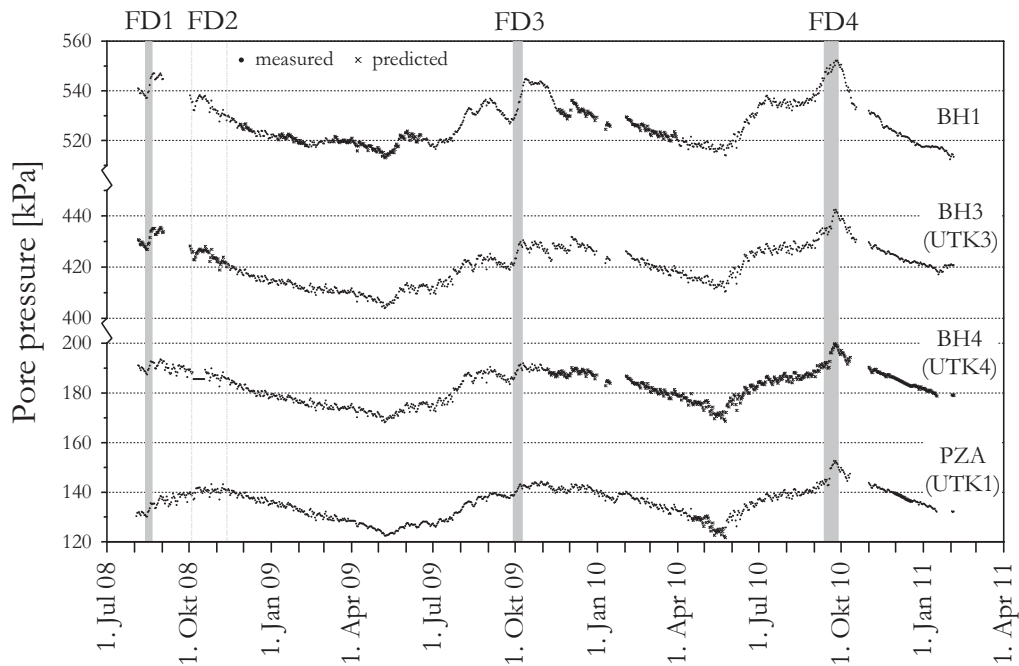
Figure 6.22
Porewater pressures in the standpipe piezometers BH1, BH3, BH4 and PZA on the western part of the Utiku landslide. Missing data were interpolated with neighbouring measurements. Grey vertical lines indicate the periods of faster displacements detected by the GPS measurements.

6.3.4 Laboratory testing

Strength parameters of the clay layer forming the shear zone of the Utiku landslide were obtained by laboratory testing, using core samples from drill holes carried out in 2008. The material was tested by consolidated drained ring shear experiments in the GNS Science laboratory in Avalon.

The testing results showed no post-peak drop in shear strength, indicating that the clayey material is not subject to softening behaviour. The Mohr-Coulomb strength parameters were $\varphi = 8.3°$ and $c = 4$ kPa (Massey 2010). Similar results were found by Kilsby (2007) for undisturbed field samples taken from the adjacent Confluence landslide, which is located on the opposite side of the Hautapu River and moving on the same clay layer as the Utiku landslide.

Mineralogical investigations on similar clayey material indicate that the material is composed of silty sandy clay with 30-35% smectite matrix (Reyes 2007). The high content of smectite minerals suggests a high sensitivity to water. No creep experiments have been carried out with the clay material. Therefore, no information about the time dependent behaviour of the material is available.

The strength properties of the Tarare Sandstone, both intact bedrock and landslide debris, were characterised by triaxial and ring shear tests, respectively. The parameters are listed in Table 6.10.

Table 6.10
Overview of the Mohr-Coulomb shear strength parameters of the materials involved in the Utiku landslide (from Massey 2010).

Material	Test	Friction angle	Cohesion
Clay, basal shear zone	Ring shear	$\varphi = 8.3° \pm 1°$	$c = 4 \text{ kPa} \pm 6 \text{ kPa}$
Tarare Sandstone, intact bedrock	Triaxial	$\varphi_{peak} = 45° \pm 10°$	$c_{peak} = 300 \text{ kPa} \pm 50 \text{ kPa}$
Tarare Sandstone, landslide debris	Ring shear	$\varphi_{peak} = 28° \pm 5°$	$c_{peak} = 0$

6.3.5   Landslide geometry

The geometry of the Utiku landslide is a slim procumbent wedge, which is formed by essentially three persistent planes:

▪ a slightly inclined, low-strength clay layer, forming the major motion surface of the wedge (dip direction/dip 230°/7°);

▪ a steep lateral scarp (65°/60°) cutting through Tarare Sandstone and orientated roughly perpendicular to the clay layer; this lateral scarp confines the wedge to the west, forcing the body to move parallel to the two planes intersection line rather than in the clay layer dip direction; and

▪ a steep headscarp, orientated 110°/60°, cutting through Tarare Sandstone and releasing the landslide mass on the upper slope.

Cross-section A-A'

NNW   SSE

landslide retrogression

1964 reactivated landslide boundary

SH1   BH1   NIMT   BH3, UTK3   BH4, UTK4 cross section B-B'   PZA, UTK1   Hautapu River

head scarp

clay layer

50 m

Cross-section B-B'

WSW   ENE

lateral scarp

BH3, UTK3   BH1, cross section A-A'   BH4, UTK4   PZA, UTK1   Hautapu River

clay layer

50 m
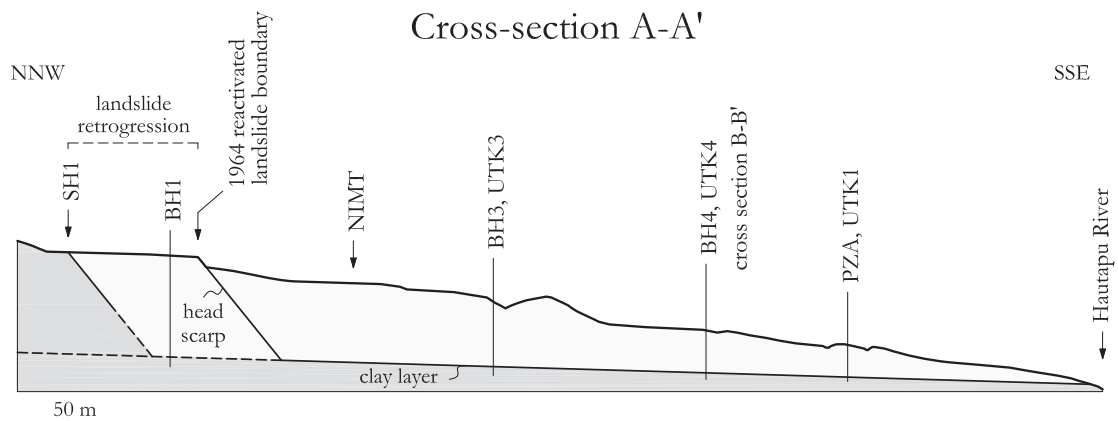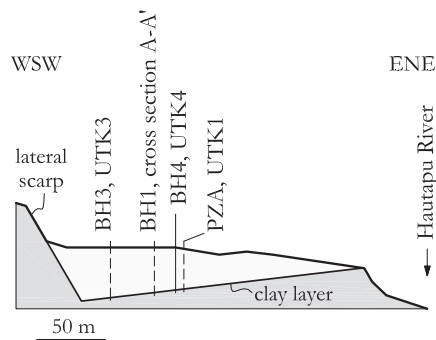
Figure 6.23
Longitudinal (A-A') and transverse (B-B') cross-sections through the Utiku
landslide mass. Section traces are orientated parallel and perpendicular to the
wedge intersection line (refer to Figure 6.16 and Figure 6.18).

These three surfaces confine a wedge-shaped rock body with a gently increasing
thickness from the toe to the headscarp and from east towards west. Longitudinal
and transverse cross-sections through the landslide, orientated parallel and perpen-
dicular to the direction of movement, are shown in Figure 6.23. The intersection
line formed by the clay layer and the lateral scarp is orientated dip direction/dip
154°/2°; the released rock volume is kinematically constrained to move parallel to it.
This is consistent with the observed motion bearings of 145°-155° inferred from the
GPS monitoring.

The shear resistances on the releasing planes are very different. Both the lateral and the headscarp of the Utiku landslide are developed in massive Tarare Sandstone. These shear surfaces are assumed to comprise comminuted sandstone developed during the former displacements of the landslide. Tarare Sandstone landslide debris is characterised in the laboratory with a moderate friction angle of 28°. The clayey material in the bedding-parallel shear zone was sampled from drilling cores. Ring shear testing results indicate, that the material is in situ at residual strength with a very low friction angle of 8°. Both materials exhibit no or a negligible cohesion (Table 6.10).

Figure 6.24 shows a graphical wedge analysis in the stereographic projection. The hatched area indicates the safe zone for the resultant force to plot, for the landslide wedge to be stable. Two szenarios are evaluated: i) the lateral scarp without friction, and ii) the lateral scarp with $\varphi = 28°$. The 3D-analysis indicates that friction in the lateral scarp significantly enlarges the safe zone and, thus, has a clear effect on landslide stability.
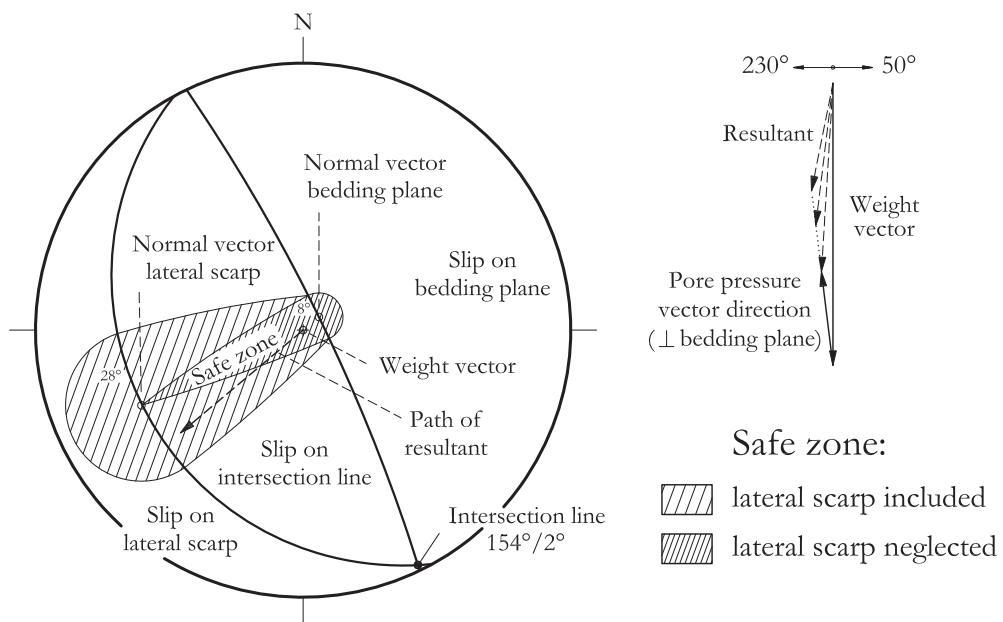
Figure 6.24
Wedge stability analysis in the stereographic projection. The dashed line marks the path of the resultant force when the pore pressure in the basal shear zone increases.

In the following, the landslide stability and deformation analyses are performed on a two-dimensional cross-section parallel to the motion direction of the landslide mass (cross-section A-A', Figure 6.23). Any strength developed in the western lateral scarp is neglected, although this assumption represents a clear simplification of the three-dimensional problem.

6.3.6   Stability analysis

For the two-dimensional stability analysis the Simplified Janbu method is applied. The friction angles of the headscarp and the clay layer are assumed with 28° and 8°, respectively, in accordance with the ring shear testing results. The cohesion of both materials is small and thus neglected.

The specific weight of the Tarare Sandstone, forming the bulk landslide mass above the slip surface, is assumed with 21 KN/m³, according laboratory values from Read & Miller (1990). The whole slope is assigned the same specific weight, as no specific information about the groundwater level and, thus, saturation is available. The porewater pressures measured at different points of the basal shear zone are directly introduced in the model. Between the points, pore pressure values are linearly interpolated.

In order to evaluate the impact of the changing piezometric conditions on the slope stability, the pore pressures are varied according the piezometric measurement results. The two-dimensional analysis yields for all conditions a state of the slope close to limit equilibrium. The detailed stability analysis results over time are shown in Figure 6.25. The calculated Factor of Safety values range between η =1.06-1.07 for the low porewater pressures in autumn months, and drop below η =1.01 for the maximum observed porewater pressure values in spring 2010. Hence, Factor of Safety minima correlate with porewater pressure maxima.
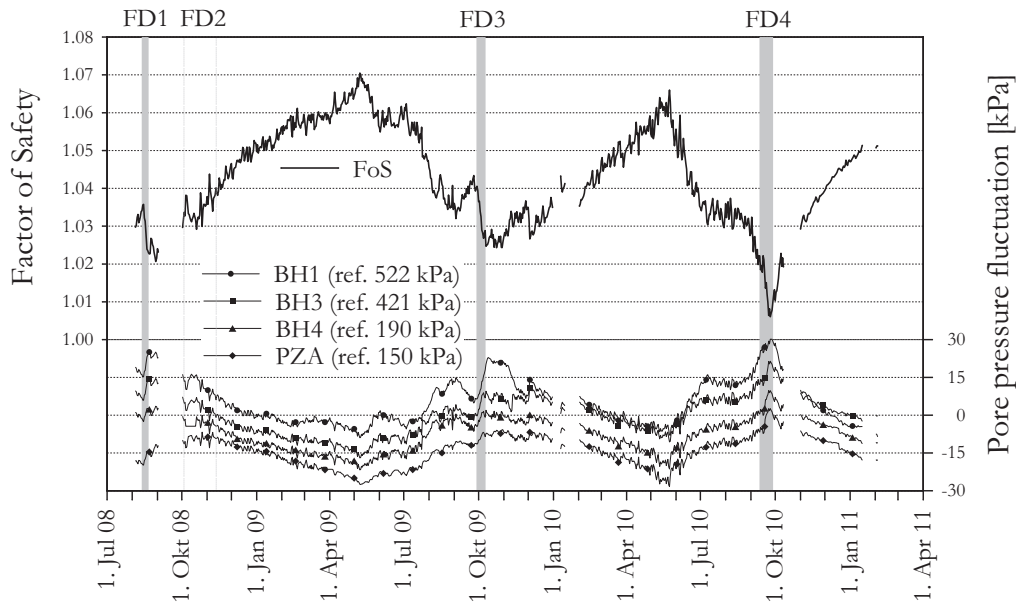
Figure 6.25

Results of the Factor of Safety calculation. Grey vertical lines indicate the
periods of faster displacements detected by the GPS measurements.
Relative pore pressure changes are shown in the bottom as a reference.

6.3.7 Creep analysis using CrEAM

The relationship between the porewater pressure fluctuations and the displacement
behaviour of the Utiku landslide is investigated with the effective stress based calcu-
lation scheme for translational slides (E-CrEAM*trans*). The aim is to reproduce the
measured displacement characteristics of the landslide based on the changing pie-
zometric conditions in the slope. As the viscous behaviour of the basal shear zone
material has not been investigated by laboratory tests and, thus, no viscous parame-
ters are available for the direct model input, a back analysis is performed.

The relationship between the in situ effective stresses and the time dependent de-
formation in the basal shear zone is formulated by the modified Vulliet-Hutter rela-
tionship. This constitutive model accounts for both the deviatoric and hydrostatic
stress conditions. It is therefore suitable for investigating the effects of pore pres-
sure fluctuations.

The basal shear zone is assumed 50 mm thick, which represents an average value for the thickness of the clay layer. Based on the observed horizontal displacement rates and the measured porewater pressures, the in situ viscous parameters of the shear zone, i.e. the rate factor $A^{VH_{MC}}$ and the exponent $m^{VH_{MC}}$, are back calculated by a heuristic (trial-and-error) process. An adequate parameter set was approximated with a rate factor of $A^{VH_{MC}} = 5.6 \cdot 10^{-9}$ s^{-1} and an exponent $m^{VH_{MC}} = 220$.

The back calculated creep velocities for the period July 2008 - February 2011, as well as the underlying relative pore pressure fluctuations are shown in Figure 6.26. Therein, the velocity peaks coincide with the pore pressure maxima. By contrast, the modelled velocity peaks do not precisely correlate with the observed velocities peaks, as the latter precede the pore pressure peaks.
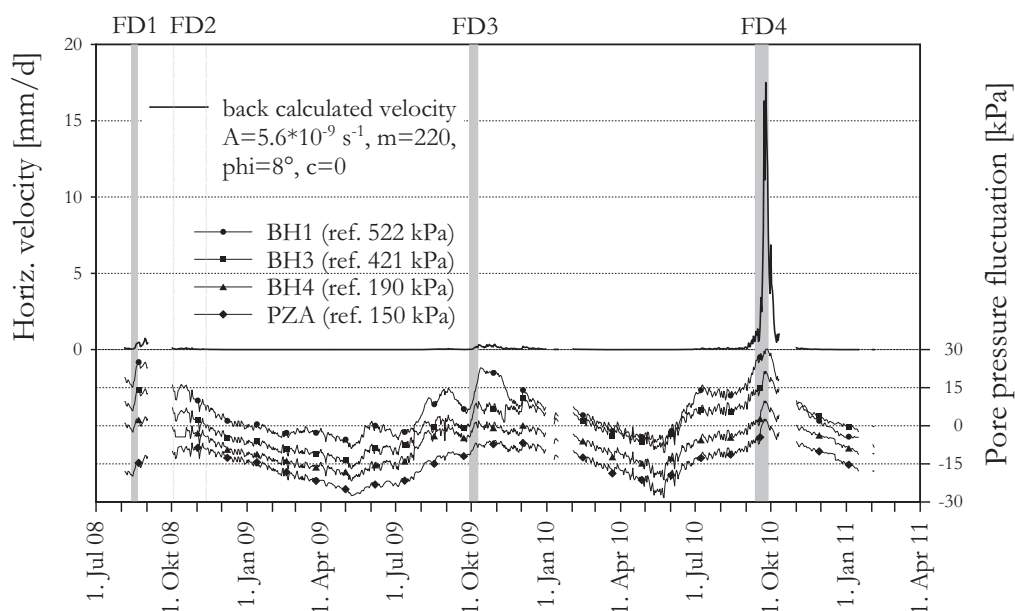
Figure 6.26
Top: Modelled horizontal velocities of the Utiku landslide in time, using E-CrEAM^{trans}. Bottom: Relative pore pressure fluctuations.

A detail of the observed and modelled velocities during the seasonal pore pressure maximum and the associated increased activity of the landslide in September 2010 (FD4) is depicted in Figure 6.27. The shape and the magnitude of the observed and modelled velocity peaks are similar. However, the modelled peak velocity follows the observed peak velocity with a time lag of 4-6 days.
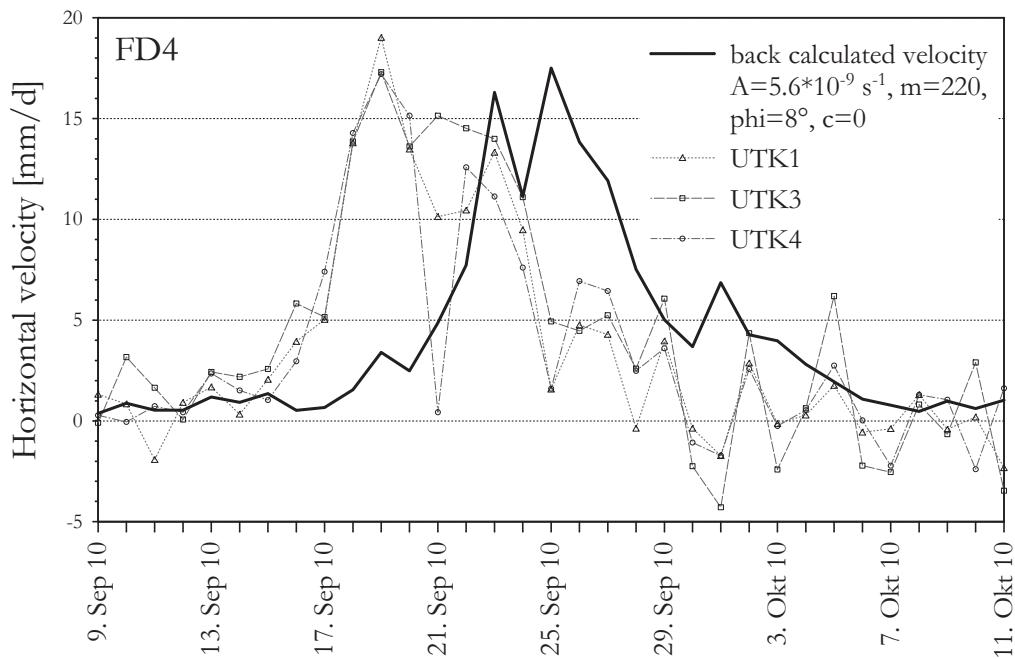
Figure 6.27

Detail of the modelled and observed horizontal velocities at the three
GPS points along the cross section A-A' (UTK1, UTK3 and UTK4).
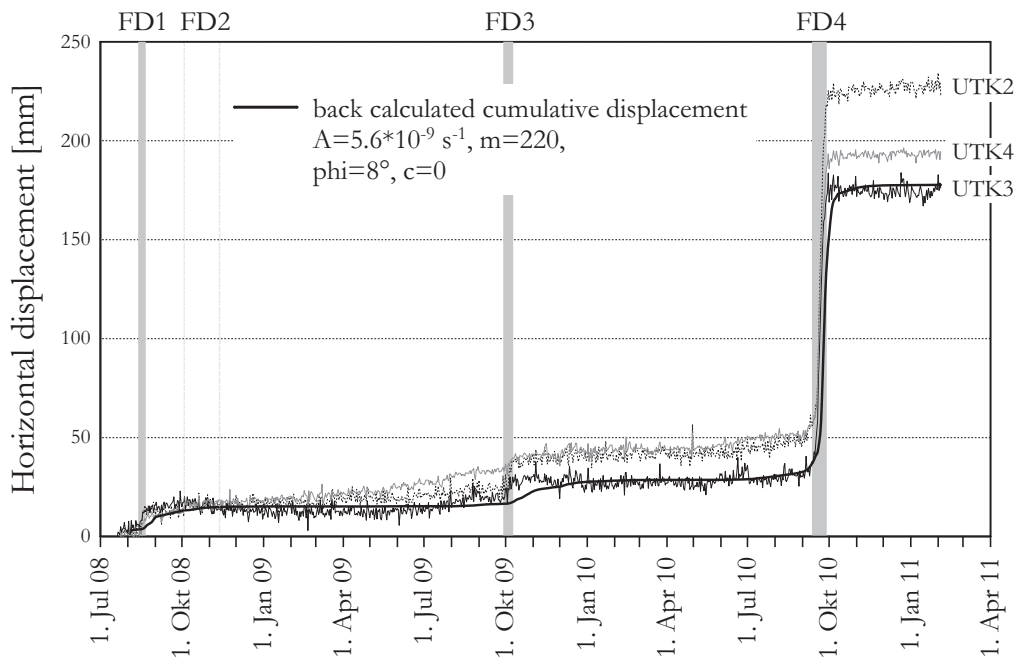
Figure 6.28

Cumulative horizontal displacement as observed by GPS monitoring and
back calculated with E-CrEAM*trans*.

Figure 6.28 shows the modelled cumulative horizontal displacement of the landslide obtained by integration of the calculated velocities over time. The overall displacement characteristics as recorded by high-resolution GPS measurements is well reproduced. However, the time lag between observed and modelled enhanced landslide activity is notable.

Figure 6.29 shows the results of a parameter sensitivity study with respect to the viscous parameters $A^{VH_{MC}}$ and $m^{VH_{MC}}$. Therein, each parameter set was fitted to yield the same final cumulative displacement for the considered time period.
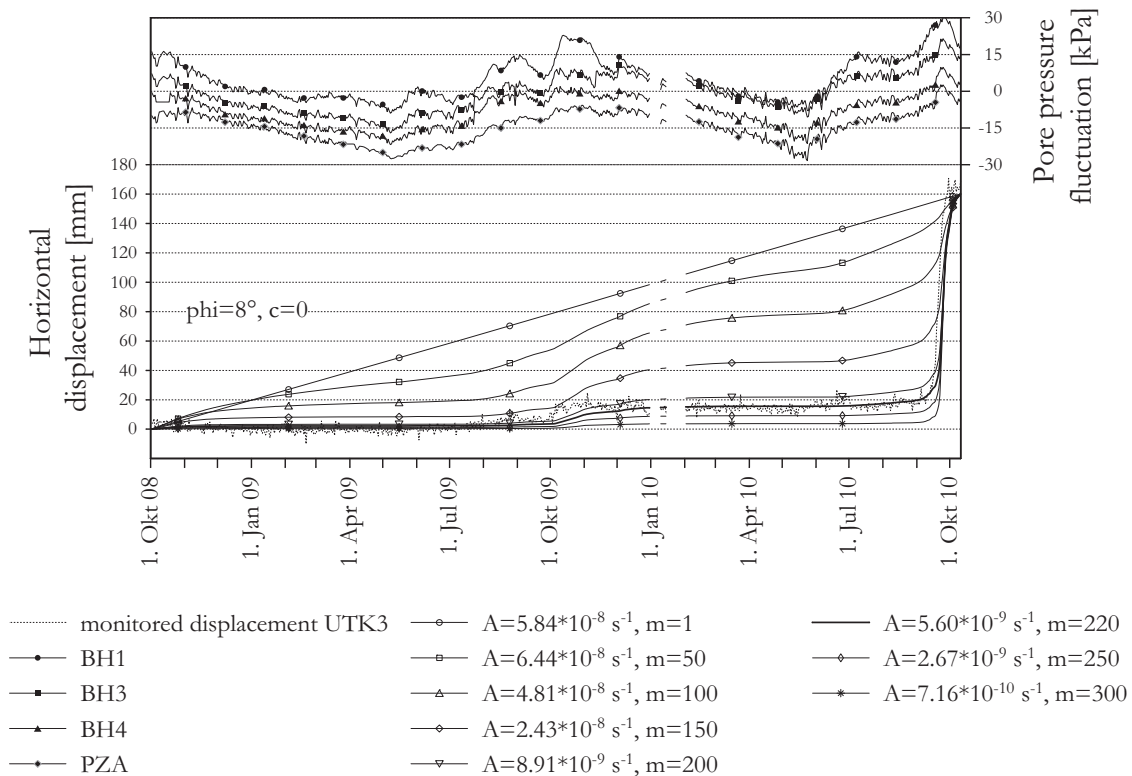
Figure 6.29
Parameter sensitivity study of the CrEAM back calculation with respect to the rate factor $A^{VH_{MC}}$ and the exponent $m^{VH_{MC}}$.
Top: Relative pore pressure fluctuations as monitored in the landslide.
Bottom: Model results using different parameter sets, depicted as cumulative displacements plots.

The parameter set with exponent $m^{VH_{MC}} = 1$ assigns a linear relationship between strength mobilisation (i.e. the ratio of shear stress and shear strength) and strain rate. This assumption yields hardly notable velocity variations, based on the observed pore pressure fluctuations of 30 kPa. The model results show a semi-linear cumulative displacement plot. With rising exponent, the velocity variations caused by the fluctuating pore pressures increase, leading to open S-shaped displacement curves. The high value for the exponent $m^{VH_{MC}} = 220$ as approximated in order to fit the observed displacement pattern (e.g. at GPS point UTK3) reflects an extremely high nonlinearity of the stress-strain rate relationship. The latter induces a high sensitivity of landslide activity to changes in effective stress conditions.

6.4   Case study discussion

The 3D-geometry of the Utiku landslide was investigated with a two-dimensional cross-section parallel to the main path of motion. The stability analysis using the Simplified Janbu approach yields for all conditions a state of the slope close to limit equilibrium. This is in accordance with the findings of Massey (2010), who evaluated the stability of the Utiku landslide using the approach of Morgenstern & Price (1965) and different assumptions for the interslice force angle. These results indicate that the selected interslice force angle function does not significantly affect the magnitude of the Factor of Safety. The Factor of Safety timeseries calculated in this work can be considered to be conservative, as i) the Simplified Janbu approach does not account for any internal strength of the sliding mass; and ii) the shear resistance developed in the western lateral scarp is not taken into account in the calculations.

The analysis of the Utiku landslide with CrEAM investigated the relationship between the pore pressure fluctuations and the displacements occurring in the basal shear zone. No creep experiments were conducted with the clayey material of the shear zone and, therefore, no forward calculation of displacement rates was conducted with CrEAM. According the back calculation results, the clayey material is highly sensitive to pore pressure fluctuations. As the basal shear zone is saturated at all stages, the sensitivity arises from changing effective stresses rather than from water adsorption of the smectite minerals.

The back calculation with the effective stress based CrEAM using the modified Vulliet-Hutter constitutive relationship replicates both the long term slow displacement behaviour of the landslide as well as the short term faster displacements.

Modelled velocity peaks coincide with pore pressure maxima in the basal shear zone. However, the high temporal resolution of both the monitored geodetic and piezometric data reveals that increased slope displacement rates are not synchronous with the pore pressure maxima, but precede the latter by several days. Therefore, slope velocities rise and partially cease before the actual pore pressure peak is reached. This time lag could not be reproduced with the modelling approach applied in this study, indicating that there is at least one additional influencing process acting in the landslide system, which is not taken into account in the calculation scheme. Possible mechanisms include i) buttressing effects in the western lateral scarp; ii) a strain or strain-rate-dependency of the material behaviour in the bounding surfaces; or ii) a systematic time error in the piezometric measurements.

The lateral scarp is presumed to have an appreciable effect on the landslide displacement behaviour. Elevated pore pressures in the clay layer cause reduced effective normal stresss and, thus, reduced shear resistances in this plane, promoting dip-slip movements of the wedge towards the western lateral scarp. These movements increase the normal stress and, thus, the shear resistance in the lateral scarp, leading to a self-stabilization of the landslide mass before the pore pressure maximum is reached. A three-dimensional approach would be required in order to investigate this relationship.

6.5 Case study conclusions

The seasonal deformation behaviour of the Utiku landslide was investigated using the effective stress based Creep Equilibrium Analysis Method for translational slides (E-CrEAM^{trans}). The aim of the study was to reproduce the relationship between rainfall-triggered pore pressure rises and increased displacement rates of the landslide.

The analysis was perfomed as a back calculation by iterating on the viscous parameters in the basal shear zone. Three faster displacement events observed in a 31 month monitoring period as well as the interseasonal slower displacement of the landslide can be fitted with an acceptable precision by means of a viscous parameter set, using the monitored pore pressure fluctuations as a basis. The high back calculated exponent $m^{VH_{MC}} = 220$ indicates that the clayey material in the basal shear zone is highly sensitive to changes in porewater pressure. Laboratory creep test on the material would be desirable in order to evaluate these findings.

The modelling results show the ability of E-CrEAM^{trans} to replicate the observed acceleration and decelerations stages which result from fluctuating piezometric conditions. The model is however not able to reproduce the observed time lag of several days between enhanced slope activity and pore pressure maxima. This divergence is not yet sufficiently understood and is presumed to be caused by one or more additional influencing mechanisms which are not accounted in the applied calculation scheme.

The Utiku landslide is only one of over 7,000 mapped large landslides in Tertiary-age sedimentaty rocks in New Zealand (Dellow et al. 2005). The majority are deep-seated (depth of movement > 10 m) translational landslides with similar deformation characteristics as the Utiku landslide (Massey 2010). This study improves the understanding of the relationship between rainfall induced changes in the groundwater regime and changing displacement rates of this type of landslide, and aims to make an advance in landslide movement prediction.

CHAPTER 7

Summary and Conclusions

7.1 Preamble

In the previous decades, many creeping landslides were intensively investigated from the geological point of view, including surface mapping of geological units and geomorphological features, and subsurface investigation by means of dill-holes and adits (e.g. Agliardi et al. 2001; Ambrosi et al. 2006; Borgatti et al. 2005; Barla et al. 2005, 2010c; Kalenchuk 2010; Noverraz 1996; Schneider-Muntau 2012, Zangerl et al. 2010a,b). Moreover, long-term time series of groundwater monitoring as well as surface and subsurface survey data exist for many sites (e.g. Barla et al. 2010c; Bonzanigo et al. 2007; Carey 2011; Francois et al. 2007; Massey 2010 in press; Thüringer Fernwasserversorgung 2007; Zangerl & Engl 2009, Zangerl et al. 2010a). Much less attention has been paid so far to the geomechanical understanding of creeping landslides.

This work is dedicated to the better understanding of creeping landslide behaviour. The thesis forges a bridge connecting the time dependent rheology of geomaterials and its constitutive formulation, the principles of mechanics and the development of novel modelling algorithms to an applied landslide analysis.

The thesis is divided into two parts. The theoretical framework of the analytical approach for the analysis of creeping landslides referred to as the "Creep Equilibrium Analysis Method" is introduced in the first part. The application and evaluation of the novel methodology on two case studies is presented in the second part.

7.2 Summary of CrEAM Theory

7.2.1 Principles

The fundamental assumption of the Creep Equilibrium Analysis Method (CrEAM) is that deformation of a viscous layer under the load of a rigid hanging wall mass occurs as steady state deformation. This assumption is satisfied for landslides characterised by strain localization in a basal shear zone that exhibits constant deformation in time, and relatively stiff sliding bodies.

The displacement rate of such a system is governed by both the viscous properties and the stress distribution in the basal shear zone. The stress state is a priori unknown, since it is a function of both the geometry and weight of the overburden sliding mass and the properties of the basal shear zone. For CrEAM, the self-weight of the shear zone is neglected and, therefore, the stress state across the shear zone profile is constant.

In order to determine the stress distribution along the basal shear zone and the corresponding deformation rate of the landslide system, CrEAM combines equilibrium requirements, kinematical constraints, and constitutive relationships to a single-form algorithm. The interrelationships of these three model components of CrEAM are shown in Figure 7.1.
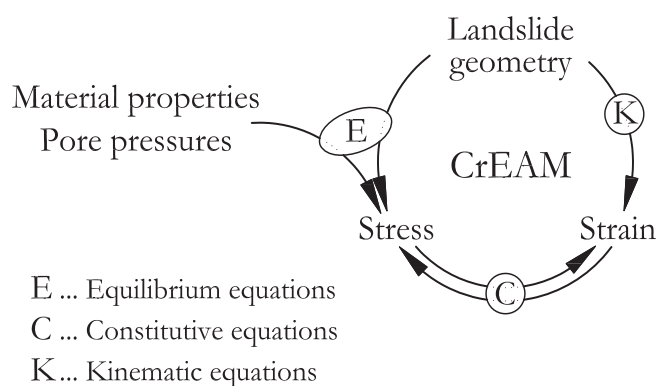
Figure 7.1
Interrelationship of CrEAM components.

For calculation purposes, the landslide system is discretized by an assembly of virtual slices. Mechanical interaction between the elements impose the system to behave as a continuum.

A crucial characteristic of the landslide analysis with CrEAM is that the geometric aspects and, thus, the kinematics of slope movement, remain constant. This is in contrast to most numerical solutions which focus on the progressive deformation evolution of a system. They thus include the geometry as a variable, which interacts with both the equilibrium and constitutive components of the model (compare with Figure 7.1). The constant geometry assumption is reasonable for CrEAM, as the approach is designed for the analysis of instantaneous and short-term behaviour of creeping landslides, where the geometry change in time is negligible.

The implemented constitutive models include both linear and nonlinear deviatoric stress based relationships as well as more advanced effective stress based relationships. Depending on the boundary conditions, the creep velocity of a slope system is determined in a straightforward or iterative calculation procedure.

7.2.2 Comparision of constitutive models

CrEAM algorithms have been developed using different viscous models, leading to a number of specific solution approaches. The implemented constitutive formulations represent different methods for describing the interrelationship between stress and creep rate in the basal shear zone (compare with Figure 7.1).

The following constitutive models were considered:

- Newton
- Bingham
- original Norton
- modified Norton
- original Vulliet-Hutter
- modified Vulliet-Hutter

The Newton and Bingham models are classical linear-viscous formulations, whereas the Bingham relationship includes an additional yield component denoting a creep threshold. The original and modified Norton models describe the stress-strain rate relationship in terms of a power law and represent the nonlinear equivalents to the Newton and Bingham formulations. Similar to the Norton approach, both Vulliet-Hutter models employ a power law formulation, but are based on a stress ratio concept and include a failure criterion in the formulation. Differences between the original and modified Vulliet-Hutter relationships arise from different failure criterion definitions.

The above constitutive models can be separated into two classes, i.e.

- deviatoric stress based models (Newton, Bingham, original and modified Norton)

- effective stress based models (original and modified Vulliet-Hutter)

The deviatoric stress based approaches relate the creep rate directly and exclusively to the shear stress in the viscous layer, while the effective stress based relationships include the normal stress as an additional influencing factor. The latter is significant for describing viscous behaviour of soils and rocks, since also the strength of these materials is strongly related to the prevailing confining normal stress.

For practical purposes, the deviatoric stress based viscous models are straightforward to use, and the corresponding CrEAM algorithms relatively simple. However, for materials whose shear resistance increases with effective normal stress, the deviatoric stress based models are not able to sufficiently describe the viscous deformation behaviour. Consequently, the associated deviatoric stress based CrEAM approaches have limited validity for dry and partly saturated shear zones as well as for saturated shear zones under fully drained conditions.

The effective stress based constitutive models involve hydrostatic and deviatoric stress components, and the corresponding CrEAM algorithms are resultingly more complex. Since the viscous models incorporate the stress-creep rate relationship in a more generic form, the effective stress based CrEAM approaches can better replicate the influences of effective normal stress variations (e.g. induced by seasonal groundwater fluctuations).

7.3 Advantages and limitations of CrEAM

CrEAM offers a relatively straightforward analysis tool for estimating the steady-state deformation characteristics of slides in soil and rock that deform in response to creep deformation within a basal shear zone.

The focus of CrEAM is global landslide behaviour. In an equivalent way to the conventional limit equilibrium methods for stability analysis, the model is based on rigid body mechanics. The approach simulates deformation of the basal shear zone, while it neglects secondary deformation processes such as the internal strain of the sliding mass and superficial processes.

The successful application of the conventional limit equilibrium methods for many decades showed that such pragmatic approaches are able to lead to relevant results if the boundary conditions of the landslide problem (geometry, material properties, groundwater conditions and pore pressures) are properly accounted in the calculations (Lang et al. 2011; Fell et al. 2000; Duncan & Wright 2005).

Similar to the limit equilibrium methods for stability analysis, CrEAM requires relatively few input parameters and is characterised by a low calculation effort. It is therefore well suited for back calculations and comprehensive sensitivity analyses. Moreover, the relatively simple concept of the approach facilitates the implementation and evaluation of different constitutive relationships. CrEAM can therefore assist in both investigating the characteristics of material models and evaluating the effects of parameter uncertainties.

The major limitations of CrEAM arise from the inherent assumptions of the approach:

▪ CrEAM is restricted to the analysis of landslides with steady-state behaviour, i.e. slopes which exhibit constant displacement rates in time under constant boundary conditions.

▪ CrEAM assumes plane strain conditions and is therefore intended for the two-dimensional analysis of slopes.

▪   The thickness of the basal shear zone should be small in comparison to the overburden sliding mass since the shear zone self-weight is neglected in the calculation.

▪   The current algorithms are designed for single-mode deformation patterns (pure translational, pure rotational); composite deformation mechanims (e.g. translational-rotational) are not adressed.

7.4   Key findings from the case studies

The investigation of the deep-seated Beauregard rockslide and the shallow-seated Utiku landslide give evidence that CrEAM is capable of simulating variations in landslide deformation rates induced by seasonally fluctuating piezometric conditions.

It is shown that the modelling output is related to the assumed geomechanical model of the landslide, which includes both the landslide geometry and the rheology of the involved materials. Various effects are listed and discussed below.

▪ Effects of constitutive relationships

The magnitude of model response to an imposed pore pressure rise in the slope strongly depends on the implemented constitutive relationship. Based on the comparative study at the Beauregard rockslide, the deviatoric stress based algorithms generally yield insignificant velocity increases, while the effective stress based algorithms are more sensitive and predict relevant velocity changes. The effective stress based CrEAM with the modified Vulliet-Hutter model showed excellent results for both the Beauregard rockslide and the Utiku landslide. Therefore, E-CrEAM^{rot} or E-CrEAM^{trans} with the modified Vulliet-Hutter model are recommended for the investigation of groundwater induced velocity variations of creeping landslides.

▪ Effects of viscous parameters

All model results indicate that the viscous material parameters employed in the different constitutive relationships (i.e. viscosity, rate factor, exponent, yield shear stress) have a major impact on the model output. An indication about the sensitivity of the individual parameters was provided by the generic analyses for the infinite slope model in Section 5.5. In practice, viscous parameters should be determined with great care, as the results strongly depend on their values.

The Beauregard case study revealed significant discrepancies between laboratory and in situ creep parameters, based on the differing outcomes from forward analyses and back analyses. Use of laboratory parameters overestimated the slope creep velocity by several orders of magnitude. A distinct trend between triaxial and direct shear test based parameters was discernable: triaxial creep parameters approximated the back calculated creep parameters better than the direct shear based equivalents.

Generally, back calculated viscosities (used in the deviatoric stress based constitutive models) are higher and rate factors (in the effective stress based models) are lower than determined in the laboratory. This is reasonable, as the tested shear zone samples comprised only fine-grained material and are not representative for the inhomogeneous structure of the in situ shear zone, which contains also significant portions of gravel- and boulder-sized components. Therefore, the bulk in situ creep resistance of the shear zone might be considerably higher, which is reflected in the back calculated parameters.

▪ Effects of landslide geometry

Uncertainties with respect to the landslide geometry, including the kinematic mechanisms and the thickness of the active layer, played a secondary role for the modelled creep magnitude, as was shown in the Beauregard case study.
The results of the Utiku landslide study evidence that three-dimensional effects arising from a wedge geometry cannot be accounted by CrEAM. Nevertheless, the two-dimensional analysis parallel to the main path of landslide motion can assist to investigate the relationship between pore pressure rises and enhanced displacement rates.

7.5 Potential of CrEAM

CrEAM is a pragmatic investigation tool for the analysis of creeping landslides. It is based on an analytical solution and is thus transparent, relatively easy to understand, and requires minimal calculation time.

Despite its simplicity, CrEAM can lead to relevant results if the boundary conditions of the problem (geometry, material properties, groundwater conditions and pore pressures) are properly represented in the calculations. The major prerequisite for successful landslide analysis with CrEAM is therefore a profound knowledge about the geology and hydrogeology of a slope, and the reliable interpretation of surface and subsurface monitoring data.

A potential of CrEAM relates to the back analysis of landslide behaviour. Since geotechnical material parameters which are determined in small-scale laboratory tests are rarely suitable for representing the state in nature, back analysis of landslide behaviour based on observed displacement rates is widely applied in geotechnical practice. The low calculation effort of CrEAM makes this methodology well suited for such endeavours.

The successful reproduction of past landslide deformation patterns by modelling is a crucial preprequisite for predicting landslide behaviour under changed boundary conditions in the future. This is especially interesting for the design and efficiency analysis of potential remediation measures such as slope drainage, reservoir management, etc. In this context, the following philosophical viewpoint can be established: the quality of a back analysis increases with the number of reproducible events with different amplitudes. This fact emphasizes the importance of long-term monitoring data series, which serve as a basis for reliable modelling work.

Where creeping landslides are abundant in the same geological setting (as e.g. in the Tertiary sediments in New Zealand), the comprehensive analysis of one case study can have reference to other nearby landslides. While the geometry characteristics may change from case to case, the in situ creep parameters of geological units may be similar and used for forward analyses. This can be particularly interesting in the context of climate change going along with modified seasonal precipitation distributions.

7.6   Recommendations for further research

Recommendations for future research focus on a better understanding of time dependent material behaviour, and further contributions and refinements of CrEAM. Research recommendations therefore include:

- **Creep mechanics and constitutive models**

Although the time dependent behaviour of geomaterials has been increasingly investigated in the past decades, the micromechanics of creep deformation is still insufficiently understood. Further research in this field, both of experimental and numerical nature, would be desiderable. In this context, a promising Industry-Academia Partnerships and Pathways (IAPP) research project with the acronym "CREEP", standing for "Creep of Geomaterials", was funded by the 7th Framework Programme of the European Commission and commenced in February 2012 (until January 2016).

- **Landslide evolution in time**

The research presented in this thesis considers the instantaneous and short term landslide behaviour and, therefore, neglects considerations about the changing landslide geometry in time, which necessarily arises from creep deformation. Including progressive geometry change would enable to predict long-term landslide creep behaviour.

- **3D-expansion of CrEAM**

The methodology presented in this thesis is two-dimensional. While the plane strain assumption is justifiable for some slope situations, other sites clearly require a full 3D consideration (e.g. wedge-shaped landslides, laterally unconstrained ridge situations, etc.) The expansion of the present approach towards a three-dimensional equivalent would significantly enrich CrEAM.

Zusammenfassung

Viele Hänge im Lockersubstrat aber auch im Festgestein weisen geringe aber konstante Bewegungsaktivitäten mit Verschiebungsraten im Millimeter- bis Meterbereich pro Jahr auf. Vielfach handelt es sich dabei um Massenbewegungen mit gleitendem Versagensmechanismus. An der Basis der Gleitmasse findet sich dann stets ein ausgeprägter Scherhorizont variabler Mächtigkeit mit Zerreibungsprodukten des Ausgangssubstrats.

Dieser Scherhorizont kann einerseits das Resultat eines Erst- und fallweise auch weiterer Folgeversagen des Hanges sein, andererseits eine präexistierende und gravitativ reaktivierte tektonische Störungszone darstellen. Unabhängig von ihrer Genese besitzen diese lockergesteinsartigen Scherprodukte neben einer im Vergleich zum Umgebungssubstrat signifikant herabgesetzten Scherfestigkeit häufig auch eine ausgeprägte Tendenz zu viskoser Verformung.

Durch subkritische zeitabhängige (viskose) Deformation in der basalen Scherzone, die auch als Kriechen bezeichnet wird, wird die auflagernde Masse passiv hangabwärts transportiert. An der Oberfläche äußert sich dieser Prozess durch meist geringe aber stetige Bewegungsraten, welche im Laufe der Zeit zu beträchtlichen Verschiebungen führen. Häufig werden solche Hänge als „Kriechhänge" bezeichnet.

Um das zeitliche Deformationsverhalten nachbilden und analysieren zu können, wurden in dem neu entwickelten Ansatz CrEAM die Grundsätze der analytischen Stabilitätsanalyse mit viskosen Materialgesetzen verknüpft. Das Ziel war es, ein transparentes und zeiteffizient durchführbares Verfahren zur Analyse von Kriechhängen zu schaffen.

Für die Modellierung wird die Gleitmasse ähnlich der klassischen Stabilitätsanalyse in eine ausreichende Anzahl von Lamellen unterteilt. Auf das System von Lamellen wird anschließend ein Berechnungsalgorithmus angewandt, der die folgenden Randbedingungen erfüllt:

- Gleichgewicht aller im System wirkenden Kräfte
- Konstitutiver Zusammenhang zwischen Deformationsraten und Kräften (Spannungen) mittels zeitabhängigen Materialparametern
- Kinematische Kompatibilität der Verschiebungen der einzelnen Lamellen

Die Lösung des analytischen Berechnungsalgorithmus erfolgt direkt oder mittels Iteration. In beiden Fällen ist der Rechenaufwand im Vergleich zu numerischen Methoden gering.

Für die Beschreibung des zeitabhängigen Verformungsverhaltens der Scherzone können verschiedene viskose Materialgesetze herangezogen werden. Von den einfachen scherspannungsabhängigen Gesetzen stehen die linear-viskosen Modelle nach Newton und Bingham aber auch nicht-lineare Modelle wie der Norton-Ansatz zur Verfügung. Das reale Verhalten des Materials besser anzunähern vermögen scher- und normalspannungsabhängige Beziehungen wie der Vulliet-Hutter Ansatz.

Bei gegebener Geometrie und hinreichend bekannten Materialeigenschaften kann so eine Kriechbewegungsrate für das System ermittelt werden. Bekannte Bewegungsraten (z.B. aus einem geodätischen Messprogramm) erlauben ihrerseits die Rückrechnung der zeitabhängigen in-situ Materialparameter, die gegebenenfalls mit Kriechparametern aus Laborversuchen verglichen und plausibilisiert werden können.

CrEAM kann immer dann angewendet werden, wenn ein Hang unter gleichbleibenden äußeren Bedingungen stationäres Deformationsverhalten (sekundäres Kriechen) zeigt. Die Anwendbarkeit ist nicht gegeben, wenn Kriechhänge bei konstanten äußeren Bedingungen eine eindeutige Beschleunigungstendenz zeigen. In diesem Fall muss von tertiären Kriechen und damit progressivem Versagen ausgegangen werden.

CrEAM kann dazu dienen das Verständnis für das Systemverhalten von Kriechhängen zu verbessern und damit die Grundlagen schaffen, das Deformationsverhalten unter variierenden Randbedingungen (z.B. Änderung des Grundwasserhaushaltes, Zusatzlasten durch Infrastrukturen) zu analysieren und zu prognostizieren. Daneben bietet es sich durch den geringen Rechenaufwand vor allem für Parameterstudien und Sensitivitätsanalysen an. Einflüsse von Parameterunsicherheiten auf das Analyseergebnis können damit umfassend untersucht werden.

References

Agliardi, F., Crosta, G., Zanchi, A. (2001) Structural constraints on deep-seated slope deformation kinematics. – Engineering Geology, Vol. 59, pp. 83–102.

Ambrosi, C. & Crosta, G.B. (2006) Large sackung along major tectonic features in the Central Italian Alps. – Engineering Geology, Vol. 83, pp. 183–200.

Andrade, E. (1910) The viscous flow in metals and allied phenomena. – Proc. R. Soc. London, Vol. A 84, pp. 1-12.

Antolini, F. (in prep.) The use of radar interferometry and finite-discrete modelling for early warning systems of rock landslides. – PhD thesis, Politecnico di Torino.

Avula, X. (1987) Mathematical Modelling. – Encyclopedia of Physical Science and Technology ,Vol. 7, pp. 719-728.

Barla, G., Ballatore, S., Canella, G., Amici, R., Chiappone, A. (2005) La deformazione gravitativa di Beauregard e la sua interazione con una grande diga ad arco gravitá. In: Questioni di Ingegneria Geotecnica. – Scritti in onore di Arturo Pellegrino. Vol. 2.

Barla, G., Ballatore, S., Chiappone, A., Frigerio, A., Mazzà, G. (2006) The Beauregard dam (Italy) and the deep-seated gravitational deformation on the left slope. – Proceedings of the Hydropower 2006 International Conference, Kunming, October 23-25, 2006.

Barla, G., Barla, M., Debernardi, D. (2010a) New Triaxial apparatus for rocks. – Rock Mech. Rock. Eng., Vol. 43, pp. 225-230.

Barla, G., Barla, M., Martinotti, M.E. (2010b) Development of a new direct shear testing apparatus. – Rock Mech. Rock. Eng., Vol. 43, pp. 117-122.

Barla, G., Antolini, F., Barla, M., Mensi, E., Piovano, G. (2010c) Monitoring of the Beauregard landslide (Aosta Valley, Italy) using advanced and conventional techniques. – Engineering Geology, Vol. 116, pp. 218–235.

Barla, G. (2010d) Long-term behaviour of the Beauregard dam (Italy) and its interaction with a deep-seated gravitational slope deformation. – Mittteilungen für Ingenieurgeologie und Geomechanik, Band 9, 5th Colloquium "Rock Mechanics - Theory and Practice", Wien, pp. 111-125.

Barla, G., Antolini, F., Barla, M., Mensi, E., Piovano, G. (2011) Ground-Based Radar Interferometry (GBInSAR) for the monitoring of a deep-seated landslide (Aosta Valley, NW Italian Alps). – Proceedings of the 8th International Symposium on Field Measurements in GeoMechanics Berlin, Germany, September 12-16, 2011.

Baum R.L. & Reid M.E. (1992) Geology, hydrology and mechanics of the Alani‐Paty landslide, Manoa Valley, Oahu, Hawaii. – U.S. Geological Survey Open File Report 92-501, 87 p.

Belz, D.T.G. (1967) Investigation of subsidence at Utiku. – Soil and Water 1967, pp. 19-22.

Betten, J. (2002) Creep mechanics. – Springer, Berlin, Heidelberg, New York.

Bhat, D.R., Bhandary, N.P., Yatabe, R., Tiwari, R.C. (2011) Residual-state creep test in modified torsional ring shear machine: Methods and implications. – Int. J. Geomate, Vol. 1/1, pp. 39-43.

Bishop, A.W. (1955) The use of the slip circle in the stability analysis of slopes. – Geotechnique, Vol. 3, pp. 1-5.

Bishop, A.W. (1967) Progressive failure - with special reference to the mechanism causing it. – Proceedings of the Geotechnical Conference on Shear Strength Properties of Natural Soils and Rocks, Oslo, Vol. 2, pp. 142-150.

Bonzanigo, L., Eberhardt, E., Loew, S. (2007) Long-term investigation of a deep-seated creeping landslide in crystalline rock. Part I. Geological and hydromechanical factors controlling the Campo Vallemaggia landslide. – Canadian Geotechnical Journal, Vol. 44, pp. 1157-1180.

Borgatti, L., Corsini, A., Barbieri, M., Sartini, G., Truffelli, G., Caputo, G., Puglisi, C. (2005) Large reactivated landslides in weak rock masses: a case study from the Northern Apennines (Italy). – Landslides, Vol. 3, pp. 115–124.

Bowman, E.T. & Soga, K. (2003) Creep, ageing and microstructural change in dense granular materials. – Soils and Foundations, Vol. 43/4, pp. 107-117.

Bucher, S., Ulardic, C., Bousquet, R., Ceriani, S., Fugenschuh, B., Gouffon, Y., Schmid, S.M. (2004) Tectonic evolution along a transect (ECORS-CROP) through the Italian - French Western Alps. – Eclogae Geol. Helv., Vol. 97, pp. 321-345.

Calvello, M., Cascini, L., Sorbino, G. (2008). A numerical procedure for predicting rainfall-induced movements of active landslides along pre-existing slip surfaces. – Int. J. Numer. Anal. Meth. Geomech., Vol. 32, pp. 327-351.

Carey, J.M. (2011) The progressive development and post-failure behaviour of deep-seated landslide complexes. – PhD thesis, Durham University, Department of Geography, 396 p.

Cascini, L., Bonnard, C., Corominas, J., Jibson, R., Montero-Olarte, J. (2005) Landslide hazard and risk zoning for urban planning and development. - State of the Art report. – Proceedings of the International Conference on Landslide Risk Management, Vancouver. Balkema Rotterdam, pp. 199-235.

Chan, P.D.S (1999) Soil-pipeline interaction in slopes. – Master Thesis, Departement of Civil Engineering, University of Calgary, Alberta, 190 p.

Chen, Z.Y. & Morgenstern, N.R. (1983) Extensions to the generalised method of slices for slope stability analysis. – Canadian Geotechnical Journal, Vol. 20, p. 104-119.

Chigira, M. (1992) Long-term gravitational deformation of rocks by mass rock creep. – Engineering Geology, Vol. 32, pp. 157-184.

Chigira, M. & Kiho, K. (1994) Deep-seated rockslideavalanche preceded by mass rock creep of sedimentary rocks in the Akaishi Mountains, central Japan. – Engineering Geology, Vol. 38, pp. 221-230.

Corominas, J., Moya, J., Ledesma, A., Loret, A., Gili, J.A. (2005) Prediction of ground displacements and velocities from groundwater level changes at the Vallcebre landslide (Eastern Pyrenees, Spain). – Landslides, Vol. 2, pp. 83-96.

CREEP – Creep of geomaterials. www.ntnu.edu/creep (called on January 7, 2013)

Cruden, D.M. & Varnes, D.J. (1996) Landslide types and processes. In: Turner, K. A. & Schuster, R. L. (Eds.) Landslide: Investigation and Mitigation. – Special report 247, Transportation Research Board, Washington, pp. 36-75.

Dellow, G.D., McSaveney, M.J., Stirling, M.W., Berryman, K.R. (2005) A probabilistic landslide hazard model for New Zealand. In: Pettinga, J.R. & Wandres, A.M. (Eds.) Geological Society of New Zealand 50th annual conference, November 28 to Dezember 1, 2005. – Geological Society of New Zealand miscellaneous publication 119A, 24 p.

Desio, A. (1973) Geologia applicata all` ingegneria. – 3[a] edizione, Hoepli editore, Milano, 1193 p.

Di Benedetto, H. & Tatsuoka, F. (1997) Small strain behavior of geomaterials: Modelling of strain rate effects. – Soils and Foundations, Vol. 37/2, pp. 127-138.

Duncan, J.M. & Wright, S.G. (2005) Soil Strength and Slope Stability. – 1st edition, Wiley, 312 p.

Emery, J.J. (1971) Finite element analysis of creep problems in soil mechanics. – PhD thesis, University of British Columbia, Vancouver, 155 p.

Engl, D.A., Fellin, W., Zangerl, C. (2008) Scherfestigkeiten von Scherzonengesteinen - Ein Beitrag zur geotechnischen Bewertung von tektonischen Störungszonen und Gleitzonen von Massenbewegungen. – Bulletin für angewandte Geologie, Vol. 13/2, pp. 63-81.

Engl, D.A., Fellin, W., Kieffer, D.S., Zangerl, C. (2010) A novel approach for assessing the deformation characteristics of rockslides. In: Williams et al. (Eds.) Geologically Active. – Taylor & Francis Group, London, pp. 2875-2882.

Eshraghian, A., Martin, C.D., Morgenstern, N.R. (2008a). Hazard Analysis of an active slide in the Thompson River Valley, Ashcroft, British Columbia, Canada. – Canadian Geotechnical Journal, Vol. 45, pp. 297-313.

Eshraghian, A., Martin, C.D., Morgenstern, N.R. (2008b) Movement triggers and mechanisms of two earth slides in the Thompson River Valley, British Columbia, Canada. – Canadian Geotechnical Journal, Vol. 45, pp. 1189-1209.

Feda, J. (1992) Creep of soils and related phenomena. – Developments in Geotechnical Engineering 68, Elsevier Amsterdam, 422 p.

Fell, R., Hungr, O., Leroueil, S., Riemer, W. (2000) Keynote lecture - Geotechnical engineering of the stability of natural slopes, and cuts and fills in soil. – GeoEng 2000 Conference, Melbourne Australia, Technomic, Lancaster, pp. 21-120.

Fellenius, W. (1927) Erdstatische Berechnungen mit Reibung und Kohäsion (Adhäsion) und unter Annahme kreiszylindrischer Gleitflächen. – Ernst & Sohn, Berlin.

Fellenius, W. (1936) Calculations of the Stability of Earth Dams. – Proceedings of the Second Congress of Large Dams, Washington D. C., Vol. 4, pp. 445-463.

Fellin, W. (2004) Ambiguity of safety definition in geotechnical models. In: Fellin, W., Lessmann, H., Oberguggenberger, M., Vieider, R. (Hrsg.): Analyzing Uncertainty in Civil Engineering. – Springer, pp. 17-31.

Fellin, W. (2011) Abschätzung der Standsicherheit von annähernd unendlich langen Kriechhängen. – Geotechnik, Vol. 34/1, pp. 22-31.

Ferrari, A., Ledesma, A., González, D.A., Corominas, J. (2011) Effects of the foot evolution on the behaviour of slow-moving landslides. – Engineering Geology, Vol. 117, pp. 217-228.

Francois, B., Tacher, L., Bonnard, Ch., Laloui, L., Triguero, V. (2007) Numerical modelling of the hydrogeological and geomechanical behaviour of a large slope movement: the Triesenberg landslide (Liechtenstein). – Canadian Geotechnical Journal, Vol. 44, pp. 840-857.

Fredlund, D.G. & Krahn J. (1977) Comparison of slope stability methods of analysis. – Canadian Geotechnical Journal, Vol. 16, pp. 121-139.

Fredlund, D.G., Krahn, J., Pufahl, D.E. (1981) The relationship between limit equilibrium slope stability methods. – Proceedings of the 10th International Conference on Soil Mechanics and Foundation Engineering, Stockholm, Vol. 3, pp. 409-416.

Glastonbury, J. & Fell, R. (2008a) A decision analysis framework for the assessment of likely post-failure velocity of translational and compound natural rock slope landslides. – Canadian Geotechnical Journal, Vol. 45/3, pp. 329-350.

Glastonbury, J. & Fell, R. (2008b) Geotechnical characteristics of large slow, very slow, and extremely slow landslides. – Canadian Geotechnical Journal, Vol. 45/7, pp. 984-1005.

Grøneng, G., Lu, M., Nilsen, B., Jenssen, A.K. (2010) Modelling of time dependent behavior of the basal sliding surface of the Åknes rockslide area in western Norway. - Engineering Geology, Vol. 114, pp. 414-422.

Gündogdu, B. (2011) Relations between pore water pressure, stability and movements in reactivated landslides. – Master Thesis, Middle East Technical University, 115 p.

Haupt, P. (2000): Continuums Mechanics and Theory of Materials. – Springer, Berlin, Heidelberg, New York.

Höwing, K. D. & Kutter, H. K. (1985) Time dependent shear deformation of filled rock joints: a keynote lecture. - In: Stephansson, O. (Ed.) Fundamentals of rock joints: Proceedings of the international Symposium on Fundamentals of Rock Joints. Björkliden/Sweden, September 15-20, 1985, pp. 113-122.

Hutchinson, J.N. (1988) Morphology and geotechnical parameters of landslides in relation to geology and hydrogeology. – Proc. 5th Int. Symp. On Landslides, Lausanne, Balkema, Rotterdam, pp. 3-35.

Janbu, N. (1954). Application of Composite Slip Surface for Stability Analysis. – European Conference on Stability of Earth Slopes, Stockholm, Vol. 3, pp.43-49.

Janbu, N. (1973). Slope Stability Computations. – Embankment Dam Engineering, Casagrande Volume, pp. 47-86.

Kalenchuk K.S. (2010) Multi-Dimensional Analysis of Large, Complex Slope Instability. – PhD Thesis, Department of Geological Sciences and Geological Engineering, Queen's University Kingston, Canada, 449 p.

Ker, D. S. (1972) Renewed movement on a slump at Utiku. – N.Z. Journal of Geology and Geophysics, No. 13, pp. 996-1017.

Kilsby, C. (2007) An engineering geological appraisal of the Utiku Landslide, North Island, New Zealand. – Master Thesis, University of Portsmouth, pp. 19-27.

Koukis, G., Sabatakakis, N., Ferentinou, M., Lainas, S., Alexiadou, X., Panagopoulos, A. (2009) Landslide phenomena related to major fault tectonics: rift zone of Corinth Gulf, Greece. – Bull. Eng. Geol. Environ. Vol. 68, pp. 215–229

Krieg, S. (2000) Viskoses Bodenverhalten von Mudden, Seeton und Klei. – Veröffentlichungen des Instituts für Bodenmechanik und Felsmechanik der Universität Karlsruhe, Heft 150.

Kuhn, M. R. & Mitchell, J. K. (1993) New perspectives on soil creep. – J. Geotech. Engng, ASCE 119, No. 3, pp. 507-524.

Lade, P.V. & Liu, C.-T. (1998) Experimental study of drained creep behaviour of sand. – J. Eng. Mech., ASCE 124, No. 8, pp. 912-920.

Lang, H.-J., Huder, J., Amann, P., Puzrin, A.M. (2011) Bodenmechanik und Grundbau - Das Verhalten von Böden und Fels und die wichtigsten grundbaulichen Konzepte. – Springer Verlag (9. Auflage).

Leroueil, S. & Marques, M.E.S. (1996). State of the Art on the importance of strain rate and temperature effects in geotechnical engineering. – ASCE Convention, Washington, Geotechnical Special Publication No. 61, pp. 1-60.

Leroueil, S. (2001) Natural slopes and cuts: movements and failure mechanisms. – Geotechnique, Vol. 51/3, pp. 195-244.

Leung, C.F., Lee, F.H., Yet, N.S. (1996) The role of particle breakage in pile creep in sand. – Canadian Geotechnical Journal, Vol. 33, pp. 888-898.

Linser, M. (2009) Vergleich verschiedener geotechnischer Versuche mit Gesteinszerreibungsprodukten (Kakiriten) zur Bestimmung der Scherparameter. – Diploma thesis, University of Innsbruck.

Liu, J. & Zhou, R. (2000) Scale effects in the creep parameters of fractured rock masses. – GeoDenver 2000 - Trends in Rock Mechanics, August 5-8, 2000, Geotechnical Special Publications 102, pp. 103-112.

Loew, S., Ebneter, F., Bremen, R., Herfort, M., Luetzenkirchen, V., Matousek, F. (2007) Annual opening and closure of alpine valleys. – Felsbau, Vol. 25/5, pp. 60-65.

Lomnitz, C. (1955) Creep measurements in igneous rocks with some applications to aftershock theory. – PhD thesis, California Institute of Technology Pasadena, California, 111 p.

Losert, W., Geminard, J.-C., Nasuno, S., Gollub, J.P. (2000) Mechanisms for slow strengthening in granular materials. – Physical Review E Vol. 61/4, pp. 4060-4068.

Lowe, J. & Karafiath, L. (1959) Stability of earth dams upon drawdown. – Proceedings of the First PanAmerican Conference on Soil Mechanics and Foundation Engineering, Mexico City, Vol. 2, pp. 537-552.

McDowell, G.R. (2003) Micromechanics of creep of granular materials. – Geotechnique, Vol. 53/10, pp. 915-916.

Macfarlane, D.F. (2009). Observations and predictions of the behaviour of large, slow-moving landslides in schist, Clyde Dam reservoir, New Zealand. – Engineering Geology, Vol. 109, pp. 5–15.

Mahr, T. & Nemcok, A. (1977) Deep-seated creep deformations in the crystalline cores of the Tatry Mts. – Bulletin of the International Association of Engineering Geology, Vol. 16, pp. 104–106.

Malan, D.F., Drescher, K., Vogler, U.W. (1998) Shear creep of discontinuities in hard rock surrounding deep excavations. – Proceedings of the third International Conference on Mechanics of Jointed and Faulted Rock. Vienna/Austria, April 6-9, 1998, pp. 473-478.

Mang, H. & Hofstetter, G. (2008) Festigkeitslehre. – Springer Verlag Wien-New York, 3. Auflage, 487 p.

Mansour, M.F., Morgenstern, N.R., Martin, C.D. (2011). Expected damage from displacement of slow-moving slides. – Landslides, Vol. 8, pp. 117-131.

Marcato, G., Mantovani, M., Pasuto, A., Silvano, S., Tagliavini, F., Zabuski, L. (2009) Assessing the possible future development of the Tessina landslide using numerical modelling. – In: Malet, Remaitre, Bogaard (Eds.) Landslide processes, CERG editions Strasburg, pp. 327-332.

Martinotti, M.E. (2010) Creep behaviour of cataclastic rock in massive rock slopes. – PhD thesis, Politecnico di Torino, 233 p.

Massey, C.I. (2010) The dynamics of reactivated landslides: Utiku and Taihape, North Island, New Zealand. – PhD thesis, Durham University, 338 p.

Massey, C.I., Petely, D.N., McSaveney, M.J. (in press) Patterns of movement in reactivated landslides. – Engineering Geology.

Massironi, M., Bistacchi, A. V., Dal Piaz, G., Monopoli, B., Schiavo, A. (2003) Structural control on mass-movement evolution: A case study from the Vizze Valley, Italian Eastern Alps. – Eclogae Geologicae Helvetiae, Vol. 96, pp. 85–98.

MATLAB, Version 7.0.4. The MathWorks Inc.

Miller, S.M., Barla, G., Piovano, G., Barla, M. (2008) Geotechnical and temporal risk assessment of a large slope deformation. – 42nd US Rock Mechanics Symposium and 2nd U.S.-Canada Rock Mechanics Symposium, San Francisco (USA) June 29th - July 2nd, 2008.

Mitchell, J. K. (1993) Fundamentals of soil behavior. – 2nd Ed., John Wiley & Sons, New York.

Morgenstern, N.R. & Price, V.E. (1965) The analysis of the stability of general slip surfaces. – Geotechnique, Vol. 15/1, pp. 79-93.

Morgenstern, N.R. & Sangrey, D.A. (1978) Methods of stability analysis. In: Schuster R.L. et al. (Eds.) Landslides - Analysis and Control. – Transportation Research Board, National Academy of Sciences, Washington D.C., Special Report 176, pp. 155-177.

Morgenstern, N.R. (1995) The role of analysis in the evaluation of slope stability. – 6th Int. Symp. On Landslides, Christchurch, Balkema, Rotterdam, Vol. 3, pp. 1615-1629.

Norton, F.H. (1929) Creep of steel at high temperatures. – Mc Graw-Hill, New York.

Noverraz, F. (1996) Sagging or deep-seated creep: fiction or reality? – Proc. 7th Int. Symp. on Landslides, Trondheim (Norway), Balkema, Rotterdam, pp. 821-828.

Ortigao, J.A.R. (1995) Soil mechanics in the light of critical state theories. – Balkema Rotterdam, 299 p.

Panet, M. (1969) Discussion of K.W. John's Paper (ASCE Proc. Paper 5865, March 1968). – Journal of the Soil Mechanics and Foundation Division, ASCE, Vol. 95, No. SM2, pp. 685-686.

Petely, D.N. & Allison, R.J. (1997) The mechanics of deap-seated landslides. – Earth surface Processes and Landforms, Vol. 22, pp. 747-758.

Petterson, K.E. (1955) The early history of circular slip surfaces. – Geotechnique, Vol. 5, pp. 275-296.

Picarelli, L., Urciuoli, G., Russo, C. (2004) Effects of groundwater regime on the behavior of clayey slopes. – Canadian Geotechnical Journal, Vol. 41/3, pp. 467-484.

Poirier, J.-P. (1985) Creep of crystals - High-temperature deformation processes in metals, ceramics and minerals. – Cambridge University Press.

Piovano, G. (2012) Combined finite-discrete element modelling of key instabilities in deep-seated landslides from massive rock slope failure. – PhD thesis, Politecnico di Torino, 312 p.

Puzrin, A.M. & Schmid, A. (2011) Progressive failure of a constrained creeping landslide. – Proceedings of the Royal Society A, Vol. 467, pp. 2444-2461.

Radbruch-Hall, D. (1978) Gravitational creep of rock masses on slopes. In: Voight, B. (Ed.). Rockslides and avalanches natural phenomena. – Developments in Geotechnical Engineering, Vol. 14, Elsevier, Amsterdam, pp. 608-657.

Read, S.A.L. & Miller, P.J. (1990) Characterisation and classification of New Zealand Tertiary age sedimentary soft rocks. In: Bridge design and research seminar 1990, Vol. 4: Road engineering in soft rock materials. - RRU Bulletin 84, pp. 1-25.

Reiner, M. (1958) Rheology. In: Flügge, S. (Ed.): Handbuch der Physik. – Band 6, pp. 434-550.

Renk, D. (2006) Geotechnische Untersuchungen von Gleitzonenmaterialien großer Hangbewegungen. – Diploma thesis, University of Karlsruhe, 119 p.

Reyes, A.G. (2007) Petrological study of selected Taihape landslide rock samples. – The Institute of Geological and Nuclear Science Science Report 2007/32.

Sarma, S.K. (1973) Stability analysis of embankments and slopes. – Geotechnique, Vol. 23, pp. 423-433.

Sarma, K. (1987) A note on the stability analysis of slopes. - Geotechnique, Vol. 37, pp. 107-111.

Selby, M.J. (1993) Hillslope materials and processes. – Second edition. Oxford University Press, England, 270 p.

Schneider-Muntau, B., Katzenbach, R., Fellin, W. (2005) Numerical modelling of creeping landslides: Applicability of material properties determined in laboratory experiments. – International Symposium on Latest Natural Disasters, Sofia (Bulgaria), pp. 234-243.

Schneider-Muntau, B., Renk, D., Marcher, T., Fellin, W. (2006) The importance of laboratory experiments for Finite Element calculations in landslide investigations. In: Nadim, F., Pöttler, R., Einstein, H., Klapperich, H. & Kramer, S. (Eds.) Geohazards. – ECI Symposium Series, Lillehammer (Norway).

Schneider-Muntau B. (2012) Zur Modellierung von Kriechhängen. – PhD thesis, Universität Innsbruck, 263 p.

Singh, A. & Mitchell, J.K. (1968a). General stress-strain-time function for soil. – Journal of the Soil Mechanics and Foundations Division, ASCE, Vol. 94, No. SM1, pp. 21-46.

Singh, A. & Mitchell, J.K. (1968b). Closure: General stress-strain-time function for soil. – Journal of the Soil Mechanics and Foundations Division, ASCE, Vol. 95, No. SM6, pp. 1526-1527.

Singh, D.P. (1975) A study of creep of rocks. – Int. J. Rock Mech. Min. Sci. & Geomech. Abstr., Vol. 12, pp. 271-276.

Skempton, A.W. (1985) Residual strength of clays in landslide, folded strata and the laboratory. – Geotechnique, Vol. 35, No. 1, pp. 3-18.

Spencer, E. (1967) A method of analysis of the stability of embankments assuming parallel interslice-forces. – Geotechnique, Vol. 17, pp. 11-26.

Spencer, E. (1973) Thrust line criterion in embankement stability analysis. – Geotechnique, Vol. 23, pp. 85-100.

Stout, M.L. (1977) The Utiku landslide, North Island, New Zealand. – Geological Society of America, Reviews in Engineering Geology, Vol. 3, pp. 171-184.

Strauhal, T. (2009) Mineralogische und geotechnische Eigenschaften von tektonisch- und massenbewegungsbedingten Kakiriten. – Diploma thesis, University of Innsbruck.

Tavenas, F. & Leroueil, S. (1981) Creep and failure of slopes in clays. – Canadian Geotechnical Journal, Vol. 18/1, pp. 106-120.

Ter-Stepanian, G. (1966) Type of depth creep of slopes in rock masses. – Problems Geomech., Vol. 3, pp. 49-69.

Ter-Stepanian, G. (1975) Creep of clay during shear and its rheological model. – Geotechnique, Vol. 25/2, pp. 299-320.

Thornton, C. & Zhang, L. (2003) Numerical simulations of the direct shear test. – Chemical Engineering & Technology, Vol 26/2, pp. 153-156.

Thuro, K., Eberhardt, E., Gasparini M. (2004) Deep-seated creep and its influence on a 1.5 GW Hydroelectric power plant in the Himalayas. – Felsbau, Vol. 22/2, pp. 60-66.

Thüringer Fernwasserversorgung (2007) Hangbewegung Gabel - Ein Beitrag zur Talsperrensicherheit. – Infobroschüre, Druckerei Schöpfel Weimar, 57 p.

U.S. Army Corps of Engineers (1970) Stability of Earth and Rock-Fill Dams. – EM 1110-2-1902. U.S. Army Engineer Waterways Experiment Station, Vicksburg, MS.

U.S. Army Corps of Engineers (2003) Engineering and Design - Slope Stability. – EM 1110-2-1902, Washington, DC.

Van Asch, T.J.W., Van Beek, L.P.H., Bogaard, T.A. (2007) Problems in predicting the mobility of slow-moving landslides. – Engineering Geology, Vol. 91, pp. 46-55.

Van Asch, T.W.J. & Van Genuchten, P.M.B. (1990) A comparison between theoretical and measured creep profiles of landslides. – Geomorphology, Vol. 3, pp. 45-55.

Van Mises, R. (1913) Mechanik der festen Körper im plastisch deformablen Zustand. – Göttin. Nachr. Math. Phys., Vol. 1, pp. 582-592.

Van Mises, R. (1928) Mechanik der plastischen Formänderungen von Kristallen. – Zeitschrift für angewandte Mathematik und Mechanik (ZAMM), Band 8, pp. 161-185.

Varnes, D.J. (1978) Slope movements - Types and Processes. In: Schuster, R.L.& Krizek, R.J. (Eds.) Special Report 176, Landslides: Analysis and Control. – National Research Council, Washington, pp. 11-33.

Vogelhuber, M. (2007) Der Einfluss des Porenwasserdruckes auf das mechanische Verhalten kakiritisierter Gesteine. – PhD thesis, ETH Zürich, No. 17079, 317 p.

Vulliet L. & Hutter K. (1988a) Set of constitutive models for soils under slow movement. – Journal of Geotechnical Engineering, Vol. 114/9, pp. 1022-1041.

Vulliet, L. & Hutter, K. (1988b) Viscous-type sliding laws for landslides. – Canadian Geotechnical Journal, vol. 25/3, pp. 467-477.

Zangerl, C. & Engl, D.A. (2009) Entwicklung kinematischer Modelle von Massenbewegungen auf Basis von Deformationsmessungen. In: Online Datenerfassung, berührungslose Messverfahren, 3D-Modellierung und geotechnische Analyse in Geologie und Geotechnik – Beiträge zur COG-Fachtagung 2009, Verlag Wichmann, p. 222-233.

Zangerl, C., Eberhardt, E., Perzlmaier, S. (2010a) Kinematic behaviour and velocity characteristics of a complex deep-seated crystalline rockslide system in relation to its interaction with a dam reservoir. - Engineering Geology, Vol. 112, pp. 53-67.

Zangerl, C., Prager, C., Engl, D.A. (2010b) Self-stabilisation mechanisms of slow rock slides in crystalline bedrock (Tyrol, Austria). In: Williams et al. (Eds.) Geologically Active. – Taylor & Francis Group, London, pp. 903-910.

Appendix

Note: Shaded equations also appear in the main part.

A.1 Viscous models: Derivations for infinite slope conditions

Complementary derivations to Chapter 3

(a) Newton

Hook's law of an elastic spring

$$l_\Delta = \frac{F}{K} \tag{A.1}$$

indicates that the displacement l_Δ of a spring is proportional to the force F pulling the latter. The Hook's spring constant K represents the inherent resistance of the spring and its inverse acts as a proportionality factor between the displacement l_Δ and the force F.

Assuming an ideal-elastic body under uniaxial stress conditions, (A.1) can be reformulated as

$$\varepsilon = \frac{\sigma}{E} \tag{A.2}$$

where ε and σ are the normal strain and normal stress, and E is the Young's modulus (modulus of elasticity) of the material.

For an ideal-elastic isotropic body subjected to a three-dimensional stress state, the Hook stress-strain relationship is generalized as (Mang & Hofstetter 2008; Ortigao 1995)

$$
\boldsymbol{\varepsilon} =
\begin{bmatrix}
\varepsilon_{11} \\
\varepsilon_{22} \\
\varepsilon_{33} \\
\varepsilon_{12} \\
\varepsilon_{23} \\
\varepsilon_{13}
\end{bmatrix}
= \frac{1}{E}
\begin{bmatrix}
1 & -v & -v & 0 & 0 & 0 \\
-v & 1 & -v & 0 & 0 & 0 \\
-v & -v & 1 & 0 & 0 & 0 \\
0 & 0 & 0 & 1+v & 0 & 0 \\
0 & 0 & 0 & 0 & 1+v & 0 \\
0 & 0 & 0 & 0 & 0 & 1+v
\end{bmatrix}
\begin{bmatrix}
\sigma_{11} \\
\sigma_{22} \\
\sigma_{33} \\
\sigma_{12} \\
\sigma_{23} \\
\sigma_{13}
\end{bmatrix}
\tag{A.3}
$$

with v being the Poisson ratio defined as

$$
v = -\frac{\varepsilon_r}{\varepsilon_l}
\tag{A.4}
$$

where ε_r and ε_l are the radial and axial (longitudinal) strain determined in a uniaxial compression test.

To express linear-viscous (time dependent) deformation instead of linear-elastic (time independent) deformation, the strain $\boldsymbol{\varepsilon}$ is replaced by the strain rate $\dot{\boldsymbol{\varepsilon}}$, and the material constants are substituted by time dependent parameters i.e. the Young's modulus E is replaced by the Newtonian viscosity μ^{Newton} and the Poisson ratio v is replaced by its time dependent equivalent ϖ:

$$
\underbrace{
\begin{pmatrix}
\boldsymbol{\varepsilon} \\
E \\
v
\end{pmatrix}
}_{time-independent}
\rightarrow
\underbrace{
\begin{pmatrix}
\dot{\boldsymbol{\varepsilon}} \\
\mu^{Newton} \\
\varpi
\end{pmatrix}
}_{time-dependent}
\tag{A.5}
$$

Consequently, (A.3) modifies to

$$
\dot{\boldsymbol{\varepsilon}} =
\begin{bmatrix}
\dot{\varepsilon}_{11} \\
\dot{\varepsilon}_{22} \\
\dot{\varepsilon}_{33} \\
\dot{\varepsilon}_{12} \\
\dot{\varepsilon}_{23} \\
\dot{\varepsilon}_{13}
\end{bmatrix}
= \frac{1}{\mu^{Newton}}
\begin{bmatrix}
1 & -\varpi & -\varpi & 0 & 0 & 0 \\
-\varpi & 1 & -\varpi & 0 & 0 & 0 \\
-\varpi & -\varpi & 1 & 0 & 0 & 0 \\
0 & 0 & 0 & 1+\varpi & 0 & 0 \\
0 & 0 & 0 & 0 & 1+\varpi & 0 \\
0 & 0 & 0 & 0 & 0 & 1+\varpi
\end{bmatrix}
\begin{bmatrix}
\sigma_{11} \\
\sigma_{22} \\
\sigma_{33} \\
\sigma_{12} \\
\sigma_{23} \\
\sigma_{13}
\end{bmatrix}
\tag{A.6}
$$

In analogy to (A.4), the time dependent equivalent of the Poisson ratio, i.e. ϖ, is given by the ratio of the corresponding radial and axial strain rates $\dot{\varepsilon}_r$ and $\dot{\varepsilon}_l$

$$\varpi = -\frac{\dot{\varepsilon}_r}{\dot{\varepsilon}_l} \tag{A.7}$$

Assuming a constant volume deformation in time as commonly observed in the secondary creep stage, thus

$$\dot{\varepsilon}_{vol} = tr\left(\dot{\boldsymbol{\varepsilon}}\right) = \dot{\varepsilon}_1 + \dot{\varepsilon}_2 + \dot{\varepsilon}_3 = \dot{\varepsilon}_l + 2\dot{\varepsilon}_r = 0 \tag{A.8}$$

the ratio of the radial and axial strain rates $\dot{\varepsilon}_r$ and $\dot{\varepsilon}_l$ is determind as

$$\varpi = -\frac{\dot{\varepsilon}_r}{\dot{\varepsilon}_l} = \frac{1}{2} \qquad \text{for} \qquad \dot{\varepsilon}_{vol} = 0 \tag{A.9}$$

Assuming plane strain conditions, thus $\dot{\varepsilon}_{12} = \dot{\varepsilon}_{23} = \dot{\varepsilon}_{22} = 0$, and taking account of (A.9), equation (A.6) reduces to

$$\begin{bmatrix} \dot{\varepsilon}_{11} \\ 0 \\ \dot{\varepsilon}_{33} \\ \dot{\varepsilon}_{13} \end{bmatrix} = \frac{1}{2\mu^{Newton}} \begin{bmatrix} 2 & -1 & -1 & 0 \\ -1 & 2 & -1 & 0 \\ -1 & -1 & 2 & 0 \\ 0 & 0 & 0 & 3 \end{bmatrix} \begin{bmatrix} \sigma_{11} \\ \sigma_{22} \\ \sigma_{33} \\ \sigma_{13} \end{bmatrix} \tag{A.10}$$

with the components

$$\dot{\varepsilon}_{11} = \frac{2\sigma_{11} - \left(\sigma_{22} + \sigma_{33}\right)}{2\mu^{Newton}} \tag{A.11}$$

$$\dot{\varepsilon}_{22} = \frac{2\sigma_{22} - \left(\sigma_{11} + \sigma_{33}\right)}{2\mu^{Newton}} = 0 \tag{A.12}$$

$$\dot{\varepsilon}_{33} = \frac{2\sigma_{33} - \left(\sigma_{11} + \sigma_{22}\right)}{2\mu^{Newton}} \tag{A.13}$$

$$\dot{\varepsilon}_{13} = \frac{3\sigma_{13}}{2\mu^{Newton}} \tag{A.14}$$

Rearranging (A.12) allows to express the normal stress σ_{22} in the third dimension as

$$\sigma_{22} = \frac{1}{2}\left(\sigma_{11} + \sigma_{33}\right) \tag{A.15}$$

Introducing (A.15) in (A.11) and (A.13), respectively, yields

$$\dot{\varepsilon}_{11} = \frac{3}{4} \frac{\left(\sigma_{11} - \sigma_{33}\right)}{\mu^{Newton}} \qquad (A.16)$$

$$\dot{\varepsilon}_{33} = -\frac{3}{4} \frac{\left(\sigma_{11} - \sigma_{33}\right)}{\mu^{Newton}} \qquad (A.17)$$

The equations (A.16) and (A.17) indicate that the normal strain rate components $\dot{\varepsilon}_{11}$ and $\dot{\varepsilon}_{33}$ are opposite in sign but equal in value, i.e. $\dot{\varepsilon}_{33} = -\dot{\varepsilon}_{11}$.

Considering an infinite slope, the normal strain (and thus the normal strain rate) parallel to the slope is suppressed, hence $\dot{\varepsilon}_{11} = 0$. Consequently, the normal strain rate perpendicular to the slope is likewise zero, thus

$$\dot{\varepsilon}_{11} = -\dot{\varepsilon}_{33} = 0 \qquad (A.18)$$

Taking account of (A.18) indicates that the difference of the normal stress components σ_{11} and σ_{33} in (A.16) has to be zero, therefore

$$\sigma_{11} = \sigma_{33} \qquad (A.19)$$

Accordingly to the Mohr circle in Figure A.1, the shear stress associated with the normal stresses $\sigma_{11} = \sigma_{33}$ is the maximum shear stress $\sigma_{13,max} = \sigma_{13}$.
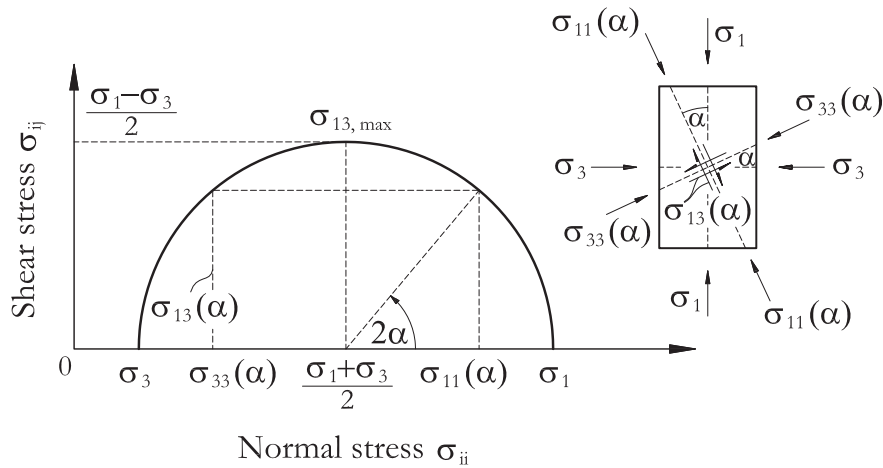
Figure A.1
Shear stress versus normal stress diagram showing the relationship of principal and general stresses by means of the Mohr circle.

Introducing (A.19) in (A.15) implicates that all normal stress components are equal

$$\sigma_{11} = \sigma_{22} = \sigma_{33} = \sigma_m \tag{A.20}$$

The stress state of a volume element parallel to the infinte slope surface is thus characterised by a hydrostatic (normal) stress σ_m, and a maximum deviatoric stress σ_{13}. The principal stress axes are rotated by $\alpha = 45° = \pi/2$ in respect to the slope inclination. Consequently, the maximum principal stress σ_1 is orientated 45° in clockwise direction form the slope dip line, while the minimum principal stress σ_3 is orientated 45° in anti-clockwise direction. This stress field causes a maximum dip slope directed shear stress.

Since the axial strain rate components vanish ($\dot{\varepsilon}_{11} = \dot{\varepsilon}_{33} = 0$), the two-dimensional equation (A.10) reduces to a simple shear geometry which can be expressed as

$$\dot{\varepsilon}_{13} = \frac{3\sigma_{13}}{2\mu^{Newton}} \tag{A.21}$$

The strain rate in the plane of deformation can be expressed in terms of an angular shear strain rate (compare with Figure A.2)

$$\dot{\gamma}_{13} = 2\dot{\varepsilon}_{13} = \frac{3\sigma_{13}}{\mu^{Newton}} = \frac{\sigma_{13}}{\bar{\mu}^{Newton}} \tag{A.22}$$

where $\dot{\gamma}_{13}$ is the angular strain rate in the $x_1 - x_3$ - plane, and $\bar{\mu}^{Newton} = \frac{1}{3}\mu^{Newton}$ denotes the Newtonian shear viscosity.

for small deformations:

$$\dot{\gamma}_{13} \cdot \frac{1}{2} \sim \dot{\varepsilon}_{13} \cdot 1$$

$$\rightarrow \dot{\gamma}_{13} \sim 2\dot{\varepsilon}_{13}$$

$\dot{\gamma}_{13}$ ... angular shear strain [radiant]
$\dot{\varepsilon}_{13}$ ... shear strain [-]
1 ... edge length of square
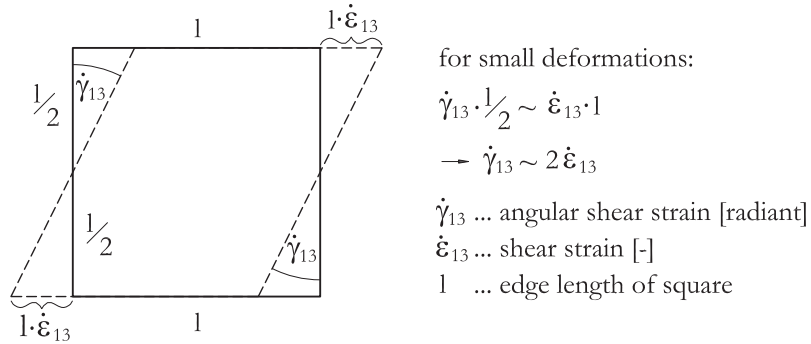
Figure A.2
Geometrical relationship of shear strain rate $\dot{\varepsilon}_{13}$ and angular shear strain rate $\dot{\gamma}_{13}$ for small strain rates (the deformation is here strongly exaggerated).

For all further plane strain considerations in this thesis, the notation is simplified to

$$\dot{\gamma}_{13} = \dot{\gamma} \qquad \sigma_{13} = \tau_{\dot{\gamma}} \tag{A.23}$$

where $\tau_{\dot{\gamma}}$ denotes the shear stress related to the shear strain rate $\dot{\gamma}$ i.e. viscous deformation analysis. Using the above simplifications allows to express Newton's model as

$$\dot{\gamma} = \frac{\tau_{\dot{\gamma}}}{\overline{\mu}^{Newton}} \tag{3.1}$$

The Newtonian shear viscosity $\overline{\mu}^{Newton}$ reflects (similar to Hook's spring constant K) the inherent resistance of the material against shear deformation in time.

(d+e) Vulliet-Hutter

Vulliet & Hutter (1988a) introduced a deviatoric and hydrostatic stress dependent creep model of the form

$$\dot{\boldsymbol{\varepsilon}} = b^{VH} \cdot \boldsymbol{\sigma}_{dev} \tag{A.24}$$

with $\dot{\boldsymbol{\varepsilon}}$ and $\boldsymbol{\sigma}_{dev}$ being the strain rate tensor and the deviatoric stress tensor, respectively, and b^{VH} is a scalar value defined as

$$b^{VH} = A^{VH} \cdot \sqrt{\frac{\sigma_{devII}^{m^{VH}-1}}{\sigma_{devII,f}^{m^{VH}}}} \tag{A.25}$$

where A^{VH} is a material-specific rate factor, m^{VH} is a dimensionless exponent, σ_{devII} is the second invariant of the deviatoric stress tensor, and $\sigma_{devII,f}$ is the second invariant of the deviatoric stress tensor at failure.

The second invariant σ_{devII} of the general deviatoric stress tensors $\boldsymbol{\sigma}_{dev}$ (or, alternatively, the principal deviatoric stress tensor $\boldsymbol{\sigma}_{dev}^{p}$) is given by

$$\sigma_{devII} = \frac{1}{2} \left(\sigma_{dev,ij} \sigma_{dev,ij} \right) = \frac{1}{2} tr \left(\boldsymbol{\sigma}_{dev}^{p\,2} \right) \tag{A.26}$$

Using the general deviatoric stress tensor $\boldsymbol{\sigma}_{dev}$ as given in expression (2.15), equation (A.26) yields

$$\sigma_{devII} = \frac{1}{2} \left[\left(\frac{2\sigma_{11} - \sigma_{22} - \sigma_{33}}{3} \right)^2 + \left(\frac{2\sigma_{22} - \sigma_{11} - \sigma_{33}}{3} \right)^2 + \ldots \right.$$
$$\left. \ldots \left(\frac{2\sigma_{33} - \sigma_{11} - \sigma_{22}}{3} \right)^2 + 2 \left(\sigma_{12}^2 + \sigma_{23}^2 + \sigma_{13}^2 \right) \right]$$

(A.27)

$$= \frac{2\sigma_{11}^2 + 2\sigma_{22}^2 + 2\sigma_{33}^2 - 2\sigma_{11}\sigma_{22} - 2\sigma_{22}\sigma_{33} - 2\sigma_{11}\sigma_{33}}{6} + \sigma_{12}^2 + \sigma_{23}^2 + \sigma_{13}^2$$

$$= \frac{(\sigma_{11} - \sigma_{22})^2 + (\sigma_{22} - \sigma_{33})^2 + (\sigma_{33} - \sigma_{11})^2}{6} + \sigma_{12}^2 + \sigma_{23}^2 + \sigma_{13}^2$$

Alternatively, for principal deviatoric stresses $\boldsymbol{\sigma}_{dev}^p$ as given in expression (2.16), the invariant σ_{devII} is obtained as

$$\sigma_{devII} = \frac{(\sigma_1 - \sigma_2)^2 + (\sigma_2 - \sigma_3)^2 + (\sigma_3 - \sigma_1)^2}{6}$$

(A.28)

Since σ_{devII} acts as the numerator in (A.25), equation (A.28) indicates that $b^{VH} > 0$ for any arbitrary stress state including a deviatoric stress portion, while $b^{VH} = 0$ for a hydrostatic stress state $\sigma_1 = \sigma_2 = \sigma_3$.[13]

Introducing the strain rate (2.10) and the deviatoric stress (2.15) as vectors in (A.24), the Vulliet-Hutter stress-strain rate relationship can be expressed by

$$\begin{bmatrix} \dot{\varepsilon}_{11} \\ \dot{\varepsilon}_{22} \\ \dot{\varepsilon}_{33} \\ \dot{\varepsilon}_{12} \\ \dot{\varepsilon}_{23} \\ \dot{\varepsilon}_{13} \end{bmatrix} = \frac{b^{VH}}{3} \cdot \begin{bmatrix} 2\sigma_{11} - \sigma_{22} - \sigma_{33} \\ 2\sigma_{22} - \sigma_{11} - \sigma_{33} \\ 2\sigma_{33} - \sigma_{11} - \sigma_{22} \\ 3\sigma_{12} \\ 3\sigma_{23} \\ 3\sigma_{13} \end{bmatrix}$$

(A.29)

Assuming plane strain conditions, thus all deformations and all shear stresses in the x_2-direction are zero, i.e. $\dot{\varepsilon}_{12} = \dot{\varepsilon}_{23} = \dot{\varepsilon}_{22} = \sigma_{12} = \sigma_{23} = 0$, (A.29) reduces to

$$\begin{bmatrix} \dot{\varepsilon}_{11} \\ 0 \\ \dot{\varepsilon}_{33} \\ \dot{\varepsilon}_{13} \end{bmatrix} = \frac{b^{VH}}{3} \cdot \begin{bmatrix} 2\sigma_{11} - \sigma_{22} - \sigma_{33} \\ 2\sigma_{22} - \sigma_{11} - \sigma_{33} \\ 2\sigma_{33} - \sigma_{11} - \sigma_{22} \\ 3\sigma_{13} \end{bmatrix}$$

(A.30)

---

[13] This result displays the inherent assumption of the Vulliet-Hutter constitutive relationship that a pure hydrostatic stress state does not induce any deformation.

Extracting the second row of the vector equation and considering that $b^{VH} > 0$ for any deviatoric stress state leads to

$$2\sigma_{22} - \sigma_{11} - \sigma_{33} = 0 \tag{A.31}$$

Rearranging (A.31) yields the normal stress component perpendicular to the plane of deformation i.e. in the x_2 - direction

$$\sigma_{22} = \frac{\sigma_{11} + \sigma_{33}}{2} = \sigma_2 \tag{A.32}$$

Introducing (A.32) in (A.30) yields

$$\begin{bmatrix} \dot{\varepsilon}_{11} \\ 0 \\ \dot{\varepsilon}_{33} \\ \dot{\varepsilon}_{13} \end{bmatrix} = \frac{b^{VH}}{2} \cdot \begin{bmatrix} \sigma_{11} - \sigma_{33} \\ 0 \\ \sigma_{33} - \sigma_{11} \\ 2\sigma_{13} \end{bmatrix} \tag{A.33}$$

Considering an infinite slope with a cubic element orientated parallel to the slope, the normal strain (and thus the normal strain rate) parallel to the slope is suppressed, thus

$$\dot{\varepsilon}_{11} = 0 \tag{A.34}$$

which implies that the difference of the normal stress components σ_{11} and σ_{33} in (A.33) has to be zero, therefore

$$\sigma_{11} = \sigma_{33} \tag{A.35}$$

and consequently

$$\dot{\varepsilon}_{33} = 0 \tag{A.36}$$

which reflects the initial constraint of constant volume deformation (i.e. $\dot{\varepsilon}_{vol} = \dot{\varepsilon}_{11} + \dot{\varepsilon}_{33} = 0$)

Introducing (A.35) in (A.32) implies that all normal stress components of the element are equal

$$\sigma_{11} = \sigma_{22} = \sigma_{33} = \sigma_2 = \sigma_m \tag{A.37}$$

Accordingly to the Mohr circle in Figure A.1, the shear stress(es) associated with the normal stresses $\sigma_{11} = \sigma_{33}$ is (are) equal to the maximum shear stress $\sigma_{13,max} = \sigma_{13}$.

The stress state of the cubic element parallel to the infinte slope surface is thus character-ised by a hydrostatic (normal) stress σ_m and a deviatoric stress σ_{13}. The principal stress axes are rotated with $\alpha = 45° = \pi/2$ in respect to the slope inclination.[14]

Since the normal strain rate components and normal deviatoric stress components vanish, the two-dimensional equation (A.33) reduces to a simple shear expression

$$\begin{bmatrix} 0 \\ 0 \\ 0 \\ \dot{\varepsilon}_{13} \end{bmatrix} = b^{VH} \cdot \begin{bmatrix} 0 \\ 0 \\ 0 \\ \sigma_{13} \end{bmatrix} \tag{A.38}$$

Comparing the findings in (A.37) with the relationship for the mean stress

$$\sigma_{22} = \sigma_2 = \sigma_m = \frac{\sigma_1 + \sigma_2 + \sigma_3}{3} \tag{A.39}$$

shows that

$$\sigma_2 = \sigma_m = \frac{\sigma_1 + \sigma_3}{2} \tag{A.40}$$

Introducing (A.37) into (A.27) and (A.40) into (A.28), respectively, simplifies the second invariant of the deviatoric stress tensor σ_{devII} to

$$\sigma_{devII} = \sigma_{13}{}^2 = \left(\frac{\sigma_1 - \sigma_3}{2} \right)^2 \tag{A.41}$$

Introducing (A.41) in (A.25) gives the scalar b^{VH} for infinite slope considerations as

$$b^{VH} = A^{VH} \cdot \frac{\sigma_{13}{}^{m^{VH}-1}}{\sqrt{\sigma_{devII,f}{}^{m^{VH}}}} \tag{A.42}$$

In order to calculate b^{VH}, the second invariant of the deviatoric stress tensor at failure $\sigma_{devII,f}$ has to be determined by using a predefined failure criterion.

---

[14]   This stress situation in an infinite slope is congruent with the findings for Newton's constitutive relation-ship (compare with point (a) of this section).

The original approach according Vulliet & Hutter (1988a) and a modified approach applied by Schneider-Muntau (2012) using the Drucker-Prager and the Mohr-Coulomb failure criterion, respectively, are presented in the following subsections (d) and (e).

(d) Original Vulliet-Hutter

In accordance with Vulliet & Hutter (1988a) the second invariant of the deviatoric stress tensor at failure is expressed by means of the Drucker-Prager failure criterion

$$\sigma_{devII,f} = \left(k + 3\xi\sigma_m\right)^2 \tag{A.43}$$

with k and ξ being factors which can be expressed in terms of the Mohr-Coulomb strength parameters, i.e. friction angle φ and cohesion c, as

$$k = \frac{6c\cos\varphi}{\sqrt{3}\left(3 - \sin\varphi\right)} \tag{A.44}$$

$$\xi = \frac{2\sin\varphi}{\sqrt{3}\left(3 - \sin\varphi\right)} \tag{A.45}$$

Introducing (A.44) and (A.45) in (A.43) yields

$$\sigma_{devII,f} = \left[\frac{6c\cos\varphi + 6\sigma_m\sin\varphi}{\sqrt{3}\left(3 - \sin\varphi\right)}\right]^2 = \left[\frac{\sqrt{12}\left(c\cos\varphi + \sigma_m\sin\varphi\right)}{3 - \sin\varphi}\right]^2 \tag{A.46}$$

Consequently, introducing (A.46) in (A.42) yields

$$b^{VH_{DP}} = A^{VH_{DP}} \cdot \sigma_{13}{}^{m^{VH,DP}-1} \cdot \left[\frac{3 - \sin\varphi}{\sqrt{12}\left(c\cos\varphi + \sigma_m\sin\varphi\right)}\right]^{m^{VH_{DP}}} \tag{A.47}$$

where $A^{VH_{DP}}$ and $m^{VH_{DP}}$ are the respective rate factor and exponent associated with the Drucker-Prager failure criterion.

Introducing (A.47) in (A.38) yields the shear strain rate $\dot{\varepsilon}_{13}$ for an infinite slope as

$$\dot{\varepsilon}_{13} = A^{VH_{DP}} \cdot \left[\frac{\sigma_{13}\left(3 - \sin\varphi\right)}{\sqrt{12}\left(c\cos\varphi + \sigma_m\sin\varphi\right)}\right]^{m^{VH_{DP}}} \tag{A.48}$$

The angular shear strain rate $\dot{\gamma}_{13}$ for an infinite slope is hence

$$\dot{\gamma}_{13} = 2\dot{\varepsilon}_{13} = 2A^{VH_{DP}} \cdot \left[\frac{\sigma_{13}(3-\sin\varphi)}{\sqrt{12}\left(c\cos\varphi + \sigma_m \sin\varphi\right)} \right]^{m^{VH_{DP}}} \tag{A.49}$$

Assuming that σ_{33} and σ_{13} represent the respective normal and shear stress in the plane parallel to the infinite slope surface and considering (A.37), thus $\sigma_m = \sigma_{33}$, allows to rewrite (A.49) as

$$\dot{\gamma}_{13} = 2\dot{\varepsilon}_{13} = 2A^{VH_{DP}} \cdot \left[\frac{\sigma_{13}(3-\sin\varphi)}{\sqrt{12}\left(c\cos\varphi + \sigma_{33} \sin\varphi\right)} \right]^{m^{VH_{DP}}} \tag{A.50}$$

Applying the notation simplifications $\dot{\gamma}_{13} = \dot{\gamma}$, $\sigma_{13} = \tau_{\dot{\gamma}}$ and $\sigma_{33} = \sigma_{\dot{\gamma}}$ yields the final formulation as follows

$$\dot{\gamma} = 2A^{VH_{DP}} \cdot \left[\frac{\tau_{\dot{\gamma}}(3-\sin\varphi)}{\sqrt{12}\left(c\cos\varphi + \sigma_{\dot{\gamma}} \sin\varphi\right)} \right]^{m^{VH_{DP}}} \tag{A.51}$$

where $\tau_{\dot{\gamma}}$ and $\sigma_{\dot{\gamma}}$ denote the shear stress and normal stress related to the shear strain rate $\dot{\gamma}$, i.e. viscous deformation analysis.

In the presence of a hydrostatic water pressure u, the normal stress $\sigma_{\dot{\gamma}}$ in (A.51) is replaced by the effective normal stress $\sigma'_{\dot{\gamma}} = \sigma_{\dot{\gamma}} - u$, leading to the formula

$$\dot{\gamma} = 2A^{VH_{DP}} \cdot \left\{ \frac{\tau_{\dot{\gamma}}(3-\sin\varphi)}{\sqrt{12}\left[c\cos\varphi + \left(\sigma_{\dot{\gamma}} - u\right)\sin\varphi\right]} \right\}^{m^{VH_{DP}}} \tag{3.6}$$

(e) Modified Vulliet-Hutter

In this approach, the Drucker-Prager failure criterion as originally suggested by Vulliet & Hutter (1988a) is substituted by the Mohr-Coulomb failure criterion.

Analogously to σ_{devII} in (A.41), the second invariant of the deviatoric stress tensor at failure $\sigma_{devII,f}$ in plane strain can be formulated as

$$\sigma_{devII,f} = \left(\frac{\sigma_1 - \sigma_3}{2} \right)^2_f \tag{A.52}$$

where $\frac{1}{2}(\sigma_1 - \sigma_3)_f$ is the maximum deviatoric stress in the $x_1 - x_3$ - plane at failure.
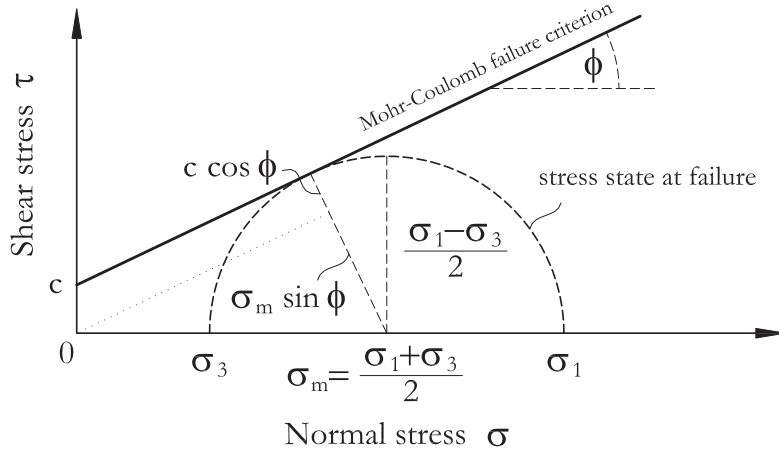
Figure A.3
Mohr-Coulomb failure criterion.

Using the Mohr-Coulomb failure criterion and considering (A.40), $\frac{1}{2}(\sigma_1 - \sigma_3)_f$ can be expressed as (see Figure A.3)

$$\left(\frac{\sigma_1 - \sigma_3}{2}\right)_f = c\cos\varphi + \left(\frac{\sigma_1 + \sigma_3}{2}\right)\sin\varphi = c\cos\varphi + \sigma_m \sin\varphi \tag{A.53}$$

Consequently, introducing (A.53) in (A.52) yields

$$\sigma_{devII,f} = \left(c\cos\varphi + \sigma_m \sin\varphi\right)^2 \tag{A.54}$$

Introducing (A.54) into (A.42) and modifying the rate factor A^{VH} to $A^{VH_{MC}}$ and the exponent m^{VH} to $m^{VH_{MC}}$, thus, both parameters now referring to the solution according the Mohr-Coulomb failure criterion, yields

$$b^{VH_{MC}} = A^{VH_{MC}} \cdot \frac{\sigma_{13}^{m^{VH_{MC}}-1}}{\left(c\cos\varphi + \sigma_m \sin\varphi\right)^{m^{VH_{MC}}}} \tag{A.55}$$

Introducing (A.55) in (A.38) yields the shear strain rate $\dot{\varepsilon}_{13}$ for an infinite slope as

$$\dot{\varepsilon}_{13} = A^{VH_{MC}} \cdot \left[\frac{\sigma_{13}}{c\cos\varphi + \sigma_m \sin\varphi}\right]^{m^{VH_{MC}}} \tag{A.56}$$

The angular shear strain rate $\dot{\gamma}_{13}$ for an infinite slope is now described as

$$\dot{\gamma}_{13} = 2\dot{\varepsilon}_{13} = 2A^{VH_{MC}} \cdot \left[\frac{\sigma_{13}}{c\cos\varphi + \sigma_m \sin\varphi} \right]^{m^{VH_{MC}}} \tag{A.57}$$

Assuming that σ_{33} and σ_{13} represent the associated normal and shear stress in the plane parallel to the infinite slope surface and considering (A.37), thus $\sigma_m = \sigma_{33}$, allows to rewrite (A.57) as

$$\dot{\gamma}_{13} = 2\dot{\varepsilon}_{13} = 2A^{VH_{MC}} \cdot \left[\frac{\sigma_{13}}{c\cos\varphi + \sigma_{33} \sin\varphi} \right]^{m^{VH_{MC}}} \tag{A.58}$$

Applying equivalent considerations as in the previous section for the original Vulliet-Hutter approach (transition from (A.49) to (A.50)), hence substituting $\sigma_m = \sigma_{33}$ and applying the notation simplifications $\dot{\gamma}_{13} = \dot{\gamma}$, $\sigma_{13} = \tau_{\dot{\gamma}}$ and $\sigma_{33} = \sigma_{\dot{\gamma}}$, yields the formula

$$\dot{\gamma} = 2A^{VH_{MC}} \cdot \left[\frac{\tau_{\dot{\gamma}}}{c\cos\varphi + \sigma_{\dot{\gamma}} \sin\varphi} \right]^{m^{VH_{MC}}} \tag{A.59}$$

As previously, in the presence of a hydrostatic water pressure u in the viscous layer, the normal stress $\sigma_{\dot{\gamma}}$ in (A.59) is replaced by the effective normal stress $\sigma'_{\dot{\gamma}} = \sigma_{\dot{\gamma}} - u$, leading to the final formula

$$\dot{\gamma} = 2A^{VH_{MC}} \cdot \left[\frac{\tau}{c\cos\varphi + \left(\sigma_{\dot{\gamma}} - u\right)\sin\varphi} \right]^{m^{VH_{MC}}} \tag{3.7}$$

A.2 Stability analysis: Extended derivations

Complementary derivations to Chapter 4 (Section 4.3)

A.2.1 Infinite slope model

Isolating the unknown forces T in (4.12) and N in (4.13), respectively, yields

$$T = \left(W + P_v\right)\sin\alpha - P_h\cos\alpha \tag{A.60}$$

$$N = \left(W + P_v\right)\cos\alpha + P_h\sin\alpha \tag{A.61}$$

Substituting (4.5) for $T = T_\eta$ in (A.60) yields

$$\frac{C + \left(N_\eta - U\right)\tan\varphi}{\eta} = \left(W + P_v\right)\sin\alpha - P_h\cos\alpha \tag{A.62}$$

Introducing (A.61) for $N = N_\eta$ and isolating the Factor of Safety η yields

$$\eta = \frac{C + \left(W + P_v\right)\cos\alpha\tan\varphi + \left(P_h\sin\alpha - U\right)\tan\varphi}{\left(W + P_v\right)\sin\alpha - P_h\cos\alpha} \tag{4.14}$$

Replacing the forces W, P_v, P_h, U and C in (4.14) by the formulations in (4.6), (4.7), (4.9) and (4.4) yields

$$\eta = \frac{\dfrac{bc}{\cos\alpha} + b\cos\alpha\tan\varphi\left[\gamma h + h_w\left(\gamma_r - \gamma - \gamma_w\right) + p_v + p_h\tan^2\alpha\right]}{b\sin\alpha\left[\gamma h + h_w\left(\gamma_r - \gamma\right) + p_v - p_h\right]} \tag{A.63}$$

By cancelling out the variable b and dividing by $\cos\alpha$, equation (A.63) can be rearranged to the final formula for determining the Factor of Safety of an infinite slope with parallel groundwater flow and additional vertical and horizontal loading

$$\eta = \frac{\dfrac{c}{\cos^2\alpha} + \tan\varphi\left[\gamma h + h_w\left(\gamma_r - \gamma - \gamma_w\right) + p_v + p_h\tan^2\alpha\right]}{\tan\alpha\left[\gamma h + h_w\left(\gamma_r - \gamma\right) + p_v - p_h\right]} \tag{4.15}$$

A.2.2   Rotational mechanism with circular slip surface

A.2.2.1   Swedish Circle $\left(\varphi = 0\right)$ method

See Section 4.3.2.1 in the main part.

A.2.2.2   Fellenius method

Introducing the simplified formulation for the total normal force $N_{\eta,i}$ (4.21) in the moment equilibrium equation (4.19) yields

$$\sum_{i=1}^{n} M_i = \left\{ \begin{array}{l} \displaystyle\sum_{i=1}^{n} \left[\left(W_i + P_{v,i} \right) \sin\alpha_i - P_{h,i} \cos\alpha_i \left(1 - \cos\alpha_i \frac{h_i}{r} \right) \right] \dots \\[2mm] \dots - \dfrac{1}{\eta} \displaystyle\sum_{i=1}^{n} \left[C_i + \left(\begin{array}{l} \left(W_i + P_{v,i} \right)\cos\alpha_i + P_{h,i} \sin\alpha_i \dots \\ \dots + \left(U_{i(i+1)} - U_{i(i-1)} \right)\sin\alpha_i - U_i \end{array} \right) \cdot \tan\varphi_i \right] \end{array} \right\} = 0 \qquad (A.64)$$

Isolating η in (A.64) yields the equation for the global Factor of Safety

$$\eta = \frac{\displaystyle\sum_{i=1}^{n} \left\{ C_i + \left[\left(W_i + P_{v,i} \right)\cos\alpha_i + P_{h,i} \sin\alpha_i + \left(U_{i(i+1)} - U_{i(i-1)} \right)\sin\alpha_i - U_i \right] \cdot \tan\varphi_i \right\}}{\displaystyle\sum_{i=1}^{n} \left[\left(W_i + P_{v,i} \right)\sin\alpha_i - P_{h,i} \cos\alpha_i \left(1 - \frac{h_i}{r} \cos\alpha_i \right) \right]} \qquad (4.22)$$

A.2.2.3   Simplified Bishop method

Substituting $N_{\eta,i}$ as defined in (4.26) in the moment equilibrium equation (4.19) yields

$$\sum_{i=1}^{n} M_i = \left\{ \begin{array}{l} \dfrac{1}{\eta} \displaystyle\sum_{i=1}^{n} \left[\dfrac{\eta \tan\varphi_i \left(W_i + P_{v,i} \right)}{\eta \cos\alpha_i + \sin\alpha_i \tan\varphi_i} \right] - \displaystyle\sum_{i=1}^{n} \left[\left(W_i + P_{v,i} \right)\sin\alpha_i \right] \dots \\[3mm] + \dfrac{1}{\eta} \displaystyle\sum_{i=1}^{n} \left[\left(C_i - U_i \tan\varphi_i \right) \cdot \left(1 - \dfrac{\sin\alpha_i \tan\varphi_i}{\eta \cos\alpha_i + \sin\alpha_i \tan\varphi_i} \right) \right] \dots \\[3mm] \dots + \displaystyle\sum_{i=1}^{n} \left[P_{h,i} \cos\alpha_i \left(1 - \dfrac{h_i}{r} \cos\alpha_i \right) \right] \end{array} \right\} = 0 \qquad (A.65)$$

Isolating in (A.65) the η outside of the summation terms yields the implicit equation for the global Factor of Safety

$$\eta = \frac{\sum_{i=1}^{n}\left[\dfrac{\eta \tan\varphi_i\left(W_i + P_{v,i}\right)}{\eta\cos\alpha_i + \sin\alpha_i \tan\varphi_i} + \left(C_i - U_i \tan\varphi_i\right)\left(1 - \dfrac{\sin\alpha_i \tan\varphi_i}{\eta\cos\alpha_i + \sin\alpha_i \tan\varphi_i}\right)\right]}{\sum_{i=1}^{n}\left[\left(W_i + P_{v,i}\right)\sin\alpha_i - P_{h,i}\cos\alpha_i\left(1 - \dfrac{h_i}{r}\cos\alpha_i\right)\right]} \tag{4.27}$$

A.2.3 Translational mechanism with irregular slip surface

A.2.3.1 Simplified Janbu method

The horizontal force equilibrium is given

- for the uppermost slice $i = 1$:
  $$P_{h,1} - N_{\eta,1}\sin\alpha_1 + T_{\eta,1}\cos\alpha_1 + E'_{\eta,12}\cos\vartheta_{12} + U_{12} = 0 \tag{A.66}$$

- for the slices $i = \{2,...,n-1\}$:
  $$\left\{ \begin{aligned} & P_{h,i} - N_{\eta,i}\sin\alpha_i + T_{\eta,i}\cos\alpha_i - E'_{\eta,i(i-1)}\cos\vartheta_{i(i-1)}... \\ & ... - U_{i(i-1)} + E'_{\eta,i(i+1)}\cos\vartheta_{i(i+1)} + U_{i(i+1)} \end{aligned} \right\} = 0 \tag{A.67}$$

- for the lowermost slice $i = n$:
  $$P_{h,n} - N_{\eta,n}\sin\alpha_n + T_{\eta,n}\cos\alpha_n - E'_{\eta,n(n-1)}\cos\vartheta_{n(n-1)} - U_{n(n-1)} = 0 \tag{A.68}$$

Based on the principle *"actio est reactio"* , the horizontal resultants of the opposite total interslice forces (E' and U) are equal in value, thus, for $i = \{2,...,n-1\}$

$$\left|\vec{E}'_{\eta,i(i+1)}\cos\vartheta_{i(i+1)} + \vec{U}_{i(i+1)}\right| = \left|\vec{E}'_{\eta,(i+1)i}\cos\vartheta_{(i+1)i} + \vec{U}_{(i+1)i}\right|$$
$$\left|\vec{E}'_{\eta,i(i-1)}\cos\vartheta_{i(i-1)} + \vec{U}_{i(i-1)}\right| = \left|\vec{E}'_{\eta,(i-1)i}\cos\vartheta_{(i-1)i} + \vec{U}_{(i-1)i}\right| \tag{A.69}$$

Therefore, in the summation of all horizontal force equilibrium equations the interslice forces cancel out

$$\sum_{i=1}^{n}\left(P_{h,i} - N_{\eta,i}\sin\alpha_i + T_{\eta,i}\cos\alpha_i\right) = 0 \tag{4.29}$$

Introducing $T_{\eta,i}$ according (4.5) in the overall horizonal force equilibrium (4.29) gives

$$\sum_{i=1}^{n}\left[P_{h,i}+N_{\eta,i}\left(\frac{\cos\alpha_i \tan\varphi_i}{\eta}-\sin\alpha_i\right)+\left(\frac{C_i-U_i \tan\varphi_i}{\eta}\right)\cdot\cos\alpha_i\right]=0 \qquad (A.70)$$

Using the slice vertical force equilibrium (4.23), the associated simplification (4.24) and the formulation (4.5), the total normal force $N_{\eta,i}$ can be expressed by (4.26) as given in Section 4.3.2.3 in the main part. Introducing (4.26) for $N_{\eta,i}$ in (A.70) and simplifying the term yields

$$\left\{\begin{array}{c}\sum_{i=1}^{n}\left[P_{h,i}+\frac{\left(\tan\varphi_i-\eta\tan\alpha_i\right)\left(W_i+P_{v,i}\right)}{\tan\alpha_i \tan\varphi_i+\eta}\right]...\\[2mm]...+\sum_{i=1}^{n}\left[\left(\frac{C_i-U_i \tan\varphi_i}{\eta}\right)\left(\cos\alpha_i+\frac{\eta\tan\alpha_i-\tan\varphi_i}{\tan\alpha_i \tan\varphi_i+\eta}\cdot\sin\alpha_i\right)\right]\end{array}\right\}=0 \qquad (A.71)$$

Isolating in (A.71) η in the numerator of the first fraction term yields the implicit equation for the global Factor of Safety

$$\eta=\frac{\left\{\begin{array}{c}\sum_{i=1}^{n}\left[P_{h,i}+\frac{\left(W_i+P_{v,i}\right)\tan\varphi_i}{\tan\alpha_i \tan\varphi_i+\eta}\right]...\\[2mm]...+\sum_{i=1}^{n}\left[\left(\frac{C_i-U_i \tan\varphi_i}{\eta}\right)\left(\cos\alpha_i+\frac{\eta\tan\alpha_i-\tan\varphi_i}{\tan\alpha_i \tan\varphi_i+\eta}\cdot\sin\alpha_i\right)\right]\end{array}\right\}}{\sum_{i=1}^{n}\left[\frac{\left(W_i+P_{v,i}\right)\tan\alpha_i}{\tan\alpha_i \tan\varphi_i+\eta}\right]} \qquad (4.30)$$

A.3 Shear zone creep deformation: Derivations

Complementary derivations to Chapter 5 (Section 5.2)

(b) Bingham

Equating the angular shear strain rate $\dot{\gamma}$ in the geometric equation (5.3) with the Bingham constitutive equation (3.2) and, subsequently, isolating v yields

$$v = 0 \qquad \qquad \text{for} \quad \tau_{\dot{\gamma}} < \tau_y^{Bingham}$$

$$v = \frac{d}{\overline{\mu}^{Bingham}}\left(\tau_{\dot{\gamma}} - \tau_y^{Bingham}\right) \quad \text{for} \quad \tau_{\dot{\gamma}} \geq \tau_y^{Bingham} \tag{A.72}$$

Isolating $\tau_{\dot{\gamma}}$ in the second equation of (A.72) gives

$$\tau_{\dot{\gamma}} = \tau_y^{Bingham} + \overline{\mu}^{Bingham} \cdot \frac{v}{d} \tag{A.73}$$

Equating (A.73) with (5.5) and isolating the shear force $T_{\dot{\gamma}}$ gives

$$T_{\dot{\gamma}} = \frac{b}{\cos\alpha}\left(\tau_y^{Bingham} + \overline{\mu}^{Bingham} \cdot \frac{v}{d}\right) \tag{5.7}$$

(c) Norton

Equating the angular shear strain rate $\dot{\gamma}$ in the geometric equation (5.3) with the constitutive equation of the modified Norton approach (3.4), and subsequently isolating v yields

$$v = 0 \qquad \qquad \text{for} \quad \tau_{\dot{\gamma}} < \tau_y^{Norton}$$

$$v = \frac{d}{\overline{\mu}^{Norton}}\left(\tau_{\dot{\gamma}} - \tau_y^{Norton}\right)^{m^{Norton}} \quad \text{for} \quad \tau_{\dot{\gamma}} \geq \tau_y^{Norton} \tag{A.74}$$

Isolating $\tau_{\dot{\gamma}}$ in the second equation of (A.74) gives

$$\tau_{\dot{\gamma}} = \tau_y^{Norton} + \sqrt[\langle m^{Norton}\rangle]{\frac{v\,\overline{\mu}^{Norton}}{d}} \tag{A.75}$$

Equating (A.75) with (5.5) and isolating the shear force $T_{\dot{\gamma}}$ gives

$$T_{\dot{\gamma}} = \frac{b}{\cos\alpha}\left(\tau_y^{Norton} + \sqrt[\langle m^{Norton}\rangle]{\frac{v\,\overline{\mu}^{Norton}}{d}}\right) \tag{5.8}$$

(d) Original Vulliet-Hutter

Equating the angular shear strain rate $\dot{\gamma}$ in the geometric equation (5.3) with the constitutive equation of the original Vulliet-Hutter approach (3.6), and isolating v yields to

$$v = 2dA^{VH_{DP}} \cdot \left\{ \frac{\tau_{\dot{\gamma}}(3-\sin\varphi)}{\sqrt{12}\left[c\cos\varphi+(\sigma_{\dot{\gamma}}-u)\sin\varphi\right]} \right\}^{m^{VH_{DP}}} \tag{A.76}$$

Isolating $\tau_{\dot{\gamma}}$ in (A.76) gives

$$\tau_{\dot{\gamma}} = \frac{\sqrt{12}\left[c\cos\varphi+(\sigma_{\dot{\gamma}}-u)\sin\varphi\right]}{3-\sin\varphi} \cdot {}^{\langle m^{VH_{DP}}\rangle}\sqrt{\frac{v}{2dA^{VH_{DP}}}} \tag{A.77}$$

Equating (A.77) and (5.5) and isolating $T_{\dot{\gamma}}$ gives the shear force according the original Vulliet-Hutter approach using the Drucker-Prager failure criterion

$$T_{\dot{\gamma}} = \frac{\sqrt{12}b\left[c\cos\varphi+(\sigma_{\dot{\gamma}}-u)\sin\varphi\right]}{\cos\alpha(3-\sin\varphi)} \cdot {}^{\langle m^{VH_{DP}}\rangle}\sqrt{\frac{v}{2dA^{VH_{DP}}}} \tag{A.78}$$

Introducing in (A.78) the substitutions

$$b(\sigma_{\dot{\gamma}}-u)=(N_{\dot{\gamma}}-U)\cos\alpha \qquad \text{and} \qquad bc=\cos\alpha C \tag{A.79}$$

yields for the original Vulliet Hutter approach

$$T_{\dot{\gamma}} = \frac{\sqrt{12}\left[C\cos\varphi+(N_{\dot{\gamma}}-U)\sin\varphi\right]}{3-\sin\varphi} \cdot {}^{\langle m^{VH_{DP}}\rangle}\sqrt{\frac{v}{2dA^{VH_{DP}}}} \tag{5.9}$$

(e) Modified Vulliet-Hutter

Equating the angular shear strain rate $\dot{\gamma}$ in the geometric equation (5.3) with the modified Vulliet-Hutter equation (3.7) and isolating v yields to

$$v = 2dA^{VH_{MC}} \cdot \left[\frac{\tau_{\dot{\gamma}}}{c\cos\varphi+(\sigma_{\dot{\gamma}}-u)\sin\varphi} \right]^{m^{VH_{MC}}} \tag{A.80}$$

Applying the same procedure as in previous subsection (d) yields the shear force $T_{\dot{\gamma}}$ as

$$T_{\dot{\gamma}} = \left[C\cos\varphi+(N_{\dot{\gamma}}-U)\sin\varphi\right] \cdot {}^{\langle m^{VH_{MC}}\rangle}\sqrt{\frac{v}{2dA^{VH_{MC}}}} \tag{5.10}$$

A.4 CrEAM algorithms: Extended derivations

Complementary derivations to Chapter 5 (Section 5.4)

In the subsequent derivations, the following substitution term is applied

$$\sqrt[m]{v} = v^{\left(\frac{1}{m}\right)} = v \cdot v^{\left(\frac{1-m}{m}\right)} = v \cdot \sqrt[m]{v^{1-m}} \tag{A.81}$$

A.4.1 Infinite slope model

See Section 5.4.1 in the main part.

A.4.2 Rotational mechanism with circular creep interface

A.4.2.1 D-CrEAM^{rot}

(c) Norton

Introducing $T_{\dot{\gamma},i}$ according (5.8) in the moment equilibrium equation (5.34) yields

$$\sum_{i=1}^{n} M_i = r \sum_{i=1}^{n} \left[\begin{array}{c} \dfrac{b_i}{\cos\alpha_i}\left(\tau_{y,i}^{Norton} + \langle m_i^{Norton}\rangle\sqrt{\dfrac{v_i\overline{\mu}_i^{Norton}}{d_i}} \right)\dots \\ \dots - \left(W_i + P_{v,i}\right)\sin\alpha_i + P_{h,i}\cos\alpha_i\left(1 - \cos\alpha_i\dfrac{h_i}{r}\right) \end{array} \right] = 0 \tag{A.82}$$

Dividing (A.82) by the radius r and taking account of the kinematical requirement of constant displacements rates at the slices bases, thus $v_i = v$, the moment equilibrium equation reduces to

$$\sum_{i=1}^{n} \left[\begin{array}{c} \dfrac{b_i}{\cos\alpha_i}\left(\tau_{y,i}^{Norton} + \langle m_i^{Norton}\rangle\sqrt{\dfrac{v\overline{\mu}_i^{Norton}}{d_i}} \right)\dots \\ \dots - \left(W_i + P_{v,i}\right)\sin\alpha_i + P_{h,i}\cos\alpha_i\left(1 - \cos\alpha_i\dfrac{h_i}{r}\right) \end{array} \right] = 0 \tag{A.83}$$

General case:

Expanding $\sqrt[\langle m_i^{Norton} \rangle]{v}$ in (A.83) according (A.81) gives

$$\left\{ v \cdot \sum_{i=1}^{n} \left[\frac{b_i}{\cos\alpha_i} \sqrt[\langle m_i^{Norton} \rangle]{\frac{v^{\left(1-m_i^{Norton}\right)} \overline{\mu}_i^{Norton}}{d_i}} \right] ... \atop + \sum_{i=1}^{n} \left[\frac{b_i \tau_{y,i}^{Norton}}{\cos\alpha_i} - \left(W_i + P_{v,i}\right)\sin\alpha_i + P_{h,i}\cos\alpha_i\left(1-\cos\alpha_i \frac{h_i}{r}\right) \right] \right\} = 0 \qquad \text{(A.84)}$$

Isolating the single v yields the implicit equation for the velocity along the base of the rottional mass, i.e.

$$v = \frac{\displaystyle\sum_{i=1}^{n} \left[\left(W_i + P_{v,i}\right)\sin\alpha_i - \frac{b_i \tau_{y,i}^{Norton}}{\cos\alpha_i} - P_{h,i}\cos\alpha_i\left(1-\cos\alpha_i \frac{h_i}{r}\right) \right]}{\displaystyle\sum_{i=1}^{n} \left[\frac{b_i}{\cos\alpha_i} \cdot \sqrt[\langle m_i^{Norton} \rangle]{\frac{v^{\left(1-m_i^{Norton}\right)} \overline{\mu}_i^{Norton}}{d_i}} \right]} \qquad \text{(5.37)}$$

Special case:

Assuming a constant exponent for all slices $m_i^{Norton} = m^{Norton}$ allows to totally extract v in (A.83), leading to

$$\left\{ \sqrt[\langle m^{Norton} \rangle]{v} \cdot \sum_{i=1}^{n} \left[\frac{b_i}{\cos\alpha_i} \sqrt[\langle m^{Norton} \rangle]{\frac{\overline{\mu}_i^{Norton}}{d_i}} \right] ... \atop + \sum_{i=1}^{n} \left[\frac{b_i \tau_{y,i}^{Norton}}{\cos\alpha_i} - \left(W_i + P_{v,i}\right)\sin\alpha_i + P_{h,i}\cos\alpha_i\left(1-\cos\alpha_i \frac{h_i}{r}\right) \right] \right\} = 0 \qquad \text{(A.85)}$$

Isolating v yields the straightforward equation for the creep velocity

$$v = \left\{ \frac{\displaystyle\sum_{i=1}^{n} \left[\left(W_i + P_{v,i}\right)\sin\alpha_i - \frac{b_i \tau_{y,i}^{Norton}}{\cos\alpha_i} - P_{h,i}\cos\alpha_i\left(1-\cos\alpha_i \frac{h_i}{r}\right) \right]}{\displaystyle\sum_{i=1}^{n} \left(\frac{b_i}{\cos\alpha_i} \cdot \sqrt[\langle m^{Norton} \rangle]{\frac{\overline{\mu}_i^{Norton}}{d_i}} \right)} \right\}^{m^{Norton}} \qquad \text{(5.38)}$$

(b) Bingham

For the linear Bingham model the exponent is set to unity $m^{Norton}=1$, modifying equation (5.38) to

$$v = \frac{\displaystyle\sum_{i=1}^{n}\left[\left(W_i+P_{v,i}\right)\sin\alpha_i - \frac{b_i\tau_{y,i}^{Bingham}}{\cos\alpha_i} - P_{h,i}\cos\alpha_i\left(1-\cos\alpha_i\frac{h_i}{r}\right)\right]}{\displaystyle\sum_{i=1}^{n}\left(\frac{b_i\bar{\mu}_i^{Bingham}}{d_i\cos\alpha_i}\right)} \tag{5.36}$$

(a) Newton

For the Newton model the yield shear stress is set to zero $\tau_{y,i}^{Bingham}=0$, modifying equation (5.36) to

$$v = \frac{\displaystyle\sum_{i=1}^{n}\left[\left(W_i+P_{v,i}\right)\sin\alpha_i - P_{h,i}\cos\alpha_i\left(1-\cos\alpha_i\frac{h_i}{r}\right)\right]}{\displaystyle\sum_{i=1}^{n}\left(\frac{b_i\bar{\mu}_i^{Newton}}{d_i\cos\alpha_i}\right)} \tag{5.35}$$

A.4.2.2 Simplified E-CrEAM^{rot}

(d) Original Vulliet-Hutter

Replacing $T_{\dot{\gamma},i}$ in the moment equilibrium equation (5.34) by the original Vulliet-Hutter constitutive relationship (5.9) yields

$$\sum_{i=1}^{n}M_i = r\sum_{i=1}^{n}\left[\begin{array}{c}\dfrac{\sqrt{12}\left[C_i\cos\varphi_i+\left(N_{\dot{\gamma},i}-U_i\right)\sin\varphi_i\right]}{3-\sin\varphi_i}\cdot\left\langle m_i^{VH_{DP}}\right\rangle\sqrt{\dfrac{v_i}{2d_iA_i^{VH_{DP}}}}\cdots\\[2mm]\cdots-\left(W_i+P_{v,i}\right)\sin\alpha_i+P_{h,i}\cos\alpha_i\left(1-\cos\alpha_i\dfrac{h_i}{r}\right)\end{array}\right]=0 \tag{A.86}$$

Dividing (A.86) by the radius r and taking account of the kinematical requirement of constant displacements rates at the slices bases, thus $v_i=v$, the moment equilibrium equation reduces to

$$\sum_{i=1}^{n}\left[\begin{array}{l}\dfrac{\sqrt{12}\left[C_i\cos\varphi_i+\left(N_{\dot\gamma,i}-U_i\right)\sin\varphi_i\right]}{3-\sin\varphi_i}\cdot\sqrt[\langle m_i^{VH_{DP}}\rangle]{\dfrac{v}{2d_iA_i^{VH_{DP}}}}\cdots\\[2ex]\cdots-\left(W_i+P_{v,i}\right)\sin\alpha_i+P_{h,i}\cos\alpha_i\left(1-\cos\alpha_i\dfrac{h_i}{r}\right)\end{array}\right]=0 \tag{A.87}$$

Substituting (5.39) for $N_{\dot\gamma,i}$ in (A.87) and simplifying the equation gives

$$\sum_{i=1}^{n}\left\{\begin{array}{l}\dfrac{\sqrt{12}\sin\varphi_i}{3-\sin\varphi_i}\cdot\left[\begin{array}{l}\left(W_i+P_{v,i}\right)\cos\alpha_i+C_i\cot\varphi_i+P_{h,i}\sin\alpha_i\cdots\\\cdots+\left(U_{i(i+1)}-U_{i(i-1)}\right)\sin\alpha_i-U_i\end{array}\right]\cdot\sqrt[\langle m_i^{VH_{DP}}\rangle]{\dfrac{v}{2d_iA_i^{VH_{DP}}}}\cdots\\[3ex]\cdots-\left(W_i+P_{v,i}\right)\sin\alpha_i+P_{h,i}\cos\alpha_i\left(1-\cos\alpha_i\dfrac{h_i}{r}\right)\end{array}\right\}=0 \tag{A.88}$$

General case:

Expanding $\sqrt[\langle m_i^{VH_{DP}}\rangle]{v}$ in (A.88) according (A.81) gives

$$\left\{\begin{array}{l}v\cdot\sum_{i=1}^{n}\left\{\dfrac{\sqrt{12}\sin\varphi_i}{3-\sin\varphi_i}\cdot\left[\begin{array}{l}\left(W_i+P_{v,i}\right)\cos\alpha_i+C_i\cot\varphi_i+P_{h,i}\sin\alpha_i\cdots\\\cdots+\left(U_{i(i+1)}-U_{i(i-1)}\right)\sin\alpha_i-U_i\end{array}\right]\cdot\sqrt[\langle m_i^{VH_{DP}}\rangle]{\dfrac{v^{\left(1-m_i^{VH_{DP}}\right)}}{2d_iA_i^{VH_{DP}}}}\right\}\cdots\\[3ex]\cdots-\sum_{i=1}^{n}\left[\left(W_i+P_{v,i}\right)\sin\alpha_i-P_{h,i}\cos\alpha_i\left(1-\cos\alpha_i\dfrac{h_i}{r}\right)\right]\end{array}\right\}=0 \tag{A.89}$$

Isolating the single v yields the implicit equation for the velocity along the base of the rotational mass, i.e.

$$v=\dfrac{\displaystyle\sum_{i=1}^{n}\left[\left(W_i+P_{v,i}\right)\sin\alpha_i-P_{h,i}\cos\alpha_i\left(1-\cos\alpha_i\dfrac{h_i}{r}\right)\right]}{\displaystyle\sum_{i=1}^{n}\left\{\dfrac{\sqrt{12}\sin\varphi_i}{3-\sin\varphi_i}\cdot\sqrt[\langle m_i^{VH_{DP}}\rangle]{\dfrac{v^{\left(1-m_i^{VH_{DP}}\right)}}{2d_iA_i^{VH_{DP}}}}\cdot\left[\begin{array}{l}\left(W_i+P_{v,i}\right)\cos\alpha_i+C_i\cot\varphi_i+P_{h,i}\sin\alpha_i\cdots\\\cdots+\left(U_{i(i+1)}-U_{i(i-1)}\right)\sin\alpha_i-U_i\end{array}\right]\right\}} \tag{5.40}$$

Special case:

Assuming a constant exponent for all slices $m_i^{VH_{DP}} = m^{VH_{DP}}$ allows to totally extract v in (A.88), leading to

$$\left\{ \begin{array}{l} \left\langle m^{VH_{DP}} \right\rangle \sqrt{v} \cdot \sum_{i=1}^{n} \left\{ \frac{\sqrt{12}\sin\varphi_i}{3-\sin\varphi_i} \cdot \left[\begin{array}{l} \left(W_i + P_{v,i}\right)\cos\alpha_i + C_i \cot\varphi_i - U_i... \\ ...+ P_{h,i}\sin\alpha_i + \left(U_{i(i+1)} - U_{i(i-1)}\right)\sin\alpha_i \end{array} \right] \cdot \left(2d_i A_i^{VH_{DP}}\right)^{\left(\frac{-1}{m_i^{VH_{DP}}}\right)} \right\}... \\ ... - \sum_{i=1}^{n} \left[\left(W_i + P_{v,i}\right)\sin\alpha_i - P_{h,i}\cos\alpha_i\left(1-\cos\alpha_i\frac{h_i}{r}\right) \right] \end{array} \right\} = 0 \quad \text{(A.90)}$$

Isolating v yields the straightforward equation for the velocity

$$v = \left\{ \frac{\sum_{i=1}^{n}\left[\left(W_i + P_{v,i}\right)\sin\alpha_i - P_{h,i}\cos\alpha_i\left(1-\cos\alpha_i\frac{h_i}{r}\right) \right]}{\sum_{i=1}^{n}\left\{ \frac{\sqrt{12}\sin\varphi_i}{3-\sin\varphi_i} \cdot \left(2d_i A_i^{VH_{DP}}\right)^{\left(\frac{-1}{m_i^{VH_{DP}}}\right)} \cdot \left[\begin{array}{l} \left(W_i + P_{v,i}\right)\cos\alpha_i + C_i\cot\varphi_i + P_{h,i}\sin\alpha_i... \\ ...+\left(U_{i(i+1)} - U_{i(i-1)}\right)\sin\alpha_i - U_i \end{array} \right] \right\}} \right\}^{m^{VH_{DP}}} \quad \text{(5.41)}$$

(e) Modified Vulliet-Hutter

The equations for the modified Vulliet-Hutter constitutive model are found by introducing (5.10) for the shear force $T_{\gamma,i}$ in the moment equilibrium equation (5.34). Following the same procedure as for the original Vulliet-Hutter approach in the previous section (d) leads to the subsequent final formulas for the constant creep velocity

General case:

$$v = \frac{\sum_{i=1}^{n}\left[\left(W_i + P_{v,i}\right)\sin\alpha_i - P_{h,i}\cos\alpha_i\left(1-\cos\alpha_i\frac{h_i}{r}\right) \right]}{\sum_{i=1}^{n}\left\{ \sin\varphi_i \cdot \left\langle m_i^{VH_{MC}} \right\rangle \sqrt{\frac{v^{\left(1-m_i^{VH_{MC}}\right)}}{2d_i A_i^{VH_{MC}}}} \cdot \left[\begin{array}{l} \left(W_i + P_{v,i}\right)\cos\alpha_i + C_i\cot\varphi_i + P_{h,i}\sin\alpha_i... \\ ...+\left(U_{i(i+1)} - U_{i(i-1)}\right)\sin\alpha_i - U_i \end{array} \right] \right\}} \quad \text{(5.42)}$$

Special case:

For a constant exponent of all slices $m_i^{VH_{MC}} = m^{VH_{MC}}$ the creep velocity is defined by the straightforward formula

$$v = \left\{ \frac{\sum_{i=1}^{n} \left[\left(W_i + P_{v,i}\right)\sin\alpha_i - P_{h,i}\cos\alpha_i\left(1 - \cos\alpha_i \frac{h_i}{r}\right)\right]}{\sum_{i=1}^{n}\left\{ \sin\varphi_i \cdot \left(2d_i A_i^{VH_{MC}}\right)^{\left(\frac{-1}{m_i^{VH_{MC}}}\right)} \cdot \begin{bmatrix} \left(W_i + P_{v,i}\right)\cos\alpha_i + C_i \cot\varphi_i + P_{h,i}\sin\alpha_i... \\ ... + \left(U_{i(i+1)} - U_{i(i-1)}\right)\sin\alpha_i - U_i \end{bmatrix} \right\}} \right\}^{m^{VH_{MC}}} \tag{5.43}$$

A.4.2.3   Ordinary E-CrEAM^{rot}

(d) Original Vulliet-Hutter

Introducing $T_{\dot{\gamma},i}$ according (5.9) into the term for the total normal force $N_{\dot{\gamma},i}$ (5.46) and taking account of the kinematical requirement of constant displacements rates at the slices bases, thus $v_i = v$, yields

$$N_{\dot{\gamma},i} = \frac{W_i + P_{v,i}}{\cos\alpha_i} - \frac{\sqrt{12}\tan\alpha_i\left[C_i\cos\varphi_i + \left(N_{\dot{\gamma},i} - U_i\right)\sin\varphi_i\right]}{3 - \sin\varphi_i} \cdot \left\langle m_i^{VH_{DP}}\right\rangle\sqrt{\frac{v}{2d_i A_i^{VH_{DP}}}} \tag{A.91}$$

By isolating the total normal forces $N_{\dot{\gamma},i}$ in (A.91) on the left hand side we obtain

$$N_{\dot{\gamma},i} = \frac{\dfrac{W_i + P_{v,i}}{\cos\alpha_i} - \dfrac{\sqrt{12}\tan\alpha_i\left(C_i\cos\varphi_i - U_i\sin\varphi_i\right)}{3 - \sin\varphi_i} \cdot \left\langle m_i^{VH_{DP}}\right\rangle\sqrt{\dfrac{v}{2d_i A_i^{VH_{DP}}}}}{1 + \dfrac{\sqrt{12}\tan\alpha_i\sin\varphi_i}{3 - \sin\varphi_i} \cdot \left\langle m_i^{VH_{DP}}\right\rangle\sqrt{\dfrac{v}{2d_i A_i^{VH_{DP}}}}} \tag{A.92}$$

The reduced moment equilibrium equation with the original Vulliet-Hutter relationship is given in (A.87). Replacing the total normal force $N_{\dot{\gamma},i}$ in (A.87) by (A.92) and simplifying the term yields

$$\sum_{i=1}^{n} \left[\begin{array}{c} \langle m_i^{VH_{DP}} \rangle \sqrt{\dfrac{v}{2d_i A_i^{VH_{DP}}}} \cdot \dfrac{\dfrac{W_i + P_{v,i}}{\cos\alpha_i} + C_i \cot\varphi_i - U_i}{\dfrac{3 - \sin\varphi_i}{\sqrt{12}\sin\varphi_i} + \tan\alpha_i \langle m_i^{VH_{DP}} \rangle \sqrt{\dfrac{v}{2d_i A_i^{VH_{DP}}}}} \cdots \\ \cdots - \left(W_i + P_{v,i}\right)\sin\alpha_i + P_{h,i}\cos\alpha_i\left(1 - \cos\alpha_i \dfrac{h_i}{r}\right) \end{array} \right] = 0 \tag{A.93}$$

Expanding the first $\langle m_i^{VH_{DP}} \rangle \sqrt{v}$ in (A.93) according (A.81) and isolating the single v yields the implicit equation for the velocity along the base of the rotational mass, i.e.

$$v = \dfrac{\displaystyle\sum_{i=1}^{n}\left[\left(W_i + P_{v,i}\right)\sin\alpha_i - P_{h,i}\cos\alpha_i\left(1 - \cos\alpha_i\dfrac{h_i}{r}\right)\right]}{\displaystyle\sum_{i=1}^{n}\left[\langle m_i^{VH_{DP}} \rangle \sqrt{\dfrac{v^{\left(1 - m_i^{VH_{DP}}\right)}}{2d_i A_i^{VH_{DP}}}} \cdot \dfrac{\dfrac{W_i + P_{v,i}}{\cos\alpha_i} + C_i \cot\varphi_i - U_i}{\dfrac{3 - \sin\varphi_i}{\sqrt{12}\sin\varphi_i} + \tan\alpha_i \langle m_i^{VH_{DP}} \rangle \sqrt{\dfrac{v}{2d_i A_i^{VH_{DP}}}}}\right]} \tag{5.47}$$

(e) Modified Vulliet-Hutter

The equations for the modified Vulliet-Hutter constitutive model are found by introducing (5.10) for the shear forces $T_{\dot{\gamma},i}$ both in the moment equilibrium equation (5.34) and in the formulation for the total normal force $N_{\dot{\gamma},i}$ (5.46). Applying the same procedure as for the original Vulliet-Hutter approach in the previous subsection (d) leads to the final formula for the creep velocity along the base of the rotational sliding mass, i.e.

$$v = \dfrac{\displaystyle\sum_{i=1}^{n}\left[\left(W_i + P_{v,i}\right)\sin\alpha_i - P_{h,i}\cos\alpha_i\left(1 - \cos\alpha_i\dfrac{h_i}{r}\right)\right]}{\displaystyle\sum_{i=1}^{n}\left[\langle m_i^{VH_{MC}} \rangle \sqrt{\dfrac{v^{\left(1 - m_i^{VH_{MC}}\right)}}{2d_i A_i^{VH_{MC}}}} \cdot \dfrac{\dfrac{W_i + P_{v,i}}{\cos\alpha_i} + C_i \cot\varphi_i - U_i}{\dfrac{1}{\sin\varphi_i} + \tan\alpha_i \langle m_i^{VH_{MC}} \rangle \sqrt{\dfrac{v}{2d_i A_i^{VH_{MC}}}}}\right]} \tag{5.48}$$

A.4.3   Translational mechanism with irregular creep interface

In analogy to the Simplified Janbu approach in the stability analysis we can assume that the difference of the vertical components of the effective interslice forces acting on a slice i are small and can be neglected, thus

$$E'_{\dot\gamma,i(i-1)} \sin \vartheta_{i(i-1)} - E'_{\dot\gamma,i(i+1)} \sin \vartheta_{i(i+1)} \approx 0 \tag{5.45}$$

Considering this assumption in (5.49) reduces the vertical force equilibrium equation to

$$W_i + P_{v,i} - N_{\dot\gamma,i} \cos\alpha_i - T_{\dot\gamma,i} \sin\alpha_i = 0 \tag{A.94}$$

Consequently, the effective interslice forces are represented in the equilibrium equations only by their horizontal components $E'_{\dot\gamma,i(i+1)} \cos \vartheta_{i(i+1)} = E'_{\dot\gamma,(i+1)i} \cos \vartheta_{(i+1)i}$. Following the principle of *"actio est reactio"*, the total horizontal resultants of opposite interslice forces are equal in value, thus, for $i = \{2,...,n-1\}$ applies

$$\left| \vec{E}'_{\dot\gamma,i(i+1)} \cos \vartheta_{i(i+1)} + \vec{U}_{i(i+1)} \right| = \left| \vec{E}'_{\dot\gamma,(i+1)i} \cos \vartheta_{(i+1)i} + \vec{U}_{(i+1)i} \right|$$
$$\left| \vec{E}'_{\dot\gamma,i(i-1)} \cos \vartheta_{i(i-1)} + \vec{U}_{i(i-1)} \right| = \left| \vec{E}'_{\dot\gamma,(i-1)i} \cos \vartheta_{(i-1)i} + \vec{U}_{(i-1)i} \right| \tag{A.95}$$

In the summation of all horizontal force equilibrium equations the interslice forces therefore cancel out, yielding

$$\sum_{i=1}^{n} \left(P_{h,i} - N_{\dot\gamma,i} \sin\alpha_i + T_{\dot\gamma,i} \cos\alpha_i \right) = 0 \tag{A.96}$$

Isolating $N_{\dot\gamma,i}$ in the vertical force equilibrium equation (A.94) yields

$$N_{\dot\gamma,i} = \frac{W_i + P_{v,i}}{\cos\alpha_i} - T_{\dot\gamma,i} \tan\alpha_i \tag{A.97}$$

Substituting $N_{\dot\gamma,i}$ in (A.96) by (A.97) yields

$$\sum_{i=1}^{n} \left[P_{h,i} - \left(W_i + P_{v,i} \right) \tan\alpha_i + T_{\dot\gamma,i} \left(\sin\alpha_i \tan\alpha_i + \cos\alpha_i \right) \right] = 0 \tag{A.98}$$

Introducing the diverse constitutive relationsships developed in Section 5.2 for $T_{\dot\gamma,i}$ in (A.98) yields different solutions for the creep velocity, as shown subsequently.

A.4.3.1 D-CrEAM^{trans}

(c) Norton

Introducing $T_{\dot{\gamma},i}$ according (5.8) in (A.98) yields

$$\sum_{i=1}^{n}\left[P_{h,i}-\left(W_{i}+P_{v,i}\right)\tan\alpha_{i}+b_{i}\left(1+\tan^{2}\alpha_{i}\right)\cdot\left(\tau_{y,i}^{Norton}+\left\langle m_{i}^{Norton}\right\rangle\sqrt{\frac{v_{i}\overline{\mu}_{i}^{Norton}}{d_{i}}}\right)\right]=0 \qquad\text{(A.99)}$$

Taking account of the required kinematical chain of slice displacements, the creep velocity v_{i} can be expressed by (5.17), changing (A.99) to

$$\sum_{i=1}^{n}\left\{P_{h,i}-\left(W_{i}+P_{v,i}\right)\tan\alpha_{i}+b_{i}\left(1+\tan^{2}\alpha_{i}\right)\cdot\left[\tau_{y,i}^{Norton}+\left\langle m_{i}^{Norton}\right\rangle\sqrt{\frac{v_{1}\overline{\mu}_{i}^{Norton}}{d_{i}}\cdot\frac{\cos\alpha_{1}}{\cos\alpha_{i}}}\right]\right\}=0 \qquad\text{(A.100)}$$

General case:

Dividing (A.100) into two portions as following

$$\sum_{i=1}^{n}\left[b_{i}\left(1+\tan^{2}\alpha_{i}\right)\cdot\left\langle m_{i}^{Norton}\right\rangle\sqrt{\frac{v_{1}\overline{\mu}_{i}^{Norton}}{d_{i}}\cdot\frac{\cos\alpha_{1}}{\cos\alpha_{i}}}\right]=...$$

$$...=\sum_{i=1}^{n}\left[\left(W_{i}+P_{v,i}\right)\tan\alpha_{i}-P_{h,i}-b_{i}\tau_{y,i}^{Norton}\left(1+\tan^{2}\alpha_{i}\right)\right] \qquad\text{(A.101)}$$

and substituting $\left\langle m_{i}^{Norton}\right\rangle\sqrt{v_{1}}$ in (A.101) by

$$\left\langle m_{i}^{Norton}\right\rangle\sqrt{v_{1}}=v_{1}^{\left(\frac{1}{m_{i}^{Norton}}\right)}=v_{1}\cdot v_{1}^{\left(\frac{1-m_{i}^{Norton}}{m_{i}^{Norton}}\right)} \qquad\text{(A.102)}$$

yields

$$v_{1}\cdot\sum_{i=1}^{n}\left[v_{1}^{\left(\frac{1-m_{i}^{Norton}}{m_{i}^{Norton}}\right)}\cdot b_{i}\left(1+\tan^{2}\alpha_{i}\right)\cdot\left\langle m_{i}^{Norton}\right\rangle\sqrt{\frac{\overline{\mu}_{i}^{Norton}}{d_{i}}\cdot\frac{\cos\alpha_{1}}{\cos\alpha_{i}}}\right]=...$$

$$...=\sum_{i=1}^{n}\left[\left(W_{i}+P_{v,i}\right)\tan\alpha_{i}-P_{h,i}-b_{i}\tau_{y,i}^{Norton}\left(1+\tan^{2}\alpha_{i}\right)\right] \qquad\text{(A.103)}$$

Isolating v_1 yields the implicit equation for the velocity of slice 1

$$v_1 = \frac{\sum_{i=1}^{n}\left[\left(W_i + P_{v,i}\right)\tan\alpha_i - P_{h,i} - b_i\tau_{y,i}^{Norton}\left(1+\tan^2\alpha_i\right)\right]}{\sum_{i=1}^{n}\left[v_1^{\left(\frac{1-m_i^{Norton}}{m_i^{Norton}}\right)}\cdot b_i\left(1+\tan^2\alpha_i\right)\cdot \sqrt[\langle m_i^{Norton}\rangle]{\frac{\bar{\mu}_i^{Norton}}{d_i}}\cdot\frac{\cos\alpha_1}{\cos\alpha_i}\right]} \tag{5.56}$$

Special case:

Assuming a constant exponent for all slices $m_i^{Norton} = m^{Norton}$ allows to totally extract v_1 in (A.101), leading to

$$\sqrt[\langle m^{Norton}\rangle]{v_1}\sum_{i=1}^{n}\left[b_i\left(1+\tan^2\alpha_i\right)\cdot\sqrt[\langle m^{Norton}\rangle]{\frac{\bar{\mu}_i^{Norton}}{d_i}}\cdot\frac{\cos\alpha_1}{\cos\alpha_i}\right] = \dots$$

$$\dots = \sum_{i=1}^{n}\left[\left(W_i + P_{v,i}\right)\tan\alpha_i - P_{h,i} - b_i\tau_{y,i}^{Norton}\left(1+\tan^2\alpha_i\right)\right] \tag{A.104}$$

Isolating v_1 yields the straightforward equation for the velocity of slice 1 as

$$v_1 = \left\{\frac{\sum_{i=1}^{n}\left[\left(W_i + P_{v,i}\right)\tan\alpha_i - P_{h,i} - b_i\tau_{y,i}^{Norton}\left(1+\tan^2\alpha_i\right)\right]}{\sum_{i=1}^{n}\left[b_i\left(1+\tan^2\alpha_i\right)\cdot\sqrt[\langle m^{Norton}\rangle]{\frac{\bar{\mu}_i^{Norton}}{d_i}}\cdot\frac{\cos\alpha_1}{\cos\alpha_i}\right]}\right\}^{m^{Norton}} \tag{5.57}$$

(b) Bingham

For the linear Bingham model the exponent is set to unity $m^{Norton} = 1$, modifying equation (5.57) to

$$v_1 = \frac{\sum_{i=1}^{n}\left[\left(W_i + P_{v,i}\right)\tan\alpha_i - P_{h,i} - b_i\tau_{y,i}^{Bingham}\left(1+\tan^2\alpha_i\right)\right]}{\sum_{i=1}^{n}\left[b_i\left(1+\tan^2\alpha_i\right)\cdot\frac{\bar{\mu}_i^{Bingham}}{d_i}\cdot\frac{\cos\alpha_1}{\cos\alpha_i}\right]} \tag{5.55}$$

(a) Newton

For the Newton model the yield shear stress is set to zero $\tau_{y,i}^{Bingham} = 0$, modifying equation (5.55) to

$$v_1 = \frac{\sum_{i=1}^{n}\left[\left(W_i + P_{v,i}\right)\tan\alpha_i - P_{h,i}\right]}{\sum_{i=1}^{n}\left[b_i\left(1+\tan^2\alpha_i\right) \cdot \dfrac{\overline{\mu}_i^{Newton}}{d_i} \cdot \dfrac{\cos\alpha_1}{\cos\alpha_i}\right]} \tag{5.54}$$

A.4.3.2 E-CrEAM^{trans}

(d) Original Vulliet-Hutter

Introducing $T_{\dot{\gamma},i}$ according (5.9) in the overall sum of the horizontal equilibrium equations (A.96) yields

$$\sum_{i=1}^{n}\left\{P_{h,i} - N_{\dot{\gamma},i}\sin\alpha_i + \frac{\sqrt{12}\cos\alpha_i\left[C_i\cos\varphi_i + \left(N_{\dot{\gamma},i} - U_i\right)\sin\varphi_i\right]}{3-\sin\varphi_i} \cdot \langle m_i^{VHDP}\rangle\sqrt{\frac{v_i}{2d_i A_i^{VH_{DP}}}}\right\} = 0 \tag{A.105}$$

Condensing the total normal forces $N_{\dot{\gamma},i}$ modifies (A.105) to

$$\sum_{i=1}^{n}\left\{\begin{array}{l}P_{h,i} - N_{\dot{\gamma},i}\left[\sin\alpha_i - \dfrac{\sqrt{12}\cos\alpha_i\sin\varphi_i}{3-\sin\varphi_i} \cdot \langle m_i^{VHDP}\rangle\sqrt{\dfrac{v_i}{2d_i A_i^{VH_{DP}}}}\right]\cdots \\ \cdots + \dfrac{\sqrt{12}\cos\alpha_i\left(C_i\cos\varphi_i - U_i\sin\varphi_i\right)}{3-\sin\varphi_i} \cdot \langle m_i^{VHDP}\rangle\sqrt{\dfrac{v_i}{2d_i A_i^{VH_{DP}}}}\end{array}\right\} = 0 \tag{A.106}$$

Introducing $T_{\dot{\gamma},i}$ according (5.9) in (A.97) and isolating $N_{\dot{\gamma},i}$ yields the total normal force as a function of the velocity v_i (equivalent to (A.92))

$$N_{\dot{\gamma},i} = \frac{\dfrac{W_i + P_{v,i}}{\cos\alpha_i} - \dfrac{\sqrt{12}\tan\alpha_i\left(C_i\cos\varphi_i - U_i\sin\varphi_i\right)}{3-\sin\varphi_i} \cdot \langle m_i^{VHDP}\rangle\sqrt{\dfrac{v_i}{2d_i A_i^{VH_{DP}}}}}{1 + \dfrac{\sqrt{12}\tan\alpha_i\sin\varphi_i}{3-\sin\varphi_i} \cdot \langle m_i^{VHDP}\rangle\sqrt{\dfrac{v_i}{2d_i A_i^{VH_{DP}}}}} \tag{A.107}$$

Introducing (A.107) in (A.106) and simplifying the term yields

$$\sum_{i=1}^{n}\left[\left(W_i + P_{v,i} - \frac{\Lambda_i \sin\alpha_i}{I_i^{DP}} \cdot \left\langle m_i^{VH_{DP}}\right\rangle\sqrt{\frac{v_i}{2d_i A_i^{VH_{DP}}}}\right)\left(\frac{\frac{\sin\varphi_i}{I_i^{DP}} \cdot \left\langle m_i^{VH_{DP}}\right\rangle\sqrt{\frac{v_i}{2d_i A_i^{VH_{DP}}}} - \tan\alpha_i}{1 + \frac{\tan\alpha_i \sin\varphi_i}{I_i^{DP}} \cdot \left\langle m_i^{VH_{DP}}\right\rangle\sqrt{\frac{v_i}{2d_i A_i^{VH_{DP}}}}}\right)\dots \atop \dots + \frac{\Lambda_i \cos\alpha_i}{I_i^{DP}} \cdot \left\langle m_i^{VH_{DP}}\right\rangle\sqrt{\frac{v_i}{2d_i A_i^{VH_{DP}}}} + P_{h,i}\right] = 0 \quad \text{(A.108)}$$

where the variables Λ_i and I_i^{DP}, respectively, substitute for the terms

$$\Lambda_i = C_i \cos\varphi_i - U_i \sin\varphi_i \tag{5.59}$$

$$I_i^{DP} = \frac{3 - \sin\varphi_i}{\sqrt{12}} \tag{5.60}$$

Taking account of the required kinematical chain of slice displacements, the creep velocity v_i can be expressed by (5.17), changing (A.108) to

$$\sum_{i=1}^{n}\left[\left(W_i + P_{v,i} - \frac{\Lambda_i \sin\alpha_i}{I_i^{DP}} \cdot \left\langle m_i^{VH_{DP}}\right\rangle\sqrt{\frac{v_1}{k_i^{\alpha VH_{DP}}}}\right)\left(\frac{\frac{\sin\varphi_i}{I_i^{DP}} \cdot \left\langle m_i^{VH_{DP}}\right\rangle\sqrt{\frac{v_1}{k_i^{\alpha VH_{DP}}}} - \tan\alpha_i}{1 + \frac{\tan\alpha_i \sin\varphi_i}{I_i^{DP}} \cdot \left\langle m_i^{VH_{DP}}\right\rangle\sqrt{\frac{v_1}{k_i^{\alpha VH_{DP}}}}}\right)\dots \atop \dots + \frac{\Lambda_i \cos\alpha_i}{I_i^{DP}} \cdot \left\langle m_i^{VH_{DP}}\right\rangle\sqrt{\frac{v_1}{k_i^{\alpha VH_{DP}}}} + P_{h,i}\right] = 0 \quad \text{(A.109)}$$

where the variable $k_i^{\alpha VH_{DP}}$ substitutes for the term

$$k_i^{\alpha VH_{DP}} = 2d_i A_i^{VH_{DP}} \cdot \frac{\cos\alpha_1}{\cos\alpha_i} \tag{5.61}$$

215

Subsequently, equation (A.109) can be splitted in two portions as following

$$\sum_{i=1}^{n}\left[\sqrt[\langle m_i^{VH_{DP}}\rangle]{\frac{v_1}{k_i^{\alpha VH_{DP}}}}\cdot\left(\frac{\Lambda_i\cos\alpha_i}{\mathrm{I}_i^{DP}}+\frac{W_i+P_{v,i}-\dfrac{\Lambda_i\sin\alpha_i}{\mathrm{I}_i^{DP}}\cdot\sqrt[\langle m_i^{VH_{DP}}\rangle]{\dfrac{v_1}{k_i^{\alpha VH_{DP}}}}}{\dfrac{\mathrm{I}_i^{DP}}{\sin\varphi_i}+\tan\alpha_i\cdot\sqrt[\langle m_i^{VH_{DP}}\rangle]{\dfrac{v_1}{k_i^{\alpha VH_{DP}}}}}\right)\right]=\ldots$$

$$\ldots=\sum_{i=1}^{n}\left[\frac{W_i+P_{v,i}-\dfrac{\Lambda_i\sin\alpha_i}{\mathrm{I}_i^{DP}}\cdot\sqrt[\langle m_i^{VH_{DP}}\rangle]{\dfrac{v_1}{k_i^{\alpha VH_{DP}}}}}{\dfrac{1}{\tan\alpha_i}+\dfrac{\sin\varphi_i}{\mathrm{I}_i^{DP}}\cdot\sqrt[\langle m_i^{VH_{DP}}\rangle]{\dfrac{v_1}{k_i^{\alpha VH_{DP}}}}}-P_{h,i}\right]$$

(A.110)

Expanding in the left-hand side of expression (A.110) the first $\sqrt[\langle m_i^{VH_{DP}}\rangle]{v_1}$ according (A.81) and isolating the single v_1 yields the implicit equation for the velocity of slice 1

$$v_1=\frac{\displaystyle\sum_{i=1}^{n}\left[\frac{W_i+P_{v,i}-\dfrac{\Lambda_i\sin\alpha_i}{\mathrm{I}_i^{DP}}\cdot\sqrt[\langle m_i^{VH_{DP}}\rangle]{\dfrac{v_1}{k_i^{\alpha VH_{DP}}}}}{\dfrac{1}{\tan\alpha_i}+\dfrac{\sin\varphi_i}{\mathrm{I}_i^{DP}}\cdot\sqrt[\langle m_i^{VH_{DP}}\rangle]{\dfrac{v_1}{k_i^{\alpha VH_{DP}}}}}-P_{h,i}\right]}{\displaystyle\sum_{i=1}^{n}\left[\sqrt[\langle m_i^{VH_{DP}}\rangle]{\frac{v_1^{1-m_i^{VH_{DP}}}}{k_i^{\alpha VH_{DP}}}}\cdot\left(\frac{\Lambda_i\cos\alpha_i}{\mathrm{I}_i^{DP}}+\frac{W_i+P_{v,i}-\dfrac{\Lambda_i\sin\alpha_i}{\mathrm{I}_i^{DP}}\cdot\sqrt[\langle m_i^{VH_{DP}}\rangle]{\dfrac{v_1}{k_i^{\alpha VH_{DP}}}}}{\dfrac{\mathrm{I}_i^{DP}}{\sin\varphi_i}+\tan\alpha_i\cdot\sqrt[\langle m_i^{VH_{DP}}\rangle]{\dfrac{v_1}{k_i^{\alpha VH_{DP}}}}}\right)\right]}$$

(5.58)

(e) Modified Vulliet-Hutter

The equations for the modified Vulliet-Hutter constitutive relationship are found by introducing (5.10) for the shear forces $T_{\dot{\gamma},i}$ both in the overall sum of the horizontal equilibrium equations (A.96) and in the formulation for the total normal force $N_{\dot{\gamma},i}$ (A.97). The same procedure as shown for the original Vulliet-Hutter approach in the previous section (d) leads to the final formula for the creep velocity v_1, i.e.

$$
v_1 = \frac{\displaystyle\sum_{i=1}^{n}\left[\frac{W_i + P_{v,i} - \Lambda_i \sin\alpha_i \cdot \sqrt[\langle m_i^{VH_{MC}}\rangle]{\dfrac{v_1}{k_i^{\alpha VH_{MC}}}}}{\dfrac{1}{\tan\alpha_i} + \sin\varphi_i \cdot \sqrt[\langle m_i^{VH_{MC}}\rangle]{\dfrac{v_1}{k_i^{\alpha VH_{MC}}}}} - P_{h,i}\right]}{\displaystyle\sum_{i=1}^{n}\left[\sqrt[\langle m_i^{VH_{MC}}\rangle]{\dfrac{v_1^{1-m_i^{VH_{MC}}}}{k_i^{\alpha VH_{MC}}}} \cdot \left(\Lambda_i \cos\alpha_i + \frac{W_i + P_{v,i} - \Lambda_i \sin\alpha_i \cdot \sqrt[\langle m_i^{VH_{MC}}\rangle]{\dfrac{v_1}{k_i^{\alpha VH_{MC}}}}}{\dfrac{1}{\sin\varphi_i} + \tan\alpha_i \cdot \sqrt[\langle m_i^{VH_{MC}}\rangle]{\dfrac{v_1}{k_i^{\alpha VH_{MC}}}}} \right)\right]}
\tag{5.62}
$$

with the substitutions Λ_i as defined in (5.59) and $k_i^{\alpha VH_{MC}}$ given by

$$
k_i^{\alpha VH_{MC}} = 2 d_i A_i^{VH_{MC}} \cdot \frac{\cos\alpha_1}{\cos\alpha_i}
\tag{5.63}
$$

A.5 Beauregard rockslide: Supplements

Supplementary data to the Beauregard case study in Chapter 6.

A.5.1 Strength experiments

The peak shear resistance of the shear zone material was investigated by Martinotti (2010) by means of Casagrande direct shear tests (normal stress range 0.5-6.0 MPa) and isotropically consolidated undrained (CIU) triaxial tests (hydrostatic stress range 5.7-8.6 MPa). Additionally, a single direct shear test was performed with the HPBPSA at an effective normal stress of 4 MPa, in order to validate the results from the Casagrande direct shear tests. The residual shear strength was investigated with ring shear experiments, however at a much lower normal stress level as the direct shear and triaxial tests (0.20-0.85 MPa). Most of the samples were undisturbed. Remoulded samples were used for the ring shear tests and partly for the direct shear tests.

The detailed boundary conditions and data of the undrained triaxial experiments are summarized in Table A.1, those of the direct and ring shear experiments in Table A.2.

Table A.1
Overview of the experimental boundary conditions and results of the isotropically consolidated undrained (CIU) triaxial experiments (data summarized from Martinotti 2010). σ'_{1f} and σ'_{3f} … effective axial and radial stress at failure; v … constant displacement rate

Experiment type	Sample name (Test Code)	Borehole drill-metre	Sample description	σ'_{1f} MPa	σ'_{3f} MPa
CIU Triaxial test v=0.02 mm/min	C.I.3(2004) Tx1	S1/04 246.60m	undisturbed, saturated	10.71	4.19
	C.I.3(2004) Tx2	S1/04 246.70m	undisturbed, saturated	13.21	5.37
	C.I.3(2004) Tx3	S1/04 246.80m	undisturbed, saturated	13.94	5.44
	C.I.4(2004) Tx4	S1/04 247.40m	undisturbed, saturated	9.98	3.70
	C.I.4(2004) Tx5	S1/04 247.50m	undisturbed, saturated	12.81	4.96
	C.I.4(2004) Tx6	S1/04 247.60m	undisturbed, saturated	14.82	5.52

Table A.2

Overview of the experimental boundary conditions and results of the direct and ring shear tests (data summarized from Martinotti 2010).

σ … total vertical stress in direct shear test (Casagrande or HPBPSA) or in the ring shear test (Bromhead); u … back pressure in the HPBPSA (corresponds to the porewater pressure in the sample); τ_{peak} … shear stress at failure of the sample (peak); τ_{res} … residual shear strength; v … constant displacement rate

Experiment type	Sample name (Test Code)	Borehole drill-metre	Sample description	σ MPa	u MPa	τ_{peak} MPa	τ_{res} MPa
	C.I.4 (2004) DS1	S1/04 247.80m	undisturbed, moist (w=10.1%)	4.49	-	2.60	-
	C.I.4 (2004) DS2	S1/04 247.78m	undisturbed, moist (w=9.2%)	5.00	-	2.88	-
	C.I.4 (2004) DS3	S1/04 247.76m	undisturbed, moist (w=9.0%)	5.54	-	3.26	-
Direct shear test Casagrande v=0.02 mm/min	C4(2003) DS4	S1-2/03 28.08m	undisturbed, moist (w=13.4%)	4.01	-	2.38	-
	C4(2003) DS5	S1-2/03 28.11m	undisturbed, moist (w=12.5%)	4.99	-	2.60	-
	C4(2003) DS6	S1-2/03 28.14m	undisturbed, moist (w=13.2%)	6.03	-	3.42	-
	C.I.1(2004) DS_Beau_001	S1/04 236.40m-236.90 m	remoulded*, moist (w=23.3%)	1.67	-	0.95	-
	C.I.1(2004) DS_Beau_002	S1/04 236.40m-236.90 m	remoulded*, moist (w=21.7%)	0.50	-	0.27	-
Direct shear test HPBPSA v=0.006 mm/min	C.I.1(2004) HPBPS_Beau_001	S1/04 236.80m	undisturbed, saturated	5.05	1.10	2.20	-
Ring shear test Bromhead v=0.225 °/min	C.I.1(2004) RS_Beau_001	S1/04 236.40m-236.90 m	remoulded*, moist (w=23.3%)	0.19 0.39 0.58	- - -	- - -	0.09 0.18 0.27
	C.I.1(2004) RS_Beau_002	S1/04 236.40m-236.90 m	remoulded*, moist (w=21.7%)	0.29 0.49 0.85	- - -	- - -	0.13 0.22 0.39

* Grain sizes larger than 0.25 mm have been sieved out

The test results were interpreted in terms of the Mohr-Coulomb failure criterion, using a linear regression analysis (Martinotti 2010, Figure A.4 and Figure A.5). Assuming a purely frictional material, thus $c = 0$, the direct shear experiments give a peak friction angle of $\varphi_{peak} = 29.7°$ while the triaxial experiments yield $\varphi_{peak} = 26.2°$.

The residual friction angle obtained from the ring shear tests is $\varphi_{res} = 24.6°$, however this value is based on experiments at a very low normal stress level. Table 6.3 in the main part summarizes the strength parameters as obtained from laboratory testing.
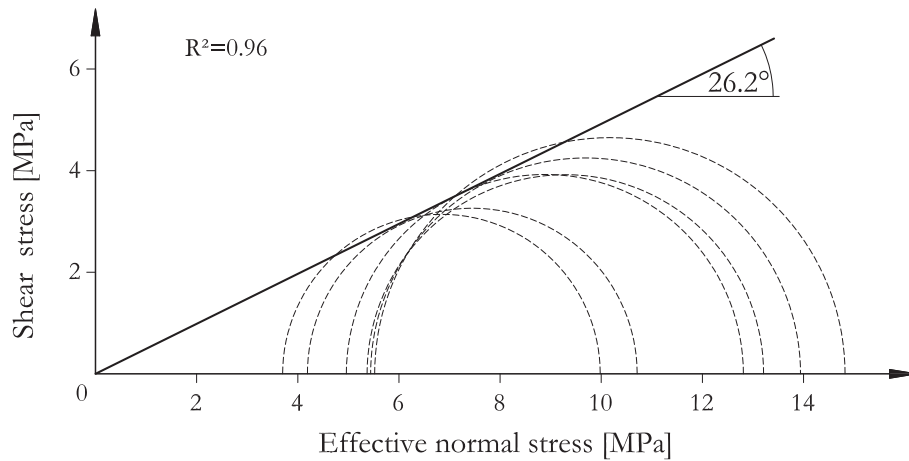
Figure A.4
Results of the isotropically consolidated undrained (CIU) triaxial tests (data from Martinotti 2010).
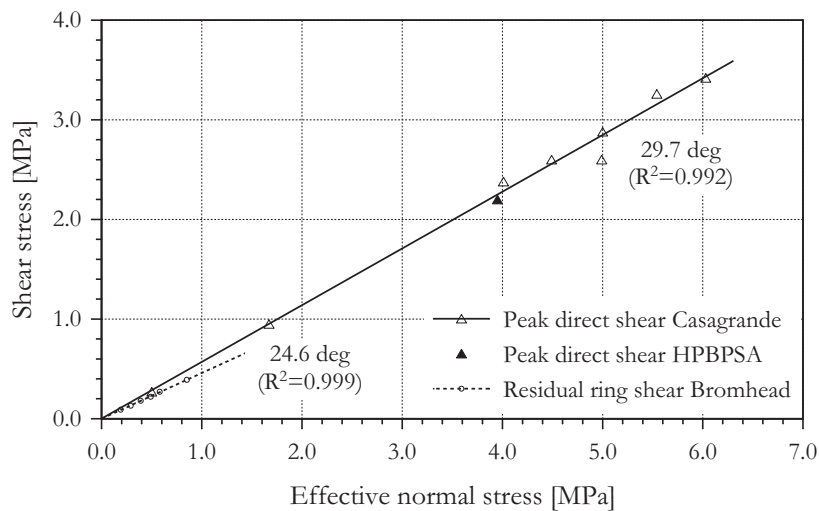
Figure A.5
Results of the direct shear (Casagrande and HPBPSA) and ring shear tests. The continuous line refers to the regression of the Casagrande direct shear results. The single direct shear experiment in the HPBPSA with back pressure is not accounted in the regression but fits well in this trend for the peak strength. The dashed line indicates the regression of the ring shear results (data from Martinotti 2010).

A.5.2 Creep experiments

A.5.2.1 Creep experiment laboratory data

Figure A.6 shows the results of the creep experiments performed by Martinotti (2010) in the direct shear setting (Casagrande and HPBPSA). The detailed testing boundary conditions and regression results are summarized in Table A.3.

Three remoulded samples were kept under constand load in the Casagrande apparatus (test codes DSc1-DSc3), using similar normal stress levels as in the strain-controlled tests for strength determination (4-5 MPa), and a shear loading corresponding to respective 71%, 82% and 85% of the failure load. Another remoulded sample was tested in the HPBPSA until reaching tertiary creep failure (HPBPS_Beau_ri003). One undisturbed sample was investigated by means of the HPBPSA in a multi-stage creep experiment. Creep deformation was observed in the first two loading steps, i.e. HPBPS_Beau_002(1) and HPBPS_Beau_002(2), while the sample immediately failed when the load was increased to a third loading level. A comparision with the other creep curves in Figure A.6 suggests that HPBPS_Beau_002(1/2) did not achieve the seconday (steady) creep stage.
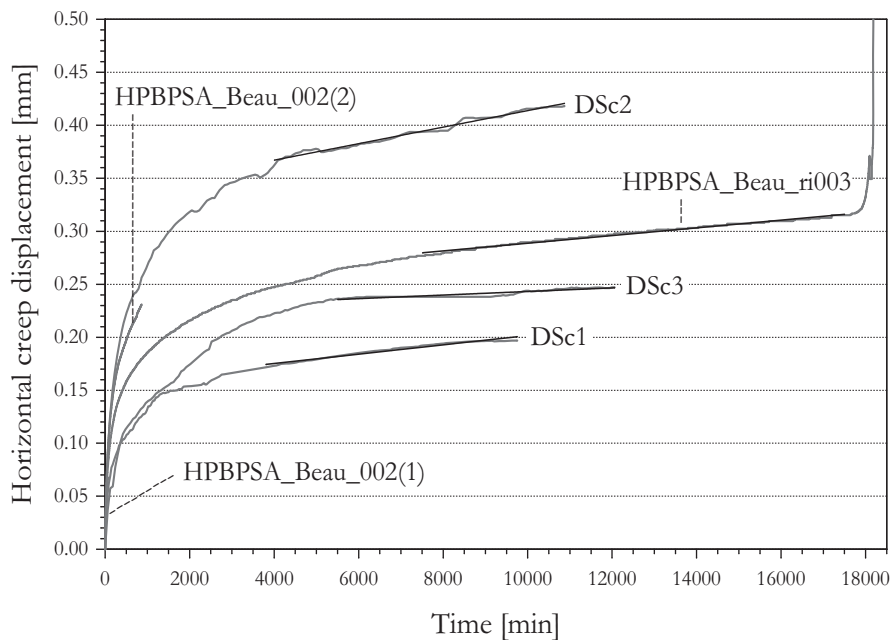
Figure A.6
Creep curves (horizontal displacement versus time, gray lines) of the creep experiments in the direct shear setting (Casagrande and HPBPSA). Black lines indicate the regression analysis results for the secondary creep stage (data from Martinotti 2010).

Table A.3

Overview of direct shear creep experiments (summarized from Martinotti 2010). σ … total vertical stress in the direct shear test (Casagrande or HPBPSA); u … back pressure in the HPBPSA (corresponds to the pore-water pressure in the sample); τ_{creep} shear stress levels inducing creep in the shear plane; t_{creep} … duration of creep observation, $\dot{s}_{creepII}$ … constant horizontal displacement rate in the secondary creep stage, $\dot{\gamma}_{creepII}$ … constant angular shear strain rate in the secondary creep stage, τ_f … shear stress necessary to induce tertiary creep (failure in the shear plane), d … gap between the upper and lower shear frame.

Experiment type	Sample name (Test Code)	Borehole drill-metre	Sample description	σ [MPa]	u [MPa]	τ_{creep} ($\%\tau_f$) t_{creep} $\begin{bmatrix} MPa \\ \% \\ min \end{bmatrix}$	$\dot{s}_{creepII}\cdot 10^{-6}$ $\dot{\gamma}_{creepII}\cdot 10^{-7}$ $\begin{bmatrix} mm/min \\ s^{-1} \end{bmatrix}$	τ_f [MPa]
Direct shear Casagrande d=0.64mm	C7(2003) DSc1	S1-2/03 27.13m	remoulded, moist (w=7.9%)	4.95	-	1.95 (71%) 9750	4.40 1.15	2.73
	C7(2003) DSc2	S1-2/03 27.13m	remoulded, moist (w=7.9%)	4.95	-	2.16 (85%) 10869	7.80 2.03	2.53
	C3(2003) DSc3	S1-2/03 7.98m	remoulded, moist (w=12.6%)	4.03	-	1.89 (82%) 12060	1.69 0.44	2.31
Direct shear HPBPSA d=0.25mm	C.I.1(2004) HPBPS_Beau_002(1)	S1/04 236.70m	undisturbed, saturated	5.00	1.11	0.90 (55%) 68	(*)	1.65
	C.I.1(2004) HPBPS_Beau_002(2)					1.35 (82%) 864	(*)	
	mix of C.I.1-5 (2004) HPBPS_Beau_ri003	S1/04 236.90- 249.90m	remoulded, saturated	5.00	1.11	1.43 (**) 18195	3.63 2.42	-

(*) Secondary creep stage not achieved
(**) Secondary creep was followed by instantaneous creep rupture

A further undisturbed sample was tested by Martinotti (2010) in a multi-stage triaxial creep experiment (Br_Tx_001). The detailed testing boundary conditions are listed in Table A.4 and shown in Figure A.7.

Secondary creep deformations were observed at two different effective normal stress levels like they are expected in situ during the low (autumn/winter) and high (spring/summer) piezometric situation in the shear zone. The total confining stress was kept constant (σ_1 =5.1 MPa; σ_3 =3.0 MPa) while the porewater pressure was changed corresponding to low and high piezometric conditions (u_1 =1.1 MPa and u_2 =1.2 MPa; see Figure A.7). After achieving secondary creep at both porewater pressures, the latter was increased until bringing the sample to failure. The overall multi-stage creep experiment lasted 135 days. The axial strain development in the sample during this time is depicted in Figure A.8. The creep curve shows an increase of the axial strain rate with increased water pressure.

Table A.4
Boundary conditions of the multi-stage creep experiment Br_Tx_001 in the High Pressure Triaxial Apparatus (HPTA). σ_1, σ_3 … total axial and radial stress kept constant during the test; u_{cr1}, u_{cr2} back pressure level (corresponding to the porewater pressure in the sample); u_f … approximate back pressure to induce failure (data from Martinotti 2010).

Experiment type	Sample name (Test Code)	Borehole drill-metre	Sample description	σ_1 MPa	σ_3 MPa	u_{cr1} MPa	u_{cr2} MPa	u_f MPa
Triaxial test	C3(2007) Br_Tx_001	S2/07 233.55-233.70m	undisturbed, saturated	5.1	3.0	1.1	1.2	1.6
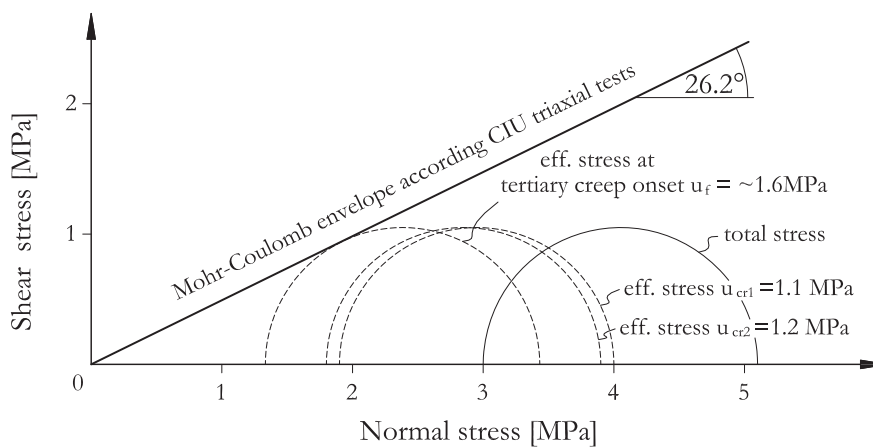
Figure A.7
Boundary conditions of the multi-stage creep experiment Br_Tx_001 in the HPTA (data from Martinotti 2010).
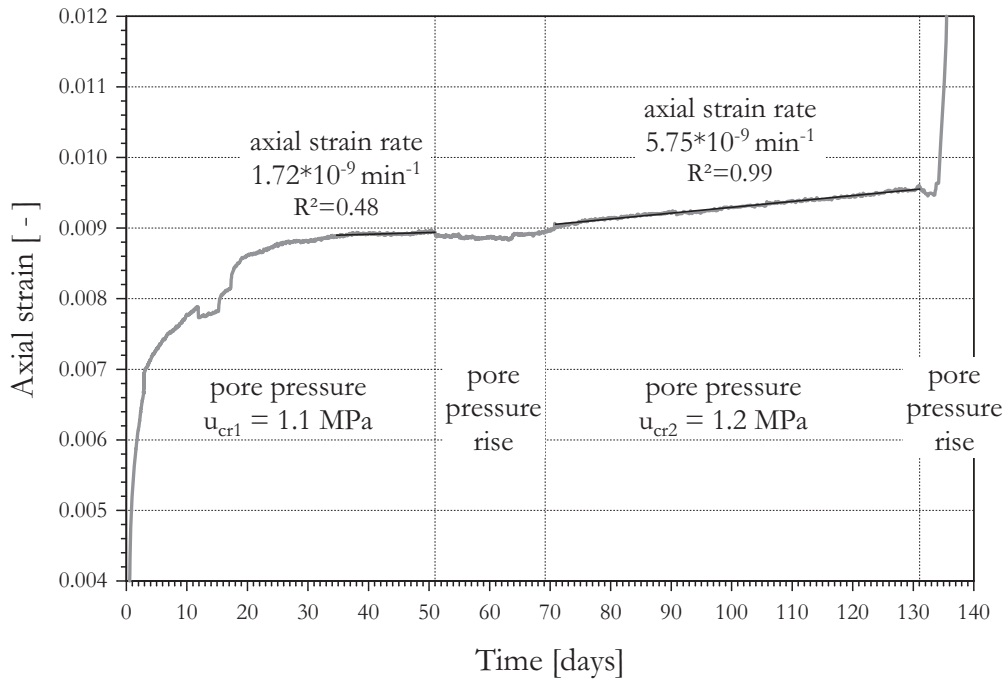
Figure A.8
Axial strain versus time plot of the multi-stage triaxial creep experiment Br_Tx_001. Secondary creep has been achieved for two different pore pressure levels (data from Martinotti 2010). The effective stress conditions are listed in Table A.4 and shown in Figure A.7.

A.5.2.2 Creep experiment interpretation

For CrEAM modelling, the creep experiment results of Martinotti (2010) are interpreted in terms of the viscous models presented in Chapter 3. The interpretations refer to the constant creep rates observed in the secondary creep stage. Separate evaluations are performed for the Casagrande direct shear creep tests (Figure A.6) and the triaxial creep test (Figure A.8), respectively. The experimental data of the HPBPSA creep tests (Figure A.6) cannot be considered, as two of three creep experiments apparently did not reach the secondary creep stage.

Table A.5 shows the regression equations for the interpretation of the direct shear creep experiments. The regression equations assume constant volume deformation, $\dot{\varepsilon}_{vol} = 0$, and $c = 0$.

Table A.5

Regression equations for direct shear creep test interpretation
(for $\dot{\varepsilon}_{vol} = 0$ and $c = 0$)

Constitutive model	Regression equation	x	y
Newton	$y = \overline{\mu}^{Newton} \cdot x$	$\dot{\gamma}_{creepII}$	τ_{creep}
Bingham	$y = \tau_y^{Bingham} + \overline{\mu}^{Bingham} \cdot x$	$\dot{\gamma}_{creepII}$	τ_{creep}
Original Norton	$y = {}^{m^{Norton}}\!\sqrt{\overline{\mu}^{Norton} \cdot x}$	$\dot{\gamma}_{creepII}$	τ_{creep}
Modified Norton	$y = \tau_y^{Norton} + {}^{m^{Norton}}\!\sqrt{\overline{\mu}^{Norton} \cdot x}$	$\dot{\gamma}_{creepII}$	τ_{creep}
Original Vulliet-Hutter	$y = A^{VH_{DP}} \cdot x^{m^{VH_{DP}}}$	$\dfrac{\tau_{creep}}{(\sigma - u)\tan\left[\arcsin\left(\dfrac{\sqrt{12}\sin\varphi}{3 - \sin\varphi}\right)\right]}$	$\dfrac{\dot{\gamma}_{creepII}}{2}$
Modified Vulliet-Hutter	$y = A^{VH_{MC}} \cdot x^{m^{VH_{MC}}}$	$\dfrac{\tau_{creep}}{(\sigma - u)\tan\varphi}$	$\dfrac{\dot{\gamma}_{creepII}}{2}$

In Table A.5, the angular shear strain rate $\dot{\gamma}_{creepII}$ during the secondary creep stage is defined as

$$\dot{\gamma}_{creepII} = \frac{\dot{s}_{creepII}}{d} \tag{A.111}$$

were $\dot{s}_{creepII}$ is the constant horizontal displacement rate in the secondary creep stage, and d is the gap between the upper and lower shear frame. This is a strong simplification since the thickness of the deformed material in the middle of the direct shear apparatus might be considerably larger.

Figure A.9 shows the regression analysis of the Casagrande direct shear creep test results (DSc1-DSc3) according the deviatoric stress based viscous models (Newton, Bingham, original and modified Norton). The result of HPBPSA_Beau_ri003 is plotted for sake of comparison but not included in the analysis.

225
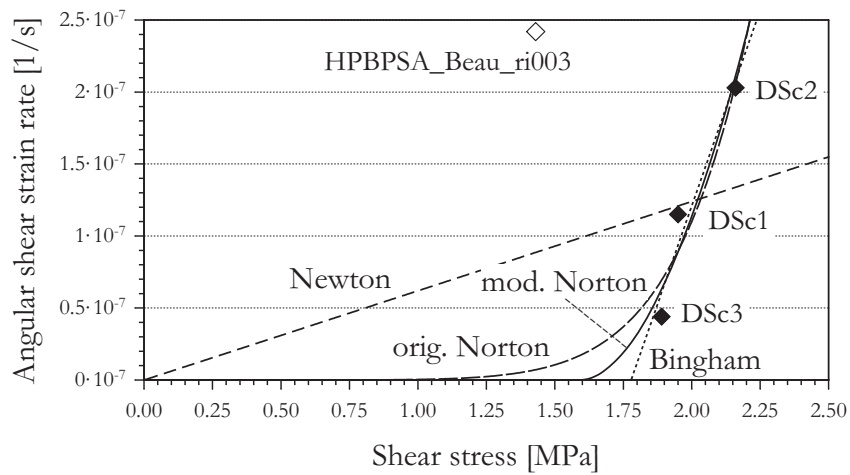
Figure A.9
Direct shear creep test results. Filled diamonds denote the Casagrande
creep tests (DSc1-DSc3). Trendlines show the interpretation of the data in
terms of the deviatoric stress based creep models. For comparison, the
unfilled diamond marks the result of the HPBPSA creep experiment
reaching the secondary creep stage (compare with Figure A.6).
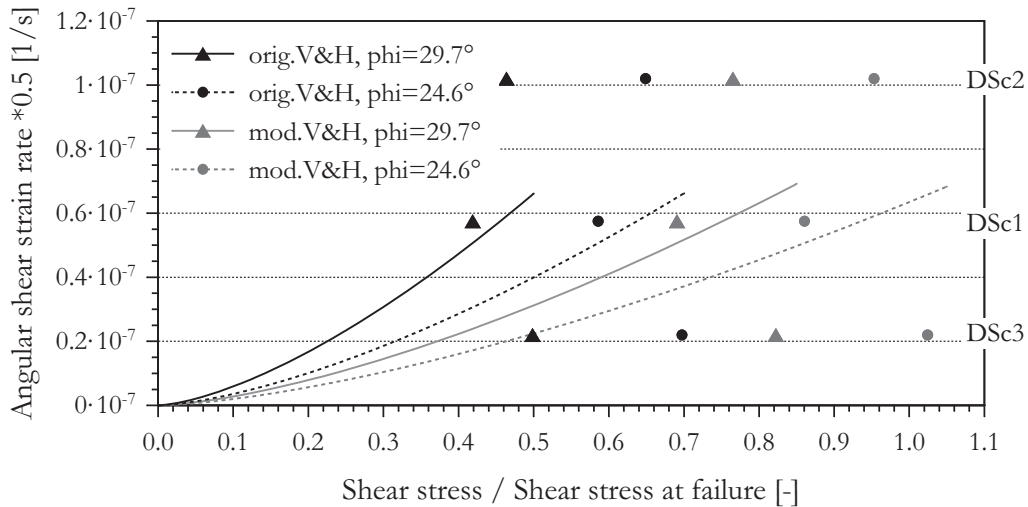
Figure A.10
Casagrande creep test results (DSc1-DSc3) plotted as angular shear strain
rate versus the ratio of shear stress and shear resistance. The three tests
plot as four different datasets because of two differing definitions in terms
of the friction angle (i.e. the values from direct and ring shear testing, see
Table 6.3), and the failure shear stress (definitions according Drucker-
Prager and Mohr-Coulomb, respectively). Trendlines indicate the interpre-
tation in terms of the original and modified Vulliet-Hutter viscous models.

Figure A.10 depicts the regression analysis of the same data (DSc1-DSc3) according the effective stress based viscous models (original and modified Vulliet-Hutter). The three data sets show no trend in the strain rate versus stress ratio plot. Consequently, the regression quality is poor and, therefore, the regression results for the viscous parameters indicate only an order of magnitude.

The two test stages of the triaxial creep experiment Br_Tx_001 are characterised by the same deviatoric stress and different effective normal stress levels (compare with Figure A.7). Referring to the deviatoric stress based constitutive relationships, the experiment can be interpreted only in terms of the one-parameter Newton viscous model. In contrast, the experiment can be evaluated in terms of the effective stress based Vulliet-Hutter models since the variable effective normal stress during the experiment affects the shear resistance which is included in these constitutive relationships (compare with Chapter 3).

Table A.6 shows the regression equations for the interpretation of the triaxial creep experiments. Since the radial strain rate was not measured in the experiment, the interpretation assumes constant volume deformation $\dot{\varepsilon}_{vol} = 0$, and $c = 0$.

Table A.6
Regression equations for triaxial creep test interpretation (for $c = 0$).

Constitutive model	Regression equation	x	y
Newton	$y = \mu^{Newton} \cdot x$	$\dfrac{3}{2}\dot{\varepsilon}_1$	$\dfrac{3}{2}(\sigma_1 - \sigma_3)$
Original Vulliet-Hutter	$y = A^{VH_{DP}} \cdot x^{m^{VH_{DP}}}$	$\dfrac{(3 - \sin\varphi)(\sigma_1 - \sigma_3)}{2\sin\varphi(\sigma_1 + 2\sigma_3)}$	$\dfrac{\sqrt{3}}{2}\dot{\varepsilon}_1$
Modified Vulliet-Hutter	$y = A^{VH_{MC}} \cdot x^{m^{VH_{MC}}}$	$\dfrac{\sigma_1 - \sigma_3}{\sin\varphi(\sigma_1 + \sigma_3)}$	$\dfrac{\sqrt{3}}{2}\dot{\varepsilon}_1$

The viscous parameter sets as obtained by the creep experiment interpretations are summarized in Table 6.4 in the main part of this thesis.